Turbulent Flow and Heat Transfer in Rod Bundles

by

Mohamed Sadok Guellouz

A thesis
presented to the University of Ottawa
in partial fulfilment of the
requirement for the degree of

DOCTOR OF PHILOSOPHY
in
MECHANICAL ENGINEERING

Ottawa-Carleton Institute for
Mechanical and Aerospace Engineering

Ottawa, Ontario, April 1998

To my parents, my first teachers

الإهداء: إلى أمي و أبي

Abstract

Presented in this study is an investigation of turbulent flow and heat transfer near narrow gaps of rod bundles. At first, practical empirical correlations for the subchannel average and the gap local heat transfer coefficients were fitted to experimental results available in the literature. Then, the thesis presents a new technique, using a pendulum, for the calibration of hot-wire anemometers over low velocity ranges, a signal analysis procedure for three-sensor hot-wire probes, and a method for the enhancement of the results of the Variable Interval Time Average (VITA) conditional sampling technique, all used in the main experimental study.

The experimental investigation was conducted in a rectangular channel with an aspect ratio of 2/3, containing a suspended rod, having a diameter equal to half the channel height. The rod was positioned so that it would form a narrow rod-wall gap with the channel base. The flow Reynolds number, based on bulk velocity and hydraulic diameter, was 140,000. Two-point correlations and conditional sampling measurements, using hot-wire anemometry, as well as flow visualization were employed in this study. The experimental investigation substantiated the occurrence of large-scale coherent structures in the gap region, documented their properties and proposed a physical model for them. An explanation for their formation and spatial configuration was also offered. The insensitivity of the intersubchannel mixing and the local heat transfer coefficient to the gap size was explained as a result of the presence of these coherent structures in the gap region. The turbulence structure in the gap region was also investigated. Measurements of the coherent, incoherent and Reynolds averaged statistical properties of the flow were presented and compared to those in turbulent pipe flow.

Acknowledgments

I wish to express deep gratitude to Professor Stavros Tavoularis for his motivating guidance and his continuous availability for constructive discussions. Professor Tavoularis allowed me the freedom to explore and learn and yet he always kept me on track. For that, I am thankful. His quick and careful editing of the manuscript and his many comments and suggestions contributed significantly to the quality of the thesis.

I wish to thank my colleagues and friends, especially Mohsen Ferchichi, for their help and for providing an enjoyable working atmosphere. I extend my thanks to the technical staff of the departmental workshop for providing assistance when needed.

This work was funded by the Natural Sciences and Engineering Research Council of Canada (NSERC), University-Industry Program, and the COG-CANDEV program through Atomic Energy of Canada Limited (AECL). Financial assistance was also provided to the author by the Scientific Mission of Tunisia.

Finally, I am indebted to Sonia for her support, encouragement, patience and mostly her understanding of how important this was to me. I am also grateful to my family for their constant moral support. I have to mention in closing my source of inspiration and the person that kept me company for most of the writing of this thesis: my daughter, Selma.

Table of Contents

List of Tables

List of Figures

Nomenclature

A	geometry parameter in Equation (3) of Chapter 2, also constant in Equations (7) and (13) of Chapter (6) and Equation (1) of Chapter (7), and subchannel flow cross section
A_e	surface area of heated element
a	exponent in the convective heat transfer correlation
B	constant in Equations (8) and (13) of Chapter 6 and Equation (1) of Chapter (7), also ratio of the equivalent diameter of surrounding subchannels and rod diameter
b	exponent in the convective heat transfer correlation
C	constant in the laminar friction factor relationship, also constant in the convective heat transfer correlation
C_f	skin friction coefficient
C_p	heat capacity
c	gap clearance
D	rod diameter
D_e	subchannel or bundle equivalent diameter
D_{eK}	equivalent diameter of the K surrounding subchannels
D_h	hydraulic diameter
D_i	hydraulic diameter of subchannel i
d	Preston tube diameter, also hot-wire diameter
E	anemometer voltage output
E_o	anemometer voltage output for zero flow velocity
E_i	anemometer voltage output when the hot-wire is placed at radius r_i on the pendulum arm
F	flow area
f	friction factor, also frequency

G geometry factor

G^* geometry parameter in Equation (3) of Chapter 2

G_i mass-velocity in subchannel i

Gr Grashof number

h convective heat transfer coefficient, also enthalpy

h_i pitch coefficient for sensor i

I ratio of the bundle average heat transfer coefficient and the circular tube coefficient

J ratio of the minimum local heat transfer coefficient and the bundle average coefficient

k thermal conductivity, also kinetic energy of turbulence, and threshold level in VITA

k_i yaw coefficient for sensor i

L length of heated element of the wall shear stress probe, also the wire length of the hot-wire probe, and streamwise distance from entrance

L_u integral length scale

l maximum vorticity length

M_{ij} mixing Stanton number

N number of detected events

Nu Nusselt number

n exponent in Equations (7) and (13) of Chapter (6) and Equation (1) of Chapter (7)

P pitch (distance between rod centers), also pressure

Pr Prandtl number

P_W subchannel wetted perimeter

p pressure fluctuation according to Reynolds decomposition

Q designates any random process

q convective heat flux, also heat flux around the periphery of the rod

R electric resistance

R_{uw} space-time correlation of the two quantities indicated in the subscript

$R(T)$ hot-wire resistance at temperature T

Re Reynolds number

Re_h Reynolds number based on the bulk velocity and the channel hydraulic diameter

Re_x Reynolds number based on free stream velocity and length along the flat plate

r	radius along the pendulum arm
r_i	radius along the pendulum arm for position i
S_1	production term for secondary flows containing the turbulent shear stress
S_2	production term for secondary flows containing the turbulent normal stresses
Str_τ	Strouhal number based on the friction velocity
T	temperature, also period of oscillation of the pendulum arm
T_∞	free stream temperature
T_m	average of wire and free stream temperatures
T_{ref}	reference temperature
T_w	wire temperature
t	time
t_j	specified time with respect to the occurrence of the structure of interest
U	streamwise velocity component, also free stream velocity for the flow over the flat plate
U_o	velocity at x=0
U_c	convection speed of the structures
U_{eff}	effective cooling velocity
u	streamwise fluctuating velocity according to Reynolds decomposition
u^*	friction velocity
$\bar{u}^*$	subchannel average friction velocity
$\|u\|$	velocity magnitude
$u_{b\,i}$	velocity component normal to sensor i and to the plane of its supporting prongs
$u_{n\,i}$	velocity component normal to sensor i and in the plane of its supporting prongs
u_p^*	friction velocity for comparable pipe flow
u_r	streamwise incoherent velocity component
$u_{t\,i}$	velocity component tangential to sensor i
V	transverse velocity component
v	transverse fluctuating velocity according to Reynolds decomposition
$\hat{var}$	localized variance
W	wall subchannel width, also spanwise velocity component
w	spanwise fluctuating velocity according to Reynolds decomposition

w_{ij} hypothetical mixing flow rate between adjacent subchannels i and j

w_r spanwise incoherent velocity component

x distance along the flat plate, also streamwise dimension

x^* variable defined in Equation (2) of Chapter (6)

y transverse dimension, normal to the bottom channel wall

y^* variable defined in Equation (2) of Chapter (6)

$\hat{y}$ radial distance between the rod-wall and the position of maximum velocity

z spanwise dimension, parallel to the bottom channel wall

z_{ij} effective mixing distance between adjacent subchannels

Greek symbols

α acceleration parameter, also expansion/contraction factor in the enhanced VITA technique, and wire angle with respect to mean flow direction

$\alpha_{average}$ average expansion/contraction factor in the enhanced VITA technique

α_t temperature coefficient of resistivity

β polar angle

γ azimuthal angle

Δ pressure-gradient parameter, also symbol indicating difference or uncertainty of a quantity when preceding it

ΔP_p pressure reading of the Preston tube

ΔT temperature difference between the hot film and the fluid

δ_i angle between sensors of the three-sensor probe, defined in Figure 7.6

ϵ turbulence kinetic energy dissipation rate, also eddy diffusivity

ϵ_{Hij} average eddy diffusivity of heat, used to model diffusion between adjacent subchannels i and j

ϵ_U root mean square of the velocity difference in half the forward swing of the pendulum

η_K Kolmogorov microscale

θ_t angular position of pendulum arm at time t

λ streamwise spacing of the structures

λ_u Taylor microscale

μ fluid dynamic viscosity

ν fluid kinematic viscosity

ρ fluid density

σ standard deviation

τ time corresponding to a reference phase

τ_w wall shear stress

ϕ peripheral coordinate

ψ probe pitch angle

Ω vorticity vector

Ω_x streamwise component of the vorticity vector

Ω_y transverse component of the vorticity vector

Ω_z spanwise component of the vorticity vector

ω angular velocity of pendulum arm

Subscripts

b bulk quantity

i referring to subchannel i, or component i of a vector

k referring to subchannel k

m quantity evaluated at the average of wire and ambient temperatures

max maximum value in the channel

r incoherent component

s quantity evaluated at the surface temperature

W quantity evaluated at the wall temperature

w quantity evaluated at the wire temperature

∞ quantity evaluated at the ambient temperature

Other Notation

$(\bar{})$ time average value

($\tilde{}$) coherent component according to the triple decomposition

($\hat{}$) variable interval time average

< > phase average

( )′ root mean square value

1

Introduction

Rod bundles form the basic configuration for almost all fuel element designs used in existing and planned nuclear power reactors. These fuel rod bundles consist of a parallel matrix of rods, containing fissile materials enclosed, for most reactors, in a Zircaloy sheath, and arranged in a compact pattern, thus resulting in the formation of interconnected flow subchannels. The coolant flowing through the channel removes the heat generated by the nuclear fission. Although it is desirable that the coolant flowing in the various subchannels be heated uniformly, this does not always happen. Temperature differences arise because of different flow rates in different sized subchannels, different heated perimeters and non-uniform power distribution across the bundle. In such cases and for bare bundles with no pressure gradients between adjacent subchannels, heat will be transferred from the hotter subchannels to the cooler ones by turbulent diffusion across the rod gaps. This process is called "intersubchannel mixing".

The maximum attainable thermal power rate that can be produced by the reactor is limited mainly by factors such as fission gas production, maximum fuel centre-line temperature , corrosion of the sheath and Critical Heat Flux (CHF). The maximum allowable fuel temperature is set in order to prevent fuel melting. Corrosion generally sets a limit on the sheath temperature. This limit corresponds to the temperature at which a

chemical reaction between the sheath and the coolant takes place. For example, when the temperature exceeds a certain value, steam reacts with zirconium in the zircaloy sheath to produce hydrogen gas and zirconium oxide. This sheath-coolant interaction is most likely to occur following the loss of cooling capability and may result in severe damage to the fuel. The Critical Heat Flux (CHF) must be avoided to prevent sheath oxidation and/or melting (Knief, 1981). Nucleate boiling produces very high heat transfer rates but, at some critical heat flux, the heat transfer deteriorates, allowing the surface temperature to increase suddenly. The heat transfer deterioration is explained by the fact that, under certain conditions, there is no more liquid near the heated surface, and heat is transferred mainly by convection and radiation through the vapour phase.

The most severe "design basis accident" is considered to be a complete rupture ("guillotine" break) of a large pipe in the primary coolant circuit. This accident is commonly categorized as a "Loss-Of-Coolant Accident" (LOCA). LOCA scenarios range from small leaks in minor piping to large ruptures of a major primary coolant line. Should a large break occur in the primary coolant circuit, the loss of pressure would cause the water near the break to "flash" into steam. As a result of the coolant loss, some of the fuel rods could be damaged and radioactive products may be released.

The accurate prediction of temperature fields and CHF characteristics, under normal and LOCA conditions, is important to the safe and economic operation of nuclear reactors. Improved predictions require a more detailed knowledge of the velocity fields in the subchannels and a better understanding of mixing between interconnected subchannels. At present, the intersubchannel mixing process has not yet been completely explained, due to the incomplete understanding of the turbulent flow structure in rod bundles and the degree by which it is affected by geometry.

Fuel rod bundles are designed such as to maintain a relatively uniform temperature under normal reactor operation. However, the geometry of parallel heated rods gives rise to a non-uniform distribution of coolant velocity around the rod periphery, which results in peripheral variations of local heat transfer coefficients and of local temperatures, in addition to the temperature differences caused by the variation of the thermal-neutron flux.

Distortions to the bundle geometry might result from the displacement or misalignment of a rod, due to flow-induced vibrations, or from the bowing of a rod under

thermal stress. A reduction in subchannel size or in gap width would cause a change in the thermalhydraulic performance of the bundle, which might lead to further temperature variation and peaking. As indicated above, temperature variation and peaking are undesirable, as they limit the allowable, safe, thermal power rate.

Therefore, the detailed knowledge of the thermalhydraulic characteristics of rod bundle flows under design and distorted geometries is essential for both the efficient and safe operation of nuclear reactors.

In addition to rod bundles, a variety of compound channel flows, in applications ranging from river hydraulics to air-conditioning and cooling of electronic devices, involve a flow parallel to a narrow gap. An understanding of the physical phenomena controlling flows parallel to narrow gaps will also be beneficial to applications in the above areas.

It was deduced from a review (presented in Chapter 2) of the available voluminous literature on the subject, that the geometric complexity and diversity of rod bundle subchannels generate a variety of phenomena not encountered in circular pipe flows. Some of these phenomena have barely been identified and explained, others have been the subject of contradictory hypotheses. In particular, insufficient knowledge is available on flow and heat transfer characteristics near narrow gaps. The only way to resolve these issues is by systematic measurement in appropriately designed and instrumented systems.

The present work is aimed at investigating the turbulent flow and the heat transfer in rod bundles. The first stage of the work was done in response to an immediate need of the nuclear industry. It was dedicated to establishing practical empirical correlations, based on experimental results available in the literature, of the subchannel-averaged and the minimum local heat transfer coefficients with geometrical factors of rod bundles. The second stage and main part of the work addresses the physics of turbulent flows in narrow gaps. Understanding and documenting the flow phenomena controlling turbulent transport in the gap region constitutes, in the long term, the only approach with potential to offer flow and heat transfer solutions free of, or weakly relying on, empiricism. This part of the work involves an experimental investigation of the turbulence structure in the narrow rod-wall gap of a rectangular channel, with an aspect ratio of 2/3, containing a suspended rod, having a diameter equal to half the channel height. This simple test-section geometry with a relatively open aspect, rather than a full rod-bundle, was selected in order to isolate the effect of the

gap. The experimental investigation substantiates the occurrence of large-scale coherent structures in the gap region, documents their statistical properties and proposes a physical model for them. Also presented are developments or improvements of experimental techniques that were realized during the course of this research.

It is hoped that the results of the present study will contribute to the physical understanding of flows parallel to narrow gaps, in general, and bundle flows, in particular, and would be useful towards further development of thermalhydraulic codes for reactor design and safety analyses.

2

Literature Review

To help situate the problem and assess current knowledge in the field, a critical review of the available literature on the subject represents the first step in a research program. Our interest in the flow and heat transfer in the gap region of rod bundles is part of a program aimed at investigating the flow and heat transfer characteristics in rod bundles with distorted geometries. The material has been divided in sections, which occasionally overlap, but clearly identify the main phenomena that are relevant to this field. Although emphasis has been given to experimental studies of isothermal flows in relatively simple rod bundle arrays, heat transfer investigations have also been reviewed. A thorough review of computational studies, summarized in Table 2.1, has also been performed (Guellouz and Tavoularis, 1992b). For conciseness, only its main conclusions are included here.

2.1 Friction Factor and Wall Shear Stress Distributions

Gunn and Darling [1963] reported friction factor measurements for four ducts, illustrated in Figure 2.1, over a Reynolds number range from 200 to 100,000. The experimental results showed that the transition to turbulence in non-circular conduits occurred at lower Reynolds numbers than those for transition in circular pipes. In the

transition region, the sharp increase of the friction factor, characteristic of the circular pipe, was substantially diminished in the non-circular sections. In fact, the transition took place over a wider range of Reynolds numbers. Gunn and Darling [1963] observed that this would apparently occur in sections with large wall shear stress variations. They further noted that the coexistence of turbulent and laminar flows in such ducts suggests either that the transition to turbulence takes place in stages, with one part of the flow first becoming turbulent and followed by others, or that the part of the channel which first became turbulent is gradually widening. For fully turbulent flows, the friction factors for all channels, excepting the four-rod bundle, were lower than values based on the Nikuradse relation for circular pipe flow. It was observed that, if two sections had close values of the friction factors in the laminar regime, they would also have close values in the turbulent regime. Similarly, sections with turbulent friction factors close to the corresponding values in round pipes were seen to have laminar friction factors comparable to those in pipe flow. For laminar flows in non-circular conduits, the friction factor obeys the relationship

$$f=\frac{C}{Re} \tag{1}$$

where the constant C is characteristic of the section geometry.

Ibragimov et al [1967] proposed a procedure to calculate the friction factor for turbulent flows in non-circular channels, especially in rod bundles. They explained that the friction factor in various channels differs significantly from the values for circular tubes (e.g. the Blasius formula), because the correct value of the hydraulic diameter in complicated geometries would be different from that estimated based on the usual definition (i.e. four times the cross sectional area divided by the wetted perimeter). They stated that, unlike in wide channels, in a narrow element the transfer of large-scale eddies along the wetted perimeter, leading to a smoothing of the velocity variation, would be difficult. Thus, the resulting velocity distribution could be rather irregular with maxima and minima occurring at locations possibly between geometrical extremes or symmetry points.

Rehme [1973] presented a method for the prediction of friction factors of turbulent flow in non-circular channels. First, he reviewed a work by Maubach (because the original publication of Maubach is not available, we shall convey Rehme's presentation of the

relevant information). In addition to relation (1) for laminar flow, Maubach defined the turbulent relationship

$$G=\frac{U_{max}-U_b}{u^*} \tag{2}$$

where U_{max} is the maximum velocity, U_b is the bulk velocity and u^* is the friction velocity. He was able to prove that G was a geometric factor and that for each channel shape, G has a characteristic value, independent of the channel roughness and the flow Reynolds number. Rehme [1973] noted two common characteristics of channels with variable circumferential wall shear stress: a) a variable curvature of the walls (either, as in the case of annuli, with different radii of curvature of the walls or, as in the case of triangular ducts, with discontinuities in the curvature of the wall in the corners), and b) the existence of zero shear stress lines in the flow field. The channel can be subdivided, along these lines, into parallel subchannels, across the boundaries of which, there is no net momentum transport. Taking advantage of this subdivision, and using the smooth circular tube relations, Maubach derived an expression for the friction factor of the entire channel as

$$\sqrt{\frac{8}{f}}=A\left[2.5\ln\left(Re\sqrt{\frac{f}{8}}\right)+5.5\right]-G^* \tag{3}$$

with

$$A=\sum_{i=1}^{n}\sqrt{\frac{D_i}{D_H}\frac{F_i}{F}} \tag{4}$$

and

$$G^*=-\sum_{i=1}^{n}\left[2.5\ln\left(\frac{1}{2}\frac{D_i}{D_H}\sqrt{\frac{D_i}{D_H}}\right)-G_i\right]\sqrt{\frac{D_i}{D_H}\frac{F_i}{F}} \tag{5}$$

D_i and D_H are, respectively, the hydraulic diameter of each subchannel and of the entire channel; F and F_i are the entire flow area and the subchannel area; and A and G^* are

geometric parameters which were demonstrated to be independent of the flow conditions.

The friction factors in laminar and turbulent flows, normalized by the circular tube friction factor, showed similar behaviours with respect to channel geometry, although the dependency was more marked in laminar flows. This confirmed the observations of Gunn and Darling [1963]. The method proposed by Rehme [1973], called the G^*-method, was based on this similarity and, as noted by him, it is only justified by the good agreement between its predictions and the available data for various non-circular channels. The G^*-method consists of relating the A and G^* constants to C. So, it requires only the knowledge of the geometry factor, C, for laminar flow, which can be calculated easily for most channels occurring in practice. Then, the corresponding values of A and G^* are used in Equation 3, in order to calculate the friction factor for turbulent flow for the given geometry and Reynolds number. This method tested well for triangular ducts, eccentric annuli and rod bundles. However, influences of coherent structures and of secondary flows, known to exist in non-circular geometries, are not taken into account by this method.

Presser [1971] performed an experimental investigation in a rod cluster modelling a nearly infinite, triangular array, rod bundle, with pitch to diameter (P/D) ratios of 1, 1.02, 1.05, 1.2 and 1.67 and over a Reynolds number range from 200 to 200,000. He found the empirical coefficients in the turbulent and laminar flow relations for the friction factor to depend on the P/D ratio. In fact, for turbulent flows, a strong variation of the friction factor was observed for P/D from 1 to 1.05 and a milder variation for P/D between 1.05 and 2. For greater P/D ratios no systematic dependence of the friction factor on P/D was seen.

Rehme [1972] distinguished four parameters characterising the rod bundle geometry: the pitch to diameter ratio, P/D, the wall-subchannel width to diameter ratio, W/D, the number of rods in the bundle and the shape of the channel. His study was limited to the hexagonal arrangement of rods, while both P/D ($P/D=W/D$) and the number of rods were varied. A total of twenty five test sections were used, with Reynolds numbers ranging from 600 to 5×10^5, P/D varying from 1.025 to 2.324 and the number of rods being 7, 19, 27 or 61. Rehme [1972] observed that the number of rods in the bundle had no effect on the friction factor calculated based on the bundle hydraulic diameter. Also, the P/D influence on f was seen to be very weak for $P/D>1.1$. Nevertheless, defining a characteristic length so that the friction factor curves for all rod bundles would collapse appears to be impossible,

even in the laminar regime. A sudden change from laminar to turbulent flow could not be detected for most of the studied rod bundles. However, an area of transition, in which the friction factor coefficient gradually changed from an essentially laminar behaviour to a turbulent one, was observed. Rehme [1972] further introduced the ``equivalent annular zone" concept. The ``equivalent annular zone" is defined as the annular zone of the same area as the hexagonal elementary cell around each rod in an infinite rod bundle. Rehme [1972] noted that this concept led to good approximations in rod bundles with $P/D>1.2$, for which the wall shear stress was relatively constant around the perimeter of the rod. For smaller P/D ratios, the friction factors were below those of the equivalent annular zone. According to Rehme [1972], this resulted from the non-uniform wall shear stress and velocity distributions. The ``equivalent annular zone" friction factor value represents an upper limit to the friction factors in rod bundles. In fact, channel walls and irregularities in the rod bundle array tend to lower the friction factor. The latter was seen to depend on the P/D ratio. It increased rapidly from 60% of the circular tube value at $P/D=1$ to approximately 100% at $P/D\approx1.08$. For higher ratios, the friction factor increased to only 110% of the pipe flow value for $P/D\approx2$.

Marek et al [1973] used two square array rod bundles with respectively 9 and 16 rods. The P/D ratio was 1.283 and the Reynolds number varied from 10^4 to 3×10^5. Heated and isothermal experiments were performed. Marek et al [1973] showed that the ``equivalent annular zone" is also the upper limit for the friction factor for square arrays. They observed that a bundle with a specific P/D ratio and $W/D<P/D$, would exhibit, as W/D was increased, an increase in the friction factor up to a flat maximum at $W/D\approx P/D$. This maximum was seen to approach the value for an infinite rod bundle, as the number of rods increased.

Marek et al [1973] stated that their measured results with and without heating showed that the correlation of friction factor suggested by Taylor [1967], for laminar and turbulent flows in smooth pipes with different bulk and wall temperatures, would also be applicable to rod bundles. The method of correlation proposed by Taylor [1967] was motivated by the limitations of the available correlations based on the film temperature (half the sum of the surface and bulk temperatures). His empirical correlation is a modified (based on experimental data of seven investigators) form of the Koo, Drew and McAdams relation (McAdams, 1942). In turbulent flow, it yields

$$\frac{f}{2} = \left(0.0007 + \frac{0.0625}{Re_s^{0.32}}\right)\left(\frac{T_b}{T_s}\right)^{0.5} \qquad 0.35 \le T_s/T_b \le 7.35 \tag{6}$$

Kjellström's [1974] estimates of the central subchannel friction factor supported the prediction method of Rehme [1973] and were higher than the friction factor for a smooth tube. Kjellström [1974] found the variation of the wall shear stress not to be monotonous within each subchannel, with the maximum wall shear stress occurring at an angle 10 to 12° from the open flow area towards the gap. A similar effect has been noted by Carajilescov and Todreas [1975] and Hooper [1980] in triangular and rectangular array rod bundles, respectively.

Kacker [1973] measured wall shear stress distributions in an eccentric annulus with a diameter ratio of 5.68 and a two-rod section, with the same inner and outer tube diameters. For the annulus case, he found the maximum wall shear stress on the rod surface to occur at an angular position 60° from the position of maximum flow area. Similar behaviour was observed by other investigators in non-circular geometries where secondary flows were seen to be active. The maximum wall shear stress variation around the rod perimeter was about 13%. The wall shear stress (normalized by their respective averages) on both the pipe wall and rod surface was independent of the Reynolds number in the range 3.7×10^4 to 2.15×10^5. In the two-rod geometry, the maximum wall shear stress on the rod surface occurred in the gap between the two rods. The maximum variation of the wall shear stress was 10%, in this case, with a large angular sector (about 75°), where the distribution was nearly uniform. Kacker [1973] explained the observed shear stress uniformity to the increased momentum transfer due to secondary flows.

Fakory and Todreas [1979] performed measurements of wall shear stress in a triangular subchannel (P/D=1.1). For Reynolds numbers larger than 9,000, their wall shear stress distributions (normalized by the corresponding average values) for different Reynolds numbers were similar. They observed a monotonic variation of the wall shear stress around the rods, with the peak at the maximum flow area. They concluded that no detectable secondary flow effects were present.

Abdelghany and Eichhorn [1986] measured wall shear stress distributions in a 3×6

square rod array with P/D=4/3 and W/D=2/3. They obtained maxima near the maximum flow area and minima close to the gaps between the rods and the walls. They observed an influence of the corners and the side walls on the shear stress distribution. The average wall shear stress around the rod surface was smaller for rods closer to the corner and larger for rods in the centre of the bundle. On the other hand, the peak-to-peak variation was largest for rods closest to the corner. Their measured velocity profiles, plotted in semi-logarithmic coordinates, had the same slope as the law-of-the-wall but a smaller intercept. They attributed this difference to the effects of velocity gradients, due to the curvature of the isovelocity lines and to the effects of secondary flows. They used the Clauser plot with the law-of-the-wall to estimate the local friction factor from the velocity data. The distributions determined in this way agreed well with the measured ones.

Trupp and Azad [1975] found a friction factor higher than the one corresponding to pipe flow at the same Reynolds number. They postulated a relation similar to the one commonly used for pipe flow, i.e. $f=C\,Re^{-n}$. Least square fitting to their data provided values of the constants C and n, which were shown to be a function of P/D. However, they warned that the resulting expressions for C and n should be applied with caution to other similar situations. Their measured local wall shear stress did not increase monotonically from the gap to the open flow area as predicted by computational schemes ignoring secondary flows. As a possible explanation, it was inferred that secondary flows acted to smoothen the wall shear stress distribution.

Hooper and Rehme [1984] found that the minimum wall shear stress in the rod-wall gap changed relatively slightly for their three larger W/D (i.e. 1.118, 1.096 and 1.071), but the reduction became more marked for W/D=1.048 and 1.026. The authors also noticed some shift in the position of maximum shear stress towards the rod-wall gap with decreasing W/D. Although they attempted to link the observed flow features to the influence of possible mean secondary flow cells, they observed little evidence of significant secondary flow velocities, even at low W/D ratios.

In a recent study, Ouma and Tavoularis [1991b] measured the wall shear stress distributions around the central rod of a five-rod outer sector of a CANDU type 37-rod bundle. They found minima at the rod-wall and the rod-rod gaps and maxima at the open flow regions. The minimum wall shear stress at the rod-wall gap and the average one

decreased dramatically only for very small rod-wall gaps. The local friction factor not only varied appreciably around the rod as the gap decreased, but also had values much larger than the average friction factor based on the subchannel bulk velocity, due to the variability of the local flow width. Therefore, it was stated that in subchannels with strong non-uniformity of the local flow width, the use of subchannel averages to predict the variation of the local properties could lead to appreciable errors.

2.2 Measurements of Velocity Distribution and Turbulence Structure

Eifler and Nijsing [1967] performed an experimental investigation of mean velocity distribution and pressure drop in a test section modelling a triangular array rod bundle for P/D ratios equal to 1, 1.05, 1.1 and 1.15 and Reynolds numbers of 15,000, 30,000 and 50,000. They found the velocity profiles normal to the rod surface to be satisfactorily represented by the universal velocity distribution derived for circular geometries. They also found the peripheral variation of the normalized velocity to diminish slightly with an increase of the Reynolds number and to become more important at closer gap spacing.

Kacker's [1973] study was motivated by the absence of satisfactory methods to predict the magnitude of secondary flows in rod bundles or in simple non-circular ducts. He also noted the disagreement in the literature on the law-of-the-wall for flows over slender cylinders. Kacker [1973] performed an experimental investigation in an eccentric annulus with a diameter ratio of 5.68 and an eccentricity of 0.475 and a two-rod test section, with the same tube and rod diameters as in the annulus. In general, he found the velocity profiles to deviate more from the universal law-of-the-wall in the two-rod geometry than in the single rod case. Kacker [1973] attributed these deviations to the effect of the radius of curvature and to the presence of secondary flows.

Kjellström [1974] performed the first turbulence measurements in rod bundle subchannels. He focussed on the central subchannel of a triangular array with P/D=1.22 and over a Reynolds number range of 37,000 to 150,000. The mean velocity data were in general agreement with the conventional law-of-the-wall. However, the maximum velocity, in the region $y/\hat{y}\leq 0.5$ (where $\hat{y}$ is the ``local flow width", i.e. the radial distance from the surface to the line of maximum velocity), was shifted from the position corresponding to the largest

flow width. This behaviour was explained as a possible result of the action of secondary flows. The turbulence intensities, made dimensionless by the friction velocity, agreed well with those in pipe flow. He also measured the kinetic energy of turbulence, the Reynolds stresses and the radial and lateral eddy diffusivities. All of the above quantities were in reasonable agreement with the reported data for flow in circular tubes, except the lateral eddy diffusivities, which in addition to having a systematic variation with angular position, exceeded the radial diffusivities by a factor of 10, close to the rod wall, and 1.5, in the centre of the subchannel.

Rowe et al [1974] used a two-component laser-Doppler velocimeter to measure the mean velocity and turbulence characteristics in central and wall-subchannels of two square array rod bundles with P/D=1.25 and 1.125. They found relative minima of the turbulence intensity in the subchannel centres and in the rod gap centres, with values higher than typical values in pipe flow. They noted a weak Reynolds number effect for the large gap spacing (the studied range of Reynolds numbers was from 50,000 to 200,000). However, a reduction in the gap width significantly increased the intensity and modified the scale distributions, especially near the rod gap. For the small rod gap, the largest scales were found in the gap and at the subchannel centres and the smaller scale turbulence was located in the regions in between. The measured velocity correlation functions also showed this to be a region of dominant periodic flow pulsations. No significant flow pulsations were observed for larger gap spacing, and the reduction of the gap width led to stronger periodic flow pulsations. These pulsations, together with secondary flows implied from observed evidence, presumably produced increases in the turbulence intensity and the macroscales. Even though these authors presented only longitudinal macroscales, they speculated that the lateral freedom of the open array would allow large-scale turbulence to move through the gap with relative ease. In conclusion, Rowe et al [1974] noted that, in the regions adjacent to the gaps, turbulent transport would be both diffusive and convective, while in the subchannel centres and rod gaps it would be mostly diffusive.

Kried et al [1979] reviewed the laser Doppler anemometry techniques used at the Pacific Northwest Laboratory in studies of flow and heat transfer in rod bundles. The results of the bare-rod bundle flow experiments indicated the existence of significant secondary flows and flow oscillations that tended to increase with decreasing gap width.

Trupp and Azad [1975] performed a thorough study of turbulent flow in a triangular array rod bundle. The experimental *P/D* ratios were 1.5, 1.35 and 1.2 over a Reynolds number (based on the bulk velocity and the hydraulic diameter of the primary flow cell) range of 12,000 to 84,000. The isovel contours for each *P/D* studied were similar over the Reynolds number range, when normalized by the subchannel bulk velocity. This indicated that using the bulk velocity as a scaling factor was successful in removing the Reynolds number effect, except in the core of the subchannel. The use of the bulk velocity was also effective as a scaling factor for *P/D* effects in the region within a radial distance lower than the minimal radial distance between the rod-wall and the primary flow cell boundary. In this region, the isovels were basically circular arcs concentric with the rod i.e. the azimuthal variation of the local mean axial velocity was relatively weak compared to its radial variation. Outside this region the azimuthal dependence was seen to be comparable to the radial one. In fact, the isovel lines tended to become concentric with the subchannel centerline. The inclination of the isovel lines showed a distinct dependence on *P/D*. Trupp and Azad [1975] speculated that the modified law-of-the-wall and outer-law observed in their measurements were apparently due to the three-dimensionality of the flow. Similar situations existed for other ducts which involved secondary flows. The normal stresses distributions were found similar to those in pipe flow but generally lay below the pipe flow levels. The offsets increased progressively with decreasing Reynolds number and were roughly equal to $(\bar{u}^{+}-u_{p}^{+})/u_{p}^{+}$ ($\bar{u}^{+}$ and u_{p}^{+} are respectively the average friction velocities in the subchannel and an equivalent pipe flow). The turbulence intensities, scaled with the average friction velocity, and the turbulent kinetic energy showed azimuthal variations. The turbulence parameters were seen to vary linearly with the rod-spacing for the studied range of *P/D*, which represent relatively large *P/D* ratios. The main effect of decreasing gap widths on the spectra of the axial fluctuating velocity was to flatten them at the low frequencies. Trupp and Azad [1975] explained this by the fact that the largest eddies would be limited by the physical size and shape of the flow channel. Overall, Trupp and Azad [1975] found that the turbulence characteristics were comparable to those in fully developed pipe flow. Even though these two flows are fundamentally different (pipe flow is axisymmetric and has no secondary flows), they argued that, because of the low level of secondary flow velocities in rod bundle flows, a fair similarity remained.

Seale [1979a] observed that there was considerable evidence in the literature that the effective eddy diffusivity in the direction parallel to the rod surface was markedly higher than that in the direction normal to the rod surface. In fact, the effective diffusivity in the gap region appeared to exhibit a substantial anisotropy (Rehme, 1978) and the maximum anisotropy factor was found to drop with increasing gap width. Seale's measurements confirmed the very high anisotropy factors in the gap region, but he did not find any evidence of secondary flows in the velocity and temperature contours (*P/D* studied were 1.1, 1.375 and 1.833). Seale [1979a] noted that the exact roles played by the anisotropy of the effective diffusivities and the secondary flows as well as the source of the marked anisotropic diffusivities remained to be clarified. He recommended that careful and detailed measurements of the turbulence structure should be conducted in order to explain these phenomena and their physical basis.

In a second article of the same year, Seale [1979b] used the "k-ϵ" turbulence model to predict the turbulent flow in the same channels used in his previous work (Seale, 1979a). The computations were performed for isotropic and anisotropic diffusivities. In the first case, the predictions gave results comparable to the experimental ones only for a bundle with a rather open aspect ($P/D>1.3$), while, for the case of anisotropic diffusivity, the computations enabled some, but not all, of the features of the experimental results to be reproduced.

Seale [1982] noted, from a review of the literature, that the turbulence structure in rod bundles depended on the pitch to diameter ratio. For fairly open arrays ($P/D \geq 1.2$) the distributions of the normalized turbulence intensities are similar to those in circular pipe flow or in plane channels. For more closely spaced rod arrays, the turbulence structure, especially in the rod-gap region, departs markedly from that in pipe flow. An interesting observation was brought out by Kohav et al [1976], who considered the variation of the turbulence intensity along the line joining the channel centre with the gap centre in their square array subchannel (P/D=1.1, 1.2 and 1.3): the turbulence intensity increased from the channel centre up to a certain position, then decreased towards the gap centre. This position was the point of demarcation between a flow pattern characteristic of a square conduit and that of a flow between parallel plates.

Tahir and Rogers [1986] studied the turbulent flow in a central subchannel of a

triangular array rod bundle with P/D=1.06. Their axial velocity measurements, at all angular positions, were in good agreement with the universal law-of-the-wall. The measured radial eddy viscosities approached those in pipe flow at radial positions close to the wall, but were much higher than those in pipe flow away from the wall. The azimuthal eddy viscosities were considerably higher in the gap region than in the open-flow area and were much higher, in general, than the radial eddy viscosities. The anisotropic nature of the turbulent flow structure, especially in the gap region, was demonstrated from the above measurements.

Renksizbulut and Hadaller [1986] measured local wall shear stress and mean and fluctuating axial velocities in a six-rod bundle (P/D=1.15, W/D=1.123). They made no attempt to measure secondary flow vortices, but observed some evidence of their presence from the wall shear stress distributions and the isovel contour lines. They measured turbulence intensities comparable to those in pipe flow at the core of the central subchannels and higher intensities in the wall and corner subchannels. They observed that the maximum intensities were within the central subchannels and not at the gaps. Renksizbulut and Hadaller [1986] noted that the structure of turbulence in the gap region was considerably different than the structure in pipe flow. By comparing their results to those found in the previous literature, they concluded that, with comparable P/D, triangular array rod bundles would produce higher turbulence intensities at the gap than square arrays would.

D'Arcy and Schenk [1985] used an LDA fibre optic probe to study flows in a complete CANDU type 37-rod bundle, including spacers and endplates. Two bundles were installed upstream of the test bundle. Two configurations were considered: one with all rods of consecutive bundles aligned and the second with a misalignment of the rods by 20°, thus with the adjacent endplates nearly aligned.

Tavoularis et al [1988] studied turbulent flow in a 60° sector of a 37-rod bundle, focussing on an inner square subchannel. The experimental Reynolds number was 50,000 for two test conditions: a single bundle and two bundles in tandem (aligned and mis-oriented by 15 and 30°). They have also studied the effect of rod spacers. Their measurements included wall shear stress, static pressure, mean axial velocity, turbulent intensity, Reynolds shear stresses, correlations, scales and probabilities. At the entrance region, the measured autocorrelation curves had a typically ``isotropic'' appearance in the subchannel core but presented large, persistent oscillations in the rod gap region. Away from the entrance, the

two-point correlations had no apparent periodicity and resembled the shapes of such quantities in turbulent pipe flows.

Ouma and Tavoularis [1991b] presented detailed turbulent flow measurements in a five-rod outer sector of a CANDU type 37-rod bundle. The measurements were conducted for the design geometry and with the central rod displaced towards the external tube wall and/or towards a neighbouring rod. They presented, mostly in contour form, measurements of the mean velocity, Reynolds stresses and turbulent intensities in the wall and inner subchannels. Isotachs bulged towards narrow gaps with the bulging becoming more pronounced as the rod-wall gap decreased. They also presented autocorrelation coefficients and turbulent scales.

Meyer [1991] performed an experimental study in a heated 37-rod bundle with P/D=1.12, arranged in triangular array in a hexagonal channel. He focussed on a central subchannel. In addition to the wall shear stress, wall temperature and mean velocity and temperature distributions, Meyer [1991] measured turbulent quantities such as the turbulent kinetic energy, the Reynolds stresses and the turbulent heat fluxes.

Hooper [1980] performed turbulence measurements in a six-rod square array bundle, with P/D ratios of 1.194 and 1.107. All of his measurements were independent of the Reynolds number over the range 48×10^3 to 156×10^3. The turbulence structure was found to be similar to the one in pipe flow only for the radial traverse along the diagonal of the subchannel. In the gap region, the turbulence structure departure from the axisymmetric flow structure was found to depend strongly on the P/D ratio. For example, at the gap centerline the azimuthal turbulence intensity reached 1.4 times and 1.6 times respectively, the equivalent one in pipe flow for P/D=1.194 and 1.107. In addition to the six components of the symmetrical Reynolds stress tensor, Hooper [1980] measured the turbulent kinetic energy. He suggested, based on the distributions obtained near the gap region, that turbulence was transported into this area by a single secondary flow cell. Measurements of the mean velocity direction, although of poor resolution, seemed to support the existence of a single secondary flow cell.

Hooper and Wood [1984] re-analysed the measurements of Hooper [1980] for P/D=1.107. They used the axial momentum equation to show that the wall shear stress distribution is determined primarily by the pressure gradient and the transverse shear

stress $\overline{uw}$ which implies a negligible effect of the mean secondary flow. They have also demonstrated the failure of a commonly used closure assumption in models of stress-induced secondary flow in reproducing the experimental stress distributions in rod bundle flows at small *P/D* ratios.

Rehme performed a series of experimental studies (1977, 1978, 1979, 1980, 1982, 1985, 1987a, 1987b, 1987c, 1987d, 1988, 1989) on a four-rod bundle contained in a rectangular channel (Figure 2.2) for several *P/D* and *W/D* ratios ($1.036<P/D<1.42$ and $1.026<W/D<1.42$) and for a range of Reynolds numbers (from 5×10^4 to 2×10^5). He did not observe any evidence for the existence of secondary flows, although some of his measured distributions (e.g. axial turbulence intensity and kinetic energy of turbulence) showed some effects that could be associated with secondary flows. According to Rehme, the striking feature of the turbulent flow structure was its high anisotropy factor, defined as the ratio of the azimuthal eddy viscosity to the radial one. The anisotropy factor not only depended on the *P/D* and *W/D* ratios but also showed a strong dependence on the local position both radially and azimuthally. The highest anisotropy factors were measured in the gaps of the cross-section. In fact, while the radial eddy viscosity was almost independent of the circumferential position, the azimuthal eddy viscosity was found to have a strong dependence on the local position: it assumed very high values in the gaps and its lowest values in the open-flow area at the centre of the subchannel. Its variation with the non-dimensional distance from the wall was found to be similar for all angular positions. The values first increased with increasing distance from the wall to a maximum value and decreased slightly when approaching the line of maximum velocity. The results of Rehme showed that the structure of turbulent flow in rod bundles, especially in the gap region, differs widely from the well-documented one in circular pipe flow. This difference became more pronounced as the gap width decreased. Close to the wall the normalized radial eddy viscosities agreed with the pipe flow data and were higher for $y/\hat{y} > 0.3$. The values of the axial turbulence intensity were generally higher than the pipe flow data, even for relatively open gaps. They were minimal in the open flow area, where they were closest to the pipe flow values for the maximum velocity line. In contrast with the circular tube data, the variation of the radial turbulent shear stress with distance from the wall was not linear. Depending on the circumferential position, it followed a curve that was always higher than

the circular tube line. On the other hand, Rehme found excellent agreement between the experimental data and the law-of-the-wall established for circular tubes. The kinetic energy of turbulence was observed to decrease from high levels at the walls to levels comparable with the results for pipe flow away from the wall. However, in narrow subchannels the level of the kinetic energy became much higher than that in circular tubes. Rehme's axial turbulence intensity measurements presented a relative maximum in the rod-wall gap region (about 20-25° from the gap centre). This relative maximum increased considerably with decreasing gap width. Based on the high valued, almost constant distribution of the axial turbulence intensity, Rehme [1987a] concluded that the source of such high levels was not associated with the normal wall generation mechanism. The azimuthal turbulence intensity was found to increase from a value comparable to the one for pipe flow in the open flow region to high levels in the gap. It reached a relative maximum in the rod-rod gap, but its absolute maximum was located at the centre of the rod-wall gap. This maximum was seen to increase as the gap width decreased. In the gap region, the azimuthal intensity increased with distance from the wall, which implies that these high levels could not be caused by transport through secondary flows, because the levels at the centre were higher than those close to the wall. Rehme's results concerning the axial and azimuthal intensities suggest a turbulence generating mechanism that is not directly coupled to the local wall conditions. The presence of energetic large-scale structures and an almost periodic momentum exchange process through the gap was implied from the large-scale structure of the azimuthal velocity component.

Wu and Rehme [1990] performed additional experiments using the set-up described above. They found that the wider the gap between the rod and channel wall was, the higher the peak value of maximum axial velocity would be. Inversely, the wall shear stress variation was seen to be higher for lower *W/D* ratios. The same trend was observed for the peak value of the axial turbulence intensity. The increased levels of turbulence, both in the axial and azimuthal directions depended mainly on the relative gap size and were essentially independent of the bundle configuration as a whole, i.e. the phenomena in one region, e.g. a rod-wall gap, were nearly independent from the phenomena in the other region, e.g. a rod-rod gap.

Hooper and Rehme [1984] presented results of two experimental series: one

conducted in the above described four-rod channel (*P/D*=1.071 and 1.036 and *W/D* ratios ranging from 1.026 to 1.118) and the other in a six-rod bundle (*P/D*=1.194 and 1.107). Most of the four-rod bundle results were reviewed earlier. The results in the six-rod channel were in good agreement with the four-rod bundle results. In fact, the axial turbulence intensity was found to be considerably higher than the pipe flow data for the whole gap area, except in the rod wall vicinity, where it seemed to approach the pipe flow values. The distribution of the axial intensity suggests the possible superposition of two turbulence production mechanisms: the conventional turbulence production mechanism, present in the near wall region having large mean axial velocity gradient and another mechanism, active in the central region. The azimuthal intensity was also considerably higher than the pipe flow results and essentially independent of the wall distance. The peak value of the azimuthal intensity was approximately 25% of the local axial velocity (Hooper, 1983), a level at least one order of magnitude higher than any possible level of secondary flow velocities. The measured Reynolds stress distributions for this channel had the same general features as the ones for the four-rod bundle. The azimuthal Reynolds stress exhibited good antisymmetry about the gap. Using the same results, Hooper and Wood [1984] demonstrated that the circumferential gradient of the azimuthal Reynolds stress made a substantial contribution to the axial momentum balance in the centre of the gap.

Hooper and Rehme [1984] also reported mass diffusion results across the rod gap. The dispersion and possible azimuthal translation of a nitrous oxide gas plume injected parallel to the rod axis and near the rod surface were measured by an infrared gas analyser. The obtained results indicated that the turbulent diffusion rates in the azimuthal direction were approximately independent of azimuthal angle for locations equidistant from the rod surface. This was explained by the existence of multiple secondary flow cells. However, no non-zero secondary flow velocities were resolved for this geometry. The magnitude of the velocity fluctuations in the azimuthal direction was at least equal to that of the axial velocity fluctuations. Both velocity components were found to have almost periodic large-scale structures; their auto-correlation functions indicated a periodic component with the same frequency (92 Hz) as the one identified in all measured auto- and cross-correlations. Both velocity components were well correlated for a considerable distance from the gap, indicating that a periodic intersubchannel momentum exchange process extended over an

important part of the subchannels. In addition, this high correlation through the gap was significant, considering that the secondary flow cells would not be expected to cross the symmetry line in the gap (Hooper, 1983). The radial turbulent velocity component was highly reduced in magnitude and there was little evidence of any large-scale structure associated with it. This component had no significant spatial cross-correlation. An antiphase relationship was observed for the large-scale structure of the axial velocity component in neighbouring subchannels. On the other hand, there was no evidence of a phase difference for the azimuthal component on either side of the subchannel boundary. Although it is difficult to determine the phase of a signal that is changing in amplitude and frequency, Hooper [1983] suggested that the antisymmetry of the azimuthal Reynolds stress was connected to a phase shift between the axial and azimuthal velocity fluctuations. The 92 Hz frequency represented an average frequency of the cyclic subchannel momentum exchange process for the particular Reynolds number. This cyclic exchange became more intense as the gap width was reduced (Hooper, 1983). Its frequency was shown to have a linear relationship with the flow Reynolds number for a fixed bundle geometry. Hooper and Rehme [1984] concluded that mass, momentum and heat transfer processes in the rod-gap region were dominated by an energetic and almost periodic azimuthal turbulent velocity component.

Meyer [1991] and Krauss and Meyer [1996] reported measurements in inner and wall subchannels of a 37-rod bundle arranged in a triangular array, with P/D=1.12, and contained in a hexagonal channel. Their measured distributions of such turbulent quantities as turbulent stresses, rms temperature fluctuations and turbulent heat fluxes are compatible with the presence of large scale structures in the regions of rod-rod and rod-wall gaps.

2.3 Mixing in Rod Bundles

Rogers and Todreas [1968] classified coolant mixing between interconnected subchannels in rod bundles into two types: natural mixing and forced mixing. Forced mixing is induced by the presence of pin spacers or grids in the flow channel. If these pins or grids divert part of the flow in a preferred direction, it is called flow sweeping. However, if the flow break up is done in a random fashion, it is called flow scattering. These authors have

also distinguished between two different mechanisms of natural mixing: turbulent interchange and diversion cross-flow. Turbulent interchange results from natural eddy diffusion between subchannels, while diversion cross-flow is a directed flow caused by radial pressure gradients between adjacent subchannels, which can be induced by gross differences between the subchannel heat flux distributions, differences in subchannel equivalent diameters or pin eccentricity or bowing. The diversion cross-flow and the flow sweeping are directional mixing mechanisms, while the other two are non-directional. The following discussion will be limited to turbulent interchange.

There are two approaches used in the analysis of mixing due to turbulent interchange, the "lumped parameter" or subchannel approach and the "local analysis" or "microscopic approach". The former approach, also termed "macroscopic", assigns average values to the different subchannels, while the latter one accounts for the continuous variations of the intensity and scales of the turbulence, the local temperature and the velocity gradients.

The "lumped parameter" approach was the first to be adopted. It became an important tool in establishing the thermal performance of fuel rod bundles, because of its capability to handle arbitrary geometric arrangements, arbitrary rod heat flux distribution, single or two-phase flow conditions and its potential to include effects of fuel rod spacers. The application of this approach requires information on the exchange coefficients for the various transport processes between the subchannels. The subchannel analysis, assumes the bundle to be a continuously interconnected set of parallel flow subchannels that are coupled to each other by mixing. The fluid characteristics (averaged over the subchannel) of subchannel i are transported to subchannel j over a distance, z_{ij}, called the "effective mixing distance". Energy balance, accounting for the heat transported by the hypothetical mixing flow rate, w_{ii} (this type of mixing does not involve a net mass transfer between subchannels; w_{ij} represents the turbulent transport due to pressure and flow fluctuations), and the heat transported by transverse diffusion across the gap (with clearance, c) between the two subchannels i and j (modelled using an average eddy diffusivity, $\bar{\epsilon}_{II_{ii}}$) gives (Rogers and Todreas, 1968)

$$w_{ij}(h_i - h_j) = \rho c \bar{\epsilon}_{II_{ii}} \left(\frac{\overline{dh}}{dz} \right)_{ij} \tag{7}$$

which, with the approximation

$$\left(\frac{\overline{dh}}{dz}\right)_{ij} = \frac{h_i - h_j}{z_{ij}} \tag{8}$$

becomes

$$w_{ij} = \frac{\rho c \overline{\epsilon}_{H_{ij}}}{z_{ij}} \tag{9}$$

The above result could have been reached using the mixing-length theory and a finite difference approximation (Rowe et al, 1974). By analogy to turbulent convective heat transfer, the mixing Stanton number, M_{ij}, was defined as the ratio of the hypothetical transverse flow rate per unit area to the axial flow rate in one of the subchannels, i.e.

$$M_{ij} = \frac{w_{ij}}{G_i c} = \frac{\rho \overline{\epsilon}_{H_{ij}}}{G_i z_{ij}} \tag{10}$$

Various methods have been proposed to calculate the mixing distance, z_{ij}, and the effective diffusivity, $\overline{\epsilon}_{H_{ij}}$ (e.g. by Rogers and Tarasuk, 1967 and by Ingesson and Hedberg, 1970). Later, Arkhipov [1984] emphasized the importance of mixing in rod bundle thermal hydraulic analyses. He attributed the deviations between the experimental data and calculation results to the poor modelling of the intersubchannel mixing and proposed an approximate correction for the effect of mixing on the velocity distribution.

Rogers and Todreas [1968] reviewed available work on turbulent mixing.. Omitting details on the assumptions and solutions of these studies, we shall present only results considered to be the most relevant in characterizing mixing. In the discussion of the results of Rapier [1967] they stated that, for the same gap clearance, mixing rates would generally be different for different geometries or different gap shapes. For gap shapes formed by circular elements, they noted that the mixing rate for smooth surfaces was either essentially independent of gap clearance or increased slightly with it. In summary, all reviewed correlations predicted that the mixing Stanton number decreased with increasing Reynolds number; that the mixing rate increased following a power law of the mass-velocity with exponents in the range between 0.68 and 0.90; and that the mixing rate depends weakly on

P/D. On the latter issue it may be noted that as *P/D* approaches 1, the mixing rate would eventually decrease; however, there was no indication on the critical *P/D* ratio below which the mixing rate would decrease visibly. They concluded their review by recommending that more work should be carried on large-scale models to study the effect of gap size and subchannel shape on the intersubchannel mixing.

Renksizbulut and Hadaller [1986] commented on the relationship between intersubchannel turbulent mixing and rod spacing, *c*. Substituting in Equation (9) the eddy diffusivity expression, used by many investigators (Rogers and Todreas, 1968)

$$\frac{\epsilon}{\nu} \propto Re.f^{1/2} \tag{11}$$

they obtained

$$\frac{w_{ij}}{\mu} \propto \frac{Re.c}{z_{ij}} f^{1/2} \tag{12}$$

Keeping in mind that the friction factor is a function of the gap spacing and the Reynolds number, for the mixing to be nearly independent of *c*, the effective mixing distance has to be roughly proportional to *c*. Renksizbulut and Hadaller [1986] noted that for this to be true, there must be additional transport processes near the gap, which supplement turbulent diffusion as the gap width is decreased.

Galbraith and Knudsen [1972] studied turbulent mixing between adjacent square-square subchannels for *P/D* ratios of 1.011, 1.028, 1.063, 1.127 and 1.300 and for Reynolds numbers ranging form 8,000 to 30,000. Mixing was calculated from measured tracer (fluorescent dyes in water) concentration at the entrance and exit of the test section. They found turbulent mixing to be a function of the subchannel Reynolds number and *P/D*. In fact, the eddy diffusivity increased with both quantities and approached a limiting value, at high Reynolds numbers and large *P/D*, corresponding to eddy diffusivity values in turbulent pipe flow. For the smallest rod spacing studied (*P/D*=1.011), the intersubchannel mixing was very different from the ones at higher *P/D* ratios. Galbraith and Knudsen [1972] associated this behaviour to the existence of nearly laminar flow in the gap between the two subchannels.

Ramm et al [1974] noted that the onset of laminarization, near gaps of rod bundles, would affect the magnitude of transport phenomena within the rod arrays. They have studied thermal mixing using a theoretical model developed by Ramm et Johannsen [1972]. To simulate typical tracer-type experiments, calculations were performed assuming that the rods were unheated and the flows in adjacent subchannels were initially at uniform but different temperatures. Ramm et al [1974] found that turbulent transport was dominant at high Reynolds numbers and Prandtl numbers. The conditions at which deviations from the turbulence-dominated behaviour started, depended on the Reynolds number, Prandtl number and geometry. At sufficiently low Reynolds number, the transport between subchannels became essentially molecular in nature. It was observed that at Reynolds numbers corresponding to the onset of laminarization, the thermal mixing flow-rate started to decrease with the Reynolds number, tending to approach the values for laminar flow.

Skinner et al [1969] used a mass transfer analogy (nitrous oxide as tracer in air) to study mixing in smooth and roughened rods. They measured only mean concentration in complete subchannels at various planes downstream of the injector. They defined and calculated an effective diffusivity for mass transfer in the gap. Comparison with values of viscosity suggested that the rate of transfer of the nitrous oxide would be greater than can be accounted for by turbulent diffusion alone. They attributed the high rate to secondary flows and presented a model for them. Away from the gap, they found that the transport level could be explained by turbulent diffusion. Ingesson and Kjellström [1970] commented on the work of Skinner et al [1969] and stated that there was no experimental evidence to justify their secondary flow model.

Ibragimov et al [1966] distinguished between two momentum transfer mechanisms, a gradient transfer of momentum and a convective transfer of momentum. The first mechanism accounts for molecular friction and the action of small-scale turbulent eddies and is governed by the local characteristics of the flow. The second mechanism accounts for the large-scale motion of eddies and depends mainly on the geometric features of the channel as a whole; its effects would be stronger in channels with strongly varying cross-sectional shape (e.g. closely packed rod arrays), in which cases neglecting the convective transfer of momentum may lead to considerable error. Following the analysis of Ibragimov et al [1966], Rowe et al [1974] suggested, based on a review of the results of

Kjellström [1974], that secondary flows and possibly other macroscopic flow processes may affect flows in rod bundles, and cause phenomena that cannot be explained by conventional eddy diffusion concepts. Scalar transport due to macroscopic pulsations would increase transport beyond levels predicted by mixing length theories. Rowe et al [1974] observed evidence of the presence of secondary flows and periodic flow pulsations (discussed in a subsequent section), which according to them, would enhance turbulent interchange to compensate for a decrease in rod gap spacing. Using such arguments, Rowe et al [1974] explained the insensitivity of mixing to the gap width reduction over a rather wide range of sufficiently large gaps (at least those corresponding to $P/D>1.125$). They have also noted a subchannel shape effect on the intersubchannel mixing.

Rogers and Tahir [1975] studied mixing using a tracer technique. They calculated the overall mixing rate from the inlet and exit concentrations, the subchannel flow conditions and geometries and the length of the mixing section and established a new correlation for turbulent interchange in triangular arrays. Over its range of validity ($1.03<P/D<1.40$), their correlation confirmed earlier findings that mixing is a strong function of Reynolds number and a weak function of P/D. Rogers and Tahir [1975] acknowledged the finding of Rowe et al [1974] and concluded that both secondary flows and the convective large-scale periodic pulsations would contribute in enhancing the turbulent interchange mixing. Tahir and Rogers [1979] further attributed differences between turbulent interchange predictions of empirical models and analytical solutions to the effect of secondary flows, which were neglected in the analytical models.

Singh and St. Pierre [1972] studied turbulent mixing between adjacent square subchannels, employing as tracers methane in air and potassium nitrate in water. The Schmidt number of the latter was about 1,000, while that of the former was close to unity. The choice of tracers was made in order to inspect the importance of molecular diffusion. In fact, if the latter played an important role, the mixing rates for water would be lower than the ones for air. It was observed that mixing rates increased with Reynolds number over the range 1,300 to 38,000. Variation of the P/D ratio from 1.018 to 1.102 showed that the mixing was dependent on the Reynolds number and gap width. Singh and St. Pierre [1972] speculated that the effects of secondary flows on mixing rates should be a function of Reynolds number, P/D ratio and subchannel type. They noted that these effects should be

small at high Reynolds number and large *P/D* ratios, where turbulent transport plays an important role, and increase as Reynolds number and *P/D* ratio are reduced, until molecular diffusion becomes predominant. Rogers and Tahir [1975] speculated that secondary flows would carry turbulence from the subchannel interior into the gap region. As the gap width is reduced while maintaining a constant Reynolds number, the increasing strength of secondary flows would carry more turbulent fluid into the gap region, thus explaining the weak dependence of mixing on *P/D*. In any case, it is important to note (Rogers and Tahir, 1975) that secondary flows are not an independent mixing mechanism, but act in conjunction with turbulent diffusion to increase mixing rates above values that would otherwise be encountered. The ultimate mechanism of mixing is still turbulent diffusion.

Seale [1979a] noted that the exact roles played by the anisotropy of the effective diffusivities and the secondary flows in the scalar transport remain to be clarified. He (Seale, 1979b) also performed computations using isotropic and anisotropic diffusivities. The anisotropic predictions compared favourably in many aspects with the experimental findings; for example, they reproduced the relative insensitivity of the mixing rate to a reduction in the gap width. He concluded that his results did not support the role attributed to secondary flows in enhancing the intersubchannel mixing rates.

Seale [1981] further studied the effect of the subchannel shape on heat transfer through the gap. The strong influence obtained was explained as a direct consequence of the anisotropy of the effective diffusivity. This influence appeared to be characterized by the ratios P/D_e (D_e being the subchannel equivalent diameter) and *P/D*. He found that secondary flows, for both computations with isotropic and anisotropic diffusivities, did not significantly alter the results, even though they increased the gap Stanton number by 10% to 15%. Comparing his results to the Rogers-Roschart [1972] correlation, he indicated that the latter is unlikely to predict correctly the subchannel shape effect. According to Rogers [1983] this statement is irrelevant, because Seale applied the correlation under conditions for which it was not supposed to be valid. It was also noted that the Rogers-Roschart [1972] correlation gave excellent agreement with Seale's results within its validity range.

The controversy on this issue has continued in recent years. For example, the results of Hooper and Rehme [1984] indicate that the role of secondary flows seemed to be minimal, at least for their experimental conditions. In contrast, Vonka [1988b] analysed the

role that secondary flows can play as a transport mechanism and found their contribution to the transport of heat and momentum in the radial and circumferential directions to be significant: for example, he estimated their contribution to the circumferential transport to amount to about 50%.

Recently, the formation in the gap region of large scale structures has been documented (see Section 2.5). The importance of their contribution to the intersubchannel mixing was demonstrated by Rehme [1992], Möller [1992] and Wu and Trupp [1994], who attempted to derive mixing correlations based on measured spectra and Möller's [1991] physical model of the large scale structures.

2.4 Secondary Flows

Fully developed turbulent flow in straight, non-circular channels is of three dimensional nature, not only regarding its turbulence structure, but also regarding its mean velocity field. The mean velocity vector at any point in the flow can be decomposed into an axial component (parallel to the channel axis) and a transverse component normal to it. This transverse component forms a flow pattern known as secondary flow, which can be regarded as superimposed upon the axial mean flow.

According to Nakayama and Chow [1986], Nikuradse was the first to deduce, in 1926, the existence of this secondary motion from the bulging of axial velocity contours. He explained the displacement of the contour lines towards the narrow regions (in his case, the corners of a rectangular duct) by the presence of a transverse motion in the plane of the cross-section.

It is now recognized (Haque et al, 1983) that the secondary velocities, even though they amount to only a small percentage of the axial velocity, have a significant effect upon the mean axial velocity distribution, the wall shear stress distribution and the local heat transfer rate, although, for small values of the Prandtl number, the effect on heat transfer is less important (Ibragimov et al, 1971). Moreover, the bulk properties of the flow are also strongly influenced by secondary flows (Melling and Whitelaw, 1979).

The first explanation of the phenomenon was given by Prandtl, who postulated that secondary flows were the result of the turbulent fluctuations along the isovels resulting in

a net flow normal to the local isovel, wherever a variation in isovel curvature occurred. He suggested that the anisotropy of the transverse turbulent stresses would be responsible for the generation of the secondary motion.

As pointed out by Perkins [1970], there are two different categories of secondary flows. According to Prandtl's classification, secondary flows of the first kind are those produced by turning or skewing the primary flow, e.g. in curved ducts. Secondary flows of the second kind are flows caused by non-uniformities in wall turbulence. It is the latter that are discussed here.

The axial component of the vorticity equation for steady, fully developed turbulent flow is

$$\rho U_2 \frac{\partial \Omega_1}{\partial x_2} + \rho U_3 \frac{\partial \Omega_1}{\partial x_3} = \frac{\partial^2}{\partial x_2 \partial x_3}(\rho \overline{u_3^2} - \rho \overline{u_2^2}) - \left(\frac{\partial^2}{\partial x_2^2} - \frac{\partial^2}{\partial x_3^2} \right) \rho \overline{u_2 u_3} + \mu \left(\frac{\partial^2 \Omega_1}{\partial x_2^2} + \frac{\partial^2 \Omega_1}{\partial x_3^2} \right) \qquad (13)$$

The left side of this equation represents the rate of change of vorticity in the transverse plane by convection. This term describes the growth and attenuation of the secondary motion. The last term on the right side represents the viscous stresses effects, i.e. the diffusion of vorticity down its gradient, tending to make vorticity evenly distributed in space. The remaining terms on the right, which are spatial derivatives of the Reynolds stresses, serve as sources for the production of axial vorticity. Reynolds stresses are produced by turbulence and do not depend on the secondary flows for their existence. They depend on the Reynolds number, spatial position and the shape and roughness of the channel. Therefore, the secondary flows originate from and are sustained by an imbalance of turbulent stresses. Figure 2.3 illustrates how a second order derivative of the normal stresses is able to produce a rotational acceleration of a fluid element about the streamwise axis. In fact, the normal stress distributions of Figure 2.3, give a positive first term on the left side of Equation (13), inducing a clockwise rotation about the streamwise axis. In view of the well known "closure problem" of turbulence, the magnitude and distribution of the Reynolds stresses cannot be determined analytically, although, for specific geometries, some approximations can provide a qualitative estimate. In any case, experimental studies are needed for quantitative and accurate evaluation of the stress distribution.

Most of the experimental investigations that have been performed involved

rectangular (including square) channels. A few studies were concerned with triangular and trapezoidal ducts. Rod bundle flow received increasing attention in recent years.

Brundrett and Baines [1964] investigated turbulent flow in a square duct. It was evident from their measurements that the turbulent field was more distorted by secondary flows than the mean field was. They evaluated the contribution of the two vorticity production terms and concluded that, for their flow geometry, the normal stress term was dominant nearly everywhere. The turbulent shear stress term was found to be an order of magnitude smaller than the normal one and, furthermore, its second order derivatives tended to be self-cancelling. Diffusion of vorticity was found to be most intense near the wall and towards the corners and thus it should be associated with the viscous stresses, which are largest in these regions. Brundrett and Baines [1964] further stipulated that the convection of vorticity must take place from the region of production to the region of diffusion. Zones of vorticity production would be balanced by vorticity convection away from these zones. Similarly, vorticity diffusion would be balanced by vorticity convection towards zones of low production. They studied the Reynolds number effect, by non-dimensionalizing the vorticity equation by a cross-section Reynolds number, based on the friction velocity. Examining the equation obtained, they observed that all terms, except the diffusion term, were independent of Reynolds number. In fact, for fully turbulent flows, those properties not associated with the dissipation of energy did not vary with Reynolds number. Therefore, for the equation to be balanced, the normalized vorticity diffusion term must be constant, i.e. the second order derivatives of the streamwise vorticity should vary inversely with the Reynolds number. This was further verified by the fact that the diffusion term was found to be significant only in the wall region, which is correlated by the inner law and, thus, must depend on the Reynolds number. This explained the observed increase in corner penetration of the secondary flows and increased uniformity of the wall shear stress distribution with increasing Reynolds number. In their conclusions, Brundrett and Baines [1964] speculated that the increased proximity of the secondary flows to the wall with increasing Reynolds number is a phenomenon similar to the decreasing thickness of the viscous sublayer under similar conditions.

Leutheusser [1963] observed that the distributions of the axial mean velocity and the wall shear stress tended towards greater uniformity with increasing Reynolds number and

speculated that at extremely high Reynolds numbers the secondary flows should vanish, as the turbulent stresses would approach complete uniformity.

The measurements of Gessner and Jones [1965] confirmed the above observation. In fact, they showed that the strength of secondary flows (when normalized with either the centerline velocity or the bulk velocity) decreased with increasing Reynolds number. They explained this behaviour as being the result of increased turbulent mixing at high Reynolds numbers, which tended to reduce gradients of the turbulent stresses in the flow.

Tracy [1965] conducted an experimental study of flow in a rectangular channel. He postulated that secondary flows would transport particles possessing a relatively higher momentum into regions where the particles would have, on the average, a lower momentum. The latter particles would be accelerated until an equilibrium is reached between the momentum so transported and the additional shear stresses created by the higher velocities. To satisfy continuity, the inward flow must be accompanied by an equivalent outward flow, which would lead to a system of closed secondary streamlines.

Hinze [1973] studied secondary flows for a flow through a rectangular conduit, with one of its long sides partly roughened. He found quite strong secondary velocities (the maximum value being roughly 4% of the maximum axial velocity), with their stagnation point not coinciding with the point of maximum axial velocity, but coinciding roughly with the point of zero shear stress, thus confirming the presence of a non-gradient type of transport.

Speziale [1986] stated that secondary flows would occur in ducts of non-circular cross-section only if the axial mean velocity gave rise to some non-zero difference in the transverse normal Reynolds stresses. In any case this is a necessary but not sufficient condition. In fact, as noted by Haque et al [1983], an examination of the turbulence measurements in an axisymmetric circular pipe flow showed that both the difference of the transverse normal Reynolds stresses and its derivative with respect to the radial direction were non-zero everywhere. However, derivatives with respect to the peripheral direction were zero, which explains the absence of secondary flows in circular pipe flows. Furthermore, Haque et al [1983] compared the distribution of the difference of the transverse Reynolds stresses in circular and non-circular ducts. The only difference they found was the dependence on the peripheral coordinate in the vicinity of the wall, in the case of the non-

circular ducts. They concluded that the gradient of the normal stress difference in the peripheral direction was the important term in the production of axial vorticity and secondary flows.

Speziale [1986] also considered the Reynolds stress transport equation to evaluate the role that various higher order turbulence correlations played in the generation of secondary flows. He found that secondary flows arose exclusively from the higher-order turbulence correlations, such as the third-order diffusion correlation, the pressure gradient-velocity correlation and the dissipation rate correlation. He concluded his work by stressing on the importance of correcting the deficiency (as far as secondary flows are concerned) of available closure models in the modelling of the dissipation rate correlation.

Launder and Ying [1972] investigated experimentally flows through rough and smooth square ducts. They concluded that the secondary flow velocities, when normalized by the average friction velocity, were practically the same for the smooth and the rough ducts, while if the bulk or centerline velocities were used instead, the values would have been twice as large for the rough duct. The friction velocity was also appropriate in removing the Reynolds number dependence of the secondary flows in the smooth duct.

Similarly, Aly et al [1978] found that the secondary flow velocities at different Reynolds numbers in an equilateral triangular duct scaled satisfactorily with the average friction velocity. However, they also found that, in contrast with the square duct case (Brundrett and Baines, 1964), the normal stress vorticity production predominated over most of the cross-section, the exception being the corner regions, where the shear stress term contributed significantly. Compared to the square duct case, the peak value of the shear stress in the triangular channel was not displaced as far towards the corner. Due to momentum transport by secondary flows, the wall shear stress over the central half of each wall was found to be constant within a few percent.

All of the above discussed channel geometries contained one or more symmetry planes. The 30°/60° right triangular duct used by Hurst and Rapley [1991] had no symmetry planes, so the flow in this case was expected to be fully influenced by the duct walls. Hurst and Rapley [1991] attributed the higher levels of the turbulence to the shape effects rather than to the effects of the Reynolds number, which in their case was higher than those in the other studies (Aly et al, 1978, and Brundrett and Baines, 1964). It appeared from their

results that conventional normalization with the friction velocity would not provide the often assumed independence from the Reynolds number. The inadequacy of the equivalent or hydraulic diameter in correlating non-circular duct friction factors was clearly evident from their measurements. This confirmed the findings of Leuthcusser [1963], who showed that the relationship between friction factor and Reynolds number (e.g. the Blasius relation) could not be universal, even if the equivalent diameter were used as the characteristic length parameter of the cross-section. The hydraulic diameter of a given cross-section is, by definition, the corresponding parameter of a ``shapeless" conduit with an equivalent cross-section. So, the use of a hydraulic diameter would be legitimate for the comparative description of channel with different cross-sectional shapes, but not as a characteristic length for the description of the flow dynamics. The presence of acute internal angles in ducts, creating sharp deviations from the circular geometry, the simultaneous occurrence of laminar and turbulent flow regions in narrow passages (Eckert and Irvine, 1956) and the occurrence of secondary flows make it impossible to correlate all flow dynamics using a single parameter, including the hydraulic diameter. As an illustration, Eifler and Nijsing [1967] have shown that the use of a hydraulic diameter would be inadequate for flow resistance predictions in rod bundles with *P/D* less than 1.08.

Prinos et al [1988] performed turbulence measurements in a trapezoidal duct with an angle of 64° and an aspect ratio (defined as the ratio of the short side to the height) of about 3.0. The maximum velocity was found to occur in a region approximately half way between the centreplane and the side wall. The isovel pattern in the region affected by the walls suggested the presence of relatively strong secondary flows. They observed that the contours appeared to be approximately symmetrical about the corner bisectors, thus inferring that each corner bisector separated a pair of independent secondary flow cells. Prinos et al [1988] also found that roughening one of the parallel walls had the effect of shifting the isovel contour lines towards the smooth wall. In fact, the flow pattern changed dramatically (normal stresses were doubled and shear stresses were tripled) to the extent that secondary flows in the corner between a smooth and rough wall were suppressed.

The trapezoidal duct used by Khalifa and Trupp [1988] had about the same angle (60°) as the one used by Prinos et al [1988] but a lower aspect ratio (about 0.77). Khalifa and Trupp [1988] found two counter-rotating secondary flow cells in the duct corners, one on

each side of the corner bisector. The maximum measured secondary velocity represented only 2.2% of the bulk velocity. It appeared that their measurements agreed well with the law of the wall. Also, the friction velocity was found to render their data fairly independent of the Reynolds number. Khalifa and Trupp [1988] explained the higher turbulence intensities (compared to an equivalent pipe flow) by the presence of secondary flows, which convected highly turbulent fluid generated near the walls to the central regions, thus causing turbulence intensities at a given location to be higher than they would be otherwise. The obtained turbulence intensities were interrelated linearly, with coefficients comparable to those found by Seale [1982] for his simulated rod bundle channel. This fact is important to turbulence modelling, because both the latter geometry and the trapezoidal duct have more than three secondary flow vortices in each primary flow cell.

Subbotin et al [1971] observed in their triangular array rod bundle a curvature in the isotachs for P/D=1.05. They attributed this fact to the existence of secondary flows. No distinct curvature was detected in the isotachs for P/D=1.1 and 1.2. For P/D=1.05, they observed, based on the distributions of the local bulk velocities, an intense transfer of mass and momentum by the secondary flow streams.

Kacker [1973] measured secondary flow velocities in an eccentric annulus (with a diameter ratio of 5.68 and an eccentricity of 0.475) and a two-rod test section, with the same tube and rod diameters as the annulus. In the annulus case, he detected a single secondary flow vortex per primary flow cell (which was in this case, half the circular tube section). In the two-rod geometry, he found two secondary flow vortices per primary flow cell (i.e. a quarter of the tube section): a large vortex and a smaller one located between the centre of the tube and the rod surface; the total flow in the second vortex was nearly 60% of the flow in the larger one.

Kjellström's [1974] measurements of the lateral velocities showed that a large-scale circulation was present in his triangular array test section. Deduction of this circulation indicated the existence of secondary flow cells, with velocities (although with significant scatter) less than 1% of the average axial velocity. Although he did not resolve the number of secondary flow cells present in a primary flow cell, his kinetic energy measurements were incompatible with a two-cell flow pattern. Kjellström [1974] also showed that very small secondary flows (of the order of 0.3% of the axial velocity in his case) would result in a

convective momentum transport of the same magnitude as the turbulent transport, thus explaining the high mixing rates reported by some investigations.

Even though Trupp and Azad [1975] did not measure directly secondary flows, they were able to infer their existence from the wall shear stress and the turbulent kinetic energy distributions. Calculations involving the mean energy equation allowed them to conclude that a single secondary flow cell was probably present in each primary flow cell; that the convection of mean energy by the secondary flow was roughly of about the same magnitude as transport by the turbulence; and that the strength and influence of these flows increased with decreasing *P/D*.

Carajilescov and Todreas [1976] performed an experimental and numerical (using a one-equation statistical turbulence model) study of turbulent flows in an interior subchannel of a triangular array rod bundle. Their experimental determination of secondary velocities was inconclusive. However, they were able to predict numerically a pair of counter-rotating secondary vortices in a primary flow cell. The vortex closest to the gap was very weak compared to the second vortex, which affected only regions away (by at least 12°) from the gap. So, the gap region was not sensibly affected by secondary flows. As the gap width was reduced from *P/D*=1.217 to 1.123, they predicted that the large vortex became smaller and the vortex in the gap region became larger. As will be seen later, in most of the literature, a single secondary flow vortex per primary flow cell has been predicted for the triangular array rod bundle, at least for the lower values of *P/D*. They predicted higher secondary velocities (normalized with the bulk velocity) as the Reynolds number increased.

Trupp and Aly [1979] also used a one-equation turbulence model to predict secondary flows in a triangular array rod bundle. Their numerical model was tested against their measurements in a triangular duct (Aly et al, 1978) discussed earlier. They observed that the normal stress vorticity production term predominated everywhere in the flow cell. It was inferred from the location of maximum vorticity that the gap region did not act as a corner for the studied range of *P/D*=1.12 to 1.35. They predicted a single vortex in each primary flow cell. The secondary flows were seen to become weaker with increasing gap widths and, presumably, to vanish for sufficiently large gaps. Extrapolation using the obtained results suggested that this may have occurred when *P/D* exceeded 1.5. On the other hand, as the gap width was increased, there was an increased penetration of the secondary

flow streamlines into the gap region. The secondary velocities were not found to scale well with either the average or the local friction velocity. Trupp and Aly [1979] explained that this happened because the Reynolds number dependence varied spatially, i.e. because the secondary flow cell shifted and was distorted with changing Reynolds number. In fact, when normalized by the bulk velocity, the secondary velocities increased less in the gap region than they did in the central part of the flow cell. All of the above results of Trupp and Aly [1979] were obtained with the use of isotropic eddy viscosities. However, by imposing anisotropic values of the eddy viscosities, the predicted secondary flows were found to be weaker, due to a reduction in the vorticity production. The effect of increasing the anisotropy factor on the wall shear stress was found to be very similar to that achieved by increasing the secondary velocity level. Even though the two mechanisms are physically very different, they are not completely independent. Secondary flows arise mainly due to anisotropy in the Reynolds stresses, but, while convecting fluid, they generate mean shear stresses, thus influencing the distribution of the Reynolds shear stresses and, by the same token, the eddy viscosities. Trupp and Aly [1979] concluded that isotropic analyses would overestimate the strength of secondary flows in rod bundles, which are known to have anisotropic eddy diffusivities.

Tahir and Rogers [1979] reported measured secondary velocities in a triangular rod array with P/D=1.06. Their tangential velocity profiles suggested the presence of a single secondary flow vortex in each primary flow cell. The secondary flow pattern predicted by Rapley and Gosman [1986] (they applied a finite-volume calculation method using simplified algebraic versions of the Reynolds stress transport equations) was in agreement with the above measurements of Tahir and Rogers [1979]. For P/D=1.06 and 1.123, a single secondary flow vortex was predicted, while an additional minor vortex near the gap was found for P/D=1.20. Rapley and Gosman [1986] noted that the observed decrease of secondary flow levels with P/D was consistent with the argument of Hinze [1973], which linked the strength of secondary motions directly with the amount of peripheral variation in wall shear stress.

Seale [1982] performed measurements and numerical predictions in a simple duct (Figure 2.4) that simulated two interconnected subchannels of a rod bundle with P/D=1.20. Beside the secondary flows in the corners of the channel, he obtained two large rotating cells

between the flat wall and the rod and one cell in the gap region between the rod and the axis of symmetry. The two large cells moved fluid from the core of the duct and directed it towards the flat side walls above the rods. The gap cell convected fluid down the centerline and returned it to the core along the rod surface. He observed that, if the secondary flows were excluded from the computations, then his predictions would not match the measurements, no matter how the empirical constants were optimized. His computational work confirmed the equalizing effect of secondary flows on the wall shear stress variation around the walls of the duct.

Vonka [1988a] used a laser Doppler velocimeter to measure secondary flow velocities in a triangular bare rod bundle (P/D=1.3) for two Reynolds numbers equal to 60,000 and 175,000. The obtained secondary motion was accompanied by a weak flow redistribution due to developing flow. The cross-flow and the secondary flow were separated assuming superposition. The average secondary velocity was of the order of 0.1% of the bulk velocity. The experimental results resolved one vortex per primary flow cell, in contrast with the numerical results of Carajilescov and Todreas [1976] and Rapley and Gosman [1986]. The vortex centre was roughly at 20° from the gap and at slightly more than half the distance from the wall to the subchannel symmetry plane. Vonka [1988a] noted that the Reynolds number dependence was not resolved with certainty from his results. However, the following trends were observed: similar forms of the velocity profiles were obtained for both Reynolds numbers; and the total tangential flow, normalized by the bulk velocity, was smaller for the lower Reynolds number, while, if normalized by the friction velocity, it seemed to be independent of the Reynolds number.

Slagter [1988] performed a numerical study, using a one-equation eddy viscosity turbulence model and an algebraic stress transport model, for the same conditions of the experimental work of Vonka [1988a]. The obtained results compared favourably with the experimental ones. Suppression of the secondary flows increased the wall shear stress variation around the perimeter of the rod, while their presence resulted in more uniform distributions of the axial velocities in the subchannel.

Vonka [1988b] evaluated the contribution of the secondary flows to turbulent transport in rod bundles and observed that this contribution in the radial direction was significant. Also, his experimental data indicated that the secondary flows contributed to the

circumferential transport of momentum by forming two transporting streams in opposite directions: one in the wall region and the opposite at some distance from the wall. When these transporting streams were averaged separately over a radial traverse, they were found to be quite strong. The analysis showed that about half of the total circumferential transport was due to secondary flows.

Even though no significant secondary flows were recognized in the study of Hooper and Rehme [1984], according to Vonka [1988b], the absolute value of the calculated balance term (introduced to satisfy the momentum equation based on their experimental measurements) was sufficiently large to leave room for a significant contribution of secondary flows to the transport of momentum. This is in contradiction with the findings of Hooper and Wood [1984] (reviewed earlier), who demonstrated, based on the same information, the negligible size of the mean secondary flows.

Using the analogy between the transport of momentum and heat, Vonka [1988b] expressed the above results in terms of heat transfer. He suggested that, in the radial direction, secondary flows could improve the heat transfer coefficients, while, in the circumferential direction, they would help smoothen out circumferential temperature variations. The contribution of secondary flows to the transport of heat in both directions was found to be significant. It is to be noted here that the secondary velocities measured by Vonka [1988a] were very weak, probably due to the fairly open aspect of the rod bundle used. Nevertheless, their contribution to the turbulent transport was seen to be considerable. It is expected that this contribution would become more important with decreasing gap widths, where the secondary flows would become stronger.

2.5 Large Scale Structures Near Narrow Gaps

The existence of periodic flow pulsations in rod bundle flows was first revealed by the study of Rowe et al [1974]. Even though most of their measured autocorrelation functions displayed a nearly exponential decay with little or no evidence of dominant periodic behaviour, they observed significant periodic flow pulsations in the region between the gap and the subchannel centre for P/D=1.125. No significant flow pulsations were seen for larger gap spacing and the reduction of the gap width led to stronger periodic flow

pulsations in the region adjacent to the rod gap.

Tapucu [1977] and Tapucu and Merilo [1977] studied diversion cross-flow between two parallel square channels interconnected by a long lateral slot, thus modelling adjacent rod bundle subchannels. The present discussion will be limited to their pressure measurements, performed using pressure transducers placed along the slot in each channel. Tapucu [1977] associated the observed systematic waviness of the mean pressure along each channel with the pressure difference oscillations between the channels. Tapucu and Merilo [1977] detected the existence of such oscillations based on the axial variation of the measurements, even though they were not able to measure simultaneously the pressure difference at different locations along the slot. They further noticed that this phenomenon was more visible for comparable and/or high channel inlet flow rates. To obtain a better view of these oscillations, Tapucu and Merilo [1977] used a visualization technique, by injecting tiny PVC spheres into the flow along the slot. The fluid particles seemed to follow a sinusoidal path, whose wave length seemed to increase with increasing gap clearance. The flow visualization also showed that there was a slight shift of the particle path along the slot, i.e. the maxima and minima were not always at the same downstream positions. Tapucu and Merilo [1977] could not reach conclusive results either on the wave length or the amplitudes, because their pressure difference measurements along the slot were not simultaneous.

Tavoularis and Stapountzis [1983] and Tavoularis et al [1984] performed flow visualization in a 60° sector of a 37-rod bundle, using water flow visualization techniques such as the injection of chemically reacting dye and air-bubbles. In retrospective, the waviness of their streaklines and the observed high mixing seem to indicate, even for the bare bundle, the presence of large scale structures in the gap region (W/D=1.170).

Rehme's measurements (reviewed earlier) also suggested the presence of an almost periodic momentum exchange process through the gaps of rod bundles. Rehme [1987a] speculated that this intersubchannel flow pulsation was caused by a static pressure instability between the subchannels. This periodic momentum transport was observed (Rehme, 1987c) to exist even for the relatively large value of the ratio W/D=1.30.

Hooper and Rehme [1984] confirmed the above findings. They observed that the frequency of the periodic flow pulsations had a linear relationship with the flow Reynolds number and that the cyclic momentum exchange became more dominant as the gap width

was reduced (Hooper, 1983). They speculated that the flow pulsations were generated by an incompressible-type, parallel-channel instability, the origin of which can be explained as follows. If the mass flow in one subchannel decreased, the local axial pressure gradient for this subchannel would also decrease, thus generating a transverse pressure difference between itself and the neighbouring subchannels. For small gaps, the local intersubchannel static pressure fluctuations and the phase lag between axial and azimuthal velocity components would make this an unstable situation, leading to vortex shedding in the gap region.

Abdelghany and Eichhorn [1986], in answering a discussion of their article by Rehme, questioned whether the phenomena found by Hooper [1983] could be classified as "coherent structures" and whether the same results would be obtained in larger rod arrays (such as theirs). They stated that no regularity (similar to Hooper's) was observed in their hot wire signals, taken in a rod bundle with P/D=4/3.

Möller [1991] continued the work of Hooper and Rehme in order to determine experimentally the origin of the flow pulsations observed earlier and their dependency on the bundle geometry and Reynolds number. His power spectra of the azimuthal velocity components showed a very pronounced peak at 62.5 Hz, at a location where the azimuthal turbulence intensity had a local maximum, and a weaker peak at the same frequency at a location 1.76 gap-widths from the gap (W/D=1.072). The spectra of the pressure difference (measured with two microphones placed symmetrically on the two sides of the gap) showed an even more pronounced peak at the same frequency as the peak in the velocity fluctuation spectra. The frequency of the flow pulsations was found to increase with increasing Reynolds number and diminishing gap width. Möller [1991] defined the Strouhal number

$$Str_{\tau}=\frac{f.D}{u^{*}} \tag{14}$$

where f represents the peak frequency in the spectra and D is the rod diameter. The Strouhal number was observed to depend only on the gap width and not on the Reynolds number. In fact, the Strouhal number was found to be inversely proportional to the gap width. Möller's [1991] correlation analysis confirmed the findings of Hooper and Rehme, by showing flow pulsations to propagate over a large region of the subchannel.

Based on the above results and the distribution of the vorticity normal to the wall, Möller [1991] proposed a model to explain the observed phenomena. According to him, the stochastic nature of the turbulent flow would lead to instantaneously different velocity profiles on the two sides of the gap with instantaneously different vorticity distributions. Because the transverse motion of the eddies would not be obstructed, they would continue to rotate and cross the gap while being transported by the main flow. Similarly, eddies rotating in the opposite direction would cross the gap from the adjacent subchannel and so forth. This local phenomenon would propagate throughout the subchannel. The resulting motion would be similar to a Von Kármán vortex street transported by the main flow with a stable and ordered pattern. The flow pulsations were, therefore, explained as a phenomenon generated by the turbulent motion itself. The particular geometry of rod bundles leads to the quasi-periodic behaviour. Möller [1991] concluded that the turbulence structure in the gap region was a coherent structure and that it is this motion that would be mainly responsible for the mass exchange between the subchannels of rod bundles. It is to be noted that the model of Möller [1991] consists of a street of counter-rotating two-dimensional vortices having their centres on the gap centreline. Even though this model is not contradictory to his measurements, one can show that a model in which the centres of the counter rotating vortices alternate symmetrically on each side of the gap centerline is also fully compatible with Möller's [1991] results. It is simply that his correlation measurements can not resolve this issue. Furthermore, physical considerations would indicate that these structures would have a strongly three-dimensional character. This fact is not represented in the model of Möller [1991].

According to Möller's [1991] explanation, and in concordance with Hooper and Rehme [1984], the large scale structures are generated by a parallel channel instability, the origin of which can be related to the stochastic nature of turbulent motion. For this to hold, there should be no structures present in the gap region of the test-section used in the present work (since it does not represent two subchannels interconnected through a narrow gap, but rather a single channel enclosing a suspended rod), especially under laminar flow regime. It will be shown in Chapter 9 that this is indeed not the case.

Horanyi et al [1989] performed temperature measurements in a sodium cooled 4-rod test-section ($P/D=W/D=1.147$), geometrically similar to the one used by Rehme [1987a] and

Möller [1991]. Their power density spectra and cross-correlations of the temperature fluctuations confirmed earlier findings concerning the formation of a street of vortices in the gap region. They explained their results using the phenomenological model of Möller [1991]. However, they have indicated, without evidence, the existence of two counter-rotating vortices on each side of the gap. Also, the manner in which they have staggered these vortices is not supported by physical considerations.

Wu and Trupp [1993] performed turbulence measurements in a trapezoidal section containing a single rod. They followed the same methodology and gave the same interpretation of their measurements as Hooper and Rehme [1984] and Möller [1991].

The important contribution of the large scale structures to the inter-subchannel mixing was demonstrated by Rehme [1992], Möller [1992], Wu and Trupp [1994] and Kim and Park [1997], who attempted to derive mixing-correlations for the "lumped parameter" type of analyses of rod bundle flows based on measured spectra and Möller's [1991] physical model of the structures. These correlations could be improved based on more physically sound models.

Meyer and Rehme [1994] presented some very relevant measurements in two compound channels, one formed by two rectangular subchannels interconnected by a lateral slot and the other consisting of a rectangular channel with a slot. They documented in detail the formation of strong, large scale, quasi-periodic structures in the slot region of both channels, and correlated their frequency with the slot geometry and the bulk velocity. For the case of the two rectangular subchannels interconnected by a lateral slot, they proposed a two-dimensional flow model in which counter rotating vortices, with centres on both sides of the centerline, are being convected axially within the gap. They found the streamwise spacing of the vortices to be independent of the Reynolds number and their convective speed to be roughly equal to the average of the minimum velocity, at the centre of the gap, and the velocity at the edge of the slot.

Meyer and Rehme [1995] investigated, based on a frequency analysis, the large scale coherent structures present in the slot regions of three rectangular channels equipped respectively with a slot, two fins and eight fins. They have confirmed the presence of large scale structures even for the lowest Reynolds number studied, which was, based on the slot width, equal to 150. They studied the effect of viscosity by using air, water and a water-

glycol mixture. They could not detect a systematic variation of the structures' frequency with viscosity and concluded that, within the range of their experiments, the axial spacing of the vortices is exclusively a function of the geometry of the slot, independent of velocity and viscosity.

Recently, Biemüller et al [1996] obtained qualitative agreement between their Large Eddy Simulation (LES) and their measurements in a channel consisting of two rectangular sections connected through a slot near a wall. The LES results indicate the presence of two counter-rotating vortices with centres on opposite sides with respect to the gap centerline.

2.6 Heat Transfer in Rod Bundles

Groeneveld [1973] reviewed and reanalysed earlier literature on heat transfer in multi-rod geometries to develop empirical estimates of the ratio of subchannel-averaged convective heat transfer coefficient over that in circular tubes, and the ratio of the minimum local heat transfer coefficient over the subchannel-averaged one. The work presented in Chapter 3 is meant to up-date the correlations of Groeneveld [1973]. A more exhaustive list of literature, reporting heat transfer measurements in rod bundles, can be found in Chapter 3.

A comprehensive literature review of heat transfer in triangular and rectangular rod bundle subchannels has been presented by Rehme [1987c]. In the case of an infinite triangular array, he presented a correlation by Petukhov and Roisen [1974], in which the Nusselt number in the subchannel was related to the Nusselt number of a circular tube. This correlation represented an upper limit for P/D ratios from 1 to 4. According to Rehme [1987c], the same correlation could be reasonably applied to square subchannels with $P/D>1.3$.

Palmer and Swanson [1961] studied heat transfer for air flow in a seven-rod cluster, with $P/D=1.015$ and at a Reynolds number of 20,000. They found that the average heat transfer coefficient in a triangular subchannel was approximately equal to the one for smooth circular pipe, while the peripheral variation of the local heat transfer rate varied between 0.5 and 1.3 of the average value.

Marek et al [1973] studied heat transfer in square array rod bundle. They

recommended a correlation for the upper limit of the Nusselt number, similar to the one they established for the friction factor.

Barrow et al [1984] investigated the case of a corner subchannel at W/D=1.0 and obtained a ratio of the subchannel Nusselt number to the circular tube Nusselt number equal to 0.38.

Berger and Ziai [1982] and Berger et al [1986] used an electrochemical analogy method to obtain the variation of the local Stanton number in both a single rod in a channel and in a seven-rod cluster, in which several rods could be moved or bent simultaneously.

Hoffman et al [1970] performed extensive experimental work on fluid flow and heat transfer in a seven-rod cluster and obtained the wall temperature variation around the central rod and an outer one. They also used a mass transfer analogy to obtain the heat transfer coefficient distribution for different rod-rod and rod-wall separations.

Sutherland and Kays [1966] analysed turbulent heat transfer in triangular rod arrays by solving the energy equation using the technique of superposition of fundamental solutions, which were determined experimentally. This method allows the prediction of the heat transfer performance with arbitrarily specified heat flux distributions, once the fundamental solutions are established.

Guellouz and Tavoularis [1992a] measured the local heat transfer coefficient distribution around an outer rod of a 37-rod bundle model, in which localized heating was provided by a narrow heated strip. Various rod-wall proximities were investigated. The local heat transfer coefficient was minimum near narrow gaps and maximum in open flow regions but its variation became substantial only when the gap width diminished below a certain value (e.g. W/D<1.04). These authors also conducted in-flow mean temperature and temperature fluctuation measurements. When plotted in contour form, they presented asymmetries when the heater was near the gap as well as facing the subchannel centre. These asymmetries were probably the result of the inhomogeneities of the mean velocity and the turbulent kinetic energy in the subchannel, which caused heat to diffuse in a non-uniform manner; however, the contour bulging seemed also to be compatible with anticipated secondary flow patterns and/or the presence of large scale coherent structures in the gap region. In addition to the above results, Guellouz and Tavoularis [1992a] reported probabilistic measurements of the temperature fluctuation field. They presented quantities

such as the probability density function, skewness and flatness, along with the streamwise Corrsin microscale.

Moeller [1989] reported measurements of mean temperature and temperature fluctuations in the subchannels of a fully heated four-rod bundle having P/D=1.147 and cooled by liquid sodium, thus having a Prandtl number much lower than those in water and air. He found distinct temperature maxima near the narrow gaps and minima near the subchannel centres.

Meyer [1991] and Krauss and Meyer [1996] reported measurements in a fully heated 37-rod bundle, arranged in triangular array in a hexagonal channel and having P/D=1.12. The heat flux was maintained uniform around the perimeter of the rods. Special care was taken to minimize conduction and thus any smoothing of the temperature variations due to different heat transfer rates. While Meyer [1991] focussed on an inner subchannel, Krauss and Meyer [1996] limited their tests to a wall subchannel. Both studies measured the distributions of the wall shear stress, the wall temperature and the mean in-flow velocity and temperature, as well as turbulent quantities, including the turbulent stresses, the rms temperature fluctuations and the turbulent heat fluxes.

2.7 Conclusions

A voluminous literature has been accumulated, over the years, on the turbulent flow, mixing and heat transfer in rod bundles. This problem has been studied extensively both analytically (Table 2.1) and experimentally (Table 2.2). As a result, certain aspects of bundle flow appear to be adequately understood and well within our predictive ability, at least as far as their application in nuclear reactor thermalhydraulics is concerned. On the other hand, it is also obvious that several other aspects remain the subject of controversy, either due to the contradictory results reported by different investigators or due to the limited information collected on that specific issue. The main conclusions of the above literature review can be summarized as follows:

a. Rod bundle geometries vary widely. Their bulk properties can be correlated with the shape of the subchannels, the number of rods and the values of the parameters P/D and W/D. Local conditions, especially in the vicinity of narrow gaps and contact points, could

be very sensitive to variations of these parameters within the bundle.

b. The concept of hydraulic diameter is inadequate to represent complicated geometries, including rod bundles. Therefore, the friction factor and heat transfer correlations developed for the circular pipe flow can not be applied directly to rod bundle flows by substituting the bundle hydraulic diameter for the circular pipe diameter.

c. Adequate empirical methods have been developed for predicting the overall friction factor in laminar and turbulent flows in uniform rod arrays. The performance of these methods has not been tested in non-uniform bundles, for example in mixed arrays of triangular and square subchannels. Moreover, the prediction of local friction factors from the overall or subchannel-averaged values could lead to appreciable error, because not only could the local friction factor vary appreciably around the rod, especially near narrow gaps, but it may also attain values much larger than predictions based on bundle cross-section bulk properties. The local wall shear stress variation is also sensitive to the gap width, attaining local maxima in open flow regions and local minima close to the gaps. These minima become strong functions of the gap width only for very narrow gaps (e.g. $P/D<1.1$), with negligible gap effects for P/D 1.2 . The complex peripheral variation of the wall shear stress, found in some investigations, has been associated, in earlier literature, with secondary flows, although disagreement with this inference has been voiced in recent years.

d. Secondary flows (i.e. velocity components on the transverse plane, even in fully developed flows) are known to exist in rod bundle flows, although direct measurements of them are scarce. Experimental techniques to perform such measurements are indeed cumbersome, but have been developed and applied to simpler configurations. In view of the substantial divergence of opinions concerning the strength of secondary flows and their effect on turbulent mixing across gaps, additional experimental work focussing on this subject is needed.

e. The turbulent flow structure in the subchannels of rod bundles, especially in the gap region, is markedly different from the one in circular pipe flow. Contradictory results have been obtained by different investigators, concerning the applicability of a "universal law-of-the-wall". Rod bundle flows display a strong azimuthal turbulent diffusion, nearly independent of the azimuthal position.

f. Measurements of the correlation functions in the region near the gap, for small gap

widths (W/D<1.1), have shown this to be a region of significant periodic flow pulsations associated with large scale quasi-periodic structures, which become more dominant as the gap width is reduced. It has been suggested that these structures are generated by the turbulent motion itself and that their quasi-periodic behaviour is peculiar to rod bundles. The origins of the large scale structures have been attributed to an incompressible parallel-channel instability and have also been viewed as coherent structures. Considering that the validity and generality of these statements have not yet been resolved beyond any doubt and in view of the substantial effects that such structures could have on turbulent mixing across gaps, it appears that further systematic experiments are required.

g. Turbulent interchange mixing rates across gaps, as defined by "lumped parameter" approaches, are in general different for different geometries or different gap shapes. They are greater than can be accounted for by conventional turbulent diffusion alone, thus pointing to additional transport processes, which supplement turbulent diffusion. These mixing rates depend weakly on P/D, for sufficiently large gaps. The increased secondary flow strength and especially the strengthening of convective large-scale structures as P/D decreases have been viewed as compensating for the decrease in gap width, thus explaining the insensitivity of mixing to P/D values. However, the exact role played by each of the above phenomena needs to be clarified by further work. A possible critical value of the P/D ratio, below which the mixing rates decrease markedly, and the reason for this decrease have not yet been determined.

h. Computations of bundle flows and the associated heat transfer with the use of standard turbulence models have generally been met with limited success (Guellouz and Tavoularis, 1992b). While it is known that "isotropic" types of models are entirely unsuitable and that "direct numerical simulations" are unlikely to fall within our computational capabilities in the forseeable future, there is some hope that LES or properly adjusted Reynolds stress models might permit the reliable computation of turbulent flow and heat transfer in rod bundles. The development and verification of such models will likely require additional, specialized statistical measurements.

In conclusion, the geometric complexity and diversity of rod bundle subchannels generate a variety of phenomena not encountered in circular pipe flows. Some of these phenomena have barely been identified and explained, others have been the subject of

contradictory hypotheses. In particular, insufficient knowledge is available on flow and heat transfer characteristics near narrow gaps and contact regions. The only way to resolve these issues is by systematic measurement in appropriately designed and instrumented systems. Computation of bundle flows and heat transfer by simple models has proved to be inadequate, thus pointing to the use of more sophisticated approaches.

3

Convective Heat Transfer Coefficient in Single-Phase Flow through Rod Bundles

The objective of the work presented in this chapter is to establish practical correlations of the subchannel-averaged and the minimum local heat transfer coefficients with the pitch-to-diameter ratio, *P/D*, for square and triangular subchannel shapes. The proposed correlations are empirical and based on previous heat transfer measurements available in the literature. The approach followed is similar to the one described in a report by Groeneveld [1973], which it is meant to update by taking into consideration more recent measurements and using statistical curve fitting methods. This method provides the heat transfer coefficients normalized by appropriate reference values as follows.

The subchannel-averaged, single phase, convective, heat transfer coefficient in a rod bundle is normalized by the heat transfer coefficient in a circular tube, corresponding to the same coolant, Reynolds number and Prandtl number, as

$$I = \frac{\bar{h}_{bundle}}{h_{tube}} \qquad \textbf{(1)}$$

In order to avoid large errors associated with generalized heat transfer correlations, the tube

heat transfer coefficient was evaluated, where possible, using correlations developed specifically for the given fluid. Such correlations have been listed in Table 3.1. Then, the *I*-factor was estimated from reported experimental values in heated rod bundles for a given subchannel shape and plotted against *P/D*.

The minimum local heat transfer coefficient, at the minimum gap between rods, was normalized by the corresponding subchannel-averaged heat transfer coefficient as

$$J = \frac{h_{\min}}{\bar{h}_{bundle}} \tag{2}$$

The *J*-factor was estimated directly from heat transfer measurements in a wide variety of fluids and configurations.

For the evaluation of the *I*- and *J*-factors, the heat transfer coefficients were based on a coolant temperature averaged over the entire bundle cross section because, in general, local or subchannel-averaged temperatures were not reported in the original publications. Furthermore, the average heat transfer coefficient was evaluated using the equivalent hydraulic diameter, defined as four times the flow cross-sectional area divided by the wetted perimeter, which is known to produce less scatter than the equivalent heated diameter, defined as four times the flow cross-sectional area divided by the heated perimeter, (Groeneveld, 1973).

An extensive list of experimental studies of heat transfer in rod bundles has been presented in the list of references. Due to the unavailability of the original publications, some of the data considered were taken as reported in secondary or review articles. Some relevant details of the most complete studies, which were used to establish the above correlations, have been summarized in Table 3.2 and in Figure 3.1.

3.1 The Subchannel-Averaged Heat Transfer Coefficient

3.1.1 The Effect of the Pitch-to-Diameter Ratio

Figures 3.2a and 3.2b present compiled data of the *I*-factor for triangular and square subchannels, respectively. Sets of measurements reporting data at several *P/D* ratios have

been represented with specific symbols, in order to show individual variation trends. For triangular subchannels, for which there are a lot of measurements, these sets have also been shown separately, in Figure 3.3. All other data were grouped under the "compiled data" symbol and their sources indicated in Table 3.3. As an indication of the reliability of each set of measurements, data judged to be of reduced reliability (mostly due to missing information about the experimental conditions) were represented by open circles and were assigned a weight of 1/2 in estimating statistical correlations.

There is ample evidence in the literature that the I-factor has a very weak, if any, dependence on the Reynolds and Prandtl numbers (see also section 3.1.2). Thus, it seems legitimate to disregard differences in these numbers when presenting the I-factor as function of P/D. A large scatter in the data is observed for both subchannel shapes. Even though this can be attributed in part to the relatively large uncertainties associated with heat transfer measurements, the scatter seems inevitable if one considers the widely differing overall geometries (e.g. different numbers of rods and different configurations and heating conditions of the channel walls) and fluids. These issues will be addressed separately in the following sections.

Curve fitting through the above compiled data yielded the following correlations for the I-factor:

Triangular array ($1.0 \le P/D \le 2.2$)	$I=0.836+0.462(1-e^{-3.879(P/D-1)})$
Square array ($1.0 \le P/D \le 1.6$)	$I=0.883+0.464(1-e^{-2.794(P/D-1)})$

For comparison purposes, the correlation of Groeneveld [1973] and those (for triangular and square arrays) of Presser [1967] are shown on the same graphs. Groeneveld did not provide analytical expressions; a curve fitted, in the present work, to his graphical correlation was

Triangular/square arrays ($1.0 \le P/D \le 1.5$)	$I=0.306+0.430\ P/D+0.238(1-e^{-58.58(P/D-1)})$

The correlations suggested by Presser[1967] were, as reported by Markóczy [1972],

Triangular array ($1.05 \le P/D \le 2.2$)	$I=0.9696+0.0783\ P/D-0.1283(1-e^{-2.4(P/D-1)})$
Square array ($1.05 \le P/D \le 1.9$)	$I=0.9217+0.1478\ P/D-0.1130(1-e^{-7.0(P/D-1)})$

The present two correlations, for triangular and square arrays, differ perceptibly only for $P/D < 1.1$, with a maximum deviation of 5.6% at $P/D = 1.0$. Their maximum difference from Groeneveld's correlation is also in the order of 5%, with the latter overpredicting the I-factor for $P/D < 1.15$, except for P/D very close to 1.0 where it has a sharper decrease. On the other hand, the differences between the present correlations and those of Presser are more pronounced, especially in the case of triangular arrays where the difference is of the order of 15%. It has to be noted, however, that for the low P/D range (i.e. P/D < 1.2) of interest here, all correlations agree to within a few percent.

3.1.2 The Effects of Reynolds and Prandtl Numbers

The customary empirical form of convective heat transfer correlations in fully developed channel flows is

$$Nu = C\ Re^{a}\ Pr^{b} \qquad (3)$$

In cases of significant temperature difference between the wall and the bulk of the fluid, a correction factor for the viscosity changes of the fluid is also inserted in the above expression.

Table 3.1 lists some common correlations for circular tubes, some of which are specific to a given fluid while others are meant to be more general. A review of these correlations indicates that the exponents a and b are within the following ranges

$$0.77<a<0.87 \qquad \text{and} \qquad 0.33<b<0.61$$

Heat transfer correlations in rod bundles over ranges of Reynolds and Prandtl numbers have also been presented in the same form as those in circular tubes. For example, the experimental results of the University of New Mexico (Kim and El-Genk [1989], El-Genk et al [1990, 1992 and 1993] and Su and El-Genk [1993]) yield, for heat transfer to

water flow in triangular and square array rod bundles, $a=0.8$ and $b=0.33$, with only C dependent on the array geometry. The same exponents were obtained by Miller et al [1956], while Borishanskiy et al [1971] found $a=0.85$ and $b=0.4$. Rieger [1969a&b] correlated his measurements for water and for a solution of glycol and water using $a=0.86$ and $b=0.4$. Lel'chuck et al [1977] obtained $a=0.8$ and $b=0.4$ for air flow.

When compared to the circular tube correlations, the rod bundle correlations have comparable values of the exponents a and b, which implies that the I-factor should be at most weakly dependent on the Reynolds and Prandtl numbers.

3.1.3 The Effects of the Number of Rods and of the Channel Wall

In correlating the I-factor with the P/D ratio, it is implicitly assumed that all measurements are for infinite arrays of rods, where the only geometrical variable would be P/D. In practice the infinite array geometry can be reached or asymptotically approached by using a very large number of rods in a uniform array or by using a moderate number of rods with "dummy rods" on the channel walls to simulate the infinite array. However, for obvious economic reasons, neither of these two conditions is fulfilled by the majority of reported investigations. Therefore, in most of the compiled data "finite array" effects are present, explaining in part the observed scatter.

No correction of the data is possible without introducing further uncertainties. However, one can evaluate the relative importance of the error introduced by the finite array effects based on the work of Markóczy [1972]. The latter will be summarized below and then used in an example.

Markóczy [1972] developed a general I-factor expression for every rod within a finite array

$$I = 1 + 0.9120 Re^{-0.1} Pr^{0.4} (1 - 2.0043\, e^{-B}) \qquad (4)$$

where $B=D_{eK}/D$ and Re is based on D_{eK}, defined as

$$D_{eK} = \frac{4 \sum_{k=1}^{K} A_k}{\sum_{k=1}^{K} P_{wk}} \qquad (5)$$

K is the number of subchannels surrounding the rod of interest and A_k and P_{wk} are, respectively, the flow cross-section and wetted perimeter of the k-th subchannel. One may note that for an inner subchannel D_{eK} becomes equal to the subchannel hydraulic diameter of an infinite array.

To illustrate the use of this method and evaluate the error introduced by the finite array effects, the I-factor for the case of a 4-rod square array bundle (Figure 3.4) will be compared to the one (I-factor) for an infinite square array with the same pitch-to-diameter ratio. For simplicity, it will be assumed that the Reynolds numbers, based on D_{eK}, of the finite and infinite arrays are the same.

Figure 3.5 presents samples of the results of such comparison. As expected, the amplitude of the deviation between the finite and infinite arrays is a function of the Reynolds and Prandtl numbers and the geometrical factors P/D and W/D. In fact, the finite array effect becomes more pronounced for lower Reynolds numbers, higher Prandtl numbers, low P/D values and to a lesser degree high W/D values. This dependence on W/D was also studied by equating the B values for the finite and infinite arrays, which led to a quadratic equation for W/D with coefficients depending on P/D and the geometry of the rod bundle. For the four-rod, square bundle described above, it was possible to match the finite and infinite array I-factors only for $P/D > 1.33$ (i.e. only in this range there was an acceptable solution for W/D). For W/D smaller than the root of this equation, the I-factor of the finite bundle is smaller than the one for the infinite array. This shows that one can obtain a performance similar to the one of infinite arrays without resorting to a large number of rods, but rather by choosing the appropriate W/D ratio, as, for example, done by El-Genk et al [1990]. The above finding, based on the solution of the quadratic equation, supports the physical expectation that matching the combined heat transfer in the wall- and corner-subchannels to the one in the inner subchannel would result in the same total heat transfer from the rod as if it was in an infinite array with a P/D equal to that in the inner subchannel. The heat transfer in the wall- and corner-subchannels increases with W/D to reach and exceed the value of the infinite array. In cases of very low P/D, depending on the geometry of the bundle, the wall- and corner-subchannels might have a higher heat removal than the inner-subchannel, even at $W/D = 1.0$.

It has to be noted that the four-rod bundle is an extreme case where the finite array

effect would be strongly present. This effect is expected to diminish as the number of rods is increased.

3.2 The Minimum Local Heat Transfer Coefficient

3.2.1 Implications of the Use of Apparent Local Heat Transfer Coefficients

The J-factor was defined earlier as the ratio of the minimum local heat transfer coefficient to the subchannel-averaged heat transfer coefficient. The local heat transfer coefficient requires the local bulk temperature, $T_b(\phi)$, defined as the average temperature of the fluid in a narrow subchannel sector, bounded by two neighbouring radii, the rod wall and the line of maximum velocity. According to this definition, one would like to determine J as

$$J = \frac{\dfrac{q}{T_w - T_b(\phi_{\min})}}{\overline{h}_{bundle}} \tag{6}$$

where q is the heat flux around the entire rod periphery and $\phi_{\min}$ is the peripheral position of the minimum local heat transfer. Unfortunately, the experimental determination of the temperature $T_b(\phi)$ is quite difficult. For this reason, most investigators have used the subchannel bulk temperature, $\overline{T}_b$, instead. The heat transfer coefficient calculated in this manner is referred to as the "apparent" local heat transfer coefficient. Thus, the J-factor has generally been calculated as follows

$$J = \frac{\dfrac{q}{T_w - \overline{T}_b}}{\overline{h}_{bundle}} \tag{7}$$

Because the local bulk temperature at the peripheral position of minimum heat transfer coefficient, $T_b(\phi_{min})$, would generally be higher than the subchannel bulk temperature, $\overline{T}_b$, the use of the apparent local heat transfer coefficient tends to underestimate the J-factor. To complicate things further, the ratio of the local and subchannel bulk temperatures would also be a function of the P/D ratio, array geometry and heating conditions of the opposing rod or channel wall. Thus, the error introduced in the evaluation

of the J-factor would be different for different bundle configurations. This effect would likely contribute to a scatter in the collective presentation of J-factor estimates from different experiments.

On the other hand, it is clear that an underestimation of the J-factor would result in a conservative (underestimated) estimate of the minimum heat transfer. Moreover, if one wishes to use the J-factor correlation in order to calculate the maximum peripheral temperature on the rod surface (which would, presumably, occur at the location of minimum heat transfer coefficient), one would require the subchannel average bulk temperature, which is easier to determine than the local bulk temperature.

3.2.2 Estimates of the J-Factor

Figure 3.6 presents all available data of the J-factor; the same data are also listed in Table 3.3. Due to the scarcity of local heat transfer measurements, it was decided not to differentiate between triangular and square subchannels or between inner and wall subchannels in establishing the general correlation of J with P/D. For the same reason, the Reynolds number effect on the J-factor was disregarded in the general presentation. The data present substantial scatter, which can be attributed to experimental uncertainty, differences in geometries and experimental conditions as well as the use of the apparent rather than the true local heat transfer coefficient in the evaluation of J. The data in Figure 3.6 were least square fitted by a two-exponential correlation, which, unlike a single exponential, seemed to represent well both the initial and asymptotic trends in the measurements. The effect of Reynolds number differences will be discussed in the following subsection. As an average, the correlation fitted to all data was

$$J = 0.741[1-e^{-97.90(P/D-1)}] + 0.254\,[1-e^{-7.05(P/D-1)}] \qquad (1.0 \le P/D \le 1.65)$$

Figure 3.6 also includes a graphical fit provided by Groeneveld [1973] to the J-data available at that time. For comparison purposes Groeneveld's curve was fitted by the following analytical expression

$$J = 0.267+0.280[1-e^{-250.94\,(P/D\,-\,1)}] + 0.471\,[1-e^{-9.65\,(P/D\,-\,1)}] \qquad (1.0 \le P/D \le 1.5)$$

The differences between the two expressions above appear to be well within the experimental scatter.

The above equations express the well known facts that heat transfer is relatively insensitive to the *P/D* ratio for values of this ratio higher than 1.1 and that it increases gradually as *P/D* further decreases towards 1. It is also well known that, even at low *P/D*, the heat transfer sensitivity to *P/D* remains considerably weaker than that predicted by turbulence models based on isotropic eddy diffusivity. The observed insensitivity is compatible with the hypothesis that convective heat transfer across narrow gaps is not governed by gradient transport, which is a local process, but it is mainly due to large-scale, quasi-periodic coherent structures (Rowe et al [1974], Hooper and Rehme [1984] and Möller [1991]). The latter will be the object of the studies reported in Chapters 8 and 9. It is only at the narrowest gaps (*P/D* < 1.05) that intersubchannel mixing is suppressed, resulting in a marked decrease of the *J*-factor.

3.2.3 The Effect of Reynolds Number

As mentioned above, due to the scarcity of local heat transfer measurements, the Reynolds number effect on the *J*-factor cannot be determined with certainty. One may infer that, for a fixed *P/D*, the *J*-factor would get closer to 1.0 as the Reynolds number increases, so that the use of a relatively low Reynolds number correlation at higher Reynolds numbers would likely result in a conservative estimate of the minimum heat transfer coefficient.

Figure 3.7 presents the *J*-factor measurements of Irvine (as reported by Groeneveld [1973]), plotted vs *P/D*. Family curve fitting to the data, with *Re* as a parameter, provided the following expression

$$J = 0.390 + 0.567[1 - e^{-(17.829+0.000301\,Re)\,(P/D\,-\,1)}]$$

This expression, evaluated at the Reynolds numbers of the measurements, is also plotted in Figure 3.7. Although statistically optimized, this expression does not approach the expected

asymptotes at the two limits, $P/D \to 1$ and $P/D \to \infty$. The asymptotic requirements are satisfied by the alternative expression

$$J = 1 - e^{-(19.805+0.000367\,Re)\,(P/D-1)}$$

Both expressions indicate a weakening dependence of the J-factor on Reynolds number as P/D increases. The few available measurements of Presser [1971] confirm this tendency. The J-factor, based on the measurements of Hoffman et al [1966] at P/D=1.141 for both scalloped and circular channels, was essentially constant, within a non-systematic scatter, over a Reynolds number range from 5×10^3 to 2×10^6.

To illustrate the effect of the Reynolds number on the J-factor variation, two contours of constant J (those with J= 0.90 and 0.75), calculated using the above equation, were plotted in Figure 3.8. It can be seen that the sensitivity of J to Reynolds number diminishes with increasing Re. This sensitivity is significant for $P/D < 1.05$, while for higher P/D ratios the J-factor is near 1.0, irrespective of the value of Reynolds number. Although a conclusive explanation of the Re-effect has not yet been found, one may make the following comments. The kinetic energy of locally produced, small scale turbulence increases with Reynolds number, while the intensity of large scale pulsations is less likely to be Reynolds number dependent, if one assumes an analogy with vortical structures in plane wakes and mixing layers. Therefore, the variation of the Re-sensitivity of J with P/D may be interpreted as evidence of varying contributions of small- and large-scale effects to the total turbulent heat transfer.

Following the analysis of Irvine's results, one might be tempted to rescale all data of Figure 3.6 so that they would correspond to the same "reference" Reynolds number, Re_{ref}. In principle, this could be achieved by computing a corrected value, J_{ref}, based on the expression fitted to Irvine's data. The related ratio

$$\frac{1-J}{1-J_{ref}} = e^{0.000367\,(Re-Re_{ref})\,(P/D-1)}$$

evaluated at Re_{ref}= 50,000, has been plotted in Figure 3.9. Unfortunately, the relevance of this approach cannot be tested, due to the insufficiency of data. Furthermore, the wide

differences in the various geometries do not even permit a consistent universal definition of a Reynolds number. For these reasons, although judged to be of dubious accuracy for quantitative scaling of results in distinct configurations, the above expression could be useful in estimating the *Re*-sensitivity of a *J*-factor correlation, established in a given configuration at a given *Re*.

3.3 Concluding Remarks

Based on experimental results available from the literature, empirical estimates of a) the ratio of the subchannel-averaged, convective heat transfer coefficient in single-phase flows in rod bundles over that in circular tubes and b) the ratio of the minimum local heat transfer coefficient over the subchannel-averaged one, were evaluated and presented as functions of the pitch-to-diameter ratio for both triangular and square-type subchannels. The effects of Reynolds and Prandtl numbers and of the number of rods and wall presence were also assessed.

The approach adopted here seems to be the only practical method with the current knowledge of the flow structure in rod bundles. However, once the large-scale coherent structures, the main phenomenon controlling turbulent transport in the gap region, are better understood and documented, an analytical solution for the local heat transfer coefficient may become feasible. For that, a general model for the coherent structures has to be developed, so that there would not be a need to adjust the model constants for each bundle geometry, as it is the case with the turbulence models. These models are based on the same kind of empiricism as the correlations presented here. The main part of the work is dedicated to the study of the coherent structures that form in the gap region.

4

Definitions and Analytical Description of Coherent Structures

The aim of the present chapter is to introduce definitions and derivations to be used in subsequent chapters. Only definitions and derivations not likely to be found in textbooks are presented.

4.1 Definitions of Coherent Structures

Examples of phenomena that have been classified as coherent structures include the Kelvin-Helmholtz vortices in mixing layers, the von Kármán vortices in wakes, the hairpin vortices in outer boundary layers and channel flows, the low-and high-speed streaks observed in inner boundary layers, and the quasi-stationary apex vortices attached to a Delta wing.

Despite the extensive interest in coherent structures and the large volume of work dedicated to their studies, there is no agreement upon a particular definition of coherent structures. The discussion conducted during the workshop "Whither Turbulence? Turbulence at the Crossroads", reported by El Tahry [1989], is a good illustration of this fact. Among the definitions available in the literature, one may consider the following ones as representative.

The often quoted definition of Hussain [1983] defines a coherent structure as a connected, large-scale turbulent fluid mass with a phase-correlated vorticity over its spatial extent.

An alternative definition by Berkooz et al [1993] states that coherent structures are organized spatial features which repeatedly appear (often in flows dominated by local shear) and undergo a characteristic temporal life cycle.

As reported by El Tahry [1989], according to A. Perry, coherent structures are recognizable recurring patterns that do not necessarily have an order to them. Their scale and velocity are random; however their orientations are fixed.

Also reported by El Tahry [1989] is the definition given by R. Stull in which coherent structures are regarded as entities that cause transport of momentum or tracers across a finite distance in a non-diffusive way.

Lesieur [1997] distinguishes between coherent vortices and coherent structures. He defines a coherent vortex as a region of space

1. where vorticity concentrates enough so that fluid trajectories can wind around;
2. which retains (following the flow motion) a characteristic shape during a life time longer than its local turnover time; and
3. which is unpredictable, i.e. extremely sensitive to small perturbations of initial conditions.

He defines a coherent structure as a region of space which, at a given time, has some kind of organization regarding any quantity related to the flow, including velocity, vorticity, pressure, density or temperature. This definition of coherent structures is broader than, and includes, the definition of coherent vortices. According to these definitions, all of the examples of coherent structures presented in the first paragraph of this section are coherent vortices, except for the low- and high-speed streaks observed in boundary layers, which do not satisfy condition 1, and the quasi-stationary apex vortices attached to a Delta wing, because they are predictable.

One also has to mention that some researchers have voiced their disagreement with assigning a strict nounal definition to what they consider to be essentially an adjectival concept, i.e. descriptive of that part of turbulence which is ordered (Cantwell, 1989).

4.2 Analytical Descriptions of Coherent Structures

The description of coherent structures must include phase-dependent information. For this purpose, the "phase-average" concept has been introduced. This is an artifice similar to the "time-average" concept, which is the basis of the Reynolds decomposition. The phase-average of a random process, Q, is its ensemble average at a particular phase (i.e. time relative to an identifiable characteristic event during the life time of the structure) of the structure, defined as

$$<Q(x_i, \tau)> = \frac{1}{N}\sum_{j=1}^{N} Q(x_i, t_j+\tau) \qquad (1)$$

where τ is the time corresponding to the reference phase, t_j is a specified time with respect to the occurrence of the structure of interest and x_i represents the spatial position.

Two different decompositions of the turbulent flow fields have been used in the analysis of coherent structures. These are the "double decomposition" and the "triple decomposition". In the present work, both decompositions are used, depending on the information to be extracted.

4.2.1 Double Decomposition

According to the double decomposition, a random process, Q, is considered to consist of a coherent component, $<Q>$, and an incoherent ("random") component, q_r, as follows

$$Q(x_i, t) = <Q(x_i, t)> + q_r(x_i, t) \qquad (2)$$

The double decomposition has the constraint that it cannot describe the evolution of coherent structures or the extraction of energy by coherent structures from the flow which drives these structures (Hussain, 1983).

4.2.2 Triple Decomposition

In this decomposition, any instantaneous value, Q, is considered to consist of three components: the time-average component, $\overline{Q}$, the coherent component, $\tilde{Q}$, and the incoherent component, q_r, as follows

$$Q(x_i, t) = \overline{Q}(x_i) + \tilde{Q}(x_i, t) + q_r(x_i, t) \tag{3}$$

where the time-average component and the incoherent component are identical to the mean of the Reynolds decomposition and the incoherent component of the double decomposition respectively and where the coherent component can be obtained from the phase-average, defined above, as

$$\tilde{Q} = \langle Q \rangle - \overline{Q} \tag{4}$$

The triple decomposition provides a means for studying the physics of coherent structures and their interactions with the time-mean flow and the incoherent turbulence. However, as noted by Hussain [1983], implicit in this decomposition is the assumption that the coherent structure is a perturbation of the time-mean flow. In a region occupied by a coherent structure, the entire nonrandom motion is the coherent structure. Therefore, the coherent structure is the flow itself and not a mere perturbation.

4.3 Governing Equations

The governing equations will be presented as obtained according to the triple decomposition. The equivalent equations for the double decomposition can be readily derived following a similar procedure to the one presented below (Hussain, 1983).

4.3.1 The Continuity Equations

The continuity equations for each of the three components, namely the time-average

and the coherent and incoherent components, are obtained by substituting the triple decomposition for each quantity in the instantaneous continuity equation for incompressible flow with constant density fluid and carrying out first the phase-average and then the time average. The equations obtained are (Hussain, 1983)

$$\frac{\partial \overline{U_i}}{\partial x_i}=0 \quad ; \quad \frac{\partial \tilde{U}_i}{\partial x_i}=0 \quad ; \quad \frac{\partial u_i}{\partial x_i}=0 \tag{5}$$

4.3.2 The Momentum Equations

The momentum equations for the three component fields are also obtained by substituting the triple decomposition for each quantity in the instantaneous momentum equation for an incompressible, Newtonian fluid with constant density (Hussain, 1983). Carrying out first the phase-average and then the time average, and dropping the vanishing terms, according to continuity, one obtains the time-average momentum equation as

$$\frac{\partial \overline{U_i}}{\partial t}+\overline{U_j}\frac{\partial \overline{U_i}}{\partial x_j}=-\frac{1}{\rho}\frac{\partial \overline{P}}{\partial x_i}+\nu\frac{\partial^2 \overline{U_i}}{\partial x_j \partial x_j}-\frac{\partial}{\partial x_j}\left(\overline{\tilde{U}_i\tilde{U}_j}+\overline{u_{ri}u_{rj}}\right) \tag{6}$$

Subtracting the latter from the phase-averaged equation and using continuity yields the coherent momentum equation as

$$\frac{\partial \tilde{U}_i}{\partial t}+\overline{U_j}\frac{\partial \tilde{U}_i}{\partial x_j}=-\frac{1}{\rho}\frac{\partial \tilde{P}}{\partial x_i}+\nu\frac{\partial^2 \tilde{U}_i}{\partial x_j \partial x_j}-\frac{\partial}{\partial x_j}\left(\overline{U_i}\tilde{U}_j\right)+\frac{\partial}{\partial x_j}\left(\overline{\tilde{U}_i\tilde{U}_j}-\tilde{U}_i\tilde{U}_j+\overline{u_{ri}u_{rj}}-<u_{ri}u_{rj}>\right) \tag{7}$$

The incoherent momentum equation is obtained by subtracting the phase-averaged equation from the instantaneous momentum equation as

$$\frac{\partial u_{ri}}{\partial t}+\overline{U_j}\frac{\partial u_{ri}}{\partial x_j}=-\frac{1}{\rho}\frac{\partial p_r}{\partial x_i}+\nu\frac{\partial^2 u_{ri}}{\partial x_j \partial x_j}-\frac{\partial}{\partial x_j}\left(\tilde{U}_j u_{ri}+u_{rj}\overline{U_i}+u_{rj}\tilde{U}_i+u_{rj}u_{ri}-<u_{ri}u_{rj}>\right) \tag{8}$$

The above equations contain the following additional terms: $\overline{\tilde{U}_i \tilde{U}_j}$; $<u_{ri} u_{rj}>$ and $\overline{u_{ri} u_{rj}}$. Depending on the adopted method of numerical or analytical solution , part or all of these terms would require some kind of modelling.

In the above derivations, it is implicitly assumed that the phase-average and the time-average of incoherent quantities are zero, and that the phase-average of the time-average is equal to the time-average. It is also assumed that the coherent and incoherent components are uncorrelated, so that the time-average and the phase average of their products are always zero. Using the same assumptions, one can express the turbulent stresses according to the Reynolds-decomposition as

$$\overline{u_i u_j} = \overline{\tilde{U}_i \tilde{U}_j} + \overline{u_{ri} u_{rj}} \tag{9}$$

Similarly, it can be shown that

$$<(U_i - \overline{U_i})(U_j - \overline{U_j})> = <(\tilde{U}_i + u_{ri})(\tilde{U}_j + u_{rj})> = \tilde{U}_i \tilde{U}_j + <u_{ri} u_{rj}> \tag{10}$$

These two relations allow the calculation of the time-average and the phase-average of the incoherent stresses from quantities that are easier to evaluate.

One can also develop, following a similar procedure, the energy equations and the conservation equations for other quantities such as vorticity or kinetic energy. Examples of these are presented by Hussain [1983].

5

Experimental Facilities and Instrumentation

5.1 The Flow Facility

The flow facility (Figure 5.1) is set up as an open-discharge wind tunnel, whose test section consists of a rectangular channel containing a suspended, traversable aluminum pipe ("rod") with a diameter of D = 101 mm. The hydraulic diameter and the length of the test section were, respectively, 1.59D and 54.0D. The channel was supplied with air produced by a blower through a pressure box. In order to achieve even distribution of air flow, the pressure box contraction ratio, namely the ratio of the pressure box cross-sectional area to the open test section area, was 9.4. A woven screen was stretched across the entrance of the channel to enhance the full development of the flow.

The rod was suspended at both ends as well as at a third location, placed at approximately 20D downstream of the tunnel entrance. The middle support was used to maintain the pipe straight, as much as possible. Each support was equipped with a traversing mechanism, utilizing finely threaded bolt-and-nut assemblies and dial gauges, to provide accurate positioning of the rod with respect to the plexiglass channel base. The latter contained an array of machined circular ports (Figure 5.2), which could be fitted with special plugs containing pressure taps or measuring probes. In addition to these, the channel base

had a sliding plexiglass plate, 2.8D upstream of the exit end of the tunnel, which could be used for spanwise traversing of the probes.

5.2 Pressure and Wall Shear Stress Instrumentation

Wall static pressure can be measured by using infinitesimally small, clean, burr-free, square edged surface holes with their axes perpendicular to the surface. Such holes were machined in the plexiglass plugs discussed earlier (Figure 5.3a). The static holes had a diameter of 0.61 mm.

A Validyne DP 108, variable reluctance, diaphragm type, pressure transducer is used for the measurement of the pressure. It is connected to an integrating voltmeter (TSI 1076) with a time constant selectable at 0.1, 1.0, 10 or 100 s. The voltmeter readings are taken with a resolution of 0.5 mV, which corresponds to 0.07 Pa.

Measurements of wall shear stress were conducted with the use of a flush-mounted hot-film probe. It consists of a miniature flush mounted sensor element, deposited on a quartz cylinder (TSI 1268, platinum hot-film), with a film length and width of 1.5 mm and 0.5 mm respectively. In order to perform wall shear stress measurements at various positions on the base of the channel, the probe was initially fixed on a plexiglass plug, which, however, showed evidence of local melting due to the high operating temperature of the film (250°C). To remedy this problem, a Teflon sleeve was added, as shown in Figure 5.3b.

The hot-film was operated by a constant temperature anemometer (AA-Lab Systems, model AN-1003). The signal conditioning and acquisition systems were the same as for the hot-wire anemometry, discussed below.

The Preston tube technique (Preston, 1954) was also used, by applying the analysis due to Patel [1965]. Two types of Preston tubes were employed. The first, shown in Figure 5.4, has an outer diameter of 0.72 mm and an inner to outer diameter ratio of 0.57. It was mainly used to check or calibrate the readings of the hot-film probe. A set of the second Preston tube type were available. Each consisted of a simple tube having an outer diameter of 0.79 mm and an inner to outer diameter ratio of 0.64. These were glued to the rod surface at fixed angular intervals to allow the measurement of the wall shear stress around the rod perimeter.

5.3 Hot-Wire Instrumentation

A variety of hot-wire and hot-film probes, including single, cross- and triple-sensor probes, have been used. These probes can be classified in two categories, those that are to be inserted into the flow from the exit end of the channel and those that are of the boundary layer type.

Two probes of the boundary layer type were available. A single hot-wire probe (DANTEC, model 55P14 with a wire length of 1.25 mm) and a cross-film probe (TSI, model 1249) that measures the streamwise and parallel-to-the-wall velocity components. At a later stage of the work, the cross-film probe was converted into a cross-wire probe with wire lengths and separation of 1 mm and 0.51 mm respectively. These probes were inserted through the plexiglass base of the channel and were traversed normal to it. Each probe had its own special traversing mechanism (Figure 5.5), designed and constructed for the present purpose. The top parts of the traversing mechanisms were interchangeable with the plexiglass plugs, so that they could be inserted at different positions on the channel base.

The remainder of the hot-wire probes were of the type to be inserted into the flow from the exit end of the channel. These included a single wire probe (TSI 1260AJ-T15 with a wire length of 1.30 mm) and a cross-wire probe (TSI, model 1248 with wire lengths and separation of 1 mm and 0.51 mm respectively) mounted on a mechanism, designed and constructed in the departmental workshop, permitting accurate traversing azimuthally, radially and longitudinally with respect to the rod (Figure 5.6). A three-sensor hot-wire probe (AUSPEX, AVE-3-102), that could resolve the instantaneous three-dimensional velocity vector, was also used. Its sensors had a length of 1 mm and were confined within a sphere of 1.5 mm in diameter. Their configuration is described in detail in Chapter 7. This probe, also inserted from the exit end of the channel, was traversed in the vertical and spanwise directions, with respect to the channel base, by a positioning system consisting of precision leadscrews (Unislide Assemblies) driven by stepping motors and controlled by a programmable controller/driver (Velmex Inc., model NF90).

The hot-wire and hot-film probes were operated by a multichannel constant temperature anemometer (AA Lab Systems, model AN-1003). Prior to its digitization, each analog anemometer output was conditioned, using the anemometer's built-in amplifiers and

low-pass filters. These could offset the input signal by a DC voltage between +12 and -12 Volts, amplify it by a gain, selectable within a continuous range between 1 and 20, and low-pass filter the amplified signal with cut-off frequencies selectable from a set of 12 discrete values between 380 Hz and 14 kHz.

All conditioned signals were digitized using a 16-bit analog-to-digital converter (IOtech, model ADC488/16), interfaced with a personal computer. The converter had four possible ranges of input voltages, ±1 V, ±2 V, ±5 V and ±10 V. It could sample simultaneously up to 16 single-ended or 8 differential analog input channels and digitize them consecutively with sampling frequencies up to 100 kHz per channel.

The digitized samples were transferred to the hard disk drive periodically during the acquisition. The hard disk data files were, afterwards, transferred for long term storage to magnetic tapes and at a later stage of the work to CD-ROM disks.

5.4 Temperature Measuring Instrumentation

During the preliminary tests of the flow facility and the hot-wire tests for temperature sensitivity, the local mean temperature of the air stream was measured with a glass-coated thermistor mini-probe (Fenwal Electronics, 2000 Ω), which was mounted on a slender support (2 mm diameter, 70 mm long) in order to reduce probe interference. The thermistor probe was operated with a home-made electronic circuit (Figure 5.7), providing nearly linear output. The circuit could power up to four thermistors and could provide outputs corresponding to individual thermistors as well as to differences between two thermistor voltages.

The monitoring of the flow temperature during the measurements and the calibration of the thermistor were performed with the use of a mercury thermometer having 0.1 K resolution.

5.5 The Flow Visualization Equipment

A smoke injection technique was used for flow visualization. A smoke generator (Nutem Ltd, System E) was used for that purpose. Actually, in this device an oil mist,

instead of smoke, is produced by vaporizing a colourless, non-toxic mineral oil through heating and then condensing it into tiny droplets suspended in the air and giving the impression of smoke. The oil mist was injected parallel to the air flow from an "L" shaped tube attached to a similar plug to the ones shown in Figure 5.3. The tube could be traversed normal to the channel base and in the spanwise direction if the plug were inserted on the sliding plexiglass plate. The oil mist flow rate was controlled through a valve in order to achieve isokinetic injection.

For clearer visualization, only the flow region of interest was illuminated with a thin sheet of light produced by passing a 100 mW laser beam through a cylindrical lens. The visualized flow was recorded by a video camera, which had a minimum exposure time of 0.001 s per frame and a fixed speed of 30 frames/s. For presentation here, sections of the video film were digitized, frame by frame.

5.6 The Calibration Jets

At the initial stages of the present work, a home made calibration jet was used for the characterization (e.g. the determination of the hot-wires' directional response and sensitivity to temperature) and calibrations of the hot-wire probes. As shown in Figure 5.8, the jet flow, produced by a centrifugal blower, was passed through various turbulence-reducing screens, a settling chamber and then through a 24:1 axisymmetric contraction with a 22.5 mm exit diameter. The flow could be heated using electric heaters placed immediately after the fan. At the jet exit, a probe mounting mechanism allowing the rotation of hot-wire probes in one plane can be used to determine the directional response of hot-wire probes.

At later stages of the work, a DISA calibration unit (DISA, model 55D90) became available. To generate the jet flow, compressed air from the laboratory main line was supplied to the pressure control unit (DISA, model 55D44), where it successively crossed a filter (removing particles down to 0.5 μm in size), a pressure regulator and a sonic nozzle, which produced a steady, constant, mass flow rate independently of small changes in conditions. Then, the flow entered the main jet unit, where it is conditioned by screens, flow straighteners and noise filters, and finally exited into the surrounding air through an

axisymmetric nozzle. Four interchangeable nozzles were available, with exit area sizes equal to 12, 24, 60 and 120 mm^2. The static pressure drop across the nozzle could be measured, to obtain the jet velocity. In order to enable the determination of the directional response of hot-wire probes, the unit was equipped, at the jet exit, with a probe mounting mechanism allowing the rotation of hot-wire probes in two perpendicular planes. A small appendage to the mounting mechanism was introduced to allow the probe roll angle to be varied and measured accurately. A home-made heating system was added between the exit of the pressure control unit and the inlet of the main jet unit. A variable transformer was used to adjust its power input.

6

Experimental Procedures and Accuracies

6.1 The Preston Tube Response

The Preston tube technique (Preston, 1954) was used, by applying Patel's [1965] expression

$$y^+ = 0.8287 - 0.1381x^+ + 0.1437(x^+)^2 - 0.0060(x^+)^3 \qquad 1.5 < y^+ < 3.5 \tag{1}$$

with

$$y^+ = \log\left(\frac{\tau_w d^2}{4\rho\nu^2}\right) \quad \text{and} \quad x^+ = \log\left(\frac{\Delta P_p d^2}{4\rho\nu^2}\right) \tag{2}$$

where ΔP_p is the difference between the pressure reading of the Preston tube and the static pressure and d is the outer diameter of the Preston tube.

Patel [1965] introduced a pressure-gradient parameter

$$\Delta = \frac{\nu}{\rho(u^+)^3}\frac{dP}{dx} \tag{3}$$

where ν is the kinematic viscosity of the fluid, dP/dx is the pressure gradient and u^* is the friction velocity. Δ is a measure of the severity of the pressure gradient as it affects the flow in the wall region. Patel [1965] estimated the maximum error in the Preston tube reading, due to the adverse pressure gradient, to be 3% for

$$0 < \Delta < 0.01 \quad \text{and} \quad \frac{u^* d}{\nu} \leq 200 \tag{4}$$

and 6% for

$$0 < \Delta < 0.015 \quad \text{and} \quad \frac{u^* d}{\nu} \leq 250 \tag{5}$$

For the present flow conditions and the Preston tubes used, the pressure gradient parameter is $\Delta = 2.10^{-4}$. Since the departure of the wall region velocity distribution from the inner law is gradual and small for small values of Δ (Patel, 1965), the Preston tube error due to the adverse pressure gradient in this flow is expected to be negligible.

The overall uncertainty of the wall shear stress measured with Preston tubes, accounting for the uncertainties in pressure readings and in Patel's expression, is 0.5% for a confidence level of 95% (i.e. with 20:1 odds that the true value would be inside the corresponding interval, centred about the reported value). All uncertainty analyses reported in the present work are in conformance with current international standards, outlined in ANSI/ASME [1985] and AGARD [1991].

6.2 Calibration and Testing of the Flush-Mounted Hot-Film Probe for the Measurement of Wall Shear Stress

The measurement of wall shear stress with a flush-mounted hot-film probe is based on the analogy between heat and momentum transfer. The principle of operation of this heat transfer probe can be illustrated by considering a heated element placed flush with the wall

and maintained at a constant temperature. If the element is small enough in the flow direction, the thermal boundary layer formed over it will lie entirely within the viscous sublayer, which has a linear velocity profile. The scalar (in this case temperature) transport equation, for this configuration, can be simplified by further assuming the influence of turbulent transport in the direction normal to the wall to be negligible and forced convection to predominate over natural convection and diffusion in the streamwise direction. The solution of the scalar transport equation, for the boundary conditions of constant wall temperature and constant unheated flow temperature, yields the theoretical design equation of the hot-film probe (Hanratty and Campbell, 1983)

$$\frac{q}{\Delta T} = 0.807\left(\frac{C_p k^2}{L\mu}\right)^{1/3}(\rho\tau_w)^{1/3} \tag{6}$$

where q is the convective heat flux, ΔT is the difference between the element and the fluid temperatures, ρ is the fluid density, C_p is the heat capacity of the fluid, k is the fluid heat conductivity, L is the element length and μ is the fluid viscosity.

The electrically generated heat in the element can be related to the resistance, R, and voltage across the element, E, by the relation $q = E^2/RA_e$. Assuming that the element is perfectly insulated thermally towards the wall and neglecting density variations, Equation (6) can be written as

$$E^2 = A\tau_w^{1/3} \tag{7}$$

where

$$A = 0.807A_e\Delta T\left(\frac{C_p k^2\rho}{L\mu}\right)^{1/3}$$

In practice, the heat loss to the substrate can not be neglected as it is often larger than the heat convected. For rough purposes, this heat loss can be lumped into a constant term, B, as

$$E^2 = A\tau_w^{1/3} + B \tag{8}$$

However, because of the heat losses, the assumption of a thin thermal layer contained

entirely within the linear velocity profile region is not satisfied. Thus, the convected heat can no longer be expected to vary proportionally to $\tau_w^{1/3}$. Moreover, the heat losses to the substrate and the effective length of the element are not easy to estimate. An empirical adjustment of the above equation, hopefully accounting, within a narrow calibration range, for all the above uncertainties, is

$$E^2 = A\tau_w^{\,n} + B \tag{9}$$

where the values of A, B and n would be determined by direct calibration. The value of the exponent, n, can be optimized during calibration by minimizing the rms error between the data points and the fitted calibration curve.

For its calibration, the hot-film probe has customarily been inserted in a simple flow, e.g. a circular pipe flow (Geremia, 1972) or flow in an annulus (Coney and Simmers, 1979), for which the shear stress can be estimated by other means, for example from the pressure drop. In the present work, the wall shear stress probe was initially calibrated within the boundary layer of a flat plate, for which theoretical values are known. In fact, it was shown (Roberson and Crowe, 1985) that, for a flat plate in turbulent flow and in the absence of pressure gradients, the local shear stress is given by

$$\tau_w = \rho \frac{U^2}{2} \frac{0.0577}{Re_x^{1/5}} \qquad Re_x < 10^7 \tag{10}$$

where U is the free stream velocity and Re_x is the Reynolds number based on the free stream velocity and the streamwise distance along the plate.

The flat plate (Figure 6.1) was especially constructed of plexiglass to be mounted in an open-discharge wind tunnel of rectangular cross-section, hereafter referred to as the wind tunnel. Provision was made for the adjustment of the plate height, to ensure that it is parallel to the flow velocity. The flat plate has a sharp leading edge and was fitted with pressure taps, in the form of plugs similar to those used in the single-rod channel, for the measurement of spanwise and streamwise pressure gradients.

Pressure, velocity and wall shear stress (using a Preston tube) measurements were performed to examine the possible differences between the flow conditions on the flat plate and the conditions assumed in the derivation of Equation (10).

Spanwise pressure distributions taken at 225 mm from the leading edge appear to confirm that the flow is two-dimensional. However, the streamwise measurements indicate the existence of an adverse pressure gradient (approximately 2.5 Pa/m). This departs from the theoretical assumption of zero pressure gradient.

The free-stream velocity was about 6.5 m/sec and the trace of a hot wire signal within the boundary layer indicated strong turbulent activity. At locations near the leading edge, measurements appear to conform with the logarithmic law. However, further away, the velocity profiles deviate from the logarithmic law due to the adverse pressure gradient.

Measurements of the wall shear stress on the flat plate were also conducted with a Preston tube. The parameters introduced by Patel [1965], evaluated for the flat plate used here, are within the ranges described by Equation (4), thus implying a maximum error of 3% in the Preston tube reading due to the presence of the adverse pressure gradient.

Measurements taken at 0.3 m from the leading edge indicated that, at this position, Equation (10) would overestimate the wall shear stress by about 10%. A comparison of the measured and predicted wall shear stress is presented in Figure 6.2.

To perform the calibration of the hot-film probe, the latter was placed at a location 0.3 m downstream of the leading edge. Special care was taken to have the probe plug flush with the plate surface. The probe was calibrated versus the theoretical prediction based on Equation (10). The obtained calibration equation was

$$E^2 = 114.081 + 29.59\tau_w^{0.30} \qquad (11)$$

where E is in Volts and τ_w in Pa.

In addition to the underestimation of the wall shear stress in the obtained calibration equation, the above calibration procedure was found to be cumbersome, mainly because of the need for mounting and adjusting of the flat plate in the wind tunnel. Also, possible inaccuracies could be introduced by possible misorientation or protrusion of the probe during calibration and/or measurement. To alleviate these problems, it was decided to calibrate the probe in situ (i.e. in the single-rod channel) versus the reading of the Preston tube.

The probe was inserted into the plexiglass base of the channel (457 mm upstream of the channel exit and 38 mm from the rod-wall gap in the spanwise direction), the rod was

raised sufficiently (about 50 mm from the base) to eliminate any interference effects with the Preston tube readings (no detectable effect was observed down to a rod-wall gap of 20 mm) and the wall shear stress was varied by changing the mean flow velocity. An example of calibration results is shown in Figure 6.3, corresponding to the expression

$$E^2 = 128.84+27.27\tau_w^{0.33} \qquad (12)$$

In this calibration technique, the Preston tube was placed close to the hot film probe and the static pressure was measured through a neighbouring pressure tap, aligned in the spanwise direction with the probe. The interference of the Preston tube with the hot-film reading was perceptible when the tube was located up to 31 mm downstream of the hot-film or within 4 mm on the side of the hot-film. In addition to that, the Preston tube reading was changing with axial distance, due to the axial pressure gradient in the channel. For these reasons the calibration was performed with the tip of the Preston tube at the same axial position as the hot-film probe, but displaced in the spanwise direction by 8 mm. Measurements indicated that the spanwise distribution of the static pressure was uniform, at least within the accuracy of the pressure transducer reading. Therefore, the distance between the Preston tube and the pressure tap should not introduce any appreciable error in the calibration procedure. Also, the hot-film probe and the Preston tube were placed in a region of an essentially zero shear stress gradient. Therefore, it can be anticipated that there would be no error due to differences in shear stress at the locations of the Preston tube and the hot-film probe.

A correction procedure for the effects of the fluid temperature variation is difficult to devise, especially due to the large heat loss to the substrate and the possible difference in temperature between the fluid and the wall. The transient nature of the problem, arising from the difference in heat capacity of the air and the wall, renders the construction of any model even more complex. For these reasons, it was decided to carefully plan to conduct the measurements and the calibration at the same steady fluid temperature. This is made easy by the fact that the calibration is performed in situ.

As a verification of the wall shear stress calibration method, measurements right in the gap for large gap widths (compared to the Preston tube size) were performed with both the Preston tube technique and the hot-film probe (Figure 6.4).

The effect of the orientation of the probe with respect to the main flow axis was studied by performing the calibration with the probe length parallel and perpendicular to the flow. The latter case presents the extreme case of misorientation. In fact, over the range of the calibration, the maximum error (i.e. the maximum difference between the two calibration curves), due to the above misorientation, in wall shear stress was estimated to be around 8%.

The positioning of the probe relative to the wall was found (Hanratty and Campbell, 1983) to affect strongly the response of the probe. As possible remedies, Hanratty and Campbell [1983] suggested, based on a number of studies reviewed, either calibrating the probe in situ or mounting it on a plug with a relatively large area and then transferring the entire plug. Both of these suggestions were adopted here. In addition, variations in the plexiglass thickness were accounted for by using a cathetometer and accurate shims (feeler gauges with an accuracy of ±0.025 mm) to mount the plug flush with the wall surface.

An analysis of the wall shear stress uncertainty, measured with the flush-mounted hot-film probe, was performed. The main contributors to the wall shear stress uncertainty are uncertainties in curve-fitting of the calibration data and in the determination of the reference wall shear stress. The overall uncertainty on the time mean and the variance of the wall shear stress are estimated to be respectively 3% and 6% for a confidence level of 95%.

6.3 Calibration of Hot-Wire Probes and Interpretation of Their Signals

The hot-wire probes used in the present work were generally calibrated either in one of the calibration jets or in the wind tunnel, versus a Pitot tube. The calibration equation was based on King's law of cooling

$$E^2 = A + BU^n \tag{13}$$

An example of the calibration curve of a single wire is presented in Figure 6.5. The calibration constants were determined by least square fitting to the data and the exponent was obtained by minimizing the rms deviation of the data from the fitted curve.

In order to perform measurements close to the wall and the region of small rod-wall

gaps, probes had to be calibrated at low velocities. However, this calibration was hindered by the insufficient sensitivity of conventional calibration standards (e.g. the Pitot tube) at low velocities. A new calibration technique, in which the probe was mounted on a pendulum, was developed. It is presented, in detail, in Chapter 7 along with typical calibration results and a discussion on the use of a modified King's law in the low velocity range.

For a single wire normal to the main flow direction, the velocity can be obtained from the anemometer voltage output through King's law (Equation 13). However, when the wire is not perpendicular to the main velocity vector, an effective cooling velocity, U_{eff}, is used instead of U in King's law. Neglecting cooling from tangential components to the wire and assuming an essentially two-dimensional flow, the effective cooling velocity can be related to the velocity components in its plane. For example, when the wire is in the U-V plane, the effective cooling velocity is given by

$$U_{eff} = U\cos\alpha + V\sin\alpha \tag{14}$$

where α is the wire angle with respect to the mean flow direction. It is determined experimentally using the method described in Chapter 7 for the three-sensor probe.

It can be seen that for cross-sensors the effective velocities for both sensors will yield a system formed by two equations similar to the above one. This is a system of linear equations that can be easily decoupled to solve for U and V, as

$$\begin{aligned} U &= \frac{U_{eff_1}\sin(\alpha_2) - U_{eff_2}\sin(\alpha_1)}{\sin(\alpha_1+\alpha_2)} \\ V &= \frac{U_{eff_1}\cos(\alpha_2) - U_{eff_2}\cos(\alpha_1)}{\sin(\alpha_1+\alpha_2)} \end{aligned} \tag{15}$$

A special case arises when the wire angles are respectively +45° and -45°, which are the nominal values for cross-sensor probes. For this probe configuration the two velocity components are given by

$$U = \frac{U_{eff_1} + U_{eff_2}}{\sqrt{2}}$$
$$V = \frac{U_{eff_1} - U_{eff_2}}{\sqrt{2}} \qquad (16)$$

For the measurement of two-point correlations, a simpler approach was followed, by which the overheat ratios of the two sensors in each cross-sensor probe were adjusted to provide nearly equal velocity sensitivities. The streamwise velocity fluctuation was computed from the sum of the two digitized signals and the spanwise fluctuation from their difference. As a test of this method, it was found that the voltage difference of the two sensors changed by less than 4% of the corresponding rms values over the entire velocity range of interest.

For the three-sensor probe, a more elaborate method was used to obtain the three velocity components from the anemometer outputs. This method is presented separately in Chapter 7.

Uncertainty analysis, accounting for uncertainties in curve-fitting of calibration data to King's law, in measurement of reference velocities and in the determination of sensor and probe body orientations, gave the following typical uncertainties, within a confidence level of 95%, for the cross-wire probe:

$$\Delta\overline{U}/\overline{U} \approx 2.5\%,\ \Delta\overline{V}/\overline{U} \approx 2.5\%,\ \Delta\overline{u^2}/\overline{u^2} \approx 5.0\%,\ \Delta\overline{v^2}/\overline{v^2} \approx 2.0\%,\ \Delta\overline{uv}/\overline{uv} \approx 10\%$$

For the three-sensor probe, accounting for uncertainties in curve-fitting of calibration and in the determination of sensor orientation and uncertainties due to the modelling of the sensors' response in the solution method is not a trivial task. Instead, all of the above uncertainties were lumped together and evaluated experimentally by performing measurements in the calibration jet with the probe oriented at different angles with respect to the jet axis. The uncertainty is taken as twice the standard deviation (in order to insure a 95% confidence level) of the difference between the measured velocity and the calculated velocity, based on the jet velocity and the probe orientation. As noted earlier, the discrepancies between the measured and calculated velocities are more important for larger azimuthal angles of the velocity vector. To reflect the measurements condition, only

differences measured at angles lower than 10° were considered in the uncertainty evaluation. The overall uncertainty of velocity measurements using the three-sensor probe was obtained by including uncertainties in the measurement of reference velocities with the above experimentally determined uncertainties. The resulting typical uncertainties, not accounting for uncertainties in the determination of probe body orientation, within a confidence level of 95%, are as follows:

$$\Delta\overline{U}/\overline{U}\approx 1.2\%,\ \Delta\overline{V}/\overline{U}\approx 3.5\%,\ \Delta\overline{W}/\overline{U}\approx 2.3\%,$$
$$\Delta\overline{u^2}/\overline{u^2}\approx 2.4\%,\ \Delta\overline{v^2}/\overline{v^2}\approx 2.8\%,\ \Delta\overline{w^2}/\overline{w^2}\approx 1.8\%,$$
$$\Delta\overline{uv}/\overline{uv}\approx 11\%,\ \Delta\overline{uw}/\overline{uw}\approx 8\%,\ \Delta\overline{vw}/\overline{vw}\approx 9\%$$

6.3.1 Resolutions

The cross-wire and the three-sensor probes had nearly identical sensors, but the three-sensor array occupied a larger volume than the cross-wire array, and therefore, the latter is expected to have a better spatial resolution than the former has. For that reason, the discussion of resolution will be presented for the three-sensor probe.

The main objectives of the present work are to document the "gross" properties of the flow (e.g. $\bar{U}$, u', etc) in a rectangular channel containing a single-rod, and to measure the features of the large-scale structures that form in the gap between the rod and the channel wall. Nevertheless, the ability of the probe to resolve small scale turbulence will be examined.

The orders of magnitude of the different turbulence scales present in the studied flow can be estimated based on reported measurements in similar geometries and from preliminary measurements performed in the present test section. Three characteristic lengths are of relevance: the integral length scale, L_u, the Taylor microscale, λ_u, and the Kolmogorov microscale, η_K. These were estimated to be typically

$$L_u = 19mm$$
$$\lambda_u = 5mm$$
$$\eta_K = 0.17mm$$

The sensors of the probe are contained within a spherical volume, 1.5 mm in diameter.

Therefore, the probe has a good resolution for the measurement of integral scales and larger scales e.g. the coherent structures, but is too large to resolve the Kolmogorov microscales. It is estimated, by loose extrapolation of the results of the analysis of Wyngaard [1969] for cross-wire probes, that the error in evaluating the Taylor microscale, using this probe, would be around 20%.

The use of King's law, a steady state equation, in time dependent flow is only justified when the smallest characteristic time of the flow (the convection time of eddies of the order of the Kolmogorov microscale) is sufficiently longer than the characteristic times associated with heat conduction and convection from the hot-wire (Corrsin, 1963). Estimates of these quantities for the present flow and probe indicated that steady heat losses can be used to calculate the dynamic response of the wires.

The temporal resolution is also limited by the sampling frequency of the anemometer signal. To be able to resolve events described by the Taylor microscale, it is required, according to the Nyquist criterion, that the sampling rate be at least

$$\frac{2.5}{\lambda_u / U} \approx 6635\,Hz$$

At the same time, one wishes to acquire a large enough sample to obtain a good statistical representation of the largest scales present in the flow. Based on the frequencies of the large scale coherent structures, the data records must be at least 3.5 s long to capture approximately 100 consecutive realizations.

The above requirements were best met by the following available low-pass filter settings and acquisition rates, which dictated the number of points to be acquired:

Low-pass filter: 3.8 kHz

Sampling frequency: 10 kHz

Number of points per record: 32 768

Number of records: 50

Idle time between records (to obtain statistically independent samples): 1 s

6.3.2 Correction for Temperature Sensitivity of Hot-wires

In the present work, the calibrations of hot-wire probes were not performed in the same apparatus as the measurements were. So, it is expected that the flow temperatures would be different, especially in view of the fact that the test-section blower heated the air going through it and that the room temperature varied with the time of the day. Therefore, corrections for the effects of temperature changes between calibration and measurement conditions were applied to the signals.

Starting from the empirical relation of Collis and Williams [1959] for heat transfer from cylinders in cross-flow, it can be shown that, for a flow with varying temperature, the relation between the anemometer voltage output and the velocity over the sensor is given by (Tavoularis, 1978)

$$\frac{E^2}{R(T_w)-R(T)} = A' + B' \left(\frac{T}{T_o} \right)^{-0.86+1.86n} U^n \qquad (17)$$

where $R(T)$ is the wire resistance at the specified temperature; all temperatures are expressed in K, T_w is the wire temperature and T_o=273 K. For the present cases, the variation of T was typically of the order of 1% of the value of T_o and the exponent n was in the range 0.35 to 0.5. So, the right hand side of the equation was only weakly dependent on temperature. In fact, Tavoularis [1978] demonstrated experimentally that for speeds between 5.5 and 13.5 m/s the right hand side remains effectively constant when the temperature is varied between 20 and 45 °C. All temperature effects appear through $R(T)$. The latter is related linearly to the temperature, as

$$R(T)-R(T_{ref}) = \alpha_t (T-T_{ref}) \qquad (18)$$

where T_{ref} is a reference temperature, usually the room ambient temperature, at which the wire resistance is measured. α_t is the temperature resistivity of the wire, determined experimentally by placing the hot-wire probe in a heated jet and measuring the wire resistance as the air stream temperature is varied. The slope of the resistance-temperature

linear curve is equal to the temperature resistivity (Figure 6.6).

Based on the above discussion, one can perform corrections for the effects of temperature variation on the anemometer voltage output using the following expression

$$\frac{T_w - T}{T_w - T_c} E^2 = A + B U^n \qquad \textbf{(19)}$$

where T_c is the air temperature during calibration. The ratio of temperatures on the left hand side of the above expression is exactly the correction factor of Tavoularis [1983].

7

Developments or Improvements of Experimental Techniques

During the course of the research towards documenting the flow and the coherent structures in the gap between a rod and the wall of a rectangular channel, several experimental challenges were met. The solution to these problems led, in certain cases, to the development of new techniques or the improvement of existing ones. The developments or improvements that can be considered as contributions on their own or that are general and independent of the measurements of Chapter 8 will be presented here.

The interest in a technique for calibrating hot-wire anemometry at low velocities, described in Section 7.1, arose from the fact that for very narrow gaps between the rod and the wall the velocity magnitude is reduced to ranges for which calibrations by customary methods cannot be applied.

It was apparent from a first set of measurements and from physical considerations that the "coherent" velocity, in the region between the gap and the middle of the subchannel, is three-dimensional and that the most effective and accurate means of obtaining the three components of the coherent velocity vector without losing their respective phase information would be to employ a three sensor hot-wire probe. Therefore, a method to obtain the

instantaneous velocity vector from the anemometer signal outputs of a three-sensor probe had to be developed. This method has been described in Section 7.2.

The clear and repeatable features of the coherent structures, present in the gap region of the flow of interest, observed in the velocity traces, encouraged the exploration of the applicability of conditional sampling techniques to the acquired signals. The adopted method is the Variable Interval Time Average (VITA) technique. It was observed, after preliminary tests of the technique, that improvements, based on the nature of the coherent structures, to the educed signals are possible. Section 7.3 will present a method of enhancing conditional sampling results.

7.1 A simple pendulum technique for the calibration of hot-wire anemometers over low-velocity ranges[1]

A limitation of hot-wire anemometers is that they require calibration versus some reference velocity measuring technique. While relatively high velocities (e.g. $U > 4$ m/s for air flows) in calibration facilities can be easily calculated from pressure differences obtained with pressure tubes or wall taps, at low velocities this approach is hindered by the decreasing sensitivity and accuracy of pressure measurement instrumentation. To overcome these shortcomings, several methods have been proposed to determine the reference velocity by other means. These methods can be classified as static or dynamic, depending on whether or not the hot-wire is given a movement in addition to or instead of the fluid flow.

A common static method consists of placing the hot-wire upstream of a contraction and estimating the local velocity from the measured value downstream of the contraction by using continuity and the assumption of uniform flow. Commercial calibration equipment (DISA, 1972), utilizing this approach, has a threshold of about 0.5 m/s. Obviously, this approach requires extreme care in the generation of the flow and its accuracy is limited by viscous effects. In another procedure, low velocities were induced by draining water at controlled volumetric flow rates from an air-tight chamber connected to the calibration nozzle (Christman and Podzimek, 1981). The relationship between the flow rate and the

[1] The work presented in this section has been published by Guellouz and Tavoularis [1995].

centerline velocity for fully developed laminar pipe flow has been exploited to perform calibrations at low velocities (Andrews et al, 1972 and Lee and Budwig, 1991). A calibration method in which the reference velocity is deduced from the vortex shedding frequency behind a cylinder was also proposed (Lee and Budwig, 1991).

Dynamic methods of calibration for hot-wires and hot-films include towing (Aydin and Leutheusser, 1980; Tabatabai et al., 1986; Tsanis, 1987), rotating (Pinchon, 1970; Anhalt, 1973), oscillating (Perry, 1982) and swinging (Haw et al., 1987; Haw and Foss, 1990; Bruun et al., 1989; Zabat et al., 1992) the probe by appropriate devices. All these methods require proper care to eliminate undesirable influences, such as drafts and vibrations, while some of them are also based on certain assumptions and theoretical models. The swinging arm ("pendulum") method appears to gain popularity, perhaps because of the relatively low cost and ease in fabricating the apparatus. It also appears that this method could benefit from further removal of complications in the design, operation and instrumenting of the apparatus (for example, Bruun et al. (1989) used a photocell to trigger sampling, while Zabat et al. (1992) differentiated the output of a computer-controlled solenoid). Simplification of the required assumptions and data processing procedures also appears to be feasible. An example of an assumption that appears to be unnecessary is Bruun et al's (1989) use of $A = KE_0^2$, where E_0 was the anemometer output at no-flow and K = 0.8, which would make B and n functions of the Reynolds number (Andrews at al., 1972). Therefore, we have devised a procedure that utilizes an apparatus that is either readily available in most engineering schools or easy and inexpensive to fabricate and requires no more hardware than a digital data acquisition system. The simplicity of the analysis also removes unnecessary sources of error.

Another issue associated with the measurement of low velocities with hot-wires is the uncertainty in modelling the hot-wire response at low Reynolds numbers. The most commonly used relationship for the response of a hot-wire placed normal to a stream with velocity U is the modified King's law

$$E^2 = A + BU^n \qquad (1)$$

where E is the voltage across the sensor and A, B and n are constants, to be determined by calibration. The exponent n proposed originally by King (1914), based on an analysis of

convective heat transfer from infinite cylinders, was 0.5, while several other investigators have proposed values generally in the range between 0.4 and 0.5. There is evidence, however, that different values of n would be more appropriate if calibration were restricted to a narrow range, particularly in the very low velocity range. Two physical reasons for this change of response have been identified: the lack of vortex shedding for Reynolds numbers below approximately 45 and the increasing importance of natural convection, as $Re \to 0$. Criteria for testing the importance of natural convection are expressed in terms of the Grashof number, Gr, which is the ratio of the buoyancy forces to viscous forces times the ratio of inertia forces to viscous forces. Among the available criteria, one could mention those proposed by Collis and Williams (1959)

$$Re_\infty = 1.85\ Gr_\infty^{0.39}\left(\frac{T_m}{T_\infty}\right)^{0.76} \tag{2}$$

Hatton et al (1970)

$$Re_m = 2.2\ (Gr_m\ Pr_m)^{0.418} \tag{3}$$

and Christman and Podzimek (1981)

$$Re_m = 2.00\ Gr_m^{0.50} \tag{4}$$

All of the above criteria, when evaluated for a cylindrical hot-wire with a diameter of 5 μm and typical overheats, yield lower air velocity limits for neglecting natural convection of the order of 0.05 m/s, with the corresponding $Re \approx 0.01$ (evaluated at the "film" temperature, T_m, i.e. the average of the wire and ambient temperatures).

Table 7.1 summarizes the available estimates of n in the low velocity regime. Correspondence between velocity and Re was based on the use of a 5 μm sensor, operated at $T_w = 523$ K in air of $T_\infty = 293$ K. The above results indicate that, for $U > 1$ m/s, n seems to have no systematic variation and takes values in the range from 0.4 to 0.5, established by optimal fit to calibration data. On the other hand, if a calibration is restricted to the range $U < 1$ m/s, values of n in the range from 0.5 to 1 would be more appropriate. In view of the rather scarce information on this issue, additional independent tests concerning the low-velocity value of n are needed.

A final issue to be considered in calibrating thermal anemometers with the "pendulum" method is their temporal response. Because the relative velocity during the swing of the sensor varies continuously, it would be advisable to establish whether its voltage output would be subject to significant hysteresis. Zabat et al (1992), in their study of hot-film response, introduced an acceleration parameter, α, representing the ratio of convective and acceleration time scales, as

$$\alpha = \frac{dU}{dt}\cdot\frac{d}{U^2} \tag{5}$$

and concluded that, for $\alpha < 0.085$, the heat transfer from the sensor would be essentially free of transient effects. It may be remarked, however, that even if unsteadiness would affect the calibration of hot-films, which have a relatively slow response, it is not expected to be a problem for hot-wires, at least in the low Reynolds number of present interest.

7.1.1 Outline of the procedure

The proposed new calibration technique can be summarized as follows. With the hot wire sensor mounted on the pendulum arm at a radius r, the linear velocity of the wire can be related to the angular velocity, $\omega = d\theta/dt$, of the pendulum by the expression

$$U = r\omega \tag{6}$$

Using King's law of cooling (Equation 1), the anemometer voltage output can be expressed as

$$E^2 = A + B(r\omega)^n \tag{7}$$

In the present case, a direct measurement of the angular velocity of the pendulum arm is not needed. Instead, the following method was employed to determine the calibration constants A, B and n. For the same release angle of the pendulum arm, the actual velocities, U_1 and U_2, of two hot-wire probes mounted at radii r_1 and r_2, respectively, would be related as

$$U_1 = \frac{r_1}{r_2} U_2 \tag{8}$$

Define a velocity difference as

$$\Delta U = U_1 - \frac{r_1}{r_2} U_2 \tag{9}$$

which, in terms of the corresponding voltage outputs, E_1 and E_2, of the anemometer, is expressed as

$$\Delta U = \left[(E_1^2 - A)^{1/n} - \left(\frac{r_1}{r_2} \right) (E_2^2 - A)^{1/n} \right] \frac{1}{B^{1/n}} \tag{10}$$

Although, ideally, ΔU should be identically zero, in practice it will attain non-zero values, due to both systematic (e.g. errors in the measurement of r) and random (e.g. noise) causes. The optimal estimates of the calibration constants would be obtained by minimizing the magnitude of ΔU over the entire velocity range of interest. To avoid unnecessary complications and uncertainties, it is proposed to minimize the root mean squared velocity difference, ϵ, over the accelerating half of the forward swing, given by

$$\epsilon = \sqrt{\frac{4}{T} \int_0^{T/4} (\Delta U)^2 dt} \tag{11}$$

Although optimization can easily be done by trial and error, one may also employ any of the many available multivariate optimization algorithms (for example, the method adopted in the present study is the *Simplex method* described by Borrie, 1986). For simplicity, instead of a trivariate optimization process for A, B and n, required to minimize ϵ, one may minimize the quantity $\epsilon B^{1/n}$, which only involves bivariate optimization for A and n, and then determine B by rewriting Equation (7) as

$$\frac{(E^2 - A)^{1/n}}{r} = B^{1/n} \omega \tag{12}$$

and integrating both sides over a quarter of the period of oscillation, as

$$B = \left(\frac{\int_0^{T/4} \left(\frac{E^2 - A}{r} \right)^{1/n} dt}{\theta_{T/4} - \theta_0} \right)^n \qquad (13)$$

where $\theta_{T/4}$ and θ_0 are, respectively, the maximum-velocity angle and the release angle. The expected economy in effort seems to justify the small bias introduced by this approximation.

The application of the proposed method will be illustrated by a calibration of a DANTEC 55P14 hot wire probe, having a single platinum-plated tungsten sensor, 1.25 mm long and 5 μm in diameter. The pendulum (Figure 7.1) used initially in this application was a Charpy apparatus (Avery, model 6703), originally intended for the "notched bar impact testing of metallic materials" (ASTM standard method). It consists of a 1.1 m arm with a large mass concentrated at its end. The mass of the probe and its mounting mechanism were negligibly small compared to the pendulum mass, so that changes in their position along the arm did not appreciably affect the pendulum characteristics. The release angle was fixed for all tests by a "lock and release" system and was equal to 70° from the vertical.

At a later stage of this work, a dedicated pendulum was designed and constructed (Figure 7.2). It consisted of a 1.4 m long T-section-steel-bar, forming the pendulum arm, and a concentrated mass of 9 kg, formed by joining two 0.025 m thick steel plates. Several positions on the arm were provided for the mounting of either the mass or the probe holders, thus allowing calibrations to be performed over several velocity ranges, typically for maximum velocities from 0.3 m/sec to 10 m/sec. The magnetic base of a dial gage was used as a release mechanism by magnetically holding and releasing the end of the arm. Two release angles were selected, at 90° and 20° from the vertical.

To perform a calibration, the anemometer signal was digitized, using an analog-to-digital converter board mounted on a personal computer, and recorded for half the first swing (i.e. when the probe was moving forward) after the release of the pendulum arm, with the hot-wire sensor mounted successively at two different radii. Only the first swing was considered for both radii to insure the quiescence of the surroundings, because, during subsequent swings, the probe traversed the wake of the pendulum arm formed at its previous passage. Further care was taken to shut down the air conditioning system and to eliminate

convection currents from the floor. When the hot-wire probe was mounted tangent on the Charpy apparatus, it was protruding forward to avoid the possible disturbance of the air caused by the forthcoming pendulum arm. The hot-wire sensor prongs were mounted tangent to the circular path of the sensor at each selected radius. The data were digitized at a rate of 2,000 Hz, thus giving typically about 2,000 points per half period, and smoothened by a moving average type digital filter. The repeatability and consistency of the hot-wire traces during different trials was confirmed by tests conducted for the same radius.

The matching of the angular positions corresponding to the signals E_1 and E_2, was achieved by matching the times corresponding to the positions of maximum velocity, i.e. to the minimum anemometer voltage. A smoothing algorithm was applied to the digitized signals in order to eliminate the effect of random noise. A typical pair of matched voltage traces is shown in Figure 7.3.

The present technique requires the values of at least two angular positions at two different times during the forward swing of the pendulum. In order to calibrate a probe in different velocity ranges, it would seem sufficient to utilize only the signal corresponding to a relatively narrow angle, however, the measurement or estimation of intermediate angles would introduce additional uncertainty. To minimize such uncertainty, it was decided always to use the release and maximum velocity angles and to vary the velocity range by changing the release angle, the position of the mass, or the radial position of the sensor.

7.1.2 Results and discussion

As an example of the proposed calibration procedure, Table 7.2 presents the calibration coefficients estimated from three different sets of data, using the probe described in the previous section, mounted on the home-made pendulum. As a consistency test, the maximum velocity in each case was computed from the potential energy of the pendulum, neglecting frictional losses, and it was found to agree within 2% with the corresponding values based on the hot wire calibration. As a further consistency test, the angular velocities were calculated, using the calibration equation and the signals acquired with the sensor positioned at two different radii, and were found to essentially coincide, at least during the forward swing.

Two more tests of the sensor response will be presented before discussing the calibration results. Concerning possible unsteady effects, the maximum value of the acceleration parameter, α, was estimated and was found to be roughly 0.00015, much lower than the critical value of 0.085 proposed by Zabat et al (1992). Therefore, the steady King's law would likely be applicable over the entire swing of the pendulum. The absence of hysteresis is also confirmed by the symmetry of the velocity signal before and after the maximum velocity point. Another concern, of relevance especially to case 3 (Table 7.2), was the possible effects of natural convection in the near zero velocity range, which may particularly affect the integral used in estimating the calibration constant B. The most restrictive lower velocity limit for the validity of the modified King's law (see previous section) was found to be 0.06 m/sec. Above this limit the velocity error due to convection would be negligible (note that, according to the Hatton et al (1970) correlation, at velocities as low as 0.03 m/sec the error in the indicated velocity would only be 10%). A rough estimate of the error in the value of B due to natural convection was of the order of a fraction of a percent and therefore negligible.

The values of the optimal velocity exponent in King's law in the different calibration ranges, shown in Table 7.2, are generally consistent with the previous literature. When the entire velocity range between 0 and about 4.8 m/s was considered, the optimal exponent was found to be 0.41, well within the generally accepted range for moderate speed calibrations. However, as the velocity range was restricted to lower values, the optimal exponent appeared to increase, showing a tendency to become unity, as $U_{max} \to 0$. The present measurements and some results from the literature are plotted in Figure 7.4. As an aid to the eye, the following fitted empirical relationship between the exponent and the maximum wire-Reynolds number for a particular calibration is also shown

$$n = 0.856 + 0.318 \arctan(-9{,}525\, Re_{max} + 0.753) \qquad \textbf{(14)}$$

As an illustration of the possible errors introduced in the measurement of extremely low velocities using hot wires calibrated over a relatively wide velocity range, the hypothetical measurement of velocity in the buffer layer was considered, assuming that the actual velocity profile is as measured by Reichardt (Hinze, 1975) and assuming that the friction velocity was 0.03 m/s so that the obtained profile would be within the range of the

calibration presented as case 3 in Table 7.2. The procedure was as follows. First, it was assumed that the calibration equation of case 3 correctly represented all velocities and the corresponding hypothetical voltage outputs of the anemometer were calculated. These voltages were then inserted in the calibration equation of case 1, and the corresponding velocities that would have been measured if this equation were used were computed. Figure 7.5 shows the velocity distributions obtained from the two calibration equations. It can be seen that the calibration obtained using the wider velocity range underestimates the velocity except in the region close to the wall i.e. $y^+<3$, where it overestimates it. In addition to and more important than the error in velocity would be the error in the estimate of wall shear stress based on the velocity gradient at the wall. An estimate of this error, for the example of Figure 7.5, was 36%.

7.1.3 Conclusion

A new, simple and inexpensive calibration technique in which the hot-wire probe is mounted on a pendulum was introduced. This technique could utilize the Charpy apparatus, which is available in most mechanical engineering laboratories, or an easy-to-build special apparatus. The main design considerations for this apparatus are the release angle, the mass and length of the pendulum. The mass of the system should be at least 30 times larger than the mass of the probe and its mounting mechanism to insure that placing the probe at different radii would not alter appreciably the position of the centre of mass. The length of the pendulum arm and the release angle are dictated by the required velocity calibration range, with the maximum velocity estimated by equating the potential energy of the pendulum at the release angle and its kinetic energy when it passes through the vertical position.

The exponent of the velocity in the modified King's law was found to be 0.41, for wire-Reynolds numbers less than 0.87, and increased to 0.66 and 0.84 if the latter were restricted to 0.15 and 0.08, respectively. An empirical relationship between the exponent in King's law and the calibration velocity range was fitted to the present and previous data.

7.2 Signal analysis method for three-sensor hot-wire probes[2]

A probe comprising three sensors can resolve the three-dimensional instantaneous velocity vector at a point. This represents an indispensable tool, in studies where the instantaneous velocity fields are three-dimensional in nature, and a definite advantage when correlations between different velocity components and/or turbulent stresses are to be measured. Several types of three-sensor probes, with different sensor configurations, have been developed (Bruun, 1995). These can be classified as orthogonal or non-orthogonal probes, according to whether the three sensors are mutually orthogonal or not. Among the commercial probes, the TSI 1299-20-18 hot film probe and the DANTEC 55P91 "claw-type" hot-wire probe are both orthogonal probes, while the AUSPEX AVE-3-102 is non-orthogonal.

The interpretation of hot-wire anemometry signals requires a method relating the anemometer voltage outputs to the instantaneous velocity vector. While this is trivial in the case of a single wire normal to the flow, measuring one velocity component, and relatively straightforward in the case of a cross-wire, measuring two-velocity components, for three-sensor probes this becomes quite complex as it requires solving a system of coupled non-linear equations. The arrangement of three mutually orthogonal sensors, as will be seen later, introduces simplifications that result in easier to solve, uncoupled, equations. Hence stems the appeal of using such probes. However, orthogonal probes have limitations at high turbulence intensity flows (Acrivlellis, 1980) and, more importantly, they are rarely truly orthogonal due to manufacturing imperfections.

Two approaches have been followed in the past to determine the velocity vector from the anemometer voltage outputs. In the first approach, calibrations are performed at different velocity magnitudes and angles, and the velocity vector is deduced from these calibrations using fitted equations (Butler and Wagner, 1983), a numerical search algorithm (Huffman, 1980) or a look-up table (Gieseke and Guezennec, 1993). The second approach consists of

---

[2] It was discovered after the development of the method described in this section that a similar solution was already proposed by Lekakis et al [1989]. However, the exercise was not futile since the method presented by Lekakis et al [1989], when implemented, did not yield acceptable solutions. Although an explanation has not been found, it is possible that this failure may be due to a typographical error in the expression of one of the numerous coefficients contained in that reference.

modelling the hot-wire response and solving the full hot-wire relationships. The latter approach is the one adopted here.

The analysis below aims at developing a general method of relating the instantaneous velocity vector to the anemometer voltage outputs of three-sensor probes. The developed method will then be applied to the probe of interest, namely the AUSPEX AVE-3-102 three-sensor probe, manufactured by AUSPEX Corporation.

7.2.1 Mathematical derivation

First, the anemometer voltage output for each sensor, E_i, is related to the velocity through King's law of cooling

$$E_i^2 = A_i + B_i u_{effi}^{n_i} \tag{15}$$

The effective velocity, u_{effi}, for each sensor is expressed in terms of Jørgensen's equation (Jørgensen, 1971)

$$u_{effi}^2 = u_{ni}^2 + k_i^2 u_{ti}^2 + h_i^2 u_{bi}^2 \tag{16}$$

where

u_{ni} : velocity component normal to sensor "i" and in the plane of its supporting prongs.

u_{ti} : velocity component tangential to sensor "i".

u_{bi} : velocity component normal to sensor "i" and to the plane of its supporting prongs.

k_i : yaw coefficient for sensor "i".

h_i : pitch coefficient for sensor "i".

The values of A_i, B_i, n_i, k_i and h_i, for each sensor, are determined through calibration.

The sensor configuration and the coordinate system are shown in Figure 7.6, which is specific to the AUSPEX AVE-3-102 probe, although the corresponding angles can be readily obtained for other probe configurations. The sensor-oriented velocity components u_{ni}, u_{ti} and u_{bi} can be expressed in terms of the probe-oriented components, u, v and w, of the instantaneous velocity vector and the probe geometry. In order to simplify the equations,

in all of the following analysis, one of the sensors, namely sensor 1, will be placed in the u-v plane of the Cartesian coordinate system. The resulting expressions are as follows

$$u_{n1} = u\cos(\alpha_1) - v\sin(\alpha_1)$$
$$u_{t1} = u\sin(\alpha_1) + v\cos(\alpha_1)$$
$$u_{b1} = w$$

$$u_{n2} = u\cos(\alpha_2) - (v\cos(\delta_2) - w\sin(\delta_2))\sin(\alpha_2)$$
$$u_{t2} = u\sin(\alpha_2) + (v\cos(\delta_2) - w\ \sin(\delta_2))\cos(\alpha_2)$$
$$u_{b2} = v\sin(\delta_2) + w\cos(\delta_2)$$

$$u_{n3} = u\cos(\alpha_3) - (v\cos(\delta_3) + w\ \sin(\delta_3))\sin(\alpha_3)$$
$$u_{t3} = u\sin(\alpha_3) + (v\cos(\delta_3) + w\ \sin(\delta_3))\cos(\alpha_3)$$
$$u_{b3} = v\sin(\delta_3) - w\cos(\delta_3)$$

The effective velocities can then be written as functions of the probe-oriented velocity components as

$$u_{eff1}^2 = (u\cos(\alpha_1) - v\sin(\alpha_1))^2 + k_1^2(u\sin(\alpha_1) + v\cos(\alpha_1))^2 + h_1^2 w^2 \tag{17}$$

$$\begin{aligned} u_{eff2}^2 = {} & (u\cos(\alpha_2) - (v\cos(\delta_2) - w\sin(\delta_2))\sin(\alpha_2))^2 \\ & + k_2^2(u\sin(\alpha_2) + (v\cos(\delta_2) - w\sin(\delta_2))\cos(\alpha_2))^2 \\ & + h_2^2(v\sin(\delta_2) + w\cos(\delta_2))^2 \end{aligned} \tag{18}$$

$$\begin{aligned} u_{eff3}^2 = {} & (u\cos(\alpha_3) - (v\cos(\delta_3) + w\sin(\delta_3))\sin(\alpha_3))^2 \\ & + k_3^2(u\sin(\alpha_3) + (v\cos(\delta_3) + w\sin(\delta_3))\cos(\alpha_3))^2 \\ & + h_3^2(v\sin(\delta_3) - w\cos(\delta_3))^2 \end{aligned} \tag{19}$$

The above equations are coupled, non-linear equations for u , v and w. In the case of orthogonal sensors, the particular combination of α_i and δ_i yields equations uncoupled for

u , v and w. Coupling can be worked around and a solution is possible if the velocity components are expressed in terms of the velocity magnitude, $\|u\|$, and the polar and azimuthal angles β and γ.

$$\begin{aligned} u &= \|u\| \cos(\gamma) \\ v &= \|u\| \sin(\gamma)\ \cos(\beta) \\ w &= \|u\| \sin(\gamma)\ \sin(\beta) \end{aligned} \tag{20}$$

Then, the effective cooling velocities will be given by

$$\begin{aligned} u_{eff1}^2 = \|u\|^2 [&(\cos^2(\beta)\sin^2(\alpha_1) + h_1^2 \sin^2(\beta) + k_1^2 \cos^2(\beta)\cos^2(\alpha_1))\sin^2(\gamma) \\ &+ (2k_1^2 \cos(\beta)\sin(\alpha_1)\cos(\alpha_1) - 2\cos(\beta)\sin(\alpha_1)\cos(\alpha_1))\cos(\gamma)\sin(\gamma) \\ &+ (k_1^2 \sin^2(\alpha_1) + \cos^2(\alpha_1))\cos^2(\gamma)] \end{aligned} \tag{21}$$

$$\begin{aligned} u_{eff2}^2 = \|u\|^2 [&(\cos(\beta)\cos(\delta_2) - \sin(\beta)\sin(\delta_2))^2 \sin^2(\alpha_2) + h_2^2 (\cos(\beta)\sin(\delta_2) + \\ &\sin(\beta)\cos(\delta_2))^2 + k_2^2 (\cos(\beta)\cos(\delta_2) - \sin(\beta)\sin(\delta_2))^2 \cos^2(\alpha_2))\sin^2(\gamma) \\ &+ (2k_2^2 (\cos(\beta)\cos(\delta_2) - \sin(\beta)\sin(\delta_2))\sin(\alpha_2)\cos(\alpha_2) - 2(\cos(\beta)\cos(\delta_2) \\ &- \sin(\beta)\sin(\delta_2))\sin(\alpha_2)\cos(\alpha_2))\cos(\gamma)\sin(\gamma) + (k_2^2 \sin^2(\alpha_2) + \cos^2(\alpha_2))\cos^2(\gamma)] \end{aligned} \tag{22}$$

$$\begin{aligned} u_{eff3}^2 = \|u\|^2 [&(\cos(\beta)\cos(\delta_3) + \sin(\beta)\sin(\delta_3))^2 \sin^2(\alpha_3) + h_3^2 (\cos(\beta)\sin(\delta_3) - \\ &\sin(\beta)\cos(\delta_3))^2 + k_3^2 (\cos(\beta)\cos(\delta_3) + \sin(\beta)\sin(\delta_3))^2 \cos^2(\alpha_3))\sin^2(\gamma) + \\ &(2k_3^2 (\cos(\beta)\cos(\delta_3) + \sin(\beta)\sin(\delta_3))\sin(\alpha_3)\cos(\alpha_3) - 2(\cos(\beta)\cos(\delta_3) + \\ &\sin(\beta)\sin(\delta_3))\sin(\alpha_3)\cos(\alpha_3))\cos(\gamma)\sin(\gamma) + (k_3^2 \sin^2(\alpha_3) + \cos^2(\alpha_3))\cos^2(\gamma)] \end{aligned} \tag{23}$$

The above equations are linear in $\|u\|$. Thus, the velocity magnitude can be separated from its direction by writing

$$C_I = \frac{u_{eff2}^2}{u_{eff1}^2} \quad and \quad C_{II} = \frac{u_{eff3}^2}{u_{eff1}^2} \tag{24}$$

which is equivalent to

$$C_I u_{eff1}^2 - u_{eff2}^2 = 0 \quad and \quad C_{II} u_{eff1}^2 - u_{eff3}^2 = 0$$

The special case where one of the effective velocities is equal to zero need not to be considered here, since in the flows of interest, the streamwise velocity component is always positive and non-zero.

When developed, the last two equations yield

$$\begin{aligned}
&C_I(\cos^2(\beta)\sin^2(\alpha_1) + h_1^2\sin^2(\beta) + k_1^2\cos^2(\beta)\cos^2(\alpha_1)) - h_2^2(\cos(\beta)\sin(\delta_2) + \sin(\beta)\cos(\delta_2))^2 \\
&-k_2^2(\cos(\beta)\cos(\delta_2) - \sin(\beta)\sin(\delta_2))^2\cos^2(\alpha_2) - (\cos(\beta)\cos(\delta_2) - \sin(\beta)\sin^2(\delta_2))\sin^2(\alpha_2)) \\
&\tan^2(\gamma) + (2(\cos(\beta)\cos(\delta_2) - \sin(\beta)\sin(\delta_2))\sin(\alpha_2)\cos(\alpha_2) + C_I(2k_1^2\cos(\beta)\sin(\alpha_1)\cos(\alpha_1) \\
&-2\cos(\beta)\sin(\alpha_1)\cos(\alpha_1)) - 2k_2^2(\cos(\beta)\cos(\delta_2) - \sin(\beta)\sin(\delta_2))\sin(\alpha_2)\cos(\alpha_2))\tan(\gamma) \\
&+C_I(k_1^2\sin^2(\alpha_1) + \cos^2(\alpha_1)) - k_2^2\sin^2(\alpha_2) - \cos^2(\alpha_2) = 0
\end{aligned}$$

and

$$\begin{aligned}
&C_{II}(\cos^2(\beta)\sin^2(\alpha_1) + h_1^2\sin^2(\beta) + k_1^2\cos^2(\beta)\cos^2(\alpha_1)) - h_3^2(\cos(\beta)\sin(\delta_3) - \sin(\beta)\cos(\delta_3)) \\
&-k_3^2(\cos(\beta)\cos(\delta_3) + \sin(\beta)\sin^2(\delta_3))\cos^2(\alpha_3) - (\cos(\beta)\cos(\delta_3) + \sin(\beta)\sin^2(\delta_3))\sin^2(\alpha_3)) \\
&\tan^2(\gamma) + (2(\cos(\beta)\cos(\delta_3) + \sin(\beta)\sin(\delta_3))\sin(\alpha_3)\cos(\alpha_3) + C_{II}(2k_1^2\cos(\beta)\sin(\alpha_1)\cos(\alpha_1) \\
&-2\cos(\beta)\sin(\alpha_1)\cos(\alpha_1)) - 2k_3^2(\cos(\beta)\cos(\delta_3) + \sin(\beta)\sin(\delta_3))\sin(\alpha_3)\cos(\alpha_3))\tan(\gamma) \\
&+C_{II}(k_1^2\sin^2(\alpha_1) + \cos^2(\alpha_1)) - k_3^2\sin^2(\alpha_3) - \cos^2(\alpha_3) = 0
\end{aligned}$$

Grouping terms in γ and using trigonometric identities, the following set of equations is obtained

$$\begin{aligned}
&a_1\tan^2(\gamma) + b_1\tan(\gamma) + c_1 = 0 \\
&a_2\tan^2(\gamma) + b_2\tan(\gamma) + c_2 = 0
\end{aligned} \tag{25}$$

where the coefficients are independent of γ and given by

$$a_1 = a_{11}\sin^2(\beta) + a_{12}\sin(\beta)\cos(\beta) + a_{13}\cos^2(\beta)$$
$$a_2 = a_{21}\sin^2(\beta) + a_{22}\sin(\beta)\cos(\beta) + a_{23}\cos^2(\beta)$$
$$b_1 = b_{11}\sin(\beta) + b_{12}\cos(\beta)$$
$$b_2 = b_{21}\sin(\beta) + b_{22}\cos(\beta)$$
$$c_1 = C_I(k_1^2\sin^2(\alpha_1) + \cos^2(\alpha_1)) - k_2^2\sin^2(\alpha_2) - \cos^2(\alpha_2)$$
$$c_2 = C_{II}(k_1^2\sin^2(\alpha_1) + \cos^2(\alpha_1)) - k_3^2\sin^2(\alpha_3) - \cos^2(\alpha_3)$$
$$a_{11} = C_I h_1^2 - k_2^2\sin^2(\delta_2)\cos^2(\alpha_2) - h_2^2\cos^2(\delta_2) - \sin^2(\delta_2)\ \sin^2(\alpha_2)$$
$$a_{12} = 2\cos(\delta_2)\sin(\delta_2)\sin^2(\alpha_2) - 2h_2^2\cos(\delta_2)\sin(\delta_2) + 2k_2^2\cos(\delta_2)\sin(\delta_2)\cos^2(\alpha_2)$$
$$a_{13} = -k_2^2\cos^2(\delta_2)\cos^2(\alpha_2) - h_2^2\sin^2(\delta_2) + C_I(\sin^2(\alpha_1) + k_1^2\cos^2(\alpha_1)) - \cos^2(\delta_2)\sin^2(\alpha_2)$$
$$a_{21} = C_{II}h_1^2 - k_3^2\sin^2(\delta_3)\cos^2(\alpha_3) - h_3^2\cos^2(\delta_3) - \sin^2(\delta_3)\ \sin^2(\alpha_3)$$
$$a_{22} = 2h_3^2\cos(\delta_3)\sin(\delta_3) - 2\cos(\delta_3)\sin(\delta_3)\sin^2(\alpha_3) - 2k_3^2\sin(\delta_3)\cos(\delta_3)\cos^2(\alpha_3)$$
$$a_{23} = -k_3^2\cos^2(\delta_3)\cos^2(\alpha_3) - h_3^2\sin^2(\delta_3) + C_{II}(\sin^2(\alpha_1) + k_1^2\cos^2(\alpha_1)) - \cos^2(\delta_3)\sin^2(\alpha_3)$$
$$b_{11} = 2k_2^2\sin(\delta_2)\sin(\alpha_2)\cos(\alpha_2) - 2\sin(\delta_2)\sin(\alpha_2)\cos(\alpha_2)$$
$$b_{12} = 2\cos(\delta_2)\sin(\alpha_2)\cos(\alpha_2) + C_I(2k_1^2\sin(\alpha_1)\cos(\alpha_1) - 2\sin(\alpha_1)\cos(\alpha_1)) - 2k_2^2\cos(\delta_2)\sin(\alpha_2)\cos(\alpha_2)$$
$$b_{21} = 2\sin(\delta_3)\sin(\alpha_3)\cos(\alpha_3) - 2k_3^2\sin(\delta_3)\cos(\alpha_3)\sin(\alpha_3)$$

The solution of the above set of equations is performed by letting $x=\tan^2(\gamma)$ and $y=\tan(\gamma)$ and solving the set of linear equations for x and y. If $a_1b_2-a_2b_1 \neq 0$, then

$$x = \tan^2(\gamma) = \frac{b_1c_2 - b_2c_1}{a_1b_2 - a_2b_1}$$
$$y = \tan(\gamma) = \frac{a_2c_1 - a_1c_2}{a_1b_2 - a_2b_1} \qquad \textbf{(26)}$$

However, in the case where $a_1b_2-a_2b_1=0$, γ is the solution of the quadratic equation $a_1\tan^2(\gamma) + b_1\tan(\gamma) + c_1 = 0$, if $c_1/c_2 = a_1/a_2$ or $c_1=c_2=0$, and there will be no solution otherwise.

The above expression gives γ as a function of β. Solving for β is performed by equating x and y^2. This yields, after arrangement of the terms and the use of trigonometric

identities, the following equation

$$(l_4 tan^4(\beta) + l_3 tan^3(\beta) + l_2 tan^2(\beta) + l_1 tan(\beta) + l_0) cos^4(\beta) = 0 \quad (27)$$

where

$$l_4 = c_1 b_{21}^2 a_{11} + a_{11}^2 c_2^2 - c_2 b_{11} a_{11} b_{21} - 2 a_{11} c_2 c_1 a_{21} + c_1^2 a_{21}^2 - c_1 b_{21} b_{11} a_{21} + c_2 b_{11}^2 a_{21}$$

$$\begin{aligned} l_3 = {} & c_1 b_{21}^2 a_{12} - c_1 b_{22} b_{11} a_{21} - c_2 b_{12} a_{11} b_{21} + 2 c_1^2 a_{21} a_{22} + c_2 b_{11}^2 a_{22} \\ & + 2 c_1 b_{21} a_{11} b_{22} - c_1 b_{21} b_{11} a_{22} - c_2 b_{11} a_{12} b_{21} - c_2 b_{11} a_{11} b_{22} \\ & - 2 a_{12} c_2 c_1 a_{21} + 2 a_{11} c_2^2 a_{12} + 2 c_2 b_{11} b_{12} a_{21} - c_1 b_{21} b_{12} a_{21} - 2 a_{11} c_2 c_1 a_{22} \end{aligned}$$

$$\begin{aligned} l_2 = {} & c_1 b_{21}^2 a_{13} - 2 a_{13} c_2 c_1 a_{21} + a_{12}^2 c_2^2 - c_2 b_{11} a_{13} b_{21} + c_2 b_{11}^2 a_{23} - c_2 b_{11} a_{12} b_{22} - c_1 b_{22} b_{11} a_{22} \\ & - c_2 b_{12} a_{11} b_{22} + c_2 b_{12}^2 a_{21} - 2 a_{11} c_2 c_1 a_{23} + 2 c_1 b_{21} a_{12} b_{22} - c_2 b_{12} a_{12} b_{21} - c_1 b_{22} b_{12} a_{21} \\ & + 2 c_1^2 a_{21} a_{23} + c_1^2 a_{22}^2 - 2 a_{12} c_2 c_1 a_{22} + 2 c_2 b_{11} b_{12} a_{22} + 2 a_{11} c_2^2 a_{13} + c_1 b_{22}^2 a_{11} \\ & - c_1 b_{21} b_{11} a_{23} - c_1 b_{21} b_{12} a_{22} \end{aligned}$$

$$\begin{aligned} l_1 = {} & c_2 b_{12}^2 a_{22} + 2 a_{12} c_2^2 a_{13} + c_1 b_{22}^2 a_{12} + 2 c_2 b_{11} b_{12} a_{23} - c_2 b_{12} a_{12} b_{22} - 2 a_{12} c_2 c_1 a_{23} \\ & - c_2 b_{11} a_{13} b_{22} - 2 a_{13} c_2 c_1 a_{22} - c_1 b_{21} b_{12} a_{23} - c_2 b_{12} a_{13} b_{21} + 2 c_1^2 a_{22} a_{23} \\ & - c_1 b_{22} b_{11} a_{23} - c_1 b_{22} b_{12} a_{22} + 2 c_1 b_{21} a_{13} b_{22} \end{aligned}$$

$$l_0 = -c_2 b_{12} a_{13} b_{22} - c_1 b_{22} b_{12} a_{23} + c_1 b_{22}^2 a_{13} + a_{13}^2 c_2^2 + c_2 b_{12}^2 a_{23} + c_1^2 a_{23}^2 - 2 a_{13} c_2 c_1 a_{23}$$

Equation (27) is equivalent to

$$\begin{aligned} & cos(\beta) = 0 \\ & or \\ & l_4 tan^4(\beta) + l_3 tan^3(\beta) + l_2 tan^2(\beta) + l_1 tan(\beta) + l_0 = 0 \end{aligned} \quad (28)$$

The l_i coefficients are only function of the probe geometry, the yaw and pitch coefficients

and the measured effective velocities.

It can be verified whether $cos\beta=0$ is a solution by substituting $cos\beta=0$ and $sin\beta=\pm 1$ in the expressions of a_i , b_i and c_i and equating y^2 and x. Thus, for $cos\beta=0$ to be a solution, the following equation has to be verified

$$(a_{21}c_1-a_{11}c_2)^2=(b_{11}c_2-b_{21}c_1)(a_{11}b_{21}-a_{21}b_{11}) \qquad (29)$$

in which case $\beta=\pi/2$ or $\beta=3\pi/2$. To select the right solution, one can use Equation (26) to calculate γ for each of the above β values, then substitute each pair of angles in Equations (20) and (21) to calculate $\|u\|$. The solution would be the pair that yields the same value for $\|u\|$ from both equations.

In the case where $cos\beta\neq 0$, the 4th degree equation in $tan\ \beta$ has to be solved. This will be done according to the method of Salzer [1960]. Once the value of the polar angle, β, is determined, the azimuthal angle, γ, can be calculated using Equation (26). However, the solution of Equation (28) will, most of the time, yield four values of β and hence, four values of γ. The right pair corresponds to the pair with the smallest γ angle. In fact, as explained by Lekakis et al [1989], for small flow vector variations a simple approach to remove the problem of non-uniqueness is to orient the probe in such a way that the flow vectors are always contained within a cone of angles, called the "uniqueness domain". This domain, which includes the $\gamma=0°$ direction, contains one and only one root of Equation (28), all other roots being outside the domain. For a given probe geometry, the boundary of the uniqueness domain is computed by numerically examining all solutions (β,γ) for real double roots. For example, the uniqueness domain for the present three-sensor probe (Figure 7.7) was obtained by finding, for a given value of β, the value of γ for which Equation (28) yields real double roots. To minimize computation time a search algorithm was employed.

Since Jørgensen's equation may not describe accurately the probe response to vectors close to the boundary of the uniqueness domain, due to probe support interference, thermal wakes, etc.., it is advisable in practice to restrict the velocity vectors to a domain smaller than the computed uniqueness domain (Lekakis et al, 1989). This will always be satisfied in the flow of interest, as its velocity vectors are expected to have azimuthal angles less than 10°.

In view of the above mathematical development, the solution scheme, shown in Figure 7.8, was adopted to obtain the three components of the instantaneous velocity vector from the simultaneous voltage outputs corresponding to each of the three-sensors of the triple-wire probe.

7.2.2 Probe characteristic angles and coefficients

The solution method adopted above requires the determination of the yaw and pitch coefficients, k_i and h_i for each sensor, in addition to the α_i and δ_i angles.

The determination of these angles and coefficients has been performed in the DISA Calibration Unit 55D90, described in more detail in Chapter 5. This unit produces a variable-velocity, low-turbulence free air jet in which the probe to be calibrated is placed. The unit is equipped with four interchangeable nozzles yielding jet areas of 12, 24, 60 and 120 mm^2 respectively. The largest nozzle is used here in order to ensure that all three sensors are located in the free jet core and thus cooled by the same velocity vector. The probe mounting arrangement is located at the top of a small vertical column. The positioning arrangement renders it possible to alter the flow direction relative to the probe on two calibrated axes at right angles to one another. For better accuracy, one of these axes is connected to a multiturn potentiometer which delivers a signal proportional to the angular position. For the determination of the probe roll angle, a home-made mechanism, equipped with a protractor, was added to the original unit.

7.2.2.1 Determination of the δ_i angles

The sensors of the triple wire probe are colour-coded and will be referred to, hereafter, using their colour-codes, namely red, white and blue. To determine the δ_i angles, one of the sensors was used as reference and the angles made by the other two relative to it were resolved.

The probe was placed in the jet with its axis perpendicular to the flow direction. First, the reference sensor, in this case the red sensor, was placed in the plane containing the jet axis. This is achieved by varying the roll angle. The angle corresponding to the maximum

voltage output of the anemometer is the angle for which the sensor-plane is parallel to the jet axis. To determine the relative angles, δ_i, the same technique was used to align the sensors with the flow direction. The respective angles were read off the protractor and the relative angles were calculated to be: δ_2 =δ(red-white)=121° and δ_3 =δ(red-blue)=120°. The procedure was repeated three times, with different reference sensors, and the obtained δ_i angles were found to be identical (within ±0.25°).

7.2.2.2 Determination of α_i, k_i and h_i

The probe was first calibrated in the jet with its axis aligned with the jet axis. For this calibration, King's law of cooling, Equation (15), was used where the effective velocity is expressed according to Jørgensen equation. Because the binormal component vanishes in this case, one may neglect the tangential velocity contribution and write King's law for each sensor as follows

$$E_i^2 = A_i+(B_i \cos^{n_i}\alpha_i)\ U_{jet}^{n_i} \tag{30}$$

Thus, rather than determining B_i from the calibration, the value of $B_i'=(B_i\ cos^{ni}\alpha_i)$ is obtained.

The wires were then pitched, each in its own plane, with respect to the vertical, by an angle ψ, typically between -20° and +60°. Again, neglecting tangential cooling, the anemometer voltage output would be given by

$$E_i^2 = A_i + B_i' \left(\frac{\cos(\alpha_i+\psi)}{\cos\ \alpha_i} \right)^{n_i} U_{jet}^{n_i} \tag{31}$$

Rearranging the above equation allows α_i to be calculated for each value of ψ as

$$\alpha_i = \arctan\left(\frac{\cos\psi - (E_i^2 - A_i)/B_i')^{1/n_i} / U_{jet}}{\sin\ \psi} \right) \tag{32}$$

Average values of α_i were α_{red}=45°, α_{white}=42.5° and α_{blue}=39°.

A sample of the dependence of the sensors' response to yaw and pitch is shown in

Figure 7.9. The measurements were performed by varying the yaw angle for three different roll angles, namely ϕ =0, 45 and 90°. The effective velocity can be expressed, similar to Equation (21), as

$$\begin{aligned} u_{eff_i}^2 = U_{jet}^2 [&(\cos^2(\phi)\sin^2(\alpha_i) + h_i^2 \sin^2(\phi) + k_i^2 \cos^2(\phi)\cos^2(\alpha_i))\sin^2(\psi) \\ &+ (2k_i^2 \cos(\phi)\sin(\alpha_i)\cos(\alpha_i) - 2\cos(\phi)\sin(\alpha_i)\cos(\alpha_i))\cos(\psi)\sin(\psi) \\ &+ (k_i^2 \sin^2(\alpha_i) + \cos^2(\alpha_i))\cos^2(\psi)] \end{aligned} \quad (33)$$

The yaw and pitch coefficients, k_i and h_i were optimized to obtain the best-fit between the above expression and the measured data points (Figure 7.9).

Earlier attempts to determine k_i and h_i (Jørgensen, 1971; Samet and Einav, 1985; and Mobarak et al, 1986) have established the fact that these coefficients, and especially the yaw coefficient, can not be assumed constant over a wide range of ψ angles. Since in the flow of interest the velocity vector is confined in a small cone with γ typically under 10°, the yaw and pitch coefficients will be determined for yaw angles between -20° and +20°.

Table 7.3 summarizes the probe characteristic angles and coefficients, obtained for a constant jet velocity of 8 m/s. The obtained yaw and pitch coefficients are comparable to values in the literature for similar sensors (Jørgensen, 1971; Samet and Einav, 1985; Mobarak et al, 1986; and Wagner and Kent, 1988). Also, tests run at jet velocities of 4 m/s and 8 m/s showed that there was no significant velocity effect, within the above range, on the sensors' responses to yaw and pitch. This is in agreement with the findings of Chew and Ha [1988], who reported no velocity dependence over a range from 6 m/s to 19 m/s.

7.2.3 Validation of the solution scheme and the data-processing program

Extensive tests were run on the "solution" subroutine, first with numerically generated velocity vectors, covering a wider range than the flow-expected range. Once satisfied that the solution subroutine recovers correctly the input velocities, this subroutine was integrated in the data-processing program and tested with acquired signals of the three-sensor probe. For these tests, the probe was calibrated in the DISA jet and the above determined probe angles and coefficients were used. Several long data-records were acquired

with the probe positioned at different combinations of the yaw and pitch angles. The jet velocity was measured and thus the three velocity components relative to the probe could be calculated and compared to the results of the data-processing program. The two sets of results, for the three velocity components, agreed to within 1-2% of the streamwise component for azimuthal angles less than 12°. For larger angles, the discrepancies become more important. These can be attributed to aerodynamic interference of the prongs and to thermal interference of upstream sensors on the downstream ones. There are no simple means to correct for these interferences. However, it is not expected that the flow of interest would have velocity vectors with large azimuthal angles.

7.3 Enhancement of Educed Signals by the VITA Conditional Sampling Technique

The large-scale, "coherent" structures, known to exist in many turbulent shear flows, can be readily detected from measured spatial correlations (Tavoularis and Corrsin, 1987) and velocity spectra. However, statistical techniques give only quantitative information on the time-averaged properties of such structures, losing much of their details. This is partly due to the fact that the repeating velocity patterns, when viewed at fixed points, are never sufficiently periodic to be clearly recognizable (Davies and Yule, 1975).

As it is not practical in many applications to introduce arrays of transducers to acquire sets of simultaneous measurements, conditional sampling techniques have been designed as a means of distinguishing and isolating these organized structures. According to Antonia [1981], conditional sampling and averaging has helped to close the gap between data collected in an Eulerian frame of reference with information obtained in a Lagrangian frame, as is the case for flow visualization studies.

Ensemble averages can be obtained relative to a particular phase (i.e. time relative to an identifiable characteristic event during the life time of the structure) of the structure. The conditional average, or phase-average, of a quantity, Q, is defined as

$$< Q(x_i, \tau) > = \frac{1}{N} \sum_{j=1}^{N} Q(x_i, t_j + \tau) \qquad \textbf{(34)}$$

where τ is the time corresponding to the reference phase, t_i is a specified time with respect to the occurrence of the structure of interest, N is the number of detected events, and x_i represents the spatial position. It is to be noted that, for large N, any randomness will be inherently averaged out to zero.

Sharp discrimination is not possible because of the background turbulence, thus conditional sampling results should be accepted with caution because they may represent only part of the physical activity. Needless to say, one should also demonstrate that the recognized pattern is not an artifact of the detection technique.

Conditional sampling requires triggering or conditioning criteria which are characteristic of the event or structure to be measured. The subjective choice of these criteria makes these techniques somewhat arbitrary. Blackwelder and Kaplan [1976] suggested to keep the triggering criteria to a minimum and as simple as possible, while retaining the essential features of the event to be detected. Any time in the velocity-time history can be used as a reference point provided it has a unique significance in the event to be detected and it has features that make it clearly distinguishable from the rest of the signal (Lau and Fisher, 1975).

Several criteria have been used by different investigators. Wallace et al [1977] applied simple criteria, including conditions on the time derivative of the velocity. Winant and Browand [1974] used two probes, one of which, the trigger probe, is placed at a fixed position. The arrival of the structure is detected when the velocity fluctuation sensed by the trigger probe crosses through zero with a positive slope. Browand and Weidman [1976], on the other hand, used detection criteria based on the relative maxima or minima of the signals exceeding an amplitude threshold of 1.2 times the rms value, along with other conditions on the waveform or phase-lag. They found that relaxing the requirements resulted in a greater number of detected events, but at the expense of "blurring the image". Similar observations were made by Bruun [1977], Blackwelder and Kaplan [1976] and Day et al [1993]. The two latter references used the Variable Interval Time Averaging (VITA) technique. In this method, the running averaged standard deviation of the fluctuating signal from the trigger probe is examined and used as a reference signal for the conditional sampling. The detection is achieved by using a threshold level on the obtained "localized variance". A variation of this method is presented by Bisset et al [1990], who used a Window Average Gradient

(WAG) as their detection reference signal instead of the "localized variance".

Comparisons of the performance of several conditional sampling techniques in detecting coherent structures in turbulent boundary layers, have been performed by Subramanian et al [1982] and Yuan and Mokhtarzadeh-Dehghan [1994]. Kevlahan et al [1994] presented a comparison of the identification of structures by conditional sampling techniques and other analytical techniques such as the Fourier transform, the Karhunen-Loeve orthogonal decomposition, functional pattern recognition, fractals, and wavelet transforms. They found the conditional sampling method to give the best results in addition to being the easiest to use. Its only drawback is its sensitivity to the choice of conditions.

It follows from the above review that there is no universal conditional sampling technique. One should devise and tune one's own method, depending on the structures to be identified. The choice of the detection criteria can be accomplished by inspection of the velocity traces. The legitimacy of these criteria and their effect on the obtained results have to be tested. Also, it has to be proved that the outcome is not an artifact of the method. This can be achieved by testing the technique with randomly generated signals.

7.3.1 The VITA technique

Inspection of velocity traces in the application of interest, namely flow in the rod-wall gap region of a rectangular channel containing a suspended rod, indicated the presence of clear and repeatable features that can be attributed to coherent structures (see Chapter 8). An essential feature of the observed structures is the nearly periodic large fluctuations accompanying it (this is best seen in the spanwise velocity component for traces acquired right in the centre of the gap). The detection or triggering criterion, therefore, has to retain this characteristic. According to this, an appropriate conditional sampling method is the Variable Interval Time Averaging (VITA) technique presented by Blackwelder and Kaplan [1976], and briefly described below. This technique was applied to the detection of organized structures in turbulent boundary layers (Blackwelder and Kaplan, 1976), turbulent jets (Day et al, 1993) and turbulent wakes (Antonia et al, 1987).

The variable interval time average of a quantity Q is defined by

$$\hat{Q}(x_i,t,T)=\frac{1}{T}\int_{t-T/2}^{t+T/2}Q(x_i,s).ds \qquad (35)$$

where T is the averaging time interval, which is of the order of the time scale of the phenomenon under study. It is to be noted that the conventional time-average is obtained when T tends to infinity, and the dependence on t, the time when averaging starts, is lost because of stationarity.

A localized measure of the turbulent energy is the "localized variance", obtained by applying VITA to the square of the velocity and subtracting from it the localized squared mean value. For example, when expressed as a function of the spanwise velocity component, W, the localized variance is defined as

$$\hat{var}(x_i,t,T) = \hat{W^2}(x_i,t,T) - [\hat{W}(x_i,t,T)]^2 \qquad (36)$$

A detection is made according to the following criterion

$$D(t) = \begin{cases} 1 & \text{if } \hat{var} > k\overline{w^2} \text{ and } \partial W/\partial t > 0 \\ 0 & \text{otherwise} \end{cases} \qquad (37)$$

where k is the "threshold level" and $\overline{w^2}$ is the running variance of the velocity.

The conditional average is then obtained using Equation (34), with t_j being taken midway between the beginning and end of the time period during which D(t)≠0 (D(t)=1 only during very short time intervals). The condition on the velocity time derivative was added to discriminate between flow accelerations and decelerations in order to ensure proper phase averaging.

7.3.2 Testing of the technique

Tests were conducted to determine appropriate averaging time, T, and threshold level, k. The technique was first tested using a numerically generated sine-wave. The "optimal" averaging time, i.e. one that gives the most pronounced variations, corresponding to accelerations or decelerations, in the "localized variance", was found to be equal to half the period of the sine-wave. The optimal T obtained when a sample of the spanwise velocity

component in the centre of the gap was used, was also approximately half the average period of the signal. Therefore, for the remaining of this work, the averaging time was set to approximately half the period of the passage of the structures; for a U_h=10.1 m/s, this was 25 ms.

A test during which the threshold level was varied, while VITA was applied to the same acquired signal, showed that a relatively low value of k, e.g. k=0.5, retained nearly all the signal, while a high k value, e.g. k=1.2, excluded the entire signal except for few peaks. As k increased, the magnitude of the obtained ensemble average was seen to increase, while its shape was qualitatively the same, although with a smaller period (Figure 7.10). Blackwelder and Kaplan [1976] also noted an evident trend in the results as the averaging time and the threshold level were changed. They explained this dependence by the fact that not all of the structures have the same amplitude, but a distribution of amplitudes and sizes probably exists. For higher threshold levels, only the more intense events would be detected and the conditional averages would be larger. Thus, if the detected events were truly deterministic, the threshold value should only affect the magnitude of the event and not its structure, which implies that the conditional averages should scale monotonically with the threshold value.

Figure 7.11 shows the same signals as those in Figure 7.10 normalized by their respective threshold values. Even though the difference in magnitude is less important for the normalized signals, they obviously do not scale with the threshold value. This should have been expected, because, for the educed signals to scale with the threshold value, the individual events should vary only in magnitude while keeping the same period and waveform. This is obviously not the case, as seen in the velocity traces. Furthermore, due to the small-scale turbulence and the cycle-to-cycle variation of the structures, the detection time of some events can easily be shifted, especially for low threshold values. The misalignment of events can also result in ensemble averages with attenuated magnitudes and larger periods.

If one aspires to obtain an ensemble average which is independent of the threshold value, at least over a reasonable range, and closer to the true ensemble average (this is of utmost importance, when a decomposition of the velocity into coherent and non-coherent parts is required), one should align better the individual events and then devise an averaging

method to take into account not only variations in magnitude of the events, but also variations in their period lengths.

7.3.3 Enhancement of the VITA educed signals

In view of the above observations, we developed the following method for the enhancement of ensemble averages obtained by the VITA technique. Actually, the proposed method can be applied to enhance results of any conditional sampling technique, but it will be presented in the context of the VITA technique since it is the technique adopted in this work. To help explain the method, we will consider the five detected events shown in Figure 7.12.

The method consists of an iterative procedure. As a first step, the conditional sampling technique is used to obtain a first estimate of the ensemble average. In the second step, a second pass through the same data is performed. In this pass, the time-correlation of each detected event with the previously determined ensemble average is calculated as

$$R_{w,\bar{w}}(\alpha,\Delta\tau) = \frac{\int_{\tau}^{\tau+\tau_c} \bar{w}(x_i,t)\,.\,w(x_i,t_j+\Delta\tau+t/\alpha)\,dt}{\int_{\tau}^{\tau+\tau_c} \bar{w}(x_i,t)\,dt\,.\int_{\tau}^{\tau+\tau_c} w(x_i,t_j+\Delta\tau+t/\alpha)\,dt} \qquad (38)$$

where $\Delta\tau$ is a time shift from the detection time, t_j, and τ_c is the time interval over which the correlation is calculated. τ and τ_c are selected so that the correlation will be based on the most important part of the signal i.e. covering nearly a period of the velocity variation (for the example of Figure 7.12, typically $\tau \approx 0.020$ s and $\tau_c \approx 0.040$ s). To account for the variation in period length of the detected event, the correlation functions are calculated with the event time-axis expanded or contracted by a factor, α. Typical correlation functions, for a few α values, are shown in Figure 7.13. These correspond to the middle signal of Figure 7.12. The $\Delta\tau$ value corresponding to the maximum of the correlation function gives the time by which the signal is to be shifted for the best alignment with the previously calculated ensemble average. Also, the correlation function with the highest maximum corresponds to the optimum α factor, to be used for expanding or contracting the event's time scale to match the periods of the event and the previously determined ensemble average.

Depending on the value of the highest correlation function maximum, the detected event is either rejected (e.g. for values less than 0.5) or retained for the calculation of a new ensemble average. In case the event is retained, its time scale is expanded or contracted and then shifted, according to the correlation results. Figure 7.14 shows the same five signals of Figure 7.12, after expansion/contraction and shifting. The magnitude of the ensemble average of the five manipulated signals, shown at the bottom of the graph (Figure 7.14), is remarkably higher than the ensemble average of the original signals (Figure 7.12).

Once the new ensemble average is obtained, its time-scale has to be expanded/contracted by the average of the α factors of all retained events, $\alpha_{average}$. This second step is to be repeated until convergence of successive ensemble averages is achieved. In practice, convergence is reached quickly. As an example, it can be seen in Figure 7.15 that after one pass the ensemble average remains essentially the same. Also, the number of retained events remains constant after the first pass, for which the number of rejected events is of the order of 2% of the total number of detected events. The total number of retained events is a function of the threshold value.

Figure 7.15 illustrates also the enhancement of the ensemble average. The magnitude of the velocity maximum increased by about 50%, while the negative minimum velocity more than doubled in magnitude, resulting in a clearer definition of the velocity variation. The length of the structure period became slightly smaller. However, the part of the signal corresponding to the subsequent structure was not improved. Actually, the enhanced ensemble average reached zero much earlier than the original average did (not shown in Figure 7.15). This can be explained by the jitter, phase shifts and variations in magnitude and size of the structures. In fact, due to these factors, aligning one structure and matching its period length, with the previously determined ensemble, does not necessarily improve the alignment of the subsequent structure or the matching of its period. Therefore, if one only wishes to obtain an overall picture of the flow field, including a few successive structures, it is advisable to use the original ensemble average without attempting to enhance it.

Figure 7.16 represents ensemble averages obtained using the enhanced VITA technique with different threshold levels. Contrary to the results of Figure 7.10, the ensemble averages are not strongly dependent on the threshold value. This is, perhaps, the most important outcome of the enhancement. Eliminating the dependence of the results on

subjectively chosen threshold values reduces arbitrariness, which is one of the drawbacks of conditional sampling techniques.

7.3.4 Conclusions

A method for enhancing ensemble averages obtained from conditional sampling techniques was presented. It is relatively simple to implement, however, it requires substantial additional computational time. Depending on the required accuracy for the determination of the expansion/contraction factor and the number of iterations used in the determination of the ensemble average, this is typically 5 times the original computational time, which is not excessive and easily accommodated by a powerful personal computer. The improvements are well worth the additional computational time, especially if the measurements are to be used in evaluating the statistics of coherent and incoherent components of the velocity.

Another outcome of the method is the fact that, when applied to the VITA results, it reduces substantially the dependence of the results on the threshold value, thus improving the objectivity of the technique.

8

The Measurements

8.1 Preliminary Tests

A number of preliminary tests were conducted prior to the main measurements.

The flow temperature was monitored during the operation of the flow apparatus. Figure 8.1 shows that the flow temperature reached a constant value after about 60 minutes from the starting of the fan. All measurements were taken after at least one hour of fan operation. A thermistor probe was traversed in the test section to verify the uniformity of the flow temperature. The latter was found to vary by less than 0.15 °C over the entire main measurement area. The flow temperature was always monitored during the measurements and was used to estimate appropriate temperature corrections for the hot-wire anemometry measurements. The flow rate through the duct was also monitored routinely. All reported measurements correspond to flow rates that were essentially constant in time.

Measurements of the centerline static pressure distribution along the test-section, for several rod-wall gap sizes, indicated that the pressure gradient was essentially constant in the downstream end of the channel, which implies that the mean velocity profile would be fully developed. However, as observed by Rehme [1987d], two different phenomena take place during flow development in rod bundles: a redistribution of the mass flow rates among

the different subchannels and a downstream development of the velocity profiles, as in all channel flows. Rehme [1987d] showed, for his four-rod bundle with P/D=W/D=1.148, that flow redistribution, the strength of which depends on the entrance conditions, was still present at downstream positions where the mean velocity profiles were fully developed. It was, therefore, decided to run tests to verify the symmetry of the flow distribution at the measuring station, as this is an indication of the flow redistribution between the subchannels separated by the rod.

The initial results of these tests revealed asymmetric velocity distributions. For the main measurements, however, the flow asymmetry in the test section was reduced to less than 1% of the corresponding averages by adjustment of screens in the pressure box near the channel inlet. Figures 8.2 and 8.3 illustrate the degree of symmetry achieved after these adjustments.

8.2 Reynolds Averaged Statistics

The bulk velocity, defined in the region bounded by the rod surface and the surrounding line of maximum velocity (Ouma and Tavoularis [1991b]), as

$$U_b = \frac{1}{A}\int_0^{\pi}\int_0^{r_m} U(r,\phi)\, r\, dr\, d\phi \qquad (1)$$

and calculated using Pitot tube and cross-wire velocity measurements, was found to be essentially independent of the rod-wall gap size. In the present tests, U_b = 10.1 m/s ±2%, for 1.050 < W/D < 1.250. The Reynolds number, Re_h, based on the bulk velocity and the hydraulic diameter of the entire channel, D_h=161 mm, was approximately equal to 140,000.

The variation of the mean local wall shear stress, τ_w, measured with Preston tubes around the periphery of the rod and with the hot-film probe along the channel bottom wall, is presented in Figure 8.4 normalized by the bulk dynamic pressure, $\frac{1}{2}\rho U_b^2$. The skin friction coefficient, C_f, varied only slightly for 1.100 < W/D < 1.250, but, for smaller gaps, it presented increasingly lower minima on the symmetry plane. In addition to the mean, the fluctuations of the wall shear stress along the bottom wall were also measured, using the hot-film probe. These fluctuations were quite strong, with rms values typically about 7% of the

corresponding local means. The profiles of the dimensionless rms wall shear stress, $C_f' = \tau_w'/(\frac{1}{2}\rho U_b^2)$ shown in Figure 8.4, are similar to the corresponding mean profiles.

Most of the velocity measurements presented below were performed using the three-sensor probe, according to the grid and coordinate system shown in Figure 8.5. Typical mean isotachs (i.e. contours of constant axial mean velocity), based on these measurements, are presented in Figure 8.6 for the W/D=1.100 configuration. In the region very close to the centre of the rod-wall gap, only measurements at a height equal to half the gap-width from the bottom wall were conducted, because the probe's body size was not much smaller than the gap width. Isotachs for the gap region were obtained using cross-wire velocity measurements. These are shown in Figure 8.7 along with isocontours of the axial, u', and azimuthal, u_φ', rms turbulent velocities.

The isotachs exhibited a mild bulging towards the corners of the rectangular channel. This is compatible with the effects of secondary flows known to exist in non-circular channels, for example the rectangular ducts of Gessner and Jones [1965] and Melling and Whitelaw [1976]. A more pronounced bulging towards the corners is seen for the contours of the three rms velocity fluctuations, u', v' and w' (Figures 8.8 to 8.10), and the contours of the turbulent kinetic energy, $k = 1/2(\overline{u^2} + \overline{v^2} + \overline{w^2})$, (Figure 8.11). An attempt was also made to measure the mean velocity components $\overline{V}$ and $\overline{W}$ by the three-sensor probe. In conformity with previous measurements in rectangular channels (Gessner and Jones [1965] and Melling and Whitelaw [1976]), the measured values of these velocities did not exceed 3.5% of the bulk velocity, which is comparable to the measuring uncertainty. Therefore, these results were not considered reliable enough to determine the magnitude and direction of the secondary flow (i.e. the velocity component in a plane normal to the main flow direction).

In the rod-wall gap region, the mean isotachs exhibited a strong bulging towards the centre of the rod-wall gap (Figure 8.7), which was more pronounced than the bulging towards the corners of the rectangular channel. This observation was explained in the earlier literature by the presence of strong secondary flows in the gap region. However, the contours of the rms turbulent velocities and kinetic energy are clearly incompatible with such an explanation, because secondary flows may transport turbulent activity from one region to another but can not produce it. The effect of secondary flows on such quantities as turbulent

intensities or kinetic energy would be by extending the regions of their respective maxima to regions of the flow that would otherwise have lower values. Secondary flows cannot create isolated regions of maximum turbulent activity. This is obviously not the case for the present distributions. In fact, the azimuthal, u_ϕ', and spanwise, w', rms turbulent velocities (these components coincide in the vicinity of the gap, ϕ=0) had their maxima in the centre of the gap, whereas the absolute maximum of the rms axial velocity was located at approximately one gap width from the bottom wall and half a diameter from the centerline, i.e. halfway between the subchannel centre and the gap centre. The same behaviour is noted for the turbulent kinetic energy (Figure 8.11), while v' was maximum away from the gap region, approximately at half a diameter from the bottom wall, close to the rod and facing the open flow region (Figure 8.9).

The three turbulent shear stresses were measured and are presented, normalized by the square of the bulk velocity and in contour form, in Figures 8.12 to 8.14. Away from the rod-wall gap, all of these stresses had higher levels, associated with the strong mean velocity gradients in the wall region. In particular, these stresses were larger close to walls normal to their respective planes. For example, one may notice that the contours of $\overline{uv}$ and $\overline{uw}$ became nearly parallel to, respectively, the top and side walls of the channel. The signs of these stresses were consistent with the "gradient transport" concept and opposite to the signs of the corresponding mean velocity gradients. As for the contours of the normal stresses, the effects of secondary flows are clearly noticeable in the bulging of the contours towards the corners of the channel.

In the gap region, the maxima of the $\overline{uv}$ *and* $\overline{uw}$ stresses were located at the same positions as the axial rms turbulent velocity maxima, i.e. halfway between the subchannel centre and the gap centre. The $\overline{vw}$ stress, on the other hand, had contours comparable to the contours of v'.

Figures 8.15 to 8.17 show contours of the three shear stress correlation coefficients. They have nearly the same shapes as the contours of the corresponding turbulent shear stresses.

As will be discussed in the next chapter, the variation of the turbulent stresses in the gap region can be explained by the presence of quasi-periodic, large-scale vortical structures. The existence of such structures in rod bundle flows was demonstrated in the literature.

However, the few studies available on the subject, most of which are from the same group, have not yet produced a complete description of all features of these structures. The measurements, described below, were aimed at further characterizing such structures.

8.3 Coherent Structures

8.3.1 Flow Visualization

In order to verify the existence of large-scale quasi-periodic structures in the gap of the single-rod section, flow visualization was performed. This was achieved by injecting "smoke" (actually an oil mist) through a thin tube inserted in the gap and illuminating the gap with a spanwise thin sheet of light. The visualized flow was recorded by a video camera. For better clarity, the recording was done at relatively low velocities, typically at Re_h = 16,000, and, usually, with an exposure time of 0.004 s. At higher velocities, the general appearance of the flow patterns was essentially the same, however, the obtained images were blurred. For presentation here, sections of the video tape were digitized, frame by frame. A typical sequence of digitized frames of the video film is presented in Appendix A. Animation of the visualized flow is possible by flipping the pages at a steady rate.

The visualization clearly showed the presence of large-scale pulsations, which occurred almost periodically across the gap. Turbulent diffusion was also visible, but it was obviously much weaker than the large-scale transport. Such pulsations were visible over the entire range of Reynolds numbers possible in the present setup, including laminar flows and highly turbulent flows, and persisted even for gap sizes as small as $0.025D$. The flow pulsations were not perfectly periodic at any Reynolds number, but displayed some perceptible frequency irregularities and occasional jittering. The lateral excursions of the smoke reached beyond the projection of the rod for relatively narrow gaps but they appeared to diminish progressively to about $D/8$ (on each side of the axis) as the gap widened to W/D=1.200. At first glance, this diminishing of the smoke streak amplitude may seem to indicate a decrease of the cross-sectional area of the vortices. However, the same effect could be caused by a weakening of the vortex strength and/or the increasing local convection

speed at wider gaps. Therefore, although useful in confirming the presence of pulsations, smoke streaks cannot provide conclusive information about the size and strength of the presumed vortices.

8.3.2 Velocity Fluctuation Patterns

The structure of possible coherent motions was first investigated qualitatively by inspection of the velocity signals, samples of which are shown in Figure 8.18. This approach generally confirmed the presence of quasi-periodic flow pulsations across the gap, in conformity with the flow visualization results and previous studies. The highest degree of regularity was exhibited by the w component on the centreplane of the channel and at nearby locations, while at larger distances from the centreplane the fluctuations of that component both decreased in amplitude and lost their quasi-periodic character. The u component also exhibited a quasi-periodic variation, which was most noticeable at intermediate distances from the centreplane and weakened on the centreplane as well as at relatively large distances from it. The time series provided by a fixed velocity probe is approximately the same as a streamwise profile across a structure, if one considers that the structures are convected downstream by some constant convection speed while not changing substantially in time. The present velocity signals have patterns which are generally compatible with the velocity field of an array of convected parallel vortices, distorted by small-scale turbulence and by occasional vortex interactions. Although the typical fluctuation patterns corresponding to the passage of a vortex are easily recognized by eye, they also exhibit substantial cycle-to-cycle variation and frequent phase shifts, which distort their averaging process. This can be seen by considering typical spectra of selected, quasi-periodic, velocity signals (Figure 8.19). Although these spectra generally exhibit distinct peaks, presumably corresponding to the most likely convection frequency of these structures, the peaks are fairly wide and tend to be obscured at locations where the effects of these vortices are either weak or not well represented by the selected signal. In conclusion, it is clear that the proper identification of the statistical features of these vortical structures is not an easy matter and would likely require the use of sophisticated methods, such as conditional sampling techniques.

8.3.3 Two-Point Measurements

The complete mapping of the instantaneous flow structure requires the simultaneous measurement of the velocity vectors throughout the flow region. This was not possible with the available means, but, instead, an approximate mapping was attempted by conducting two-point velocity measurements with the use of two cross-wire probes. The first probe was fixed at a position (x,y,z) and the other one was traversed to a distance $(\Delta x,\Delta y,\Delta z)$ from the fixed probe. As the present channel flow was fully developed, all statistics should be independent of the streamwise position, x; in fact, this was verified by correlation measurements performed at different x positions near the exit end of the channel. Furthermore, for these measurements, both probes were always positioned at the same distance, y, from the bottom wall, so that $\Delta y = 0$. Therefore, all measured statistical properties are only functions of $z,\Delta x,\Delta z$ and the time difference, Δt. For example, the measured two-point, space-time correlation of the streamwise velocity fluctuation is

$$R_{uu}(z,\Delta x,\Delta z,\Delta t) = \frac{\overline{u(z,t)\ u(z+\Delta z,\Delta x,t+\Delta t)}}{u'(z)\ u'(z+\Delta z,\Delta x)} \qquad (2)$$

From the above definition, one can recover the single-point autocorrelation by letting $\Delta x = \Delta z = 0$, and the two-point, space correlation by letting $\Delta t = 0$.

A set of measurements were taken with the fixed probe at the centre of the gap and the traversed probe at a distance from the bottom wall equal to half the gap width. Figure 8.20 presents the two-point correlations R_{uu} and R_{ww}, measured for several gap widths with the two probes aligned on the symmetry plane of the test section. The corresponding correlations R_{uw} and R_{wu}, not presented here, attained very low values for these probe positions. Some correlations in Figure 8.20 show clear oscillations, which can be interpreted as evidence of spatial periodicity. Such oscillations occurred only for the smaller gap widths and mostly for the spanwise velocity component. In view of other evidence for the existence of quasi-periodic flow pulsations at all considered gaps, one feels compelled to search for an explanation for the non-oscillatory appearance of most correlations in Figure 8.20. First of all, it has already been observed in the flow visualization images and the velocity signals that the repeating patterns ("coherent structures") vary substantially among themselves and

that their regular sequence is often interrupted by other, distinct, events. In particular, the latter events, which could represent structure breakdowns or mergings, introduce shifts in the spacing of consecutive structures and thus obscure their periodicity. The increasing intensity of small-scale turbulence at larger gaps further weakens the periodic appearance of velocity correlations. The differences in the appearance of the u and w correlations is compatible with the velocity pattern in the field of a sequence of vortices, centred at or near the symmetry plane. The above limitations notwithstanding, the spatial correlations in Figure 8.20 had a striking feature: they remained high over a relatively long distance, much longer than the expected size of conventional turbulent eddies.

The presence of convected, organized structures is better seen in the space-time correlations presented in Figure 8.21, in which both probes were located on the centreplane. The R_{ww}, in particular, exhibited correlation peaks larger than 0.90, which did not decay appreciably, even with streamwise probe separation as large as $\Delta x/D$=6 (not shown in Figure 8.21). This contrasts with space-time correlations in non-coherent turbulent shear flows (e.g. see Tavoularis and Corrsin, 1981), which decrease at a fast rate. A measurable correlation peak of about 0.20 was observed even for a probe separation of 43 D, with the upstream probe at 10 D from the channel entrance. These results seem to indicate that coherent structures formed close to the channel entrance and were convected downstream, often with relatively small change in their features over the entire channel length. The average convection speed, U_c, of these structures can be estimated from the above space-time correlations as the ratio $\Delta x/\Delta t_{max}$ of the streamwise probe separation over the time delay corresponding to the maximum correlation. The typical plot of Δt_{max} vs. Δx in Figure 8.22 justifies this approach, as it clearly shows that these quantities were proportional. The use of a convection speed permits the estimation of streamwise, two-point, space correlations from corresponding single-point, time correlations, which are easier to measure. This is achieved by multiplying the time shift in the single-point, time correlations by the convection speed to obtain the streamwise separation. The accuracy of these estimates is demonstrated in Figure 8.20. The above results will be further analyzed and discussed in the following chapter.

Another set of measurements that appeared to be useful was the measurement of space-time correlations with the probes separated in the spanwise as well as the streamwise

direction. A summary of such results, obtained with the fixed probe on the centreplane, and making use of the convection speed to supplement the two-point measurements, is shown in the form of iso-correlation contours in Figure 8.23. The increment in the spanwise spacing of the probes was $\Delta z = 0.1D$, while the streamwise increment, based on the convection speed of $U_c = 7.9$ m/s, was $\Delta x = 0.078D$. These results clearly prove the symmetry of the mean flow about the centreplane. In addition, the R_{uw} contours seem to indicate the presence of at least two structures with similar features, with an average streamwise spacing of about 2.1 D, for the case presented in that figure. Additional two-point, space-time correlations were taken with the fixed probe positioned off-centre. For example, Figure 8.24 shows that R_{uu} correlations peaked at time differences consistent with the concept of convected structures. The main peaks were positive or negative depending on the position of the fixed probe and the spanwise spacing of the probes. One may be tempted to use these results, in conjunction with a physical model of the dominant structures, in order to estimate the spatial features of these structures. At the same time, it must be recognized that correlation results could actually mask the distinct features of individual structures, as they are produced by indiscriminate averaging of all events. The measurements presented in the next section are designed to better distinguish and isolate the organized structures and give more detailed information on their features.

8.3.4 Conditional Sampling Measurements

The conditional sampling technique employed in this work is based on the Variable Interval Time Averaging (VITA) technique. It was introduced in Chapter 7, along with a method developed in the course of this study to enhance its educed signals.

Two probes were used for these measurements. A triggering probe, which was a cross-wire of the boundary layer type, and the measuring probe, which was the three-sensor probe. The triggering probe was placed at a fixed position in the centre of the gap, 300 mm (approximately 3 rod diameters) upstream of the measuring probe, which was traversed according to the grid shown in Figure 8.5.

Basic testing of the technique was described in Chapter 7. Further tests were performed by inspecting the technique's results for the following situations. First, the

triggering probe was placed in a region of the flow where coherent structures are known not to be measurable and the measuring probe was traversed at a few positions close and away from the gap. Then, the triggering probe was positioned again at the centre of the gap and the measuring probe was placed in the upper half of the channel, away from the flow region where coherent structures are present. In both situations, no coherence could be seen in the obtained ensemble averages, which indicates that the technique would not detect false organized structures.

The educed signals obtained by the VITA technique were also compared, for few points in the gap region, to the results of the Window Average Gradient (WAG) conditional sampling technique (Bisset et al [1990]). Both techniques yielded comparable ensemble averages, but also some phase difference, due to the difference in the detected time of arrival of the structures.

Depending on the information to be extracted, the results of the conditional sampling measurements will be presented according to either the triple decomposition or the double decomposition, defined in Chapter 4. Samples of the educed ensemble averages of the velocity vector, i.e. its coherent components according to the triple decomposition, are shown in Figure 8.25. All samples have the same phase relationship with the detection time. It can be seen that the largest variation of the spanwise coherent velocity component is in the region close to the centre of the gap, while the variation of the streamwise coherent velocity component has essentially the same magnitude up to 0.6 D from the channel centerline, but a changing phase difference from the spanwise component. Also, these two components are nearly in-phase for negative z and out-of-phase for positive z values. The transverse coherent velocity component is essentially zero close to the gap centre; it has a definite variation, though smaller than the variation of the other two components, at distances around $0.6D$, becoming stronger with distance from the bottom channel wall. These will be further analysed in the next chapter.

First, the educed signals, obtained without applying the enhancement method, are considered. These are used for the presentation of overall features of the structures, namely their shapes, spatial locations and positions relative to each other. The rationale behind this choice resides in the fact that, as indicated in Chapter 7, the enhancement method yields stronger, clearer, less attenuated, ensemble averages for the detected vortex but severely

attenuated averages for the preceding and subsequent vortices. For this reason, the enhancement method will be applied only to the properties of a single vortex.

The estimated convective speed of the structures was used to convert the time differences into streamwise distances and obtain the three-dimensional coherent velocity field. The validity of this assumption even for large time differences can be justified based on the results of the two-point correlation discussed earlier (Figure 8.20). The latter indicated that coherent structures were convected downstream relatively unchanged. The obtained three-dimensional coherent velocity field is shown in the form of iso-surface contours, for each of the three coherent velocity components, in Figures 8.26 to 8.28; the same field is visualized in Figure 8.29 by software-generated pathlines (using the TECPLOT software, by Amtec Engineering Inc.), obtained by integrating the three dimensional velocities of hypothetical particles, starting at specified spatial positions. In Figure 8.29, the streamwise velocity at each point is obtained by subtracting the convective speed of the structures from the value of the coherent velocity, according to the double decomposition. Therefore, the visualized flow field of Figure 8.29 represents an average sequence of vortices as seen by an observer travelling with a speed equal to the convective speed of the structures. It can be seen that the sections of the structures occupying the gap region are very elongated vortices, which cross the gap and extend well into the open subchannel where they curve upward, away from the centreplane. A cross-section of the above flow field at a height equal to half the gap width is shown as a vector plot and visualized by software generated pathlines in Figure 8.30. The pathlines clearly indicate the presence of a street of counter-rotating vortices, alternating on each side of the gap centreplane. The streamwise spacing of the vortices is the same as obtained from the two point correlations of Figure 8.23, i.e. about $2.1D$ for the case of $W/D = 1.100$. The spanwise spacing of the centres of the structures, based on Figure 8.30, is roughly equal to one rod diameter. However, these vortices are clearly three-dimensional and one has to be cautious in determining the spacing of three-dimensional vortices from a two-dimensional cross-section, as these distances represent the spacing of vortices in the plane of the cross-section and not necessarily the spacing of the axes of the vortices. The latter can be inclined and, therefore, cross-sections at different heights would show different spanwise spacings of the vortex centres.

The detailed properties of the vortices will now be considered, based on the results

of the enhanced VITA. According to this method, the time scale and, consequently, the streamwise distances are adjusted by the expansion/contraction factor, α, defined in Chapter 7. Instead of adjusting each of the obtained traces separately, the adjustment is performed for all the phase averages using the average value, $\alpha_{average}$, over all detected vortices, which numbered about 110,000. This value was also used to calculate the standard deviation, σ_α, and the probability density function (pdf) of the expansion/contraction factor, α. It was found that $\sigma_\alpha = 0.284\alpha_{average}$. Figure 8.31 shows that the obtained pdf of α can be approximated reasonably well by the pdf of a normal random variable. The resolution for α was $\sigma_\alpha/10$. For practical purposes, limits were imposed on the extreme values of α in the search algorithm at $\alpha_{average}-3\sigma_\alpha$ and $\alpha_{average}+2\sigma_\alpha$.

When comparing the conditionally averaged coherent velocities obtained by the VITA technique (Figure 8.25) with those obtained by the enhanced VITA technique (Figure 8.32), it is obvious that, for positions close to the gap centre, the former technique fails to detect a peak in the streamwise coherent velocity. This can be explained by the fact that the VITA technique, when ensemble averaging, does not take into account the size variations of the structures or their slight misalignment, thus leading to the averaging-out of some of their details. Away from the gap centre, the coherent velocity traces, obtained by both techniques exhibit similar variation trends, although those obtained by the enhanced VITA show less attenuation in amplitude.

From the definition of the triple decomposition (see Chapter 4), the mean of any flow quantity is equal to the mean according to the Reynolds decomposition. Therefore, Figure 8.6 also represents the mean defined by the triple decomposition.

The phase-average of any quantity is obtained by ensemble averaging its instantaneous values obtained from the educed signals of the enhanced VITA technique. The relations between the phase-averages of different terms have been introduced in Chapter 4. Using these relations, one can obtain quantities that could not be calculated directly by ensemble averaging, namely the phase-averages of the normal and shear stresses of the incoherent velocity components. For example, one can obtain the phase-average of the incoherent streamwise normal stress (i.e the square of the incoherent streamwise velocity), $\langle u_r^2 \rangle$, by subtracting the square of the coherent streamwise velocity, $(\tilde{U})^2$, from $\langle (U-\tilde{U})^2 \rangle$. Figures 8.33 to 8.36 present contours of the coherent velocity components and their

corresponding coherent and incoherent components of the normal and shear stresses in the plane at a height y equal to half the gap width from the bottom wall. In this plane, the values and variations of the $\tilde{V}$ component and its corresponding stresses were appreciably smaller than the corresponding quantities of Figures 8.33 to 8.36. For this reason, the former were not presented in contour form, but instead, samples, for few measuring positions, of $<(U-\overline{U})(W-\overline{W})>$, $<(U-\overline{U})(V-\overline{V})>$ and $<(V-\overline{V})(W-\overline{W})>$ are shown in Figures 8.37 to 8.39, where Figure 8.37 is included for comparison purposes.

The terms $\overline{\tilde{U}_i\tilde{U}_j}$ are evaluated by integrating the product $\tilde{U}_i\tilde{U}_j$ over a period corresponding to the passage of two vortices. This is achieved in practice by performing the integral between two minima of the spanwise coherent velocity component. The incoherent stresses $\overline{u_{ri}u_{rj}}$ are obtained from the difference between $\overline{\tilde{U}_i\tilde{U}_j}$ and the corresponding Reynolds-averaged stresses (see Chapter 4). All of these time-averaged stresses are presented in Figures 8.40 and 8.41.

All of the above phase-averages and time-averages will be examined in the next chapter with the scope of describing the coherent and incoherent velocity fields and characterizing the additional terms contained in Equations 6, 7 and 8 of Chapter 4.

9

Analysis and Discussion of Results

9.1 Reynolds-Averaged Flow Characteristics

Direct comparison of the present measurements with results obtained in similar channel geometries is not possible, due to the lack of such studies in the literature. Instead, qualitative comparisons will be performed with flows in closely related geometries. Some quantitative comparisons will also be presented with turbulent flows in these geometries and in reference geometries such as circular pipes and rectangular channels.

Away from the rod, the isotachs (Figure 8.6) followed patterns comparable to those in rectangular channel flows. This was also the case for the rms axial turbulent velocity (Figure 8.8). The local axial turbulent intensity was about 10% close to the walls and about 4% in the region half way between the top corner and the rod surface, comparable to typical values for fully developed turbulent flows in rectangular channels (Hussain and Reynolds [1975]) and circular pipes (Laufer [1954]). Near the top corner, the transverse and spanwise turbulent intensity levels were typically about 5%, comparable to the levels measured in rectangular ducts by Melling and Whitelaw [1976]. In the nearly square channel of Melling and Whitelaw [1976], the transverse and spanwise rms velocity fluctuations were the mirror

images of each other with respect to the corner bisector. A tendency towards such "symmetry" can be discerned from Figures 8.9 and 8.10 but only very close to the top corner. In particular, the values of the transverse rms velocity close to the top channel wall (respectively side wall) were comparable to those of the spanwise rms velocity close to the side wall (respectively top wall); however, the shapes of the contours, especially away from the corner, were measurably different. These differences can be attributed to the asymmetry of the rectangular channel with respect to the corner bisector, and also to the presence of the rod, which introduces additional geometrical asymmetry. This effect was more marked in the bottom corner of the channel, which was influenced more by the presence of the rod.

Perfect symmetry requires that the $\overline{uv}$ and $\overline{uw}$ turbulent shear stresses should be equal in magnitude and opposite in sign at points symmetrically located with respect to the corner bisector. Again, it can be seen (Figures 8.12 and 8.13) that, for the present flow situation, this was approximately the case in the top corner but not in the bottom corner of the channel.

Close to the top and side walls of the channel, isocontours of the three turbulent shear stresses were similar to those in rectangular channels (Figures 8.12 to 8.14). The effects of secondary flows are clearly noticeable in the bulging of the contours towards the corners of the channel. The corresponding correlation coefficients (Figures 8.15 to 8.17) had magnitudes comparable to those in circular pipe flows (Laufer, 1954), i.e. near 0.4 for $\overline{uv}/u'v'$ and $\overline{uw}/u'w'$ in the vicinity of respectively the top and side walls. The third correlation coefficient, $\overline{vw}/v'w'$, was essentially zero close to the channel walls. Towards the bottom wall, the dominant shear stress correlation coefficient, $\overline{uv}/u'v'$, was much lower than towards the top wall, and the shape of its contours was clearly affected by the presence of the rod.

In the vicinity of the rod-wall gap, the bulging of the isotachs (Figures 8.6 and 8.7) towards the gap was similar to the observed bulging in the measurements of Rehme [1979] in wall and corner subchannels. Away from the gap, the rather open aspect of the present channel resulted in a different flow distribution. The same peculiar contours of the rms axial turbulent velocity, as in the many measurements reported by Rehme for comparable *P/D* and *W/D* ratios, are seen in Figures 8.7 and 8.8. In the present flow configuration, because of the larger distance between the rod and the side wall, the region of maximum rms axial turbulent

velocity was further out into the subchannel than that in Rehme's results (for example Rehme, 1989). The peculiarity of the distributions of the three rms turbulent velocities will be further discussed in the next section in the context of the large scale structures present in the gap region and in an attempt to develop a physical model for these structures. In general, the level of the three rms turbulent velocities and of the turbulent kinetic energy were notably higher in the gap region than in the core of circular pipe flow. Moreover, in the gap region, in contrast with the remainder of the channel, the partition of the turbulent kinetic energy to its components $\overline{u^2}$, $\overline{v^2}$ and $\overline{w^2}$, was significantly different from that in pipe flow (Figures 9.1 to 9.3). For the circular pipe flow away from the walls, the axial normal stress contains half of the total energy, while the other two components account for approximately one quarter each (Lawn, 1971). In the position of maximum rms axial turbulent velocity, i.e. halfway between the subchannel center and the gap center, the axial normal stress amounted to 0.70 of the total, while the contributions of the transverse and spanwise components were respectively 0.12 and 0.18 of the total. In the centre of the gap, however, the $\overline{u^2}$ and $\overline{w^2}$ stresses had comparable contributions, while $\overline{v^2}$ further diminished. Typical values at $z/D=0$ were $\overline{u^2}/2k=0.44$, $\overline{v^2}/2k=0.07$ and $\overline{w^2}/2k=0.49$. This last value matches the value measured by Hooper and Wood [1984] at the center of a rod-rod gap of a square pitched rod bundle array with $P/D=1.107$.

In the gap region, the maxima of the $\overline{uv}$ and $\overline{uw}$ stresses were located at the same positions as the axial turbulent intensity maxima, namely halfway between the subchannel centre and the gap centre. The $\overline{vw}$ stress, on the other hand, had a contour distribution similar to the distribution of the v' turbulent intensity. The correlation coefficient contours had the same shapes as those of the corresponding shear stresses, with values of $\overline{uv}/u'v'$ and $\overline{uw}/u'w'$ lower than typical values in pipe flow. All of these factors infer collectively that turbulence transport in the gap region was not controlled by the "wall-turbulence", but rather by the same phenomenon that generates the peculiar high rms turbulent velocity distributions. It is to be noted that the high values of the $\overline{vw}/v'w'$ correlation close to the rod can be explained in part by the curvature of the rod surface in the y-z plane. It is only the high-valued concentric contours, located at approximately half a diameter from the bottom wall, close to the wall and facing the open flow region (i.e. near the location of the v' maximum), that are associated with the above phenomenon. It will be shown in section 9.3

that this phenomenon is the formation of coherent structures in the gap region.

9.2 Implications about Secondary Flows

As indicated in the previous chapter, the magnitudes of the measured secondary velocities were comparable to the measuring uncertainty. This relatively large uncertainty precludes any direct measurement of secondary currents, whose existence and patterns can, however, be inferred from other measured quantities.

All of the measurements presented above are consistent with the formation of secondary flow patterns near the corners of the rectangular channel. A further verification of this fact can be achieved by examining the production terms for the secondary flows (Equation 13 of Chapter 2). The first of these two terms is

$$S_1 = \left(\frac{\partial^2}{\partial y^2} - \frac{\partial^2}{\partial z^2} \right) \overline{vw} \tag{1}$$

and the second is

$$S_2 = \frac{\partial^2}{\partial y \partial z} (\overline{v^2} - \overline{w^2}) \tag{2}$$

The difference $(\overline{v^2} - \overline{w^2})$ appearing in S_2 is presented in Figure 9.4. By comparison to the variation of $\overline{vw}$, namely the term appearing in S_1 (Figure 8.14), the variation of this difference is much larger in the corner regions, which implies that S_1 would likely be negligibly small compared to S_2. Therefore, the dominant term in the production of secondary motion is the gradient of the normal stress difference in the plane perpendicular to the main flow direction, S_2, in agreement with previous studies (Brundrett and Baines, 1964, and Haque et al, 1983). Furthermore, the sign of the difference $(\overline{v^2} - \overline{w^2})$ is consistent with the measurements of Brundrett and Baines [1964], implying that the direction of the flow circulation in each of the secondary flow cells would likely be as indicated by Brundrett and Baines [1964], namely away from the corner, along the walls, and towards the corner, along the line separating the two cells.

Having established some confidence in the measurements of Figures 8.14 and 9.4,

one may try to infer, based on these measurements, information about secondary flows in the gap region.

Although the measured V and W velocities are not sufficiently accurate, it was noted that these velocities were generally smaller close to the rod than close to the corners of the rectangular channel. This implies, with some reservations, that the secondary motion in the gap region has a relatively small magnitude, compared to that in the corner regions. An additional evidence of the reduced magnitude of the secondary motion can be obtained by qualitative inspection of the variations of the quantities appearing in the production terms S_1 and S_2 (Figures 8.14 and 9.4). It is seen that most of the contours of Figure 9.4, in the region close to the rod, are essentially parallel either to the y-axis or to the z-axis, which implies that S_2 would be essentially zero in this region. The secondary motion would be, then, produced mostly by the S_1 term and, more precisely, by the variation of $\overline{vw}$ in the z-direction, as most contours of Figure 8.14 are nearly parallel to the y-axis in the gap region. Qualitatively, one may conclude that there is no evidence for the formation of secondary flows that would be strong enough to dominate flow phenomena in the gap. In addition to this, as noted in section 8.2, the distributions of the rms turbulent velocities, especially u', and the turbulent kinetic energy are incompatible with the presence of strong secondary flows in the gap region. Most of the inference of strong secondary motion, found in earlier literature on flows in rod bundles, are speculations based on the strong bulging of the isotachs towards the center of the gaps. In fact, most attempts to measure directly these secondary velocities were inconclusive (see for example Kjellström [1974] and Carajilescov and Todreas [1976]).

The intent of the above analysis was to examine whether one can justify the formation of strong secondary flows in the gap region based on Reynolds-averaged measurements. It was shown that this is not the case. Furthermore, considering the effects of the large scale structures, the use of Reynolds-averaged secondary flow production terms in the gap region becomes questionable, because this approach smears out the typical features of quasi-periodic velocity variations.

9.3 Coherent Structure Characteristics

The present measurements have further documented the previously known fact that organized, quasi-periodic, vortical structures form in the vicinity of the narrow gap of rod bundles as well as in a variety of similar configurations.

For an incorporation of the effects of these structures into a practical model, one should like to estimate their shapes, strengths, orientations and lateral extents as well as their dependence on the channel geometry and the Reynolds number. This task, however, turns out to be quite onerous. First of all, because of the narrowness of the passage, these structures are strongly three-dimensional and the motions induced by them would be non-axisymmetric and non-planar, as they turn around the structure axis and extend out of the gap towards either of the open subchannels. In light of these observations, it is clear that a full documentation of these structures requires simultaneous three-component velocity measurements. In addition, flow visualization (Section 8.3.1) revealed the presence of frequency irregularities and occasional jitter of the structures, which would distort conventional two-point velocity correlations. Nevertheless, extensive two-point correlations were performed at first and, although some of these results were superseded by the conditional sampling results, they are discussed here as they provide information about the spacing and convection speeds of the structures for different gaps, while conditional sampling was carried out for one gap size only.

9.3.1 Spacing and Convection Speed of Structures

The only features of the structures that can be estimated with relative confidence, based on the two-point correlation measurements, are their average convection speed, U_c, and their average streamwise spacing, λ. U_c, computed from the peaks of space-time correlations, decreased significantly with diminishing gap width (Figure 9.5) and approached an asymptote at $W/D > 1.25$. For rough purposes, one may approximate its variation by the fitted exponential curve

$$\frac{U_c}{U_b} = 1.04\left(1 - e^{-10.9\,W/D\,-\,10.6}\right) \tag{3}$$

The convection speed had values intermediate between the maximum mean speed in the neighbouring open subchannel and the mean speed in the gap centre. The streamwise spacing between two consecutive structures could be estimated as half the "wavelength" of the oscillations in the spatial velocity correlations or, alternatively, as

$$\lambda = \frac{U_c}{f} \tag{4}$$

where f is the frequency of the oscillations, estimated from the peak in the measured power spectra. Both approaches became increasingly uncertain as the gap width increased. Within the narrow range $1.025 \leq W/D \leq 1.100$, the vortex spacing obtained in this manner seems to vary linearly with gap width (Figure 9.6) as

$$\frac{\lambda}{D} = 18.7\frac{W}{D} - 16.3 \tag{5}$$

This is in agreement with Möller's [1991] findings that the inverse of the Strouhal number varies linearly with gap size (note that the Strouhal number is proportional to the frequency and inversely proportional to a characteristic velocity, and it is therefore inversely proportional to λ).

In the above analysis, it has been implicitly assumed, by analogy to two-dimensional wakes and mixing layers, that the vortex spacing is independent of the Reynolds number, at least within the ranges of the available rod bundle experiments. The validity of this assumption remains to be tested in the future although there is evidence that it holds for closely related geometries. In fact, Meyer and Rehme [1995] confirmed that in compound channels equipped with slots the axial vortex spacing is a function of the geometry and independent of the Reynolds number.

To help interpret the two-point correlation measurements, we have examined the fields of various arrays of two-dimensional vortices, for example a street of counter-rotating, "potential" vortices being convected with a constant velocity, U_c. Both the case with the

axes of consecutive vortices on the centreplane and the case with these axes symmetrically located with respect to the gap centreplane were considered. Each of these fields produced certain correlations that were similar to the measured ones but also correlations that were incompatible with the measurements. In conclusion, we were unable to formulate a simple physical model of coherent structures that is consistent in all its features with the two-point correlations. Additional measurements to be discussed in the next section will clarify this issue.

9.3.2 Conditionally Sampled Measurements

The results of the conditionally sampled measurements will be used primarily to construct a physical model of the structures. Representations of the flow field, such as those in Figures 8.29 and 8.30, though very useful in visualizing an otherwise complicated three-dimensional flow structure, cannot be relied upon to estimate the shape of the structures. The same limitations as those discussed in Section 8.3.1 for the flow visualization apply to the software generated pathlines. Contours of the coherent velocity components, such as the ones shown in Figures 8.26 to 8.28, are not helpful in identifying the coherent structure boundaries (Hussain, 1983). For these reasons, the discussion below will be based mostly on the coherent vorticity and the coherent velocity traces.

a) Coherent Vorticity Distribution

The three components of the coherent vorticity vector were calculated from the coherent velocity field, according to the customary definition of vorticity. The derivatives were evaluated by differentiating a polynomial fitted to typically 5 data points and centred at the location of interest. The contours of Figures 9.7 to 9.9 are representative cross-sections through constant vorticity iso-surfaces. Figure 9.7 shows a cross-section at a height equal to half the gap width of the transverse coherent vorticity calculated according to both the triple and double decompositions. Both contours confirm the presence of counter-rotating vortices with centres alternating on each side of the gap, consistently with the pathlines of Figures 8.29 and 8.30. The direction of rotation, as indicated by the sign of the vorticity in

the y direction, is such that, at the vortex front, the structure would transport fluid from the high velocity region towards the lower velocity region, i.e. the gap. This is in agreement with the direction of rotation of the coherent vortices that form in mixing layers. The contours of the vorticity according to the double decomposition are physically more meaningful than those based on the triple decomposition. In fact, the former are a better representation of the average flow field while the latter cannot approximate the instantaneous vorticity distribution, because a significant part of the instantaneous vorticity vector is generated by the velocity time-average gradient. However, it is desirable in some instances, for simplicity of interpretation, to remove the contribution of the time-average velocities and separate the coherent and the time-average vorticities. This is notably the case of Figure 9.8, where a better physical insight is achieved by omitting the time-average vorticity, which arises mostly from the high velocity gradient normal to the rod surface. The vorticity contours in this figure clearly show the vortex to extend upward into the subchannel and its size to decrease with increasing height. The successive cross-sections also show that the streamwise position of the vortex centres is a function of height from the bottom wall, which implies that the vortex axis is inclined in the x-y plane. Figure 9.9 shows cross-sections through iso-surface contours of the spanwise coherent vorticity. When combined with the transverse coherent vorticity, the latter confirms the upward curving of the vortex, away from the centreplane, as previously observed in the pathlines of Figure 8.29. The coherent streamwise vorticity was also calculated; however, its magnitude was small and no perceptible patterns were obtained.

b) Coherent Velocity Traces

Before formulating a physical model of the structures, the relevant information obtained above will be verified and complemented using the traces of the coherent velocity components shown in Figures 8.25 and 8.32. However, the direct interpretation of these velocity traces was revealed to be not an easy task. To help the interpretation, we have examined the fields of two-dimensional, counter-rotating, potential vortices with different shapes and different spatial configurations. The only vortex pattern that produced velocity traces comparable to those of Figures 8.25 and 8.32, for $-0.6 \leq z/D \leq 0.6$, is the pattern in

which the cross-section of the vortices was set to be very elongated with an "ellipse-like" shape and in which the vortices were arranged so that their centres alternated on each side of the gap centerline with the major axis of the ellipse slightly inclined with respect to the streamwise direction. This inclination angle was estimated, based on the increasing time delay for the arrival of the vortex with spanwise distance from the gap (Figure 8.32) and using the convection speed of the structures to convert time differences into streamwise distances, to be around 28°. The above vortex pattern is compatible with the vorticity results and the pathlines of Figures 8.29 and 8.30. However, as for the velocity traces, the correspondence between the measurements and the examined vortex pattern was limited to approximately the interval $-0.6 \leq z/D \leq 0.6$ and at a height y equal to half the gap width. For locations further away from the gap, it was observed that the measured coherent velocity components were essentially zero in the x-z plane passing through the middle of the gap ($y/D=0.050$), but had a measurable variation for larger y/D. The most striking characteristic, in these regions of the flow, was the distinct variation of the transverse coherent velocity component, also apparent in the contours of Figure 8.27 (recall that the latter was essentially zero close to the gap center). This variation became stronger with increasing distance from the bottom wall. In addition to this, the transverse coherent velocity component was in-phase with the spanwise coherent velocity for positive z/D and out-of-phase for negative z/D. According to the direction of rotation of the vortices and the coordinate system used here, the above observations indicate a gradual lifting out of the mid-gap plane of the "disk-like" part of the vortex cross-section present in the gap centre region. This can be also observed in the pathlines of Figure 8.29.

c) Reconstruction of a Typical Structure

Following the above discussion, it is now possible to formulate a physical model for the coherent structures that form in the gap between a rod and a plane wall. A schematic of this model is shown in Figure 9.10. It consists of a street of three-dimensional counter-rotating vortices with axes located, in an alternating sequence, on either side of the gap centreplane. The vortices are elongated in the streamwise direction with an ellipse-like cross-section. In the vicinity of the gap, the major axis of the ellipse forms an angle with the gap

centreline approximately equal to 28°. The direction of rotation is such that, at its front, each vortex transports fluid from the open flow region towards the gap region and, at its rear, it transports fluid from the gap to the open flow region. The vortices cross the gap and extend well into the opposite subchannel. In order to illustrate the three-dimensionality of the structures, consider a streamline in a frame convected by the convection speed of the structures and passing through a point, in the gap centreplane, located on the perimeter of the vortex cross-section. This streamline would be essentially two-dimensional in the immediate vicinity of the gap and in a plane parallel to the channel bottom wall, while curving upward away from the gap. As a vortex cannot end abruptly, it is speculated here that each vortex funnels at its two ends into the boundary layer vorticity near the plane wall or the rod surface, respectively. This hypothesis provides a continuous vortex tube with a self-consistent direction of rotation along its entire length.

One should emphasize at this point that the coherent structures are not deterministic. It was shown in the previous chapter that their sizes varied following a normal distribution. Not accounted for in the above analysis is the variation of their spatial locations. Besides size variations, one may also expect variations in the transverse and spanwise positions of the structures. These variations have not yet been determined.

d) Effect of Coherent Structures on the Turbulent Velocity Contours

A further verification of the model can be performed by examining the distributions of the rms turbulent velocities (Figures 8.8 to 8.10). This will also offer an explanation to the peculiar contours of these quantities in the gap region. It is to be noted that Reynolds averaging does not discriminate between velocity variations due to the presence of coherent structures and incoherent turbulent velocity fluctuations. The large-scale coherent structures have a much larger velocity variation than the small-scale turbulence. Thus, the coherent structures are expected to have, in general, a relatively large contribution to the rms turbulent velocities.

The specific effects of the vortices on the individual turbulent kinetic energy components can be estimated based on the following observations. For a vortex with an axis in the transverse direction, the streamwise component of the vortex velocity is highest in the

two regions close to each of the spanwise edges of the vortex. The spanwise regions intermediate between these two edges correspond to the region of relatively large values of the spanwise component of the vortex velocity.

According to the above vortex model, close to the gap the vortex axis is nearly parallel to the y axis, and the gap region is between the vortex axis and its spanwise edge. Therefore, this region is expected to have the highest variation of the spanwise coherent velocity component. This variation is sufficient to explain the strong bulging of the contours of the rms spanwise turbulent velocity, w', towards the gap.

The physical model of the structures also explains why the maximum u' occurred at locations between the gap and the subchannel centre. In fact, the location of maximum rms streamwise turbulent velocity, u', (Figure 8.8) corresponds, according to the model, to the region close to the spanwise edge of the vortex, which is the region of highest variation of the streamwise coherent velocity. The inclination of the contours of Figure 8.8 is consistent with the upward curving of the streamlines discussed in the previous section. This upward curving also explains why the maximum rms transverse turbulent velocity, v', was at the observed locations. Actually, as the streamline lifts upward, the transverse component of the vortex velocity becomes relatively larger.

e) Effect of Coherent Structures on the Incoherent Turbulence

At this point it is worthwhile to examine any possible relationships between phase-averaged and time-averaged, coherent and incoherent, normal and shear stresses (Figures 8.34 to 8.39). These are the additional terms that appear in the time-averaged, phase-averaged and instantaneous momentum equations when using the triple-decomposition (Equations 6, 7 and 8 of Chapter 4). A comparison of the contour levels of Figures 8.34 and 8.35 indicates that, over the region occupied by the structure, the magnitude of $<u_r^2>$ often exceeds that of $(\tilde{U})^2$, while $<w_r^2>$ is mostly constant in the streamwise direction and smaller than $(\tilde{W})^2$. Furthermore, it is seen that most of $<u_r^2>$ activity occurs in regions where the coherent velocity undergoes a local acceleration or deceleration (the regions of closely spaced contours in Figure 8.33). This indicates that the added shear, resulting from the passage of a vortex, is responsible for the production of additional incoherent turbulence.

The phase-average shear stresses (Figure 8.36) corroborate the above statement. In fact, the local maxima of the incoherent shear stress $<u_r w_r>$, which have values comparable to those of the maxima of the corresponding coherent stress, also coincide with the locations of sharp variations of the coherent velocities.

b) Incoherent Turbulence Structure

The contributions of the coherent and incoherent normal and shear stresses to the time-averaged quantities are now considered. Figure 8.40 shows $\overline{\tilde{U}^2}$, $\overline{\tilde{V}^2}$ and $\overline{\tilde{W}^2}$ along with the corresponding Reynolds-averaged normal stresses. The normal coherent transverse stress, $\overline{\tilde{V}^2}$, is essentially equal to zero. This is in agreement with the earlier observation that there was no measurable coherent component of the transverse velocity in the plane at y equal to half the gap width. $\overline{\tilde{U}^2}$ and $\overline{\tilde{W}^2}$ seem to have variation trends similar to those of the corresponding Reynolds-averaged normal stresses. This suggests that the corresponding incoherent normal stresses would be nearly constant. Figure 8.40 shows that these incoherent stresses have variations smaller than those of the corresponding Reynolds-averaged stresses and diminish towards the gap centre. This can be explained by the increased viscous damping near the narrow gap. A representative partition of the total incoherent kinetic energy for the profile presented was $\overline{u_r^2}/2k_r=0.59$, $\overline{v_r^2}/2k_r=0.14$ and $\overline{w_r^2}/2k_r=0.27$, which nearly matches the partition close to the wall in pipe flows, namely $\overline{u^2}/2k=0.57$, $\overline{v^2}/2k=0.16$ and $\overline{w^2}/2k=0.27$ (Lawn, 1971). This contrasts with the corresponding partition of the Reynolds-averaged stresses, which was substantially different from that of pipe flow (Section 9.1). Similar observations can be made for the time-average coherent shear stresses (Figure 8.41). The $\overline{\tilde{U}\tilde{V}}$ and $\overline{\tilde{V}\tilde{W}}$ shear stresses were essentially equal to zero, while the variation trends of $\overline{\tilde{U}\tilde{W}}$ were the same as those of their corresponding Reynolds-averaged normal stresses. Representative values of the incoherent shear stress correlation coefficients for this profile were $\overline{u_r v_r}/(u_r' v_r')=-0.34$, $\overline{u_r w_r}/(u_r' w_r')=-0.179$ and $\overline{v_r w_r}/(v_r' w_r')=0.08$. The value of the $\overline{u_r v_r}/(u_r' v_r')$ shear stress correlation coefficient is comparable to typical values in pipe flows i.e. near -0.4 (Laufer, 1954).

So, even though the phase-averaged incoherent stresses were found to depend on the

coherent velocity field, the time-averaged incoherent turbulence structure seems to match that in pipe flows.

9.4 Reconfirmation of the Coherent Structures and an Explanation for their Formation

In closing, we should like to reconsider the hypothesis that the flow patterns found here can be formally classified as coherent structures, according to the established definitions and to attempt to explain the mechanism that leads to their formation.

A coherent structure, according to Hussain [1983], is a flow module with instantaneous phase-correlated vorticity. Although the instantaneous vorticity was not measured in the present work, the use of a triggering probe at a fixed position permitted the phase-alignment of all conditionally sampled measurements. The observed presence of significant non-zero vorticity in the conditionally averaged flow field is deemed to be sufficient evidence of the presence of instantaneous phase-correlated vorticity in the studied flow.

The present patterns also conform with the description of coherent structures given by Berkooz et al [1993], as they repeatedly appear in the flow as evidenced, for example, by the velocity traces (Figure 8.18). The two-point correlations and the conditionally sampled measurements demonstrate that these structures possess organized spatial features. Similarly, it can be easily seen that the definitions of Perry and Stull, cited in Chapter 4, apply to the structures present in the gap region.

Finally, it can be demonstrated that the present structures also conform with the definition of coherent vortices given by Lesieur [1997]. The pathlines of Figure 8.29 and the vorticity contours of Figures 9.7 to 9.9 show that the fluid trajectories wound around regions where there was coherent vorticity concentration (condition 1). The consistently high velocity correlation, even for streamwise spacings of the probes as large as several times the estimated size of the vortices, is a proof that condition 2 is satisfied. Eventhough no direct measurements have been conducted to establish or refute the fulfilment of condition 3 of Lesieur's definition, it can be implied, based on the randomness of the structures sizes (Figure 8.31) that they are sensitive to small perturbations in the initial conditions.

In conclusion, all indications confirm that the large-scale structures documented here can be formally classified as coherent structures. Having established that, one is challenged to articulate a rational explanation of the physical processes that lead to their formation. The only available explanations have been put forward by Hooper and Rehme [1984] and by Möller [1991], which associate these structures with incompressible parallel-channel instabilities, triggered by random turbulent motions. This explanation is not entirely clear and, in fact, it may not even apply to certain configurations, such as the single-rod near an infinite wall case, nor does it explain the formation of quasi-laminar coherent structures at low Reynolds numbers. A different explanation is proposed here, which relates the near-gap structures to the well-documented, quasi-two-dimensional vortices that form in two-dimensional mixing layers, under a variety of conditions, including both laminar and turbulent flows.

One may consider the near-gap vortices as forming in the mixing layer between the high-speed flow in the open subchannel core and the low-speed flow near the gap. Not only is the sense of rotation of the vortices found here compatible with this hypothesis, but also their spacing and convective speed are comparable to those in mixing layers, despite the obvious differences in the two configurations. For example, Tavoularis and Corrsin [1987] defined the maximum vorticity length, l, in two-dimensional mixing layers, as the inverse of the maximum velocity derivative in the transverse direction and found that their measurements and results compiled from available literature gave $3.4 \leq \lambda/l \leq 4.3$. The ratio of the spacing measured here between structures for W/D=1.100 and a very crude estimate of l based on the velocity variation along a curve connecting the velocity minima and maxima gave a value near 4, well within the mixing layer range. The convective speed of the near-gap structures was also found to be intermediate between the minimum speed in the gap and the higher level in the subsequent subchannel core; in mixing layers, the convective speed of the coherent structures is comparable to the average speed.

The mixing layer analogy is sufficient to predict the formation of two sequences of vortices on either side of the gap, but not the cross-channel mixing. The communication between the two subchannels through the gap opening permits both pressure adjustment and cross-flow. The organized staggering of the two vortex sequences is strongly reminiscent of the von Karman vortex shedding pattern that forms in the wake of circular cylinders, in

which boundary layer separation and vortex detachment on one side interact with those on the other side through the continuous pressure field around the cylinder. The relative spacing of wake vortices is also compatible with the near-gap vortex spacing. Therefore, it seems plausible to assume that the two vortex sequences across the gap interact in such a way that their induced velocities and pressure fields reinforce, rather than oppose, each other, with the result that each vortex is filling some space between two vortices of the opposite sequence, across the gap, as in the observed patterns. Obviously, more detailed analysis and measurements are required to completely resolve these issues, but the tentative success of the above hypotheses encourages such an undertaking.

9.5 Implications on Heat Transfer and Mixing in the Gap

The coherent structures and the large-scale transport associated with them have a significant effect on the local heat transfer in the gap and on the intersubchannel mixing, as this depends largely on the flow through the gap region.

The coherent structures have been demonstrated to be large-scale, three-dimensional, vortical structures with axes located alternately on either side of the gap plane of symmetry. These vortices induce fluid motion from the core of one subchannel, across the gap and well into the opposite subchannel. Unlike small-scale turbulence, coherent structures transport momentum and heat over large distances, replenishing the warm fluid in the gap region with relatively cooler fluid from the open flow region, and thus capable of extracting more heat from the rod surface. Also, the crossing of the gap by the large scale structures tends to reduce differences between flow velocities and temperatures within the two subchannels. It is therefore evident that the presence of coherent structures in the gap region enhances appreciably the local heat transfer in the gap and the intersubchannel mixing. However, this alone cannot explain entirely the insensitivity of the local friction factor and heat transfer coefficient to the gap size. The aim of the arguments presented below is to offer such an explanation based on the coherent structures results.

There are four factors that can influence the effects of coherent structures on the local heat transfer in the gap and on the intersubchannel mixing. These are the strength, the spacing, the convection speed and the lateral extent of the vortices. The variation of the

former three factors as a function of the gap width can be evaluated based on the present measurements. However, the lateral extent of the vortices for different gap sizes is yet to be determined. For the sake of the discussion below, it will be assumed that, for a given channel shape, this lateral extent remains essentially the same when the gap size varies. This is a conservative assumption as far as the transport by coherent structures is concerned, because a reduction in gap width would likely broaden the region of significant mean velocity variation, resulting in structures that would extend deeper into the subchannel core.

There are indications in the measurements that the vortices become stronger as the gap size diminishes. This can be, for example, implied from the increasing peaks in the spanwise velocity spectra as the gap width decreased (Figure 8.19). The fact that the mean streamwise velocity in the gap diminishes when the gap width is decreased further accentuates the coherent transport between the gap region and the subchannel centre. To illustrate this last remark, consider the motion of a fluid particle in the gap region. The larger the ratio between the spanwise and streamwise velocities, the longer this particle would be able to circulate around the vortex axis before being washed out of the channel.

It was shown earlier that the spacing of the structures, over a certain range, varied linearly with the gap width (Figure 9.6), i.e. a decrease in gap width resulted in a more closely spaced array of vortices. Therefore, there would be, at any time, a larger number of vortices per unit length along the channel. Knowing that these vortices act as flow cells bringing fluid from the subchannel centre towards the gap region, an increase in their number along the gap would tend to produce more mixing, lower fluid temperatures in the gap region and higher local heat transfer rates. In addition to this, the convection speed of the structures was observed to decrease with smaller gap widths (Figure 9.5). Using the same reasoning as in the previous paragraph, it can be seen that this results in even more lateral transport.

In summary, all of the above factors add up to somewhat counteract and compensate for the decrease in heat transfer, due to the lower mean velocities in the gap region, and the decrease in intersubchannel mixing, due to the reduced cross-sectional area between the subchannels. It is this compensating effect of the coherent structures that explains the relative insensitivity of the intersubchannel mixing to the gap size, and the relatively smaller heat transfer variation in narrow gaps compared to the variation predicted by turbulence

models based on isotropic eddy diffusivities. It is speculated here that the gap size below which the heat transfer and the mixing start to effectively decrease is the gap width for which viscous effects become important enough to hinder the coherent structures from crossing the gap. Because no experiments were presently performed with sufficiently narrow gaps, the latter hypothesis remains to be tested.

10

Conclusions and Recommendations for Further Research

10.1 Conclusions

The focus of the present study was the detailed characteristics of turbulent flow and heat transfer near narrow gaps of rod bundles. Its main accomplishments are as follows.

1. Practical empirical correlations were established for the subchannel average and the gap local heat transfer coefficients, based on experimental results available in the literature. They confirmed the weak dependence, compared to what one would expect based on turbulent diffusion alone, of the local heat transfer coefficient on the gap width .
2. A new technique, using a pendulum, for the calibration of hot-wire anemometers over low velocity ranges was developed.
3. A method for the enhancement of the results of the Variable Interval Time Average (VITA) conditional sampling technique was developed. The method not only enhanced the obtained ensemble averages, but also removed one of the major disadvantages of the VITA technique, its dependence on the threshold value.
4. The main part of the work consisted of an experimental investigation of the turbulent flow in a rectangular channel containing a circular rod, in an attempt to explain the

heat transfer relative insensitivity to the gap width. The key conclusions of this experimental investigation are listed below.

- The measured distinct distributions of the rms turbulent velocities and the turbulent shear stresses in the gap region indicate that the flow structure near the gap is far from typical "wall-turbulence".
- The distributions of the rms turbulent velocities and the turbulent shear stresses in the gap region were shown to be incompatible with the sole effects of secondary flows. In fact, the present measurements show no evidence of strong secondary flows in the gap region.
- The dominant flow patterns in the gap region were found to be large-scale, quasi-periodic, vortical structures, which were classified as coherent structures. These structures were seen to occur even for laminar flows.
- The coherent structures were likely due to the strong mean velocity differences between the open subchannel and the gap region. Previous explanations based on incompressible parallel-channel instabilities were not supported by the present results.
- A physical model of the coherent structures was formulated based on the measurements. It consists of a street of three-dimensional counter-rotating vortices with axes alternating on each side of the gap centreplane. The direction of rotation is such that the vortex front transports fluid from the open flow region towards the gap region. The vortical motions cross the gap and extend well into the opposite subchannel. In the immediate vicinity of the gap, the vortices are essentially two-dimensional and parallel to the channel plane wall. Away from the gap, the vortex perimeters curve around the rod. It was speculated, based on physical arguments, that the vortices funnel into the wall vorticity.
- The average convection speed, U_c, and the average streamwise spacing, λ, of these structures were determined as a function of the gap width. The average convection speed was found to have a value intermediate between the maximum mean speed in the neighbouring open subchannel and the mean speed in the gap centre. It decreased significantly with diminishing gap width and approached an asymptote for $W/D >$ 1.25. For rough purposes, its variation could be approximated by a fitted

exponential curve. The vortex spacing seemed to increase linearly with increasing gap width in the range $1.25 \leq W/D \leq 1.100$.

- These structures were shown to vary in size. They were approximated by a normal distribution having a standard deviation equal to 0.284 the average size.
- The phase-averaged and the time-averaged coherent and incoherent normal and shear stresses were presented for the gap region and their relative contributions to the Reynolds-averaged stresses were discussed.
- The phase-averaged incoherent stresses were found to depend on the coherent velocity field. However, the time-averaged incoherent stresses seem to match those in typical wall turbulence.
- The dependence of the intersubchannel mixing and the local heat transfer coefficient on the gap size were explained as a result of the presence of coherent structures in the gap region.

10.2 Recommendations for Further Research

The present work offered a good first step in characterizing the coherent structures that form in narrow gaps. A logical continuation of this work would be to perform experiments in rod bundles and other compound channels, in which the flow dynamical and geometrical parameters, including the channel shape, the gap width and the Reynolds number, would be systematically varied in order to determine their effects on the coherent structures. The role of the coherent structures in heat transport can also be evaluated by specially designed heated flow experiments.

On the theoretical side, it would be useful to develop quantitative models of the coherent structures and their effects, and to incorporate them in empirical correlations, for the intersubchannel mixing and the local heat transfer, and CFD codes. The Large Eddy Simulation (LES) numerical approach seems to be well suited to accommodate the effects of coherent structures. As an alternative, one may also contemplate the use finite element discretization in which the incoherent turbulence would be modelled the usual way and the coherent field would be superimposed on it as initial/boundary conditions.

References

Abdelghany, M. and Eichhorn, R., 1986, Measurements of wall shear stress in axial flow in a square lattice rectangular rod bundle, J Fluids Eng Trans ASME, 108, p 166-173.

Acrivlellis, M., 1980, Measurements by means of triple-sensor probes, J. Phys. E: Sci. Instrum., 13, p 986-992.

AGARD, 1991, Quality assessment for wind tunnel testing, AGARD Advisory Report 304, Neuilly Sur Seine, France.

Aly, A.M.M., Trupp, A.C. and Gerrard, A.D., 1978, Measurements and prediction of fully developed turbulent flow in an equilateral triangular duct, J Fluid Mech, 85, p 57-83.

Andrews, G.E., Bradley, D. and Hundy, G.F., 1972, Hot wire anemometer calibration for measurements of small gas velocities, Int J Heat Mass Transfer, 15, p 1765-1786.

Anhalt, J., 1973, Device for in-water calibration of hot-wire and hot-film probes, DISA Information, 15, p 25-26.

ANSI/ASME, 1985, Measurement uncertainty: Part 1, ANSI/ASME PTC 19.1-1985, ASME, New York, U.S.A.

Antonia, R.A. 1981, Conditional sampling in turbulence measurement, Ann Rev Fluid Mech, 13, p 131-156.

Antonia, R.A., Browne, L.W.B., Bisset, D.K. and Fulachier, L., 1987, A description of the Organized motion in the turbulent far wake of a cylinder at a low Reynolds number, J Fluid Mech, 184, p 423-444.

Arkhipov, A.P., 1984, Approximate correction for the effect of intermixing of flows in communicating subchannels on the velocity distribution over a rod bundle, Fluid Mech Sov Res, 13, p 68-73.

Aydin, M. and Leutheusser, H.J., 1980, Very low velocity calibration and application of hot-wire probes, DISA Information, 25, p 17-18.

Barbaro, M., 1988, Turbulence modelling of axial flow through a wall subchannel of a smooth rod bundle, ENEA Report RT/VEL/88/1, Bologna, Italy.

Barrow H., Hassan, A.K.A. and Avgerinos, C., 1984, Peripheral temperature variation in the wall of a noncircular duct, an experimental investigation, Int J Heat Mass Transfer, 27, p 1031-1037.

Bartzis, J.G. and Todreas, N.E., 1979, Turbulence modeling of axial flow in a bare rod bundle, J Heat Transfer Trans ASME, 101, p 628-634.

Bender, D.J. and Switick, D.M., 1968, Turbulent velocity distribution in a rod bundle, Am Soc Mech Eng Pap n° 68-WA/HT-36.

Berger, F.P. and Ziai, A., 1982, The effect of displacement and bowing in rod clusters on local heat transfer characteristics, Proc Conf ``Gas Cooled Reactors Today'', 3, p 217-222.

Berger, F.P, Erfan, A., Rapier, A.C. and Ziai, A., 1986, The effect on local heat transfer of bowing of pins in a cluster, Proc 8th Int Heat Transfer Conf, San Francisco, p 2405-2410.

Berkooz, G., Holmes, P. and Lumley, J., 1993, the proper orthogonal decomposition in the analysis of turbulent flows, Ann Rev Fluid Mech, 25, p 539-575.

Biemüller, M., Meyer, L. and Rehme, K., 1996, Large eddy simulation and measurement of the structure of turbulence in two rectangular channels connected by a gap, Engineering Turbulence Modelling and Experiments 3, Editors: Rodi, W. and Bergeles, G., p 249-258.

Bisset, D.K., Antonia, R.A. and Browne, L.W.B., 1990, Spatial organization of large structures in the turbulent far wake of a cylinder, J Fluid Mech, 218, p 439-461.

Blackwelder, R.F. and Kaplan, R.E 1976, On the wall structure of turbulent boundary layer, J Fluid Mech, 76, p 89-112.

Bobkov, V.P., Ibragimov, M.Kh., Sinyavskii, V.F. and Tychinskii, N.A., 1974, Heat exchange for flow of water in a densely packed triangular bundle of rods, Sov At Energy, 37, p 823-827.

Borishanskiy, V.M., Gotovskiy, M.A. and Firsova, E.V., 1971, The effect of pitch on heat transfer from rod clusters in longitudinal turbulent coolant flow ($Pr \geq 1$), Heat Transfer-Soviet Research, 3, p 91-99.

Borrie, J.A., 1986, Modern control systems: A manual of design methods, Prentice/Hall International, London.

Browand, F.K. and Weidman, P.D. 1976, Large scales in the developing mixing layer, J Fluid Mech, 76, p 127-144.

Brundrett, E. and Baines, W.D., 1964, The production and diffusion of vorticity in duct

flow, J Fluid Mech, 19, p 375-394.

Bruun, H.H. 1977, A time-domain analysis of the large-scale flow structure in a circular jet. Part 1. Moderate Reynolds number, J Fluid Mech, 83, p 641-671.

Bruun, H.H., 1995, Hot-wire anemometry, Oxford University Press, Oxford, England.

Bruun, H.H., Farrar, B. and Watson, I., 1989, A swinging arm calibration method for low velocity hot-wire probe calibration, Exp Fluids, 7, p 400-404.

Bürger, M., Unfried, J., Buck, M., Kullenovic, R., Rösler, S., Groll, M. and Schatz, A., 1993, Experimental examinations of the 2D-thermal-hydraulic code FRECON for single phase natural convection flows in complex structures, Nucl Eng Des, 140, p 193-209.

Butler, T.L. and Wagner, J.W., 1983, Application of a three-sensor hot-wire probe for incompressible flow, AIAA Journal, 21, p 726-732.

Cantwell, B., 1989, Future direction of turbulence research and the role of organized motion, in Whither Turbulence? Turbulence at the Crossroads, Workshop Proceedings, Ithaca, N.Y., editor: Lumley, J., p 97-131.

Carajilescov, P. and Todreas, N.E., 1976, Experimental and analytical study of axial turbulent flows in an interior subchannel of a bare rod bundle, J Heat Transfer Trans ASME, 98, p 262-268.

Cheng, S.K. and Todreas, N.E., 1986, Hydrodynamic models and correlations for bare and wire-wrapped hexagonal rod bundles - bundle friction factors, subchannel friction factors and mixing parameters, Nucl Eng Des, 92, p 227-251.

Chew, Y.T. and Ha, S.M., 1988, The directional sensitivities of crossed and triple hot-wire probes, J. Phys. E: Sci. Instrum., 21, p 613-620.

Chieng, C.C. and Lin, C., 1979, Velocity distribution in the peripheral subchannels of the CANDU-type 19 rod bundle, Nucl Eng Des, 55, p 389-394.

Christman, P.J. and Podzimek, J., 1981, Hot-wire anemometer behaviour in low velocity air flow, J Phys E: Sci Instrum, 14, p 46-51.

Colburn, A.P., 1933, A method of correlating forced convection heat-transfer data and a comparison with fluid friction, Trans Amer Inst Chem Engrs, 29.

Colburn, A.P., 1964, A method of correlating forced convection heat-transfer data and a comparison with fluid friction, Int J Heat Mass Transfer, 7, p 1359-1384.

Collingham, R.E., Yatabe, J.M., Hill, V.R. and Thorne, W.L., 1972, Experimental temperature distributions in liquid metal fast breeder reactor fuel assemblies-the effect of bowing distortion, AIChE Symposium series: Heat Transfer-Tulsa, 68, n 118, p 119-126.

Collis, D.C. and Williams, M.J., 1959, Two-dimensional convection from heated wires at low Reynolds numbers, J Fluid Mech, 6, p 357-384.

Coney, J.E.R. and Simmers, D.A., 1979, The determination of shear stress in fully developed laminar axial flow and Taylor vortex flow, using a flush-mounted hot film probe, DISA Information,24, p 9-14.

Corrsin, 1963, Turbulence: experimental methods, Handbuch der physik, vol 8, p 523-590.

D'Arcy, D.F. and Schenk, J.R., 1985, Velocity and turbulence measurements in water flowing axially through a 37-rod bundle, Int Symposium on Heat Transfer, Beijing, China.

Davies, P.O.A.L. and Yule, A.J. 1975, Coherent structures in turbulence, J Fluid Mech, 69, p 513-537.

Day, M., Sullivan, P. and Pollard A. 1993, Conditional coherent structure identification in a three-dimensional wall jet, Proc 14th Canadian Congress of Applied Mechanics, Kingston, Canada, vol 1, p 397-398.

De Lemos, M.J.S., 1988, Anisotropic turbulent transport modeling for rod-bundle, Heat Technol, 6, p 27-37.

Dingee, D.A., Bell, W.B., Chastain J.W. and Fawcett, S.L., 1955, Heat transfer from parallel rods in axial flow, Batelle Memorial Institute Report BMI-1026.

DISA, 1972, New Anemometer Calibration Equipmen,. DISA Information, 13, p 37-39.

Dittus, F.N. and Boelter, L.M.K., 1930, Heat transfer in automobile radiators of the tubular type, University of California. Berkley, Publications Engineering, 2, p 443-461.

Draycott, A. and Lawther, K.R., 1961, Improvement of fuel element heat transfer by use of roughened surfaces and the application to a 7-rod cluster, Int Dev in heat transfer, ASME, New York, p 543-552.

Eckert, E.R.G. and Irvine, Jr, T.F., 1956, Flow in corners of passages with noncircular cross sections, Trans ASME, 78, p 709-718.

Eckert, E.R.G. and Irvine, Jr, T.F., 1960, Pressure drop and heat transfer in a duct with triangular cross section, J Heat Transfer Trans ASME, 82, p 125-138.

Eifler, W. and Nijsing, R., 1967, Experimental investigation of velocity distribution and flow resistance in a triangular array of parallel rods, Nucl Eng Des, 5, p 22-42.

Eifler, W. and Nijsing, R., 1973, VELASCO - Velocity field in asymmetric rod configurations, EURATOM Report EUR 4950 e, Ispra, Italy.

El-Genk, M.S., Bedrose, S.D. and Rao, D.V., 1990, Forced and combined convection of

water in a vertical seven-rod bundle with P/D=1.38, Int J Heat Mass Transfer, 33, p 1289-1297.

El-Genk, M.S., Su, B. and Guo, Z., 1992, Forced, combined and natural convection of water in a vertical nine-rod bundle with a square lattice and P/D=1.5, AIChE Symposium series: Heat Transfer-San Diego, n 288 , 88, p 259-266.

El-Genk, M.S., Su, B. and Guo, Z., 1993, Experimental studies of forced, combined and natural convection of water in vertical nine-rod bundles with a square lattice, Int J Heat Mass Transfer, 36, p 2359-2374.

El Tahry, S., 1989, Discussion of "the role of coherent structures", in Whither Turbulence? Turbulence at the Crossroads, Workshop Proceedings, Ithaca, N.Y., editor: Lumley, J., p 170-191.

Fakory, M. and Todreas, N., 1979, Experimental investigation of flow resistance and wall shear stress in the interior subchannel of a triangular array of parallel rods, J Fluids Eng Trans ASME, 101, p 429-435.

Firsova, E.V., 1964, Heat transfer and hydraulic resistance during longitudinal flow of water along a tube bundle, USAEC Report AEC-tr-6877, p 359-362.

Galbraith, K.P. and Knudsen, J.G., 1972, Turbulent mixing between adjacent channels for single-phase flow in a simulated rod bundle, AIChE Symposium Series: Heat Transfer-Tulsa, 68 (118), p 90-100.

Gasc, B., 1966, Repartition des coefficients d'echange dans une grappe, EAES Heat Transfer Symposium on Superheated Steam or Gas, Bern, Switzerland.

Geremia, J.O., 1972, Experiments on the calibration of flush mounted film sensors, DISA Information, 13, p 5-10.

Gessner, F.B. and Jones, J.B., 1965, On some aspects of fully-developed turbulent flow in rectangular channels, J Fluid Mech, 23, p 689-713.

Gieseke, T.J. and Guezennec, Y.G., 1993, An experimental approach to the calibration and use of triple hot-wire probes, Exp Fluids, 14, p 305-315.

Gnielinski, V., 1976, New equations for heat and mass transfer in turbulent pipe and channel flow, Int Chemical Eng, 16, p 359-368.

Grimble, R.E., Bell, W.H. and Fawcett, S.L., 1954, Heat transfer and friction flow characteristics of cylindrical spacers, USAEC Report AECD-3975.

Groeneveld, D.C., 1973, Forced convective heat transfer to superheated steam in rod bundles, AECL Report, AECL-4450, Chalk River, Ontario, Canada.

Guellouz, M.S. and Tavoularis, S., 1992a, Heat transfer in rod bundle subchannels with varying rod-wall proximity, Nucl Eng Des, 132, p 351-366.

Guellouz, M.S. and Tavoularis, S., 1992b, Flow and heat transfer in rod bundles: a literature review, Technical Report UOME-BF-92-01, University of Ottawa, Ottawa, Canada.

Guellouz, M.S. and Tavoularis, S., 1995, A simple pendulum technique for the calibration of hot-wire anemometers over low-velocity ranges, Exp Fluids, 18, p 199-203.

Gunn, D.J. and Darling, C.W.W., 1963, Fluid flow and energy losses in non-circular conduits, Trans AIChE, 41, p 163-173.

Hadaller, G. and Banerjee, S., 1969, Heat transfer to superheated steam in round tubes, Atomic Energy of Canada Limited, WDI-147 Report.

Hanratty, T.J. and Campbell, J.A., 1983, Measurements of wall shear stress, in: Fluid Mechanics Measurements, editor Goldstein, R.J., Hemisphere, Washington, chapter 11, p 559-615.

Haque, M.A., Hassan, A.K.A., Turner, J.T. and Barrow, H., 1983, An observation on the origin of secondary flow in straight noncircular ducts, Wärme- und Stroffübertragung, 17, p 93-95.

Hatton, A.P., James, D.D. and Swire, H.W., 1970, Combined forced and natural convection with low-speed air flow over horizontal cylinders, J Fluid Mech, 42, p 17-31.

Haw, R.C., Ali, S.K. and Foss, J.F., 1987, Gravitationally defined velocities for a low speed hot-wire calibration, Symp on thermal anemometry (ed. Stock, D.), ASME-FED 53, p 7-14.

Haw, R.C. and Foss, J.F., 1990, A facility for low speed calibrations, Proceedings in Symp on the heuristics of thermal anemometry, ASME-FED 97, p 25-33.

Hinze, J.O., 1973, Experimental investigation on secondary currents in the turbulent flow through a straight conduit, Appl Sci Res, 28, p 453-465.

Hinze, J.O., 1975, Turbulence, Second edition, Mc Graw-Hill, New York.

Hoffman, H.W., Kidd, G.J.Jr., Lynch, F.E., Stelzman, W.J., Wantland, J.L. and Sogin, H.H., 1970, Experimental studies of the heat transfer and fluid dynamic characteristics of rod-cluster-type nuclear reactor fuel elements, ORNL 4356 Report.

Hoffman, H.J., Miller, C.W., Sozzi, G.L. and Sutherland, W.A., 1966, Heat transfer in seven-rod clusters - Influence of liner and spacer geometry on superheat fuel performance, General Electric Company, GEAP-5289 Report.

Hoffman, H.J., Wantland, J.L. and Stelzman, W.J., 1961, Heat transfer with axial flow in rod clusters, International Development in Heat Transfer, paper 65, Boulder, Colorado, p

553-560.

Hooper, J.D. , 1980, Developed single phase turbulent flow through a square-pitch rod cluster, Nucl Eng Des, 60, p 365-379.

Hooper, J.D. , 1983, The development of a large structure in the rod gap region for turbulent in line flow through closely spaced rod arrays, 4th Symposium on Turbulent shear flows, Karlsruhe, Germany, p 1.23-1.27.

Hooper, J.D. and Rehme, K., 1984, Large-scale structural effects in developed turbulent flow through closely-spaced rod arrays, J Fluid Mech, 145, p 305-337.

Hooper, J.D. and Wood, D.H., 1984, Fully developed rod bundle flow over a large range of Reynolds number, Nucl Eng Des, 83, p 31-46.

Horanyi, S., Krebs, L. and Weinkötz, G., 1989, Measurement and analysis of temperature fluctuations in the sodium-cooled 4-rod bundle TEGENA, 4th International Topical Meeting on Nuclear Reactor Thermalhydraulics: NURETH-4, Karlsruhe, Germany, p 1279-1286.

Hurst, K.S. and Rapley C.W., 1991, Turbulent flow measurements in a 30/60 degree right triangular duct, Int J Heat Mass Transfer, 34, p 739-748.

Huffman, G.D., 1980, Calibration of triaxial hot-wire probes using a numerical search algorithm, J. Phys. E: Sci. Instrum., 13, p 1177-1182.

Hussain, A.K.M.F., 1983, Coherent structures-reality and myth, Phys Fluids, 26, p 2816-2850.

Hussain, A.K.M.F. and Reynolds, W.C., 1975, Measurements in fully developed turbulent channel flow, J Fluids Eng, p 568-580.

Ibragimov, M.H., Isupov, I.A., Kobzar, L.L. and Subbotin, V.I., 1966, Calculation of the tangential stresses at the wall of a channel and the velocity distribution in a turbulent flow of liquid, Sov At Energy, 21, p 731-738.

Ibragimov, M.H., Isupov, I.A., Kobzar, L.L. and Subbotin, V.I., 1967, Calculation of hydraulic resistivity coefficients for turbulent fluid flow in channels of noncircular cross section, Sov At Energy, 23, p 1042-1047.

Ibragimov, M.H., Petrishchev, V.S. and Sabelev, G.I., 1971, Calculation of heat transfer in turbulent flow with allowance for secondary flow, Int J Heat Mass Transfer, 14, p 1033-1037.

Inayatov, A.Y., 1975, Correlation of data on heat transfer. Flow parallel to tube bundles at relative tube pitches of 1.1<s/d<1.6, Heat Transfer-Soviet Research, n3, 7, p 84-88.

Ingesson, L. and Hedberg, S., 1970, Heat transfer between subchannels in a rod bundle, 4th

International Heat Transfer Conference, 3, p 114-126.

Ingesson, L. and Kjellström, B., 1970, On gas mixing in rod bundles, Int J Heat Mass Transfer, 13, p 429-431.

Irvine, A.S., Private communication to Groeneveld [1973]. Original data in Irvine, A.S., 1961, Element spacing investigation, CGE Report R61CAD35, see also Discussion, 1961, Int. Heat Transfer Conf., ASME (J.T. Rogers, private communication).

Jeffries, R.B., 1970, Existing correlations for forced convection heat transfer to organic coolants in simple geometries- a review of world data, Atomic Energy of Canada Limited, WNRE-18 report.

Jørgensen, F.E., 1971, Directional sensitivity of wire and fiber-film probes, DISA information, 11, p 31-37.

Kacker, S.C., 1973, Some aspects of fully developed turbulent flow in non-circular ducts, J Fluid Mech, 57, p 583-602.

Kader, B.A. and Yaglom, A.M., 1972, Heat and mass transfer laws for fully turbulent wall flows, Int J Heat Mass Transfer, 15, p 2329-2359.

Kaiser, H.G. and Zeggel, W., 1987, Turbulent flows in complex rod bundle geometries numerically predicted by the use of FEM and a basic turbulence model, Nucl Eng Des, 99, p 351-363.

Kalinin, E.K., Dreyster, G.A. and Kozlov, A.K., 1969, Heat transfer in longitudinal flow through rod bundles in triangular array with different pitch-to-diameter ratios (in Russian), Inzh Fiz Zh, 6, p 47-53.

Kays, W.M. and Leung, E.Y., 1963, Heat transfer in annular passages- Hydrodynamically developed turbulent flow with arbitrarily prescribed heat flux, Int J Heat Mass Transfer, 6, p 537-557.

Kevlahan, N.K.R., Hunt, J.C.R and Vassilicos, J.C., 1994, A comparison of different analytical techniques for identifying structures in turbulence, Applied Scientific Research, 53, p 339-355.

Khalifa, M.M.A. and Trupp, A.C., 1988, Measurements of fully developed turbulent flow in a trapezoidal duct, Exp Fluids, 6, p 344-352.

Khattab, M., Mariy, A. and Habib M., 1984, Experimental heat transfer in tube bundle (Part II), Atomkernergie-Kerntechnik, 45, p 93-97.

Kim, S. and Park, G.C., 1997, Estimation of anisotropic factor and turbulent mixing rate in rod bundles based on the flow pulsation phenomenon, Nucl Technol, 117, p 340-352.

Kim, S.H. and El-Genk, M.S., 1989, Heat transfer for low flow of water in rod-bundles, Int J Heat Mass Transfer, 32, p 1321-1336.

King, L.V., 1914, On the convection of heat from small cylinders in a stream of fluid: determination of the convection constants of small platinum wires with applications to hot-wire anemometry, Phil Trans R Soc. 214A, p 373-432.

Kjellström, B., 1974, Studies of turbulent flow parallel to a rod bundle of triangular array, Report AE-487 AB Atomenergi, Sweden.

Knief, R.A., 1981, Nuclear Energy Technology, Hemisphere Publishing Corporation, New York.

Kohav, Y., Hestroni, G. and Solan, A., 1976, Velocity distribution in semiopen channels, J Fluids Eng Trans ASME, 98, p 764-766.

Kokorev, L.S., Korsun, A.S., Kostyunin, B.N. and Petrovichev, V.I., 1971, Hydraulic drag and heat transfer in turbulent flow of liquids in triangular channels, Heat Transfer-Soviet Research, 3, p 56-65.

Koziol, K., 1965, Heat transfer in turbulent flow on the shell side of nonbaffled exchangers with standard and squeezed tubes (in Polish), Chemia Stosowana, Seria B, 4, p 359-392.

Krauss, T. and Meyer, L., 1996, Characteristics of turbulent velocity and temperature in a wall channel of a heated rod bundle, Exp Thermal Fluid Sci, 12, p 75-86.

Kried, D.K., Creer, J.M., Bates, J.M., Quigley, M.S., Sutey, A.M. and Rowe, D.S., 1979, Fluid flow measurements in rod bundles using laser Doppler anemometry techniques, in: Fluid Flow and Heat Transfer over Rod or Tube Bundles, editors: Yao, S.C. and Pfund, P.A., ASME, New York, p 13-27.

Krizek, V., 1967, Strojirenstvi, 1, p 11-20.

Kutateladze, S.S. and Borishanskiy, V.M., 1966, A concise encyclopedia of heat transfer, Pergamon Press, Oxford, England.

Lau, J.C. and Fisher, M.J. 1975, The vortex street structure of 'turbulent' jets. Part 1, J Fluid Mech, 67, p 299-337.

Laufer, J., 1954, The structure of turbulence in fully developed pipe flow, NACA Report 1174.

Launder, B.E. and Ying W.M., 1972, Secondary flows in ducts of square cross-section, J Fluid Mech, 54, p 289-295.

Lawn, C.J., 1971, The determination of the rate of dissipation in turbulent pipe flow, J Fluid Mech, 48, p 477-505.

Lawson, C.G., 1971, Heat transfer from electrically heated rods during a simulated loss-of-coolant accident, AIChE Symposium series: Heat transfer aspects of commercial power generation, 67, n 119, p 1-13.

Lee, T. and Budwig, R., 1991, Two improved methods for low-speed hot-wire calibration, Meas Sci Technol, 2, p 643-646.

Lel'chuk, V.L., Shuyskaya, K.F., Sorokin, A.G. and Bragina, O.N., 1977, Heat transfer in the inlet length of fuel-elements modelling rod bundle in longitudinal air flow, Heat Transfer-Soviet Research, 9, p 100-104.

Lekakis, I.C., Adrian, R.J. and Jones, B.G., 1989, Measurement of velocity vectors with orthogonal and non-orthogonal triple-sensor probes, Exp Fluids, 7, p 228-240.

Lesieur, M., 1997, Turbulence in Fluids, Third edition, Kluwer Academic Publishers, Dordrecht, The Netherlands.

Leutheusser, H.J., 1963, Turbulent flow in rectangular ducts, J Hydraulics Division Proc ASCE, 89, p 1-19.

Levchenko, Y.D., Subbotin, V.I. and Ushakov, P.A., 1967, The distribution of coolant velocities and wall stresses in closely packed rods, Atomnaya Énergiya (English translation), 22 (3), p 262-269.

Lundberg, R.E., McCuen, P.A. and Reynolds, W.C., 1963, Heat transfer in annular passages. Hydrodynamically developed laminar flow with arbitrarily prescribed wall temperatures or heat fluxes, Int J Heat Mass Transfer, 6, p 495-529.

Marek, J., Maubach, K. and Rehme, K., 1973, Heat transfer and pressure drop performance of rod bundles arranged in square arrays, Int J Heat Mass Transfer, 16, p 2215-2228.

Maresca, M.W. and Dwyer, O.E., 1964, Heat transfer to mercury flowing in-line through a bundle of circular rods, J Heat Transfer Trans ASME, 86, p 180-186.

Markóczy, G., 1966, Heat Transfer in gas cooled clusters, EAES Heat Transfer Symposium on Superheated Steam or Gas, Bern, Switzerland.

Markóczy, G., 1972, Konvektive wärmeübertragung in längsangeströmten Stabbündeln bei turbulenter strömung I. teil: Mittelwerte über den stabumfang, Wärme- und Stoffübertragung, 5, p 204-212.

Martelli, A. and Rehme, K., 1978, Forced convection heat transfer in a rod bundle: A comparison between predictions and experimental results, Turbulent forced convection in channels and bundles, editors: Kakaç, S. and Spalding, D.B., Hemisphere Publishing Corporation, Washington, D.C., p 939-950.

McAdams, W.H., 1942, Heat Transmission, 2nd edition, Mc Graw Hill, New York, p 119.

Melling, A. and Whitelaw, J.H., 1976, Turbulent flow in rectangular duct, J Fluid Mech, 78, p 289-315.

Meyder, R., 1975, Turbulent velocity and temperature distribution in the central subchannel of rod bundles, Nucl Eng Des, 35, p 181-189.

Meyer, L., 1991, Measurements of turbulent velocity and temperature in a central channel of a heated rod bundle, Report KfK-4818, Karlsruhe, Germany.

Meyer, L. and Rehme, K., 1994, Large-scale turbulence phenomena in compound rectangular channels, Exp thermal Fluid Sci, 8, p 286-304.

Meyer, L. and Rehme, K., 1995, Periodic vortices in flow through channels with longitudinal slots or fins, 10th Symposium on turbulent shear flows, The Pennsylvania State University, University Park, August 14-16.

Miller, P., Byrnes, J.J. and Benforado, D.M., 1956, Heat transfer to water flowing parallel to a rod bundle, A.I.Ch.E. Journal, 2, p 226-234.

Mobarak, A., Sedrak, M.F. and El Telbany, M.M.M., 1986, On the direction sensitivity of hot-wire probes, Dantec Information, 2, p 7-9.

Mohanty, A.K., Haldar, S.C. and Sengupta, S., 1993, Low Reynolds number flow and heat transfer experiments in 7-rod vertical bundles, Nucl Eng Des, 143, p 83-93.

Mohanty, A.K. and Sahoo, K.M., 1988, Turbulent flow and heat transfer in rod-bundle subchannels, Nucl Eng Des, 106, p 327-344.

Moeller, R., 1989, Experimental investigations of temperature distributions and temperature fluctuations in the subchannels of the sodium-cooled four-rod bundle TEGENA 2, Exper Therm Fluid Sci, 2, p 151-164.

Möller, S.V., 1991, On phenomena of turbulent flow through rod bundles, Exper Therm Fluid Sci, 4, p 25-35.

Möller, S.V., 1992, Single-phase turbulent mixing in rod bundles, Exper Therm Fluid Sci, 5, p 26-33.

Monir, C. and Tavoularis, S., 1991, Computations of subchannel flows in a 37-rod bundle, Technical Report UOME-BF-91-09, University of Ottawa, Canada.

Monir, C. and Zeggel, W., 1990, Validation of a two-dimensional turbulent heat transport model, Thermal Hydraulics of Advanced Nuclear Reactors, ASME winter annual meeting, Dallas, Texas, p 115-123.

Nakayama, A. and Chow, W.L., 1986, Turbulent flows within straight ducts, in:

Encyclopedia of Fluid Mechanics, volume 1, editor: Cheremisinoff, N.P., Gulf Publishing Company, chapter 21, p 639-674.

Nixon, M.L., 1968, Heat transfer to water flowing turbulently in tubes and annuli, Atomic Energy of Canada Limited, CRNL-165 Report.

Ouma, B.H. and Tavoularis, S., 1991a, Turbulence structure in triangular subchannels of a reactor bundle model, Nucl Eng Des, 128, p 271-287.

Ouma, B.H. and Tavoularis, S., 1991b, Flow measurements in rod bundle subchannels with varying rod-wall proximity, Nucl Eng Des, 131, p 193-208.

Palmer, L.D., Swanson, L.L., 1961, Measurements of heat transfer coefficients, friction factors and velocity profiles for air flowing parallel to closely-spaced rods, Int Heat Transfer Conf Boulder, Colorado, paper 63.

Parette, J.R. and Grimble, R.E., 1956, Average and local heat transfer coefficients for parallel flow through a rod bundle, WAPD-TH 180 Report, Westinghouse Electric Corp, Pittsburgh.

Patel, V.C., 1965, Calibration of the Preston tube and limitations on its use in Pressure gradients, J Fluid Mech, 23, p 185-208.

Perkins, H.J., 1970, The formation of streamwise vorticity in turbulent flow, J Fluid Mech, 44, p 721-740.

Perry, A.E., 1982, Hot-wire anemometry, Oxford University Press, London.

Petukhov, B.S., 1970, Heat Transfer and friction in turbulent pipe flow with variable physical properties, Advances in Heat Transfer, 6, Academic Press, New York.

Petukhov, B.S. and Roizen, L.I., 1974, General dependencies for heat transfer in tubes of annular cross section, High Temp, 12, p 485-489; also in: Petukhov, B.S. and Roisen, L.I., 1974, Generalized dependencies for heat transfer in tubes of annular cross section, Teplofis Vysokikh Temp, 12, p 565-569.

Pichon, J., 1970, Comparison of some methods of calibrating hot-film probes in water, DISA Information, 10, p 15-21.

Presser, K.H., 1967, Wärmeübergang und druckverlust an reaktor-brennelementen in form längsangeströmter rundstabbündel, Jül-486-RB Report.

Presser, K.H., 1971, Stoffübergang und druckverlust an parallel angeströmten strabbündeln in einem grossen bereich von Reynolds-zahlen und teilungsverhältnissen, Int J Heat Mass Transfer, 14, p 1235-1259.

Preston, J.M., 1954, The determination of turbulent skin friction by means of Pitot tubes,

J Royal Aeronaut Soc, 58, p 109-121.

Prinos, P., Tavoularis, S. and Townsend, R., 1988, Turbulence measurements in smooth and rough-walled trapezoidal ducts, J Hydraul Eng, 114, p 43-53.

Ramm, H. and Johannsen, K., 1972, Hydrodynamics and heat transfer in regular arrays of circular tubes, Int Seminar on Recent Developments in Heat Exchangers, Trogir, Yugoslavia.

Ramm, H. and Johannsen, K., 1975, A phenomenological turbulence model and its application to heat transport in infinite rod arrays with axial turbulent flow, J Heat Transfer Trans ASME, 97, p 231-237.

Ramm, H., Johannsen, K. and Todreas, N.E., 1974, Single phase transport within bare rod arrays at laminar, transition and turbulent flow conditions, Nucl Eng Des, 30, p 186-204.

Rapier, A.C., 1967, Turbulent mixing in a fluid flowing in a passage of constant cross-section, TRG Report 1417 (W), UKAEA, United Kingdom.

Rapley, C.W. and Gosman, A.D., 1986, The prediction of fully developed axial turbulent flow in rod bundles, Nucl Eng Des, 97, p 313-325.

Redman, J.D., McKee, G. and Rule, I.C., 1966, The influence of surface heat flux distribution and surface temperature distribution on turbulent forced convective heat transfer in clusters of tubes in which the flow of coolant is parallel to the axes of the tubes, Proceedings of the Third Int Heat Transfer Conference, vol I, p 186-198.

Rehme, K., 1972, Pressure drop performance of rod bundles in hexagonal arrangements, Int J Heat Mass Transfer, 15, p 2499-2517.

Rehme, K., 1973, Simple method of predicting friction factors of turbulent flow in non-circular channels, Int J Heat Mass Transfer, 16, p 933-950.

Rehme, K., 1977, Anisotropic eddy viscosities in the turbulent flow through a rod bundle, 1st Symposium on Turbulent shear flows, University Park, Pennsylvania, U.S.A., p 8.41-8.48.

Rehme, K., 1978, The structure of turbulent flow through a wall subchannel of a rod bundle, Nucl Eng Des, 45, p 311-323.

Rehme, K., 1979, The structure of turbulent flow through subchannels of rod bundles, in: Fluid Flow and Heat Transfer over Rod or Tube Bundles, editors: Yao, S.C. and Pfund, P.A., ASME, New York, p 67-76.

Rehme, K., 1980, Turbulent momentum transport in rod bundles, Nucl Eng Des, 62, p 137-146.

Rehme, K., 1982, Distributions of velocity and turbulence in parallel flow along an asymmetric rod bundle, Nucl Technol, 59, p 148-159.

Rehme, K., 1985, The structure of turbulent flow through rod bundles, 3rd International Topical Meeting on Nuclear Reactor Thermalhydraulics: NURETH-3, Newport, Rhode Island, U.S.A, p 16.A.1-16.A.8.

Rehme, K., 1987a, The structure of turbulent flow through rod bundles, Nucl Eng Des, 99, p 141-154.

Rehme, K., 1987b, Turbulent flow through two asymmetric rod bundles, Heat Technol, 5, p 19-37.

Rehme, K., 1987c, The structure of turbulence in wall subchannels of a rod bundle, Atomkernenergie Kerntechnik, 49, p 145-150.

Rehme, K., 1987d, On the development of turbulent flow in wall subchannels of a rod bundle, Nucl Technol, 77, p 331-342.

Rehme, K., 1987e, Convective Heat Transfer over Rod Bundles, chapter 7, Handbook of Single Phase Convective Heat Transfer, editors: Kakaç, S., Shah, R.K. and Aung, W., Wiley-Interscience.

Rehme, K., 1988, Experimental observations of turbulent flow through wall subchannels of rod bundles, First World Conference on Experimental Heat Transfer, Fluid Mechanics and Thermodynamics, Dubrovnik, Yugoslavia, p 1705-1711.

Rehme, K., 1989, Experimental observations of turbulent flow through subchannels of rod bundles, Exper Therm Fluid Sci, 2, p 341-349.

Rehme, K., 1992, The structure of turbulence in rod bundles and the implications on natural mixing between the subchannels, Int J Heat Mass Transfer, 35, p 567-581.

Renksizbulut, M. and Hadaller, G.I., 1986, An experimental study of turbulent flow through a square-array rod bundle, Nucl Eng Des, 91, p 41-55.

Reynolds, W.C., Lundberg, R.E. and McCuen, P.A., 1963, Heat transfer in annular passages. General formulation of the problem for arbitrarily prescribed wall temperatures or heat fluxes, Int J Heat Mass Transfer, 6, p 483-493.

Rieger, M., 1969a, Etude éxperimentale du transfert de chaleur dans des faiseaux tubulaires en écoulement paralléle pour une densité du flux thermique constante dans le domaine des nombres de Prandlt moyen, Commissariat à l'énergie atomique, Report CEA-R-3599.

Rieger, M., 1969b, Experimentelle untersuchung des wärmeübergangs in parallel Durchströmten rohbündeln bei konstanter wärmestromdichte im bereich mittlerer Prandtl-zahlen, Int J Heat Mass Transfer, 12, p 1421-1447.

Roberson, J.A. and Crowe, C.T., 1985, Engineering Fluid Mechanics, Third edition, Houghton Mifflin Company, Boston, p 336.

Rogers, J.T., 1983, Comments on the effect of subchannel shape on heat transfer in rod bundles with axial flow, Int J Heat Mass Transfer, 26, p 1417-1418.

Rogers, J.T. and Chapman, T.M., 1963, The effect of element spacing on local heat transfer coefficients in rod bundles in an organic coolant, Canadian General Electric, R63CAP49 Report.

Rogers, J.T. and Rosehart, R.G., 1972, Mixing by turbulent interchange in fuel bundles. correlations and inferences, Am Soc Mech Eng Pap n°72-HT53.

Rogers, J.T. and Tahir, A., 1975, Turbulent interchange mixing in rod bundles and the role of secondary flows, Am Soc Mech Eng Pap n°75-HT31.

Rogers, J.T. and Tarasuk, W.R., 1967, Natural mixing of coolant in close-packed nuclear reactor fuel bundles, Canadian Congress of Applied Mechanics, Quebec, Canada.

Rogers, J.T. and Todreas, N.E., 1968, Coolant interchannel mixing in reactor fuel rod bundles single-phase coolants, ASME Annual Winter Meeting, New York, U.S.A.

Rowe, D.S., Johnson, B.M. and Knudsen, J.G., 1974, Implications concerning rod bundle crossflow mixing based on measurements of turbulent flow structure, Int J Heat Mass Transfer, 17, p 407-419.

Salikov, A.P., Polynovskij, Y.L. and Belyakov, K.I., 1967, Investigation of heat transfer and pressure drop of axial flow through smooth rod bundles (in Russian), Teploenergetica, 1, 13-17.

Salzer, H.E., 1960, A note on the solution of quartic equations, Mathematics of computation, 14, p 279-281.

Samet, M. and Einav, S., 1985, Directional sensitivity of unplated normal-wire probes, Rev Sci Instrum, 56, p 2299-2305.

Seale, W.J., 1979a, Turbulent diffusion of heat between connected flow passages, Nucl Eng Des, 54, p 183-195.

Seale, W.J., 1979b, Turbulent diffusion of heat between connected flow passages, Nucl Eng Des, 54, p 197-209.

Seale, W.J., 1981, The effect of subchannel shape on heat transfer in rod bundles with axial flow, Int J Heat Mass Transfer, 24, p 768-770.

Seale, W.J., 1982, Measurements and predictions of fully developed turbulent flow in a simulated rod bundle, J Fluid Mech, 123, p 399-423.

Seider, E.N. and Tate, G.E., 1936, Heat transfer and pressure drops of liquids in tubes, Industrial and Engineering chemistry, 28, p 1429.

Simonek, J., 1966, Heat transfer in a rod-type heat-producing cell, Jaderna Energie, 12, p 246-249.

Singh, K. and St. Pierre, C.C., 1972, Single phase turbulent mixing in simulated rod bundle geometries, Trans Can Soc Mech Eng, 1, p 73-80

Skinner, V.R., Freeman, A.R. and Lyall, H.G., 1969, Gas mixing in rod clusters, Int J Heat Mass Transfer, 12, p 265-278.

Slagter, W., 1978, Finite element analysis for turbulent flows of incompressible fluids in fuel rod bundles, Nucl Sci Eng, 66, p 84-92.

Slagter, W., 1988, Finite element, stream function-vorticity solution of secondary flow in the channels of a rod bundle, Int J Numer Methods Fluids, 8, p 687-704.

Sparrow, E.M., Loeffler, A.L.JR. and Hubbard, H.A., 1961, Heat transfer to longitudinal laminar flow between cylinders, J Heat Transfer Trans ASME, 83, p 415-422.

Speziale, C.G., 1986, The Dissipation rate correlation and turbulent Secondary flows in noncircular ducts, J Fluid Eng Trans ASME, 108, p 118-120.

Su, B. and El-Genk, M.S., 1993, Forced convection of water in rod-bundles, Int Comm Heat Mass Transfer, 20, p 295-300.

Subbotin, V.I., 1974, Heat exchange and hydrodynamics in channels of complex geometry, Heat Transfer 1974, Proc 5th Int Heat Transfer Conf, Tokyo, vol VI, p 89-104.

Subbotin, V.I., Ushakov, P.A., Levchenko, Y.D. and Aleksandrov, A.M., 1971, Velocity fields in turbulent flow past rod bundles, Heat Transfer Sov Res, 3 (2), p 9-35.

Subramanian, C.S., Rajagopalan, S., Antonia, R.A. and Chambers, A.J., 1982, Comparison of conditional sampling and averaging techniques in a turbulent boundary layer, J Fluid Mech, 123, p 335-362.

Šulc, V., 1989, Experimental study of temperature fields in the fast reactor fuel assemblies with regular and deformed rod bundle geometry and partially blocked flow section, NURETH-4, Karlsruhe, Germany, p 1313-1318.

Sutherland, W.A., Kays, W.M., 1966, Heat transfer in parallel rod arrays, J Heat Transfer Trans ASME, 88, p 117-124.

Sutherland, W.A., 1968, Experimental heat transfer in rod bundles, ASME Annual Winter Meeting, New York, U.S.A.

Tabatabai, M., Pollard, A. and McPhail, A., 1986. A device for calibrating hot-wire probes at low velocities, J Phys E: Sci Instrum, 19, p 630-632.

Tachibana, F., Oyama, A., Akiyama, M. and Kondo, S., 1969, Measurements of heat transfer coefficients for axial air flow through eccentric annulus and seven-rod cluster, J Nucl Sci Technol, 6, p 207-214.

Tahir, A. and Rogers, J.T., 1979, The mechanism of secondary flows in turbulent interchange in rod bundles, 7th Canadian Congress of Applied Mechanics, Sherbrooke, Canada.

Tahir, A. and Rogers, J.T., 1986, Turbulent flow structure in a closely-spaced triangular-array rod bundles, 8th International Heat Transfer Conference, San Francisco, California, U.S.A.

Tapucu, A., 1977, Studies on diversion cross-flow between two parallel channels communicating by a lateral slot. I: transverse flow resistance coefficient, Nucl Eng Des, 42, p 297-306.

Tapucu, A. and Merilo, M., 1977, Studies on diversion cross-flow between two parallel channels communicating by a lateral slot. II: axial pressure variations, Nucl Eng Des, 42, p 307-318.

Tavoularis, S., 1978, Experiments in turbulent transport and mixing, PhD thesis, Johns Hopkins University, Baltimore, Maryland, U.S.A.

Tavoularis, S., 1983, Simple corrections for the temperature sensitivity of hot wires, Rev Sci Instrum, 54, p 741-743.

Tavoularis, S. and Corrsin, S., 1981, Experiments in nearly homogeneous turbulent shear flow with uniform mean temperature gradient: Part 1, J Fluid Mech, 104, p 311-347.

Tavoularis, S. and Corrsin, S. 1987, The structure of a turbulent shear layer embedded in turbulence, Phys. Fluids, 3, p 3025-3033.

Tavoularis, S., Stapountzis, H., 1983, Subchannel flow visualization in a nuclear reactor fuel bundle, Flow Visualization III, Proceedings of the third International Symposiun on flow visualization, Sept 6-9, University of Michigan, Ann Arbor, Michigan, editor: Yang, W.J., p 777-781.

Tavoularis, S., Sitaraman, S. and Prinos, P., 1988, Measurement of turbulent flow in rod bundle subchannels, Int J Eng Fluid Mech, 1, p 471-494.

Tavoularis, S., Sitaraman, S. and Stapountzis, H., 1984, Subchannel flow visualization and measurement in a model of the 37-rod CANDU reactor fuel bundle, Technical Report UOME-BF-8406, University of Ottawa, Ottawa, Canada.

Taylor, M.F., 1967, A method of correlating local and average friction coefficients for both laminar and turbulent flow of gases through a smooth tube with surface to fluid bulk temperature ratios from 0.35 to 7.35, Int J Heat Mass Transfer, 10, p 1123-1128.

Todreas, N.E. and Kazimi, M.S., 1989, Nuclear systems I: thermal hydraulic fundamentals, chapter 10, Hemisphere Publishing Corporation, New York.

Tracy, H.J., 1965, Turbulent flow in a three-dimensional channel, J Hydraulics division Proc ASCE, 91, p 9-35.

Trupp, A.C and Aly, A.M.M., 1979, Predicted secondary flows in triangular array rod bundles, J Fluids Eng Trans ASME, 101, p 354-363.

Trupp, A.C. and Azad, R.S., 1975, The structure of turbulent flow in triangular array rod bundles, Nucl Eng Des, 32, p 47-84.

Tsanis, I.K., 1987, Calibration of hot-wire Anemometers at very low velocities. DANTEC Information, 4, p 13-14.

Vasilevich, O.S., Kolykhan, L.I. and Sheynina, A.V., 1983, Experimental study of heat transfer and hydraulic resistance in rod bundles, Akad Nauk Belorusskoj SSR, Vesti Akad Navuk BSSR, Ser Fiz-energet Navuk, Minsk, 1, p 107-111.

Vonka, V., 1988a, Measurement of secondary flow vortices in a rod bundle, Nucl Eng Des, 106, p 191-207.

Vonka, V., 1988b, Turbulent transports by secondary flow vortices in a rod bundle, Nucl Eng Des, 106, p 209-220.

Wagner, T.C. and Kent, J.C., 1988, On the directional sensitivity of hot-wires: a new look at an old phenomenon, Exp Fluids, 6, p 553-560.

Wallace, J.M., Brodkey, R.S. and Eckelmann, H. 1977, Pattern-recognized structures in bounded turbulent shear flows, J Fluid Mech, 83, p 673-693.

Wantland, J.L., 1956, Compact tubular heat exchangers, Reactor Heat Transfer Conference, New York, Part 1, Book 2, p 525-548.

Weisman, J., 1959, Heat transfer to water flowing parallel to tube bundles, Nucl Sci Eng, 6, p 78-79.

Winant, C.D. and Browand, F.K. 1974, Vortex pairing: the mechanism of turbulent mixing-layer growth at moderate Reynolds number, J Fluid Mech, 63, p 237-255.

Winterton, R.H.S., 1981, Thermal design of nuclear reactors, chapter 4, Pergamon Press, Oxford, England.

Wu, R.S. and Rehme, K., 1990, An experimental investigation on turbulent flow through symmetric wall-subchannels of two rod bundles, Nucl Technol, 89, p 103-115.

Wu, X. and Trupp, A.C., 1993, Experimental study on the unusual turbulence intensity distributions in rod-to-wall gap regions, Exp Thermal Fluid Sci, 6, p 360-370.

Wu, X. and Trupp, A.C., 1994, Spectral measurements and mixing correlation in simulated rod bundle subchannels, Int J Heat Mass Transfer, 37, p 1277-1281

Wyngaard, J.C., 1969, Spatial resolution of the vorticity meter and other hot-wire arrays, J Sci Instr, 2, p 983.

Yuan, Y.M. and Mokhtarzadeh-Dehghan, M.R., 1994, A comparison study of conditional-sampling methods used to detect coherent structures in turbulent boundary layers, Phys Fluids, 6, p 2038-2057.

Yueh, Y.S. and Chieng, C.C., 1987, On the calculation of flow and heat transfer characteristics for CANDU-type 19-rod fuel bundles, J Heat Transfer Trans ASME, 109, p 590-598.

Zabat, M., Browand, F.K., Plocher, D., 1992, In-situ swinging arm calibration for hot-film anemometers, Exp Fluids, 12, p 223-228.

Zeggel, W. and Monir, C., 1989, Prediction of natural mixing in tightly packed 7-rod-bundles (P/D=1.10), Fourth Int Topical Meeting on Nuclear Reactor Thermal-Hydraulics, Karlsruhe, Germany, p 1294-1302.

Table 2.1: Summary of computational investigations of rod bundle flows

Author(s)	Year	Turbulence Model	Technique
Bender & Switick	1968	Zero-Equation Model (ZEM), mixing length hypothesis	Finite difference
Eifler & Nijsing	1973	ZEM, prescribed radial profiles and azimuthal eddy diffusivities	Velasco code
Meyder	1975	ZEM, mixing length hypothesis, isotropic and anisotropic eddy diffusivities	Finite difference (curvilinear orthogonal coordinates)
Ramm & Johannsen	1975	ZEM, phenomenological model	Radial integration
Carajilescov & Todreas	1976	One-Equation Model (OEM)	Finite difference
Slagter et al	1978	ZEM, modified mixing length hypothesis	Finite element
Slagter	1978		
Bartzis & Todreas	1979	Two-Equation Model (TEM)	Finite difference
Seale	1979b	TEM, k-ϵ, isotropic and anisotropic eddy diffusivities	Finite difference
Trupp & Aly	1979	OEM	Finite difference
Seale	1982	TEM, k-ϵ model	Finite difference
Slagter	1982	OEM, anisotropic eddy diffusivities	Finite element
Rapley & Gosman	1986	Algebraic stress model, k-ϵ model, wall functions	Finite element
Kaiser & Zeggel	1987	ZEM, algebraic model for k, l and the eddy diffusivity	Finite element
Yueh & Chieng	1987	TEM, standard k-ϵ model	Finite difference
Barbaro	1988	TEM, k-ϵ model	Finite difference
De Lemos	1988	Algebraic stress model	Radial integration
Mohanty & Sahoo	1988	ZEM, two-dimensional eddy diffusivity model	Finite difference
		OEM, k-l model	
Slagter	1988	OEM	Finite element
Zeggel & Monir	1989	ZEM, correlation for the turbulent Prandtl number	Finite element
Monir & Zeggel	1990		
Monir & Tavoularis	1991	ZEM	Velasco code

Table 2.2: Summary of experimental investigations of rod bundle flows

Author(s)	Year	Array Geometry	Subchannel Type	P/D	W/D	Re $\times 10^{-3}$
Gunn & Darling	1963	square/triangular	corner	-	1.00	0.20 to 100
		square/triangular	wall	-	1.00	
		square	inner	1.00 1.22	- 1.11	
Palmer & Swanson	1963	triangular	inner	1.015	-	20
Eifler & Nijsing	1967	triangular	inner	1.00, 1.05, 1.10 & 1.15	-	15, 30 & 50
Levchenko et al	1967	triangular	inner	1.00	-	13.2 to 46.3
Presser	1971	triangular	inner	1.00, 1.02, 1.05, 1.20 & 1.67	-	0.20 to 200
Subbotin et al	1971	triangular	inner	1.05, 1.10 & 1.20	-	50
Galbraith & Knudsen	1972	square	inner	1.011 to 1.30	-	8 to 30
Rehme	1972	triangular	-	1.025 to 2.324	=P/D	0.60 to 500
Marek et al	1973	square	-	1.283	variable	10 to 300
Kjellström	1974	triangular	inner	1.22	-	37 to 150
Rowe et al	1974	square	central & wall	1.250 1.125	1.250	50 to 200
Rogers & Tahir	1975	triangular	inner	1.03 to 1.40	-	8.1 to 49.5
Trupp & Azad	1975	triangular	inner	1.20, 1.35 & 1.50	-	12, 84
Carajilescov & Todreas	1976	triangular	inner	1.123	-	27
Kohav et al	1976	Square	inner	1.1, 1.2 & 1.3	-	38 to 116

Author(s)	Year	Array Geometry	Subchannel Type	P/D	W/D	Re $\times 10^{-3}$
Rehme	1978 1979 1980 1982 1987a 1987b 1987c 1987d 1988 1989	triangular/square	wall	1.036 to 1.420	1.026 to 1.420	50 to 200
Chieng & Lin	1979	square/ triangular	wall	1.156	1.156	189
Fakory & Todreas	1979	triangular	inner	1.1	-	9 to 36
Seale	1979a	triangular/ square	wall	1.10, 1.375 & 1.833	1.185, 1.40 & 1.875	35 to 300
Tahir & Rogers	1979	triangular	inner	1.06	-	36
Hooper	1980	square	inner	1.194 & 1.107	-	48
Seale	1982	square/ traingular	wall	1.20	1.30	200
Hooper	1983	square	inner	1.107 1.194	-	22.6 to 207.6
Hooper & Rehme	1984	triangular /square	wall	1.071 &1.036	1.026 to 1.118	54.6 to 107
		square	inner	1.107 &1.194	-	22.6 to 207.6
Abdelghani & Eichhorn	1986	square	wall/inner/corner	4/3	2/3	67 & 79.2
Renksizbulut & Hadaller	1986	square	inner/wall/corner	1.150	1.123	500
Tahir & Rogers	1986	triangular	inner	1.06	-	36
Tavoularis et al	1988	square	inner	1.140	1.149	50 to 110
Vonka	1988a	triangular	inner	1.3	-	60 & 175
Moeller	1989	square/ triangular	wall	1.147	1.147	4 to 70
Wu & Rehme	1990	triangular/square	wall	1.148	1.045 1.074	61.1 70.7
Meyer	1991	triangular	inner	1.12	-	66
Möller	1991	triangular/ square	wall	1.072	1.072	20 to 150
Ouma & Tavoularis	1991a	triangular	inner	1.140	1.00 to 1.149	48

Author(s)	Year	Array Geometry	Subchannel Type	P/D	W/D	Re $\times 10^{-3}$
Ouma & Tavoularis	1991b	triangular	wall/inner	1.140	1.00 to 1.149	48
Guellouz & Tavoularis	1992	triangular	wall/inner	1.140	1.00 to 1.149	48

Table 3.1: Heat transfer correlations for circular tubes under fully developed conditions (from Todreas and Kazimi [1989] and Groeneveld [1973])

Reference	Re	Pr	Expression	Comments
Dittus and Boelter [1930]	$>10^4$	>0.7 $<100.$	$Nu=0.023\ Re^{0.8}Pr^{0.4}$ $Nu=0.023\ Re^{0.8}Pr^{1/3}$	Heating cooling liquid properties evaluated at the bulk temperature.
Colburn [1933]:	$>10^4$	>0.7 $<100.$	$Nu=0.023\ Re^{0.8}Pr^{1/3}$	Fluid properties evaluated at the film temperature.
Seider and Tate [1936]	$>10^4$	>0.7 $<120.$	$Nu=0.023\ Re^{0.8}Pr^{0.4}(\mu_W/\mu)^{0.14}$	Fluid properties evaluated at the bulk temperature.
Kutateladze and Borishanskiy [1966]	-	-	$Nu=0.023\ Re^{0.8}Pr^{0.4}(T_b/T_w)^{0.55}$	For gases Fluid properties evaluated at the bulk temperature.
Nixon [1968]	$>10^4$ $<327\times10^4$	-	$Nu=0.024\ Re^{0.77}Pr^{0.57}$	For Water Fluid properties evaluated at the film temperature.
Hadaller and Banerjee [1969]	$>6\times10^4$ $<6\times10^5$	-	$Nu=0.0101Re^{0.8744}Pr^{0.6112}(L/D_e)^{-0.0328}$	For superheated steam Fluid properties evaluated at the film temperature.
Jeffries [1970]	$>10^4$ $<5\times10^5$	-	$Nu=0.0243\ Re^{0.8}Pr^{0.4}$	For Organic coolants Fluid properties evaluated at the bulk temperature.

Table 3.2: Summary of experimental investigations of heat transfer in rod bundles[1]

Reference	Geometry	Number of rods	P/D	W/D	Medium	Re $\times 10^{-3}$	Comments
Miller et al [1956]	T; I	37 (∞)	1.462	-	Water	70 to 700	18 partial rods on the channel wall. 1 heated rod.
Wantland [1956]	T; I S; I	102 100	1.190 1.106	-	Water Water	5 to 16 5 to 16	Hexagonal channel.
Hoffman et al [1961]	T; I	7	1.45	-	Air	75	-
Palmer & Swanson [1961]	T; I	7 (∞)	1.015	-	Air	10 to 60	Heated strip on one rod. Hexagonal channel.
Rogers & Chapman [1963]	T; I	4	1.05, 1.08	-	Organic	18 to 110	2 heated rods and 2 dummy in a circular channel.
Firsova [1964]	T; I	7	1.2	-	Water	13 to 30	-
Hoffman et al [1966]	T; I	7	1.141	-	Air	5 to 2000	2 channels used: one circular and the other scalloped around the rods.
Gasc [1966]	T; I	19	1.25, 1.31	-	Air	150	-
Markóczy [1966]	-; I	19	1.19, 1.36, 1.52, 1.66	-	Air	60, 115, 185, 170	-
Redman et al [1966]	T; I	3	1.00, 1.10, 1.25, 1.50	-	Air	119 to 470	-
Simonek [1966]	T; I	163	1.4	-	Air, CO_2	200 to 700	-
Sutherland & Kays [1966]	T; I	6 (∞)	1.15, 1.25	-	Air	7 to 200	-
Rieger [1969]	T; I	31	1.25, 1.6	-	water, water+ glycol	10 to 200	-
Hoffman et al [1970]	T; I	7	1.26	-	Air	38 to 63	-
Borishanskiy et al [1971]	T; I	7, 7, 7 & 19	1.1, 1.3, 1.4 & 1.5	-	Water	10 to 400	-
Presser [1971]	T; I	(∞)	1.00, 1.02, 1.05, 1.20 & 1.67	-	Air	0.20 to 200	Different test sections for each P/D. Mass transfer measurements.
Marek et al [1973]	S; I,W	9, 16(∞)	1.283	1.23, 1.27	Helium	10 to 300	Square channels: one smooth and the other with 12 dummy rods.
Lel'chuk et al [1977]	T; I	7	1.17	-	Air	18 to 73	Hexagonal channel.
Berger & Ziai [1982]	Annulus T; I,W	- 17	- 1.0 to1.456	1. to 1.45 1. to 1.41	Aqueous solution	20 to 200 20 to 200	Used an electrochemical technique.
Kim & El-Genk [1989]	T; I	7	1.25,1.38, 1.50	-	Water	0.08 to 50	The hexagonal channel size was selected to provide the same flow area per heated rod.
Šulc [1989]	T; I,W	16	1.17	1.085	Sodium	-	Lozenge shaped channel.
El-Genk et al [1990]	T; I	7	1.38	-	Water	1.2 to 25	same as Kim &El-Genk [1989].
El-Genk et al [1992]	S; I	9	1.5	-	Water	0.3 to 25	Square channel.
El-Genk et al [1993]	S; I	9	1.25, 1.38 & 1.5	-	Water	0.25 to 30	Square Channel.
Guellouz & Tavoularis [1992]	T; W	5	1.14	1.00 to 1.149	Air	48	Heated strip on one rod. Trapezoidal outer sector of a CANDU 37-rod bundle.

[1] T and S refer to triangular and square arrays respectively. I and W refer to inner and wall subchannels respectively.

Table 3.3: Compilation of the *J*-factor from available heat transfer literature

Reference	Symbol	P/D	*J*	Re ×10^{-3}	Comments
Miller et al [1956]	●	1.462	1.0	70 to 700	-
Hoffman et al [1961]	●	1.45	0.96	75	-
Palmer & Swanson [1961]	●	1.015 1.015	0.51 0.68	10 50	Heated strip on one rod.
Rogers & Chapman [1963]	*	1.05 1.05 1.08 1.08	0.606 0.615 0.820 0.810	50 100 50 100	-
Firsova [1964]	●	1.2	1.0	10	Based on: No variation of heat transfer around the rod periphery
Hoffman et al [1966]	□	1.141	0.850 0.831 0.792 0.807 0.844	8.3 16.6 39.0 82.0 188.0	circular channel
	▲	1.141	0.928 0.920 0.957 0.918 0.946	8.0 16.2 36.6 85.2 132.1	channel scalloped around the rods.
Gasc [1966]	■	1.25 1.31	0.945 0.975	150	-
Markóczy [1966]	▽	1.192 1.363 1.521 1.658	0.89 0.95 0.94 0.98	30 to 60 115 185 170	-
Redman et al [1966]	◇	1.10 1.25 1.25 1.50 1.50	0.85 0.98 0.98 1.00 1.00	223-369 310.8 470.1 119.2 226.1	-
Hoffman et al [1970]	●	1.26	0.95	50	-
Presser [1971]	*	1.02 1.02 1.05 1.05 1.05 1.20	0.490 0.516 0.768 0.811 0.844 0.978	26 41 18 50 80 6 to 30	Mass transfer measurements.
Irvine	▼	1.047 1.043 1.030 1.026 1.049 1.043 1.031 1.026 1.014 1.014 1.052 1.051 1.037 1.031 1.030 1.016 1.016 1.019 1.012 1.012 1.012 1.018 1.023 1.028 1.028 1.028 1.030 1.033 1.045 1.052 1.056 1.059	0.896 0.886 0.769 0.776 0.908 0.851 0.891 0.768 0.791 0.655 0.961 0.964 0.929 0.779 0.901 0.793 0.815 0.745 0.765 0.802 0.752 0.886 0.894 0.886 0.930 0.761 0.921 0.846 0.957 0.958 0.957 0.957	80 165 215 250	From Figure 22 of Groeneveld [1973]
Berger & Ziai [1982]	○	1.023 1.042 1.070 1.107 1.176 1.255 1.362 1.464	0.75 0.85 0.88 0.91 0.94 0.96 0.99 1.00	100	Used an electrochemical technique. Annulus data.

Reference	Symbol	P/D	J	Re $\times 10^{-3}$	Comments
Guellouz & Tavoularis [1992]	▵	1.015 1.030 1.045 1.059 1.074 1.089 1.104 1.119 1.134 1.149	0.7567 0.7899 0.8697 0.8660 0.8790 0.8950 0.9025 0.9067 0.9118 0.9097	48	Heated strip on one rod. Rod-wall gap.

Table 7.1: Estimates of the exponent, n, of the modified King's law.

Author(s)	*U [m/s]*	*Re*	*n*	Comments
Collis & Williams (1959)	0.11 to 241	0.02 to 44	0.45	
Hatton et al. (1970)	< 219	< 40	0.494	
Andrews et al. (1972)	0.11 to 121	0.02 to 22	0.45	
Haw et al. (1987)	0.5 to 5.6	0.09 to 1	0.45	Observed deviation from calibration curve in the range 0.05 to 0.22 *m/s*
Aydin & Leutheusser (1980)	0.05 to 0.7 0.7 to 3	0.01 to 0.13 0.13 to 0.55	0.80 0.40	
Tsanis (1987)	0 to 0.2 0.05 to 0.7 0.7 to 3	0 to 0.04 0.01 to 0.13 0.13 to 0.55	1.0 0.60 0.41	
Bruun et al. (1988)	1 to 6	0.18 to 1.08	0.40	
Bruun et al. (1989)	1.2 to 6.5	0.22 to 1.19	0.44	Assumed $A=0.8E_o^2$

Table 7.2: Conditions and results of calibrations covering different velocity ranges.

Case #	r_m [m]	r_1 [m]	r_2 [m]	θ_e [°]	U_{max} [m/s]	Re_{max} [-]	α_{max} [S.I.]	A [S.I.]	B [S.I.]	n [-]	ϵ [m/s]
1	1.378	1.124	0.870	90	4.80	0.87	0.00015	8.314	4.470	0.41	0.037
2	1.378	0.870	0.616	20	0.80	0.15	0.00013	9.388	3.045	0.66	0.027
3	1.378	0.489	0.362	20	0.45	0.08	0.00012	9.418	3.650	0.84	0.008

Table 7.3: Characteristic angles and coefficients of the AUSPEX AVE-3-102 three sensor probe

Sensor	**δ**	**α**	**k^2**	**h^2**
red	0° (reference)	45°	0.187	1.399
white	121°	42.5°	0.077	1.296
blue	120°	39°	0.122	1.307

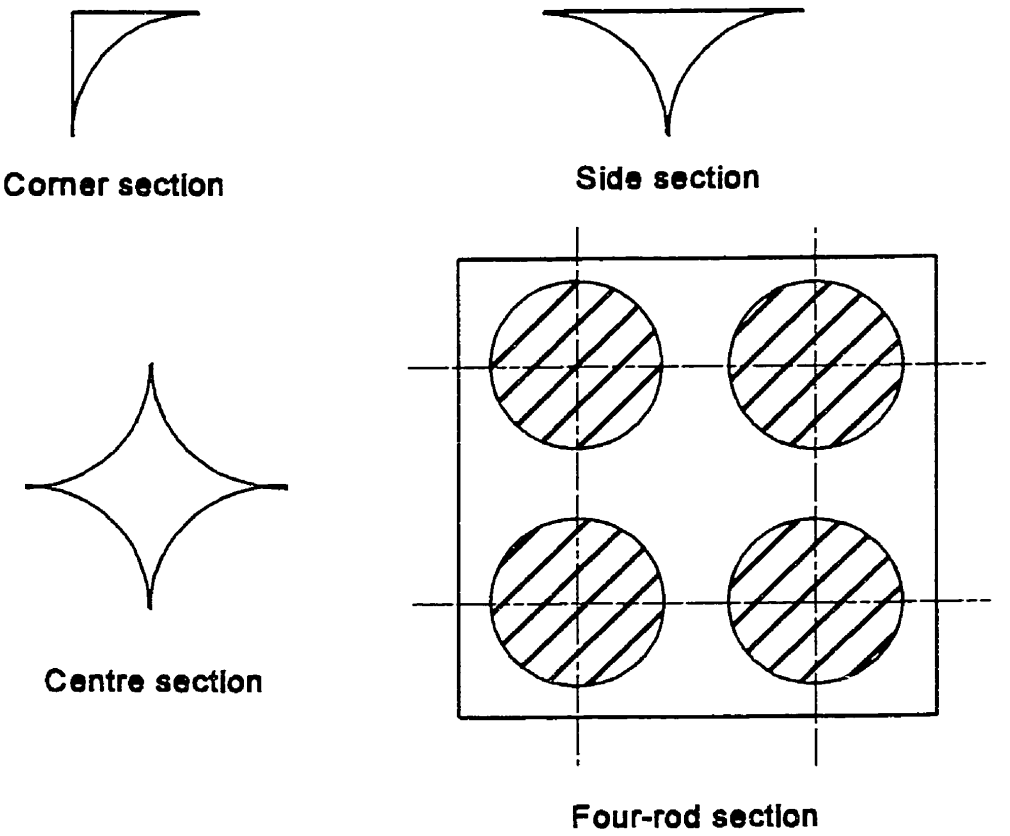

Figure 2.1 Test sections of Gunn and Darling [1963].

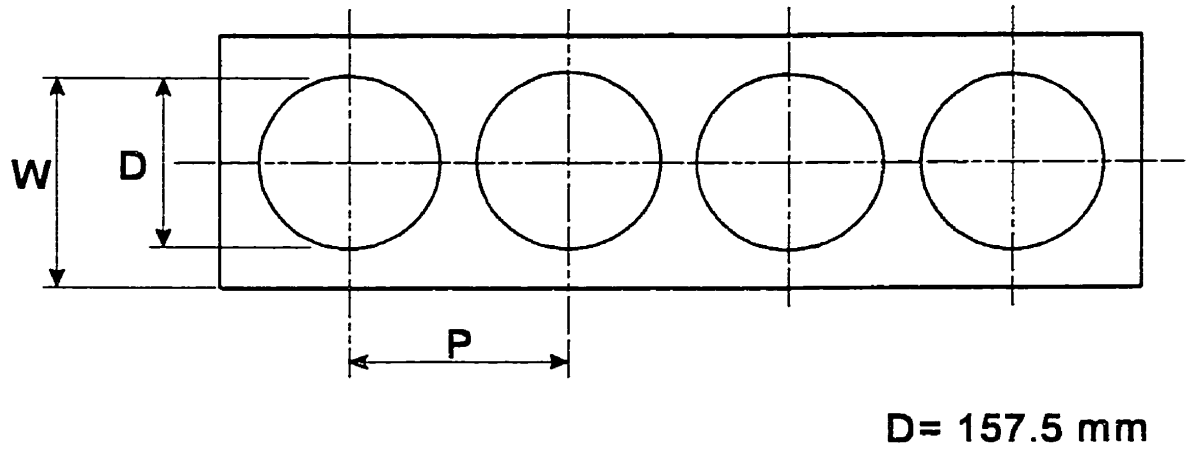

Figure 2.2 Test section of Rehme.

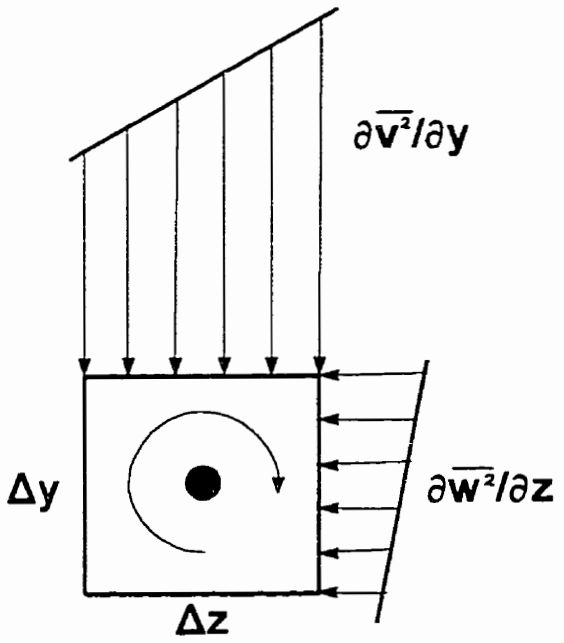

Figure 2.3 Mechanism of vorticity production (from Perkins, 1970).

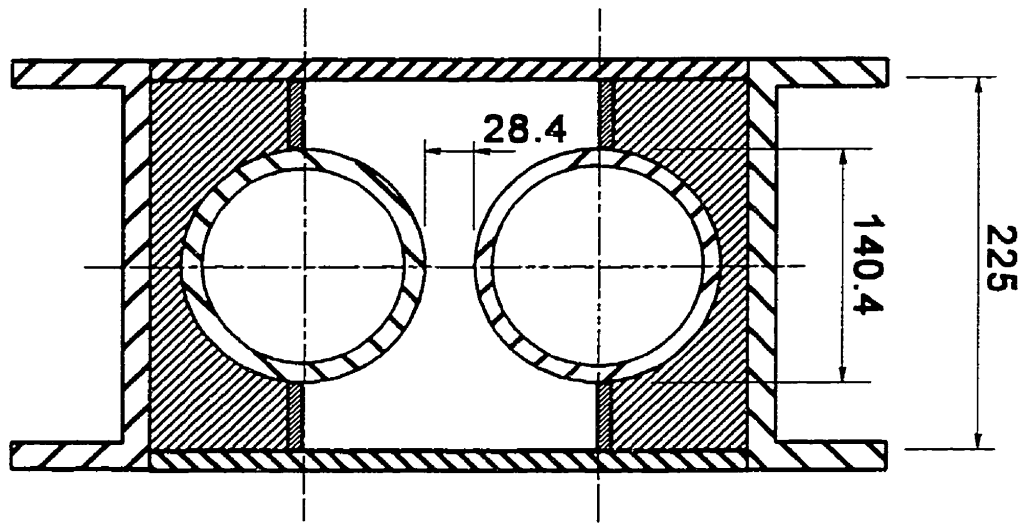

Figure 2.4 Test section of Seale [1982].

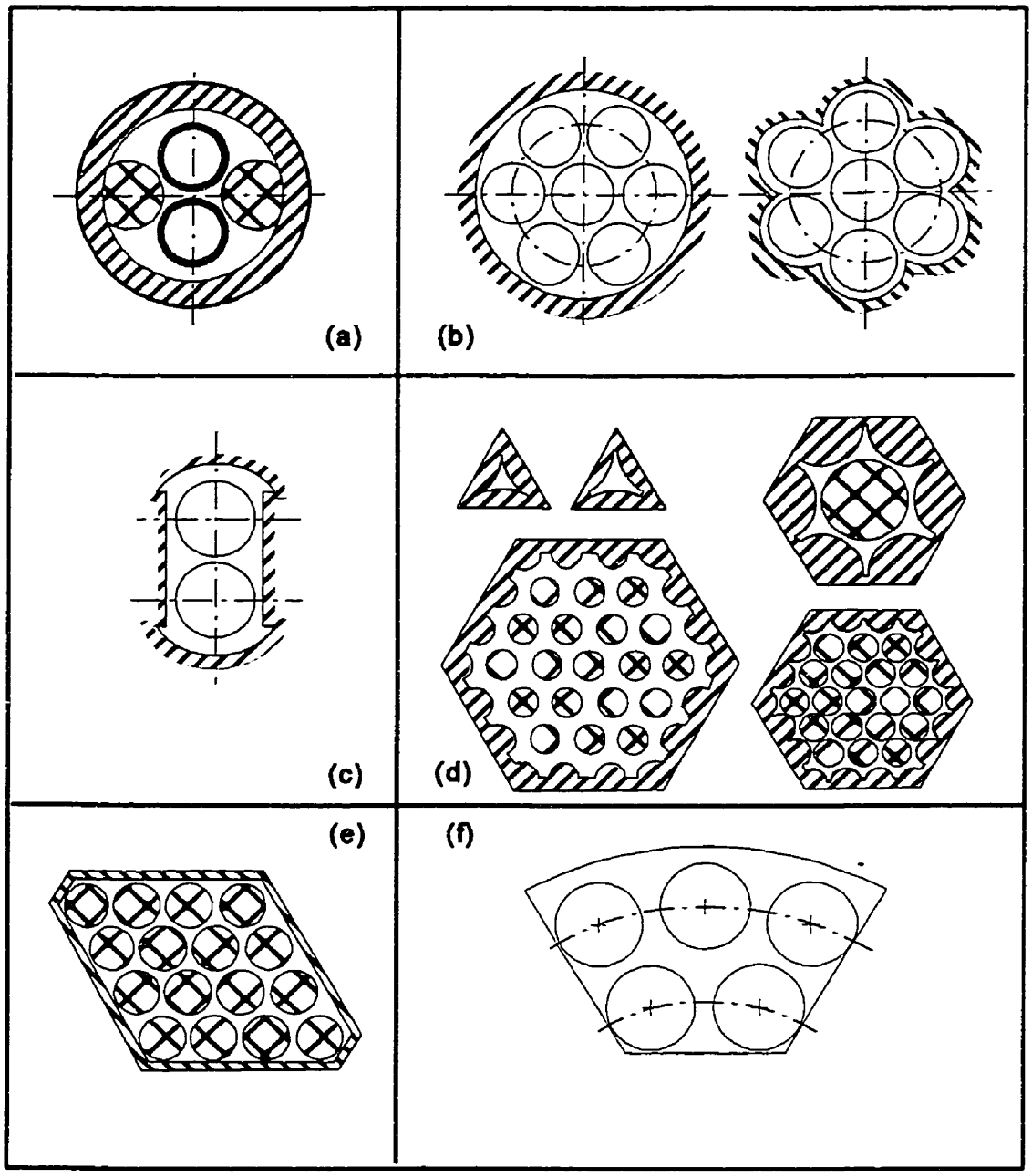

Figure 3.1 Cross-sections of the test-sections used in some previous investigations (a) Rogers and Chapman [1963], (b) Hoffman et al [1966], (c) Irvine, (d) Presser [1971], (e) Šulc [1989] and (f) Guellouz and Tavoularis [1992].

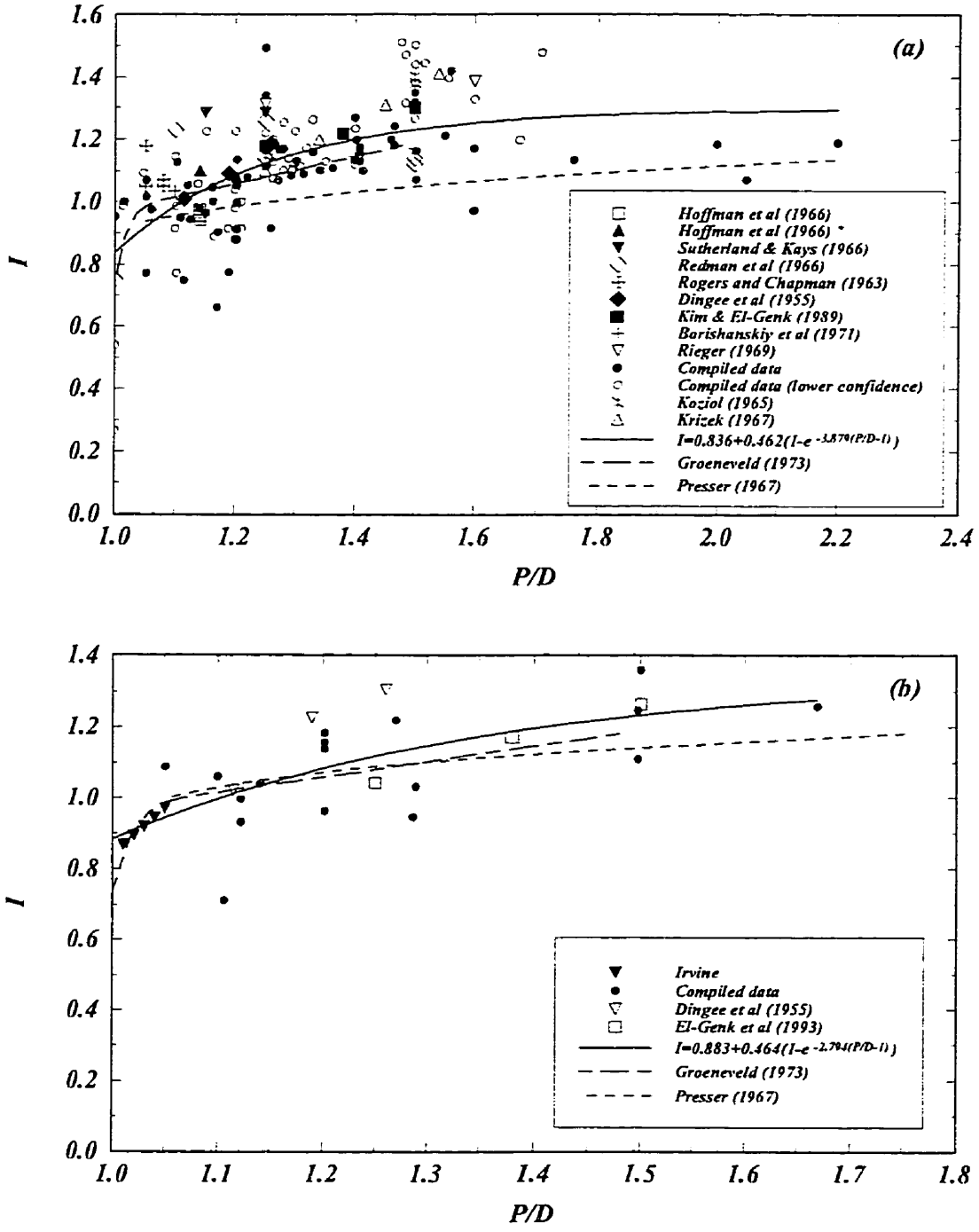

Figure 3.2 Variation of the *I*-factor with the pitch-to-diameter ratio for triangular (a) and square (b) arrays.

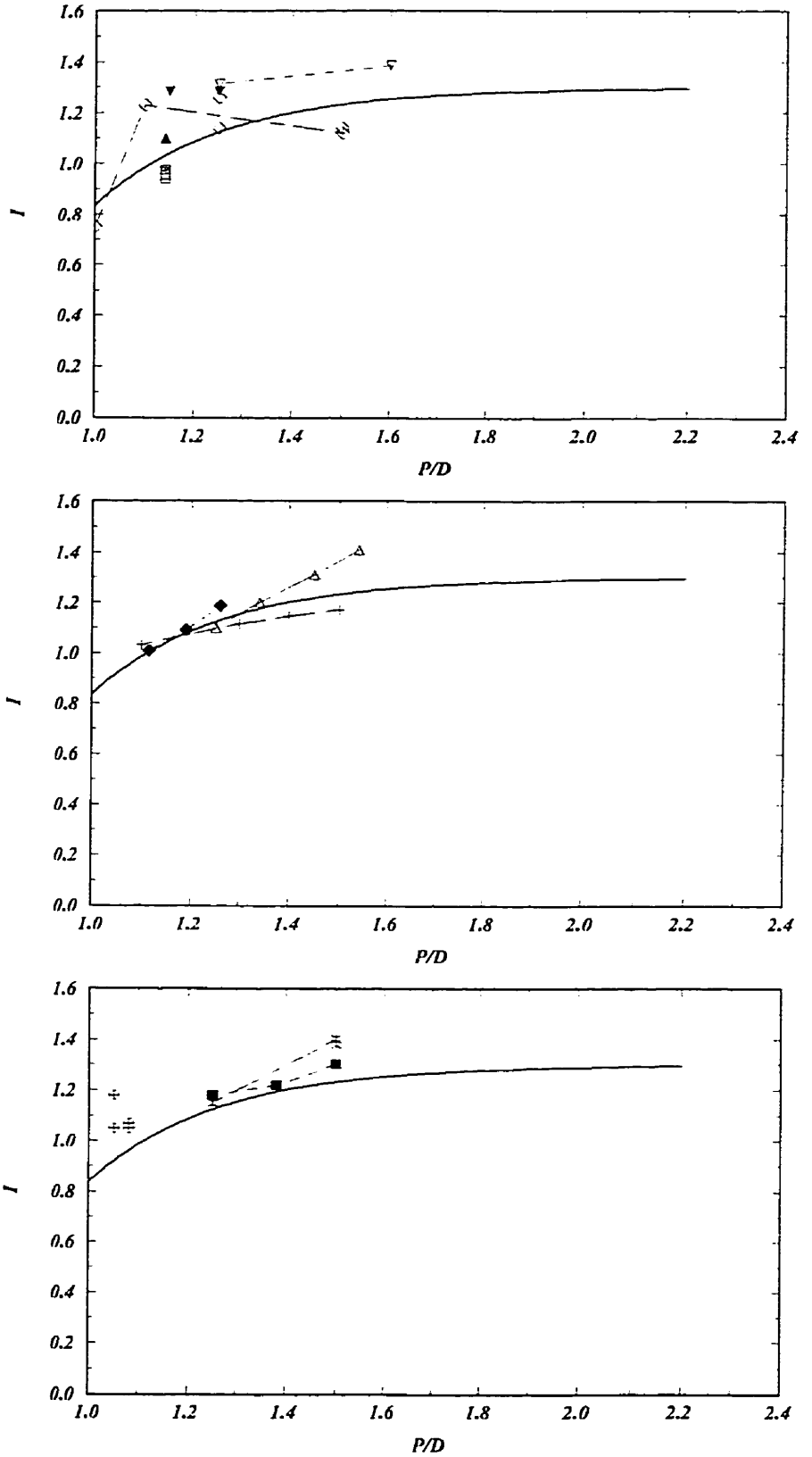

Figure 3.3 Variation of the *I*-factor with the pitch-to-diameter ratio for triangular arrays (details).

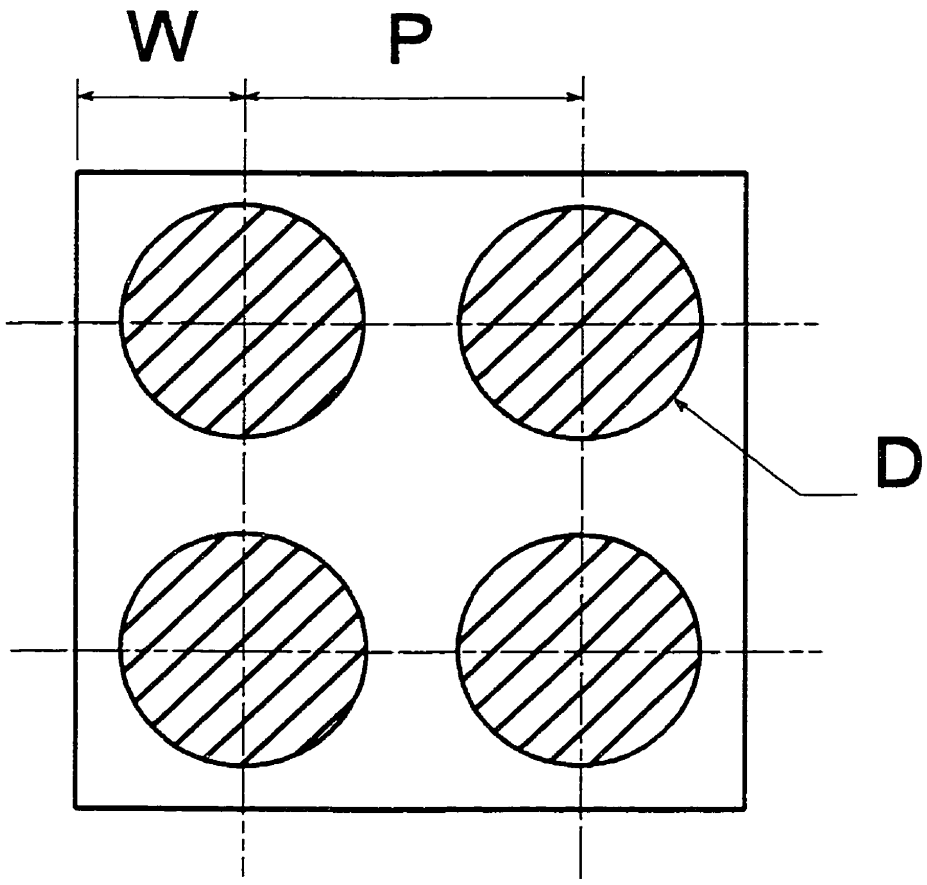

Figure 3.4 Cross-section of a four-rod, square bundle, enclosed in a channel.

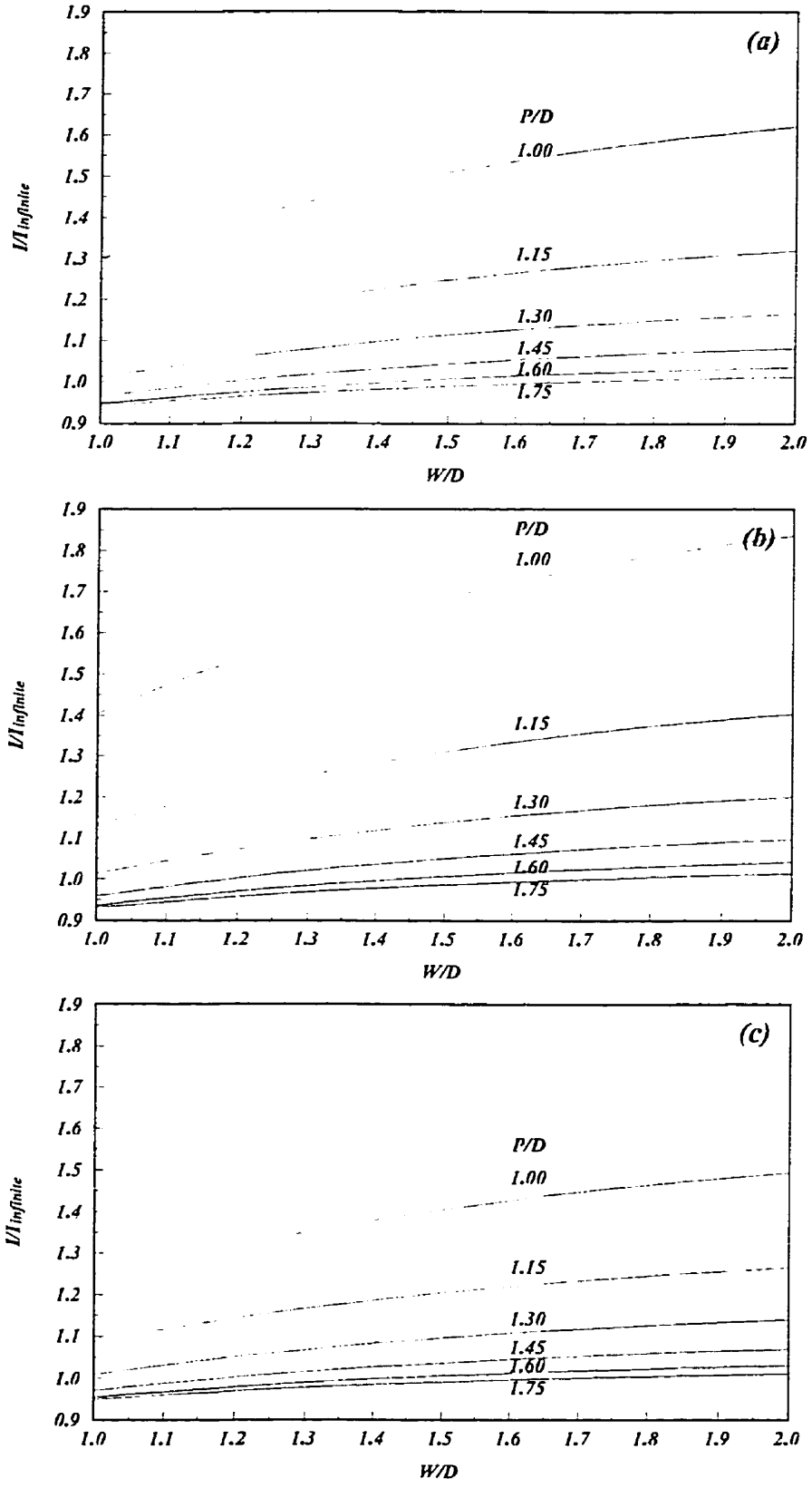

Figure 3.5 Effect of number of rods on the *I*-factor according to Equation(4). (a) $Re=10^5$; $Pr=2.0$, (b) $Re=10^4$; $Pr=2.0$ and (c) $Re=10^4$; $Pr=0.7$.

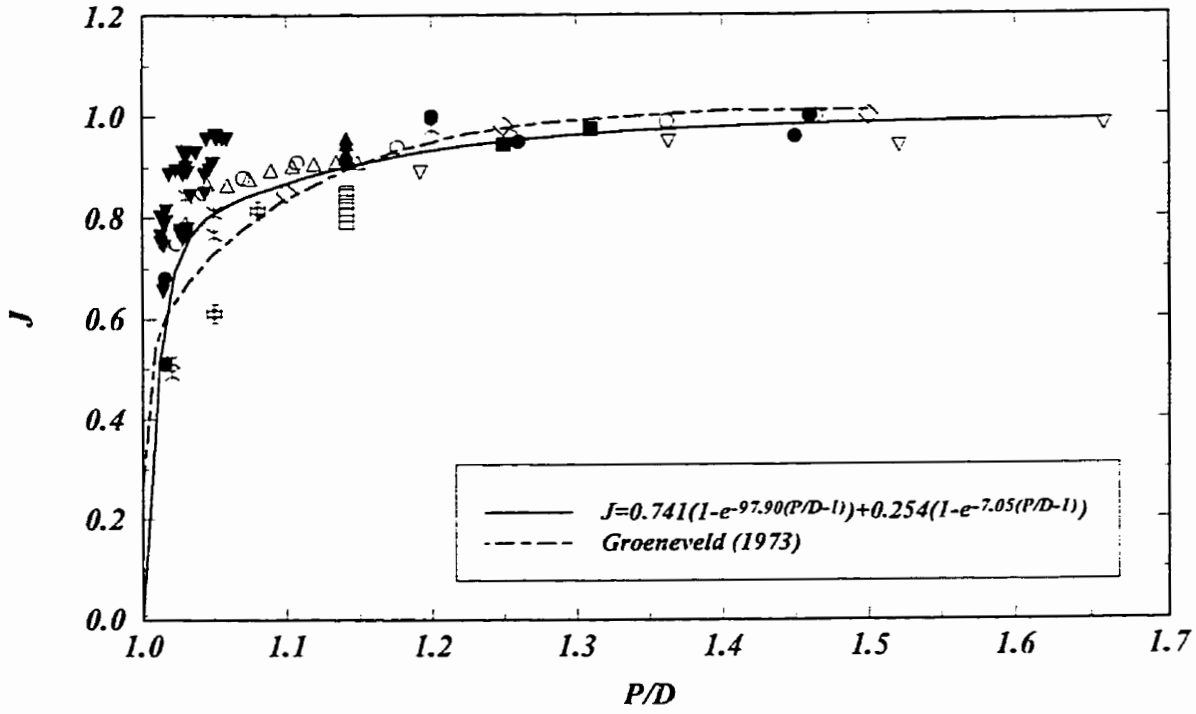

Figure 3.6 Variation of the *J*-factor with the pitch-to-diameter ratio (symbols as in Table 3.2).

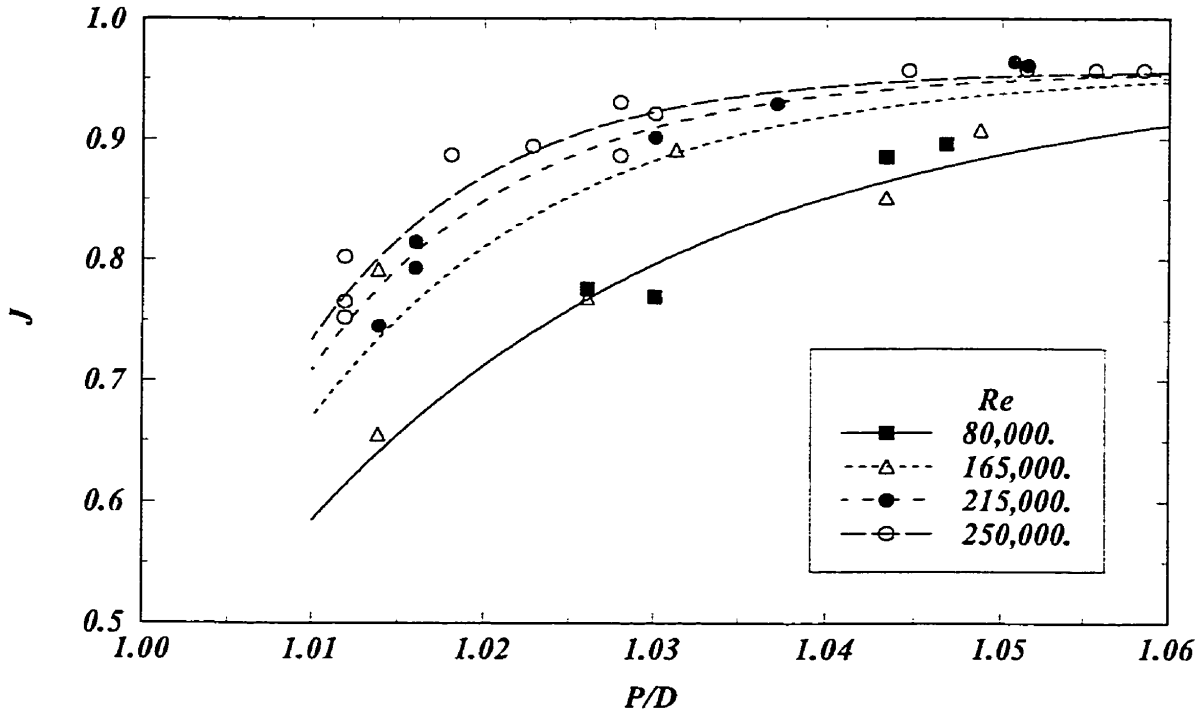

Figure 3.7 Variation of the *J*-factor with the pitch-to-diameter ratio, based on Irvine's measurements (from Groeneveld, 1973).

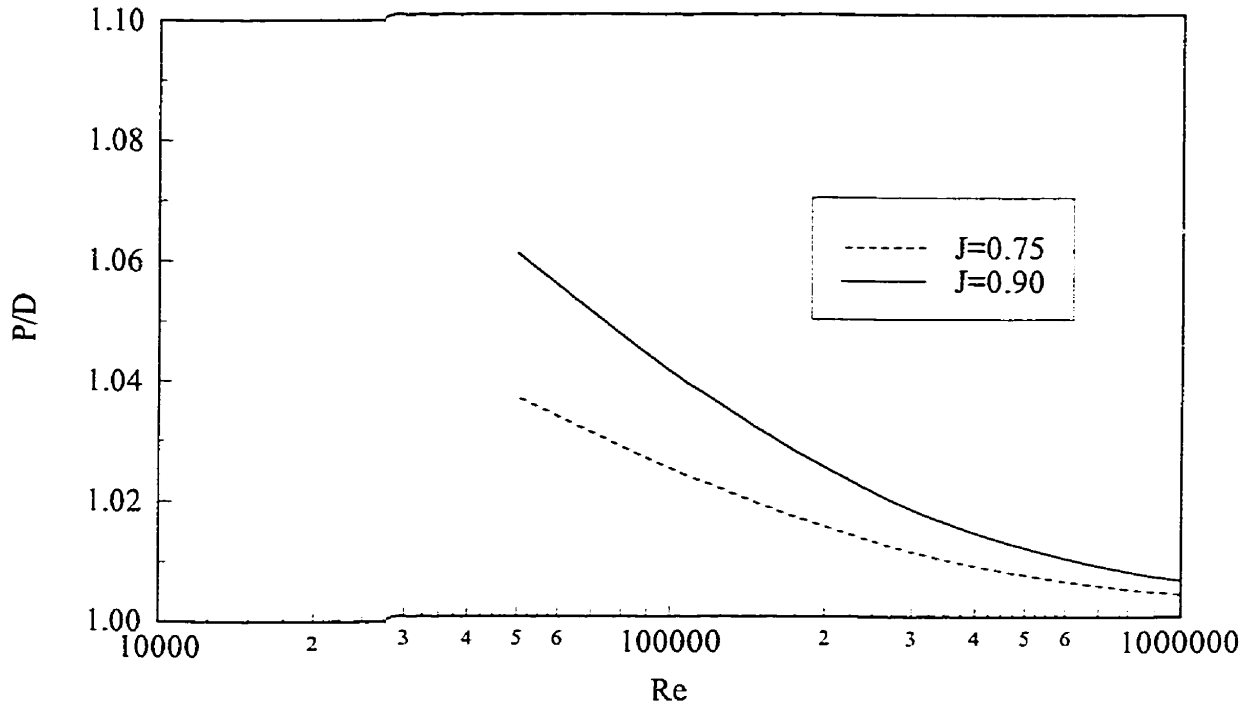

Figure 3.8 Contours of constant *J*-factor for different *P/D* and *Re*.

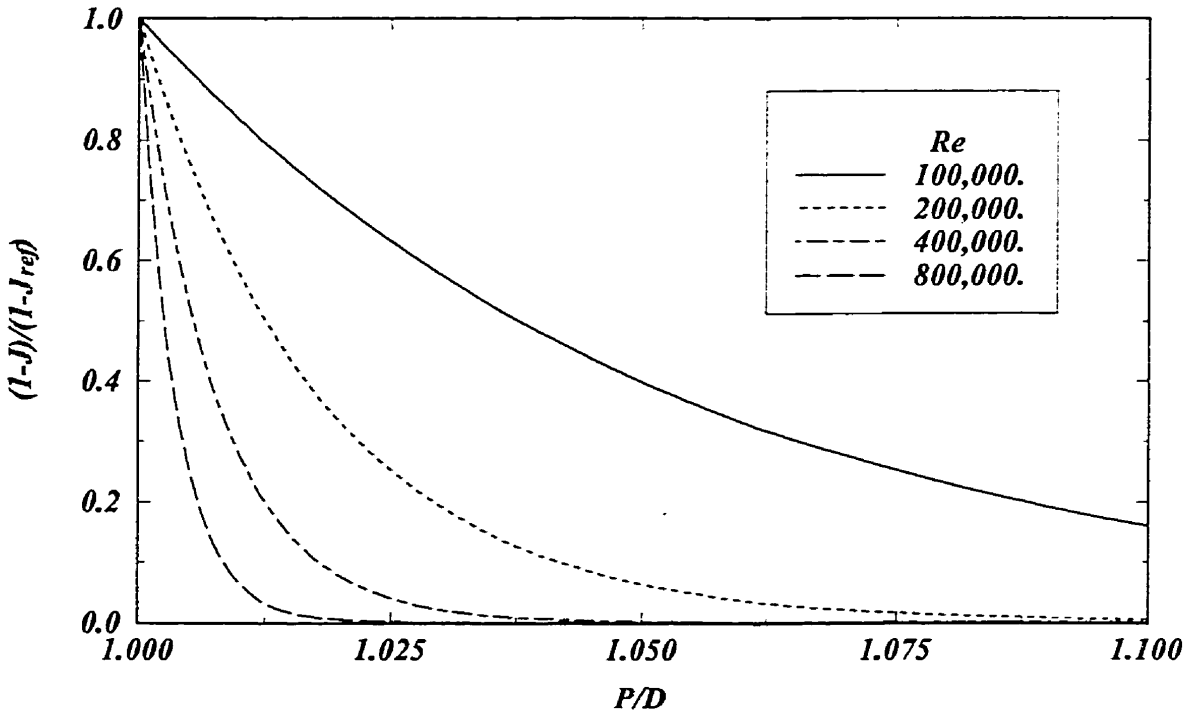

Figure 3.9 *J*-factor variation with Reynolds number.

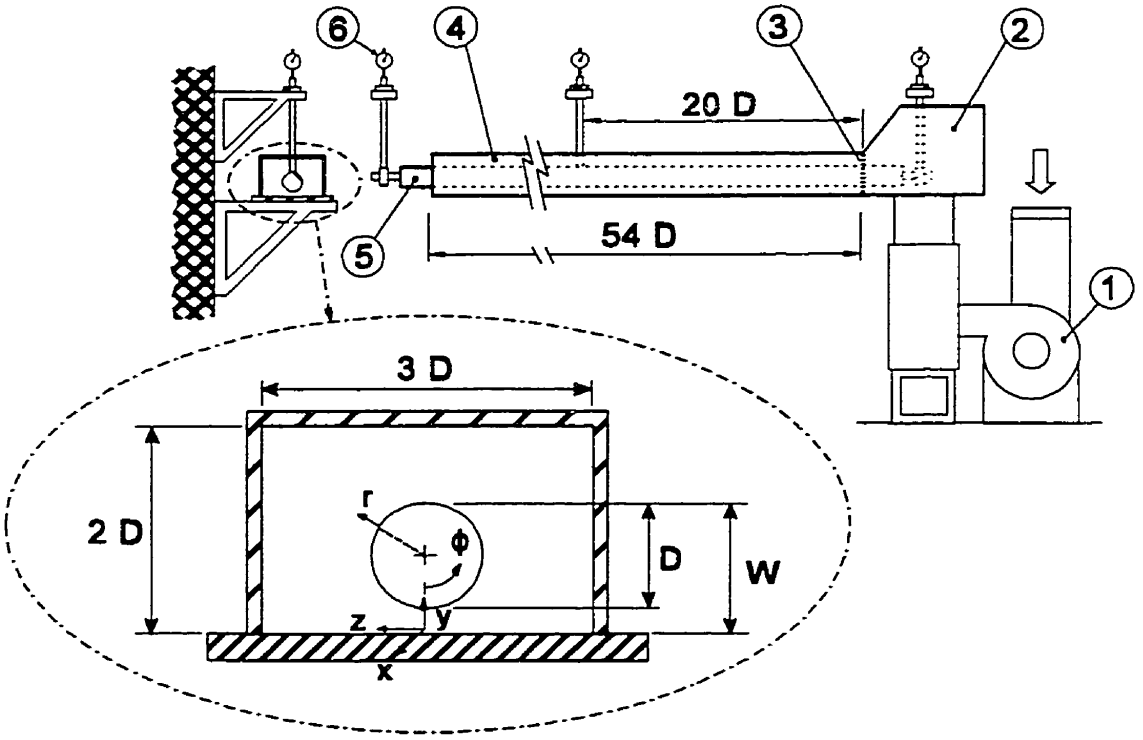

Figure 5.1 Sketch of the flow facility showing the fan (1), the pressure box (2), the woven screen (3), the flow section (4), the rod (5) and the micrometers and rod supports (6).

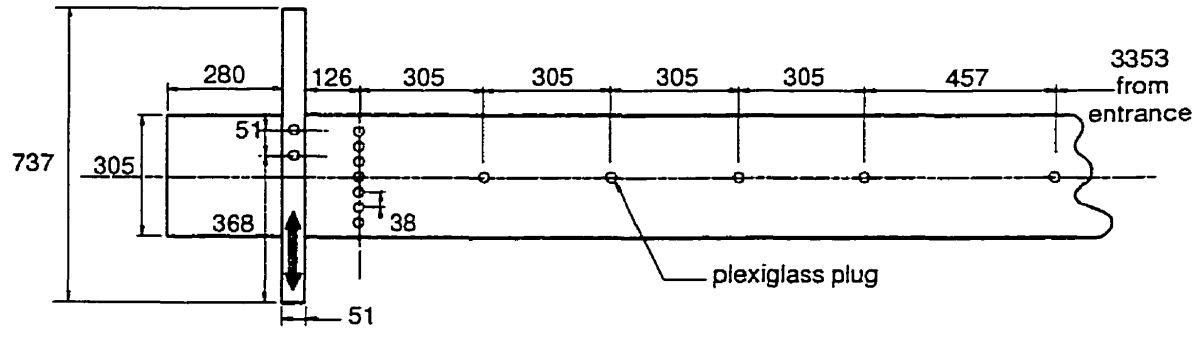

Figure 5.2 Static-holes and sliding plate positions for the test-section (dimensions in mm).

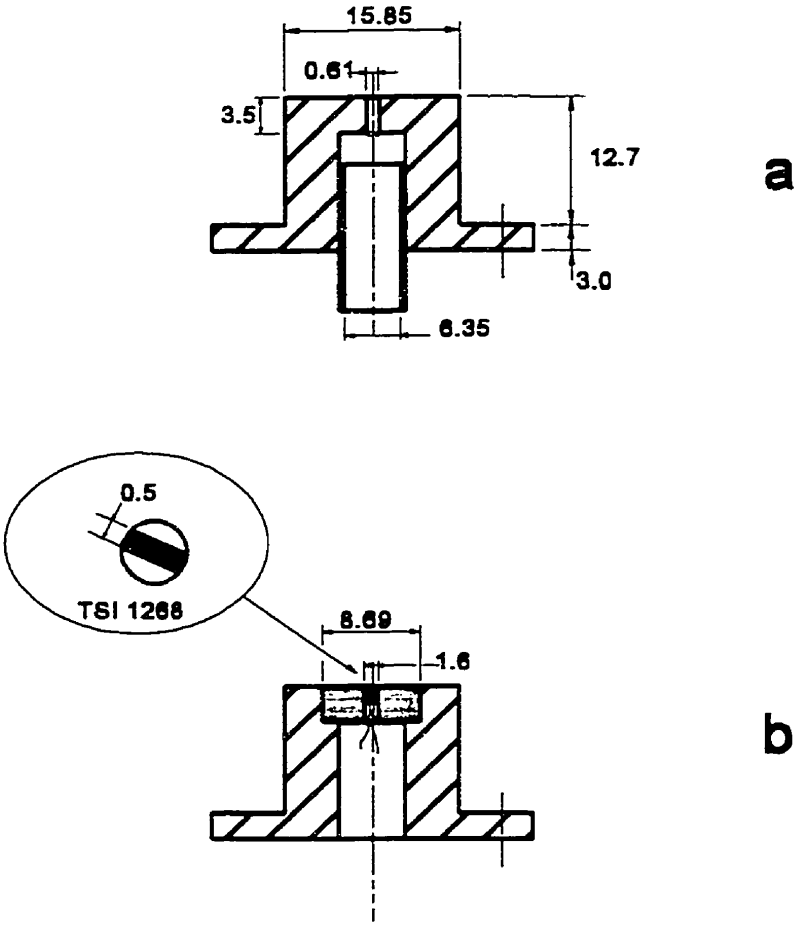

Figure 5.3 Plexiglass plug containing a) a static pressure tap and b) a flush-mounted hot film (dimensions in mm).

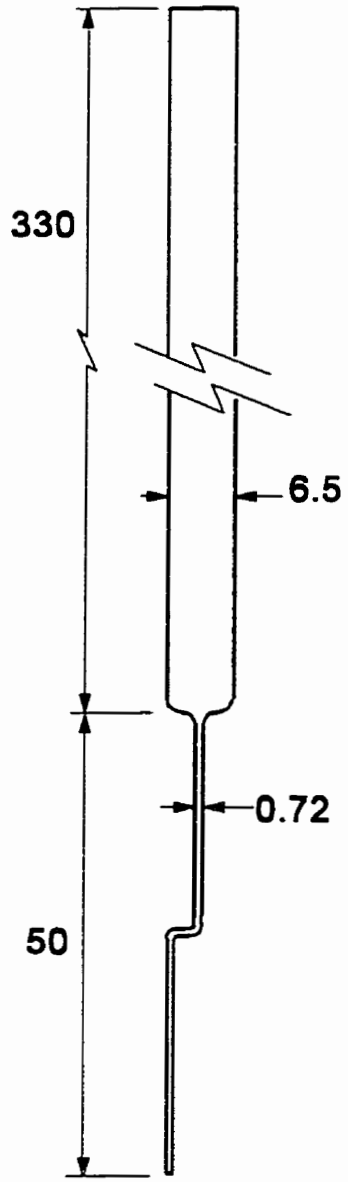

Figure 5.4 The Preston tube (dimensions in mm).

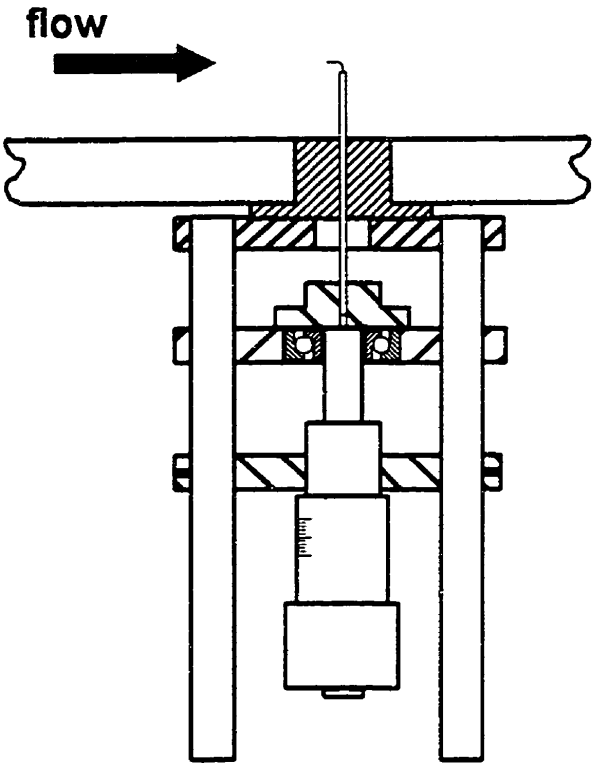

Figure 5.5 Traversing mechanism for the boundary layer probe.

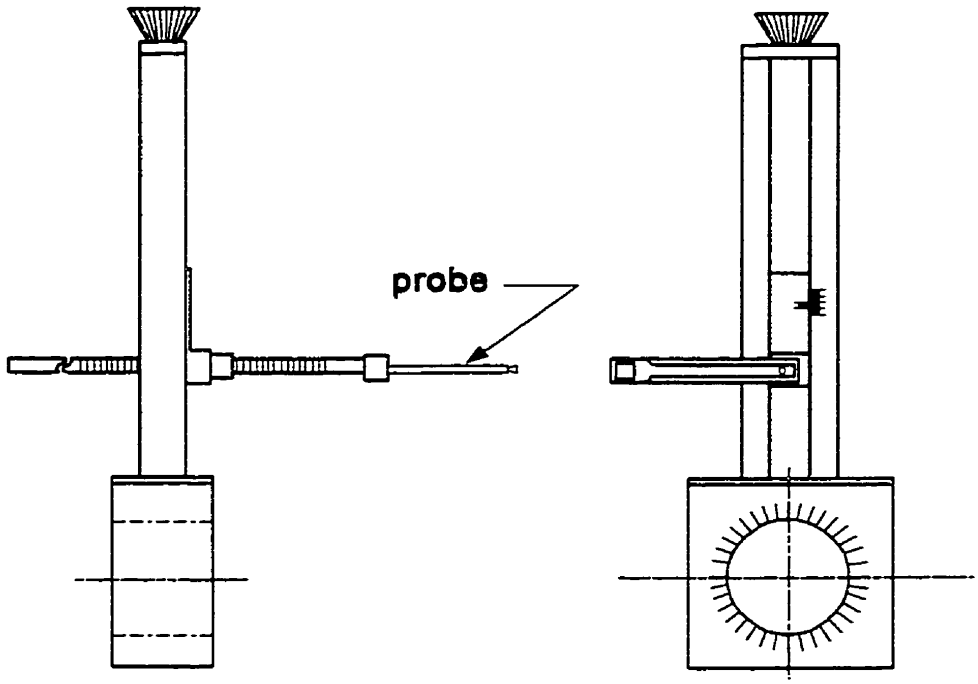

Figure 5.6 Mechanism for azimuthal, radial and longitudinal traversing of the probes.

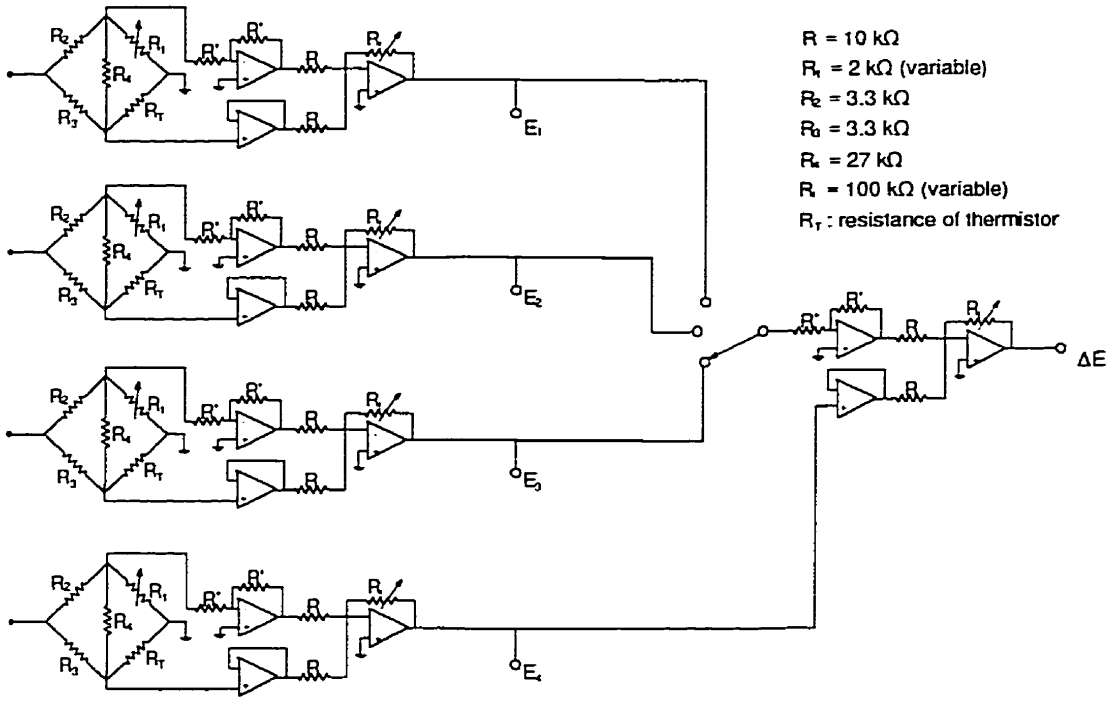

Figure 5.7 Thermistor electronic circuits.

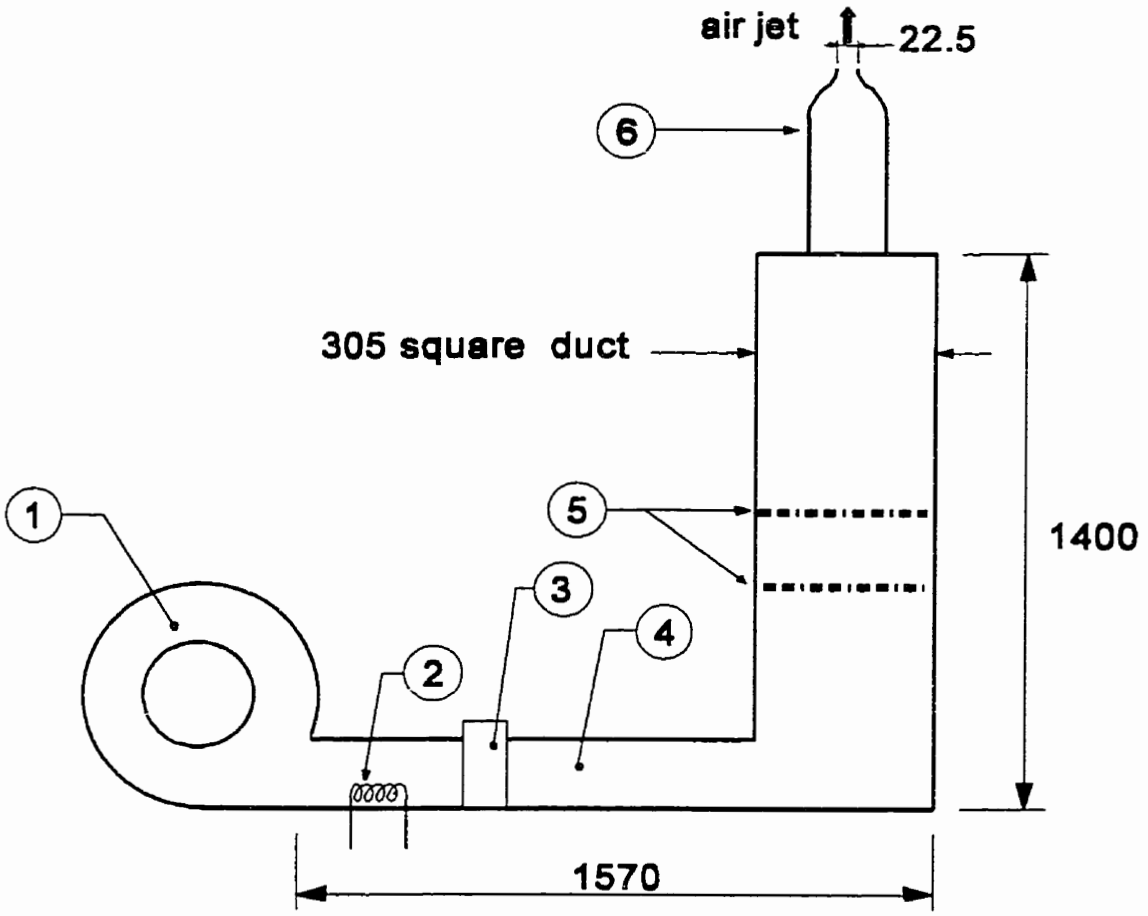

Figure 5.8 The calibration jet (dimensions in mm), showing the 1HP blower (1), the heating coil (2), the flow control valve (3), the 127mm insulated square duct (4), the turbulence reducing screens (5) and the 24:1 contraction (6).

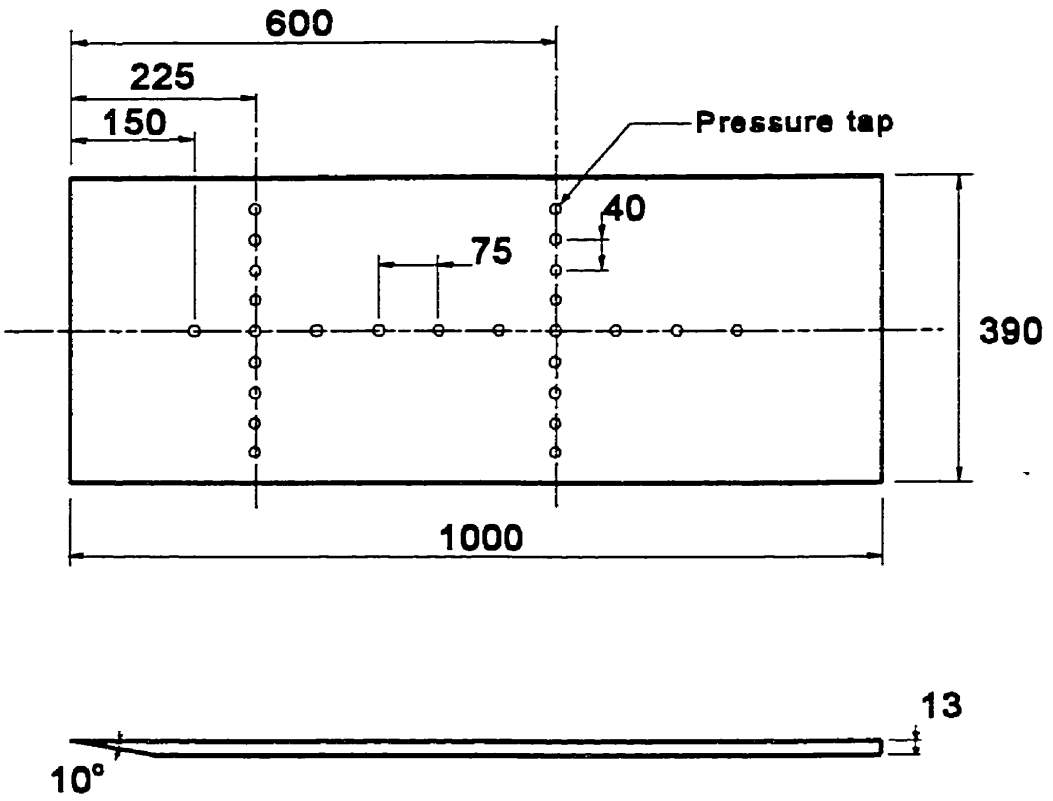

Figure 6.1 The flat plate (dimensions in mm).

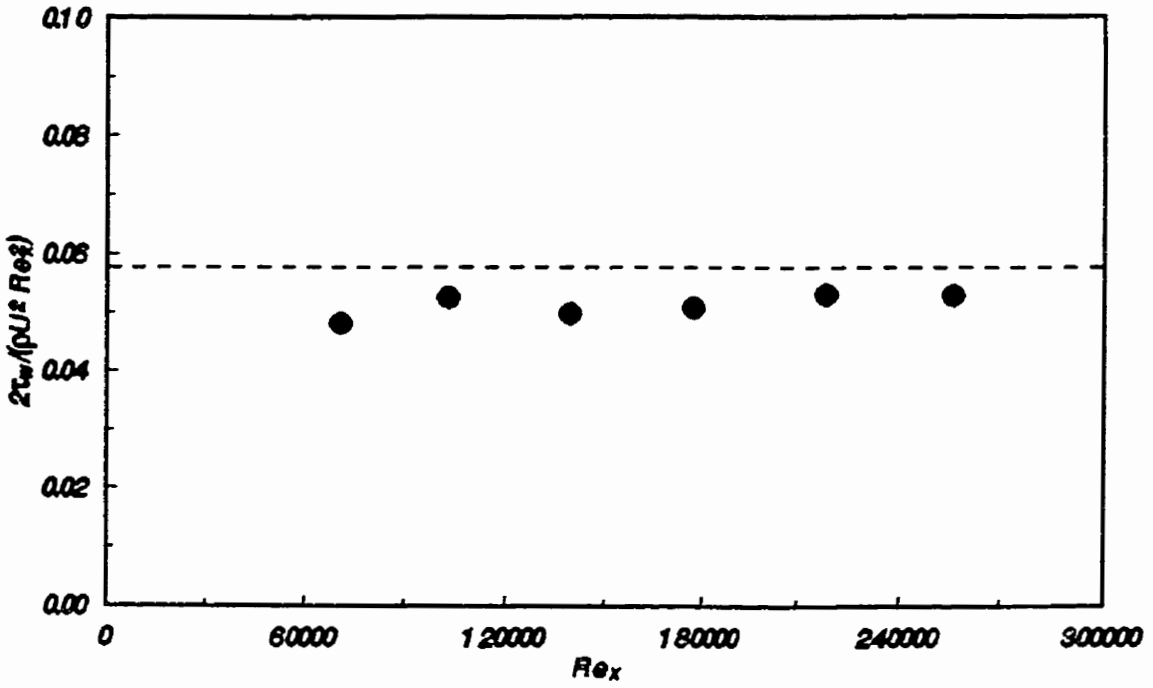

Figure 6.2 Wall shear stress measurements along the flat plate. Measured (●) and theoretical (---) values.

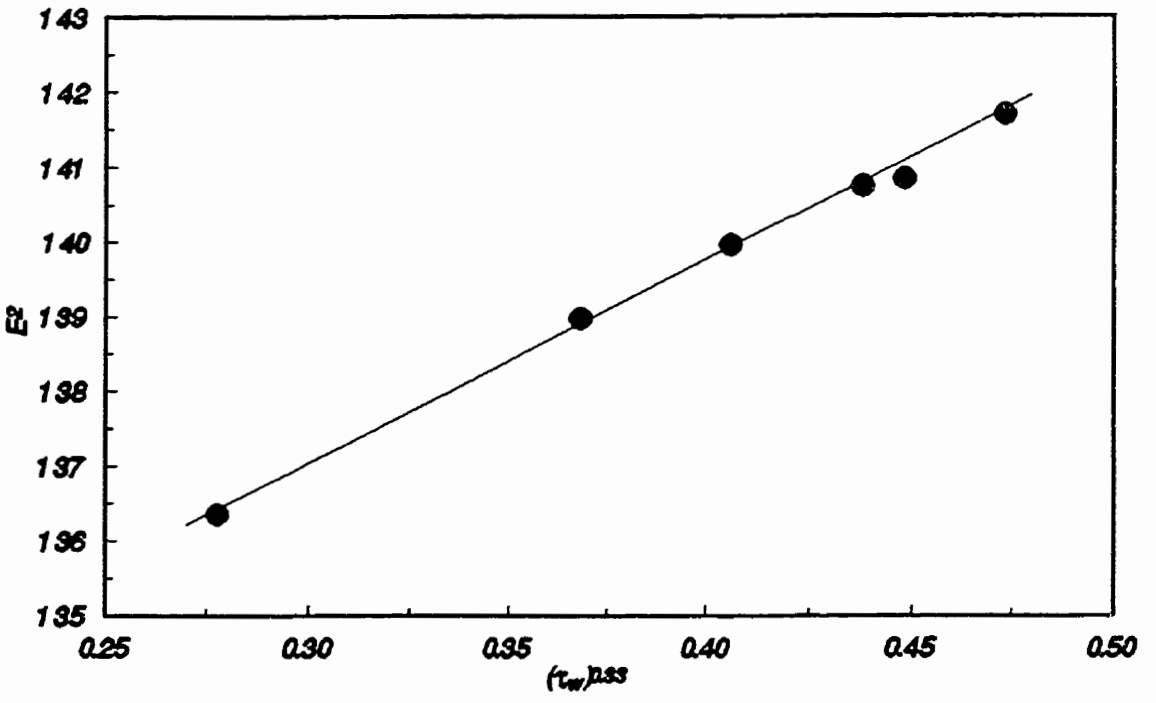

Figure 6.3 Typical calibration curve of the hot-film shear stress probe.

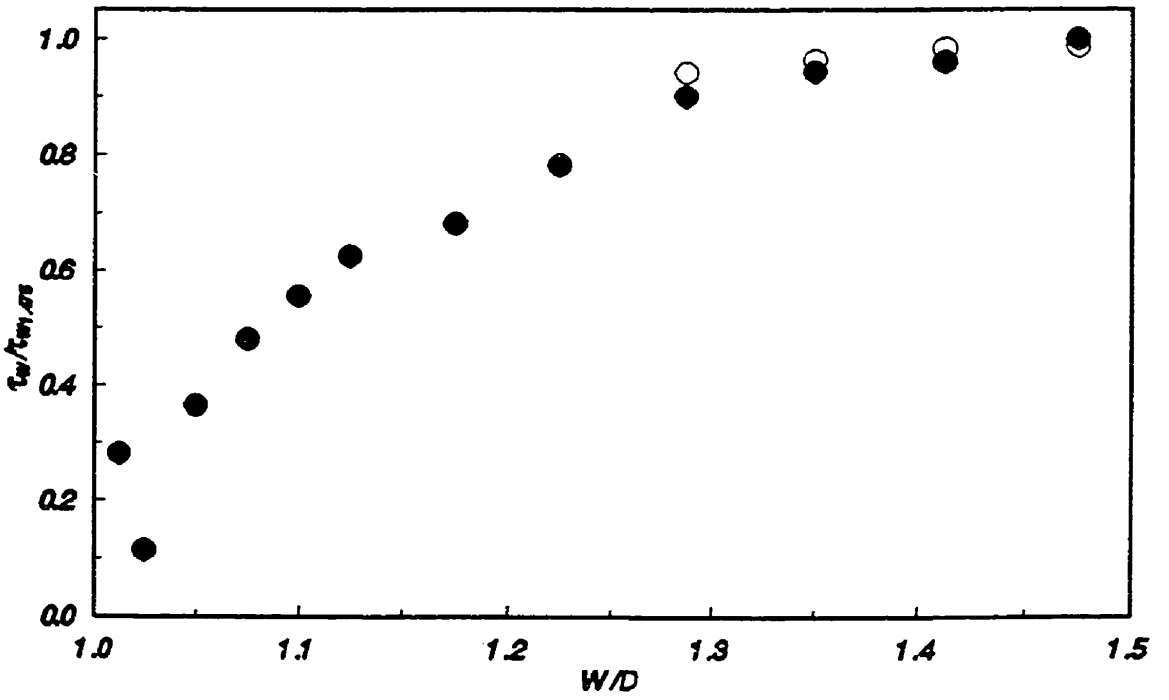

Figure 6.4 Wall shear stress variation with *W/D* at the rod-wall gap, measured with the hot-film probe (●) and with a Preston tube (○), normalized by the wall shear stress value at *W/D* = 1.475.

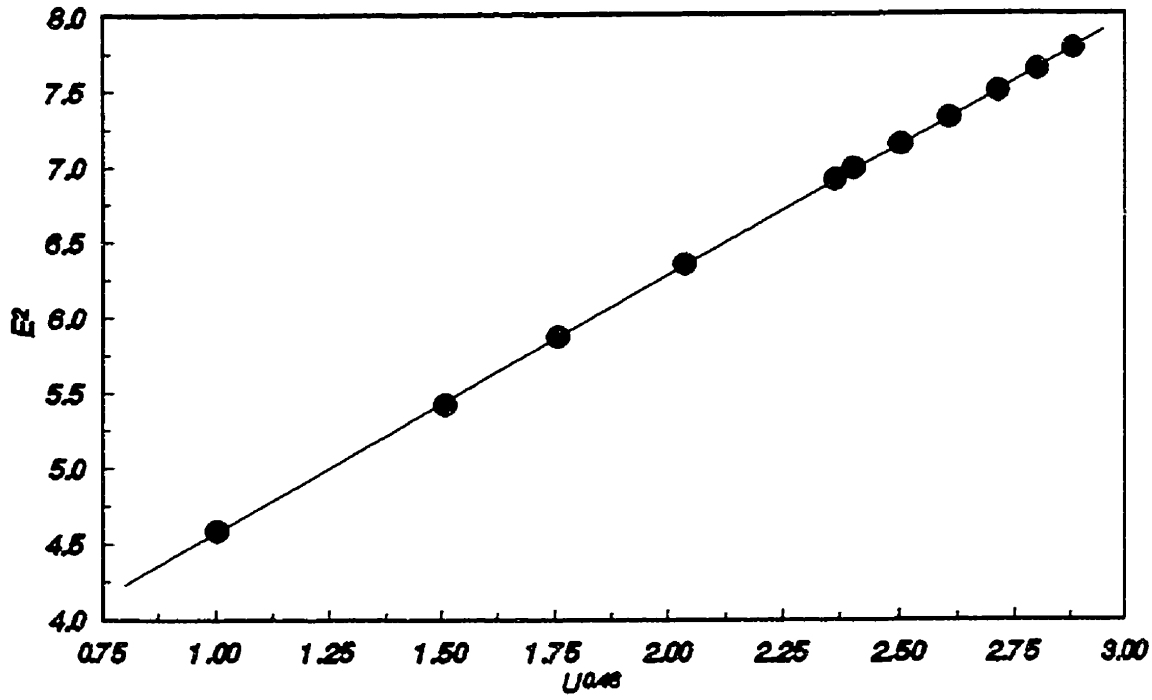

Figure 6.5 Typical hot-wire calibration curve.

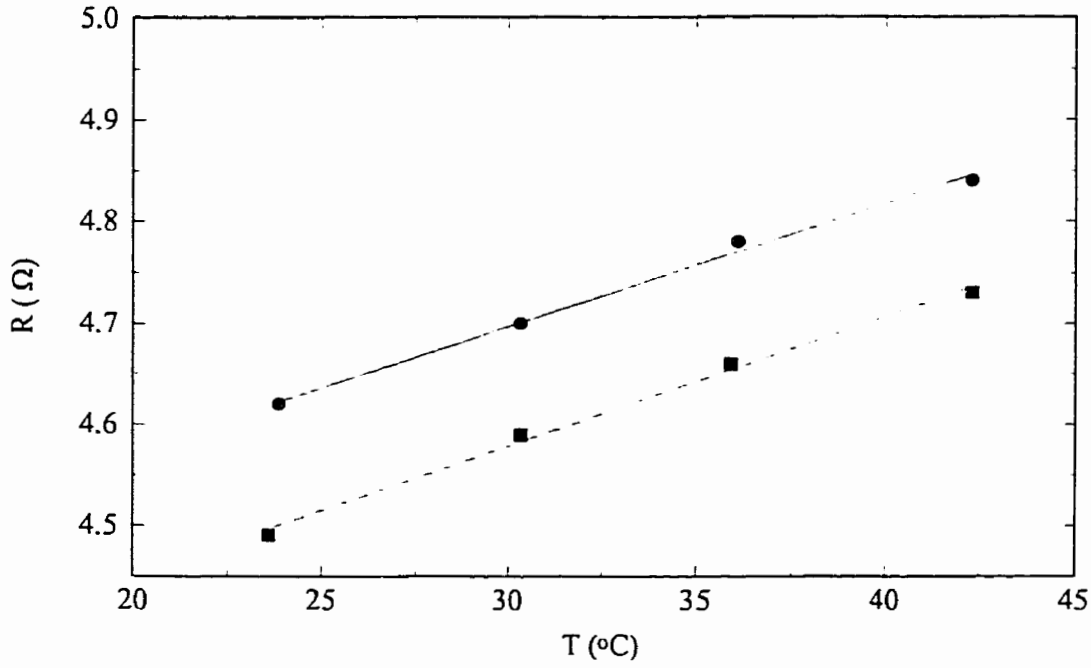

Figure 6.6 Typical resistance-temperature curves for two hot-wire sensors made of the same material, but having different lengths.

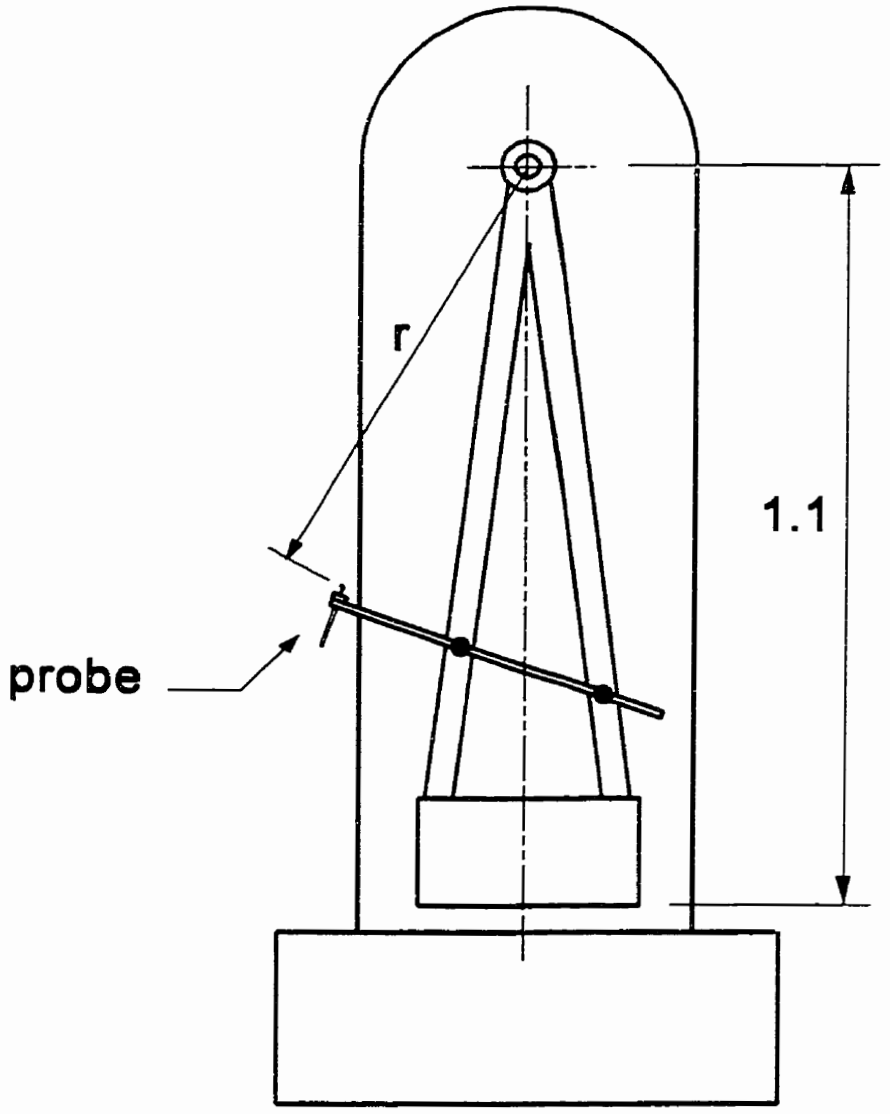

Figure 7.1 A sketch of the Charpy apparatus used as a pendulum.

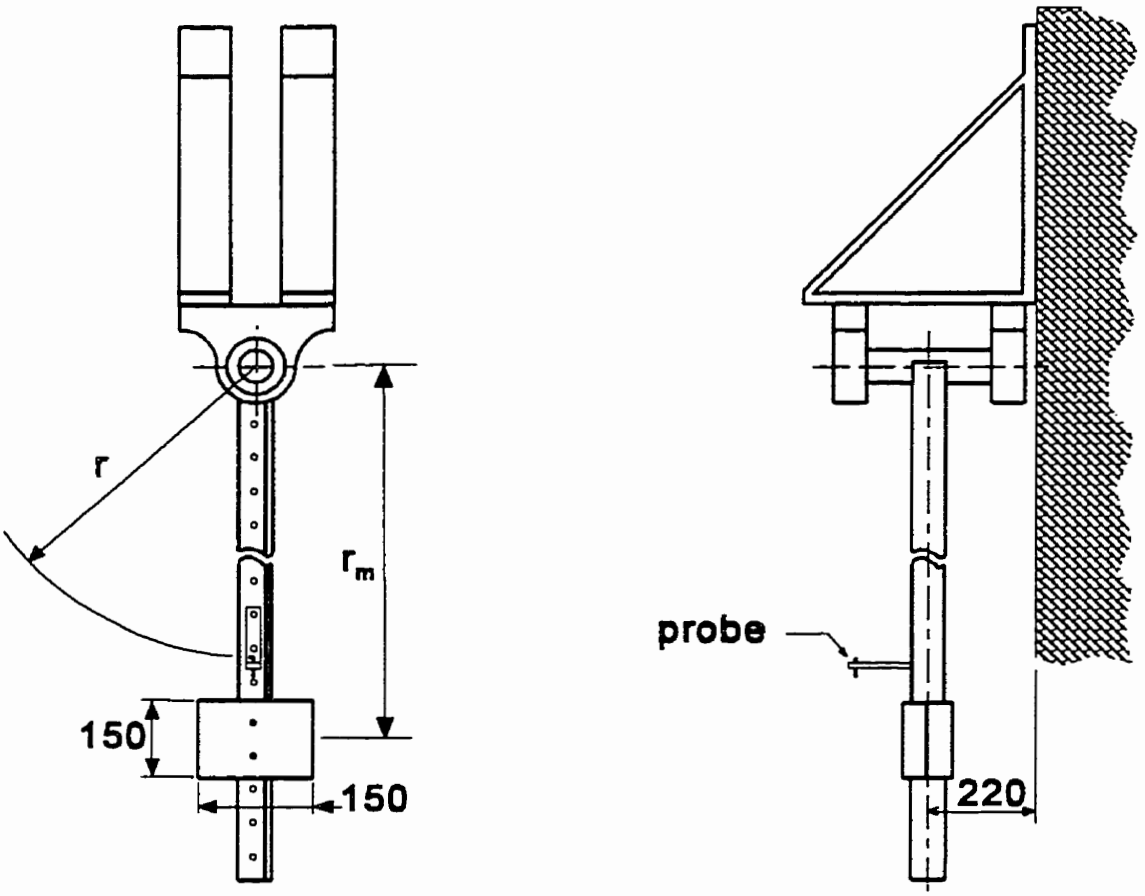

Figure 7.2 Sketch of the special calibration pendulum; r_m is the radius at the centre of the concentrated mass (dimensions in mm).

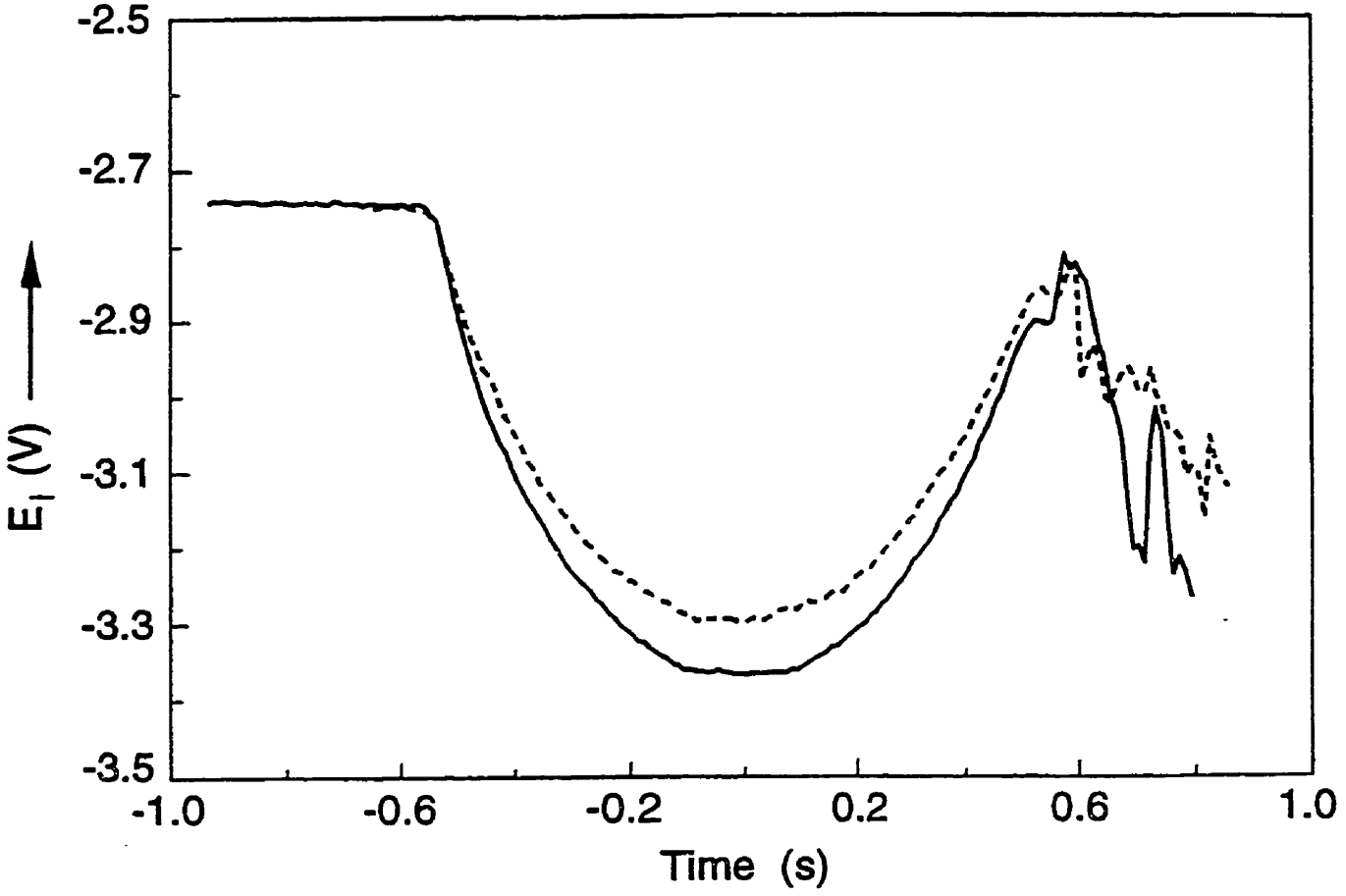

Figure 7.3 Matched hot-wire signals corresponding to case 3 in Table 7.2; Signals acquired with the sensor mounted at r_1, ——, and r_2, ---.

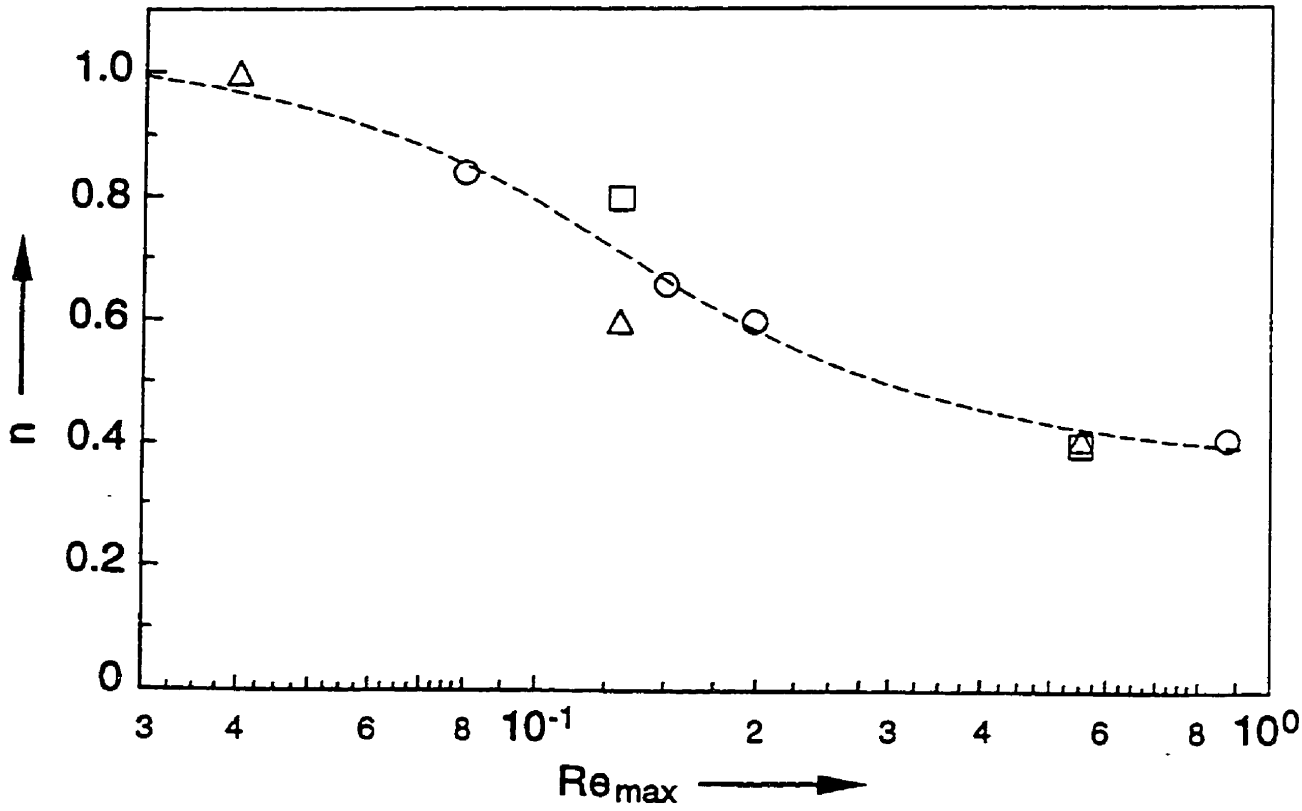

Figure 7.4 Relationship between the velocity exponent in King's law and the maximum wire-Reynolds number. ○ present data, □ Aydin and Leutheusser [1980], △ Tsanis [1987] and --- Equation (14).

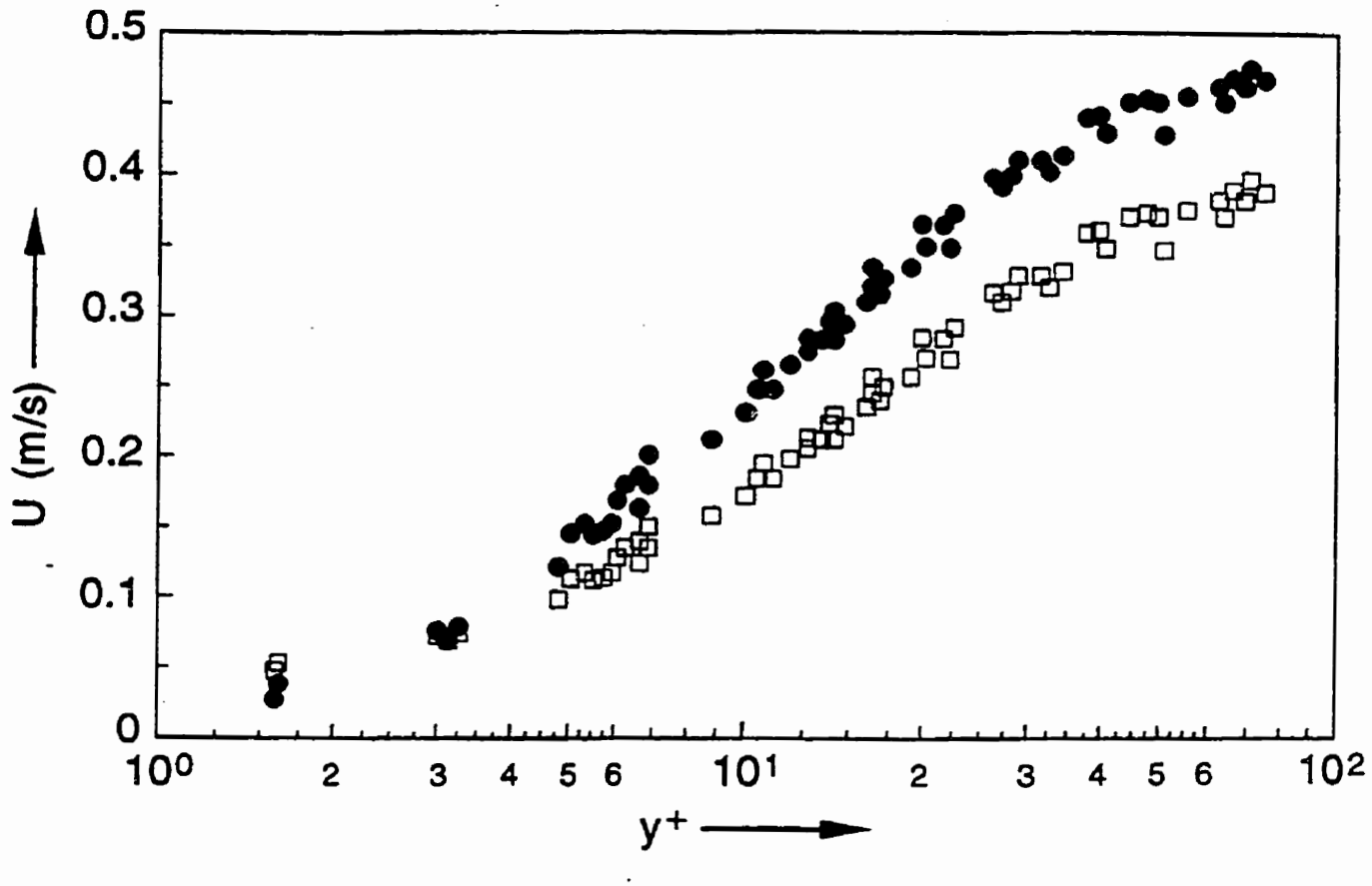

Figure 7.5 Estimated errors in the measurement of velocity in the buffer sublayer, using calibrations in different velocity ranges; ● reference profile, presumably measured using the calibration equation for case 3, ⊞ profile obtained using the calibration equation for case 1.

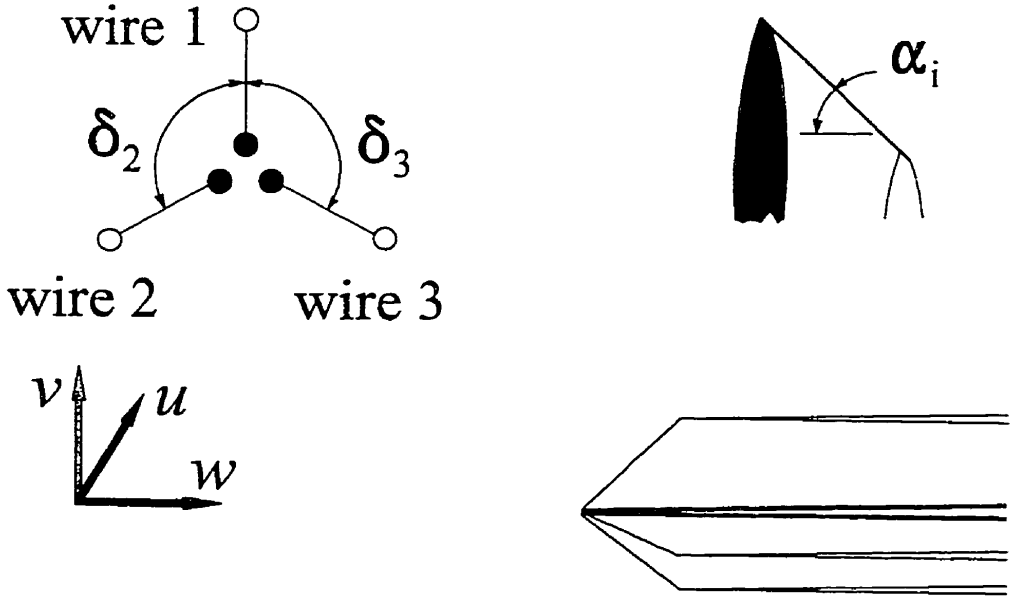

Figure 7.6 Geometry of the AUSPEX three sensor probe, showing sensor angles , α_i and δ_i , and the coordinate system.

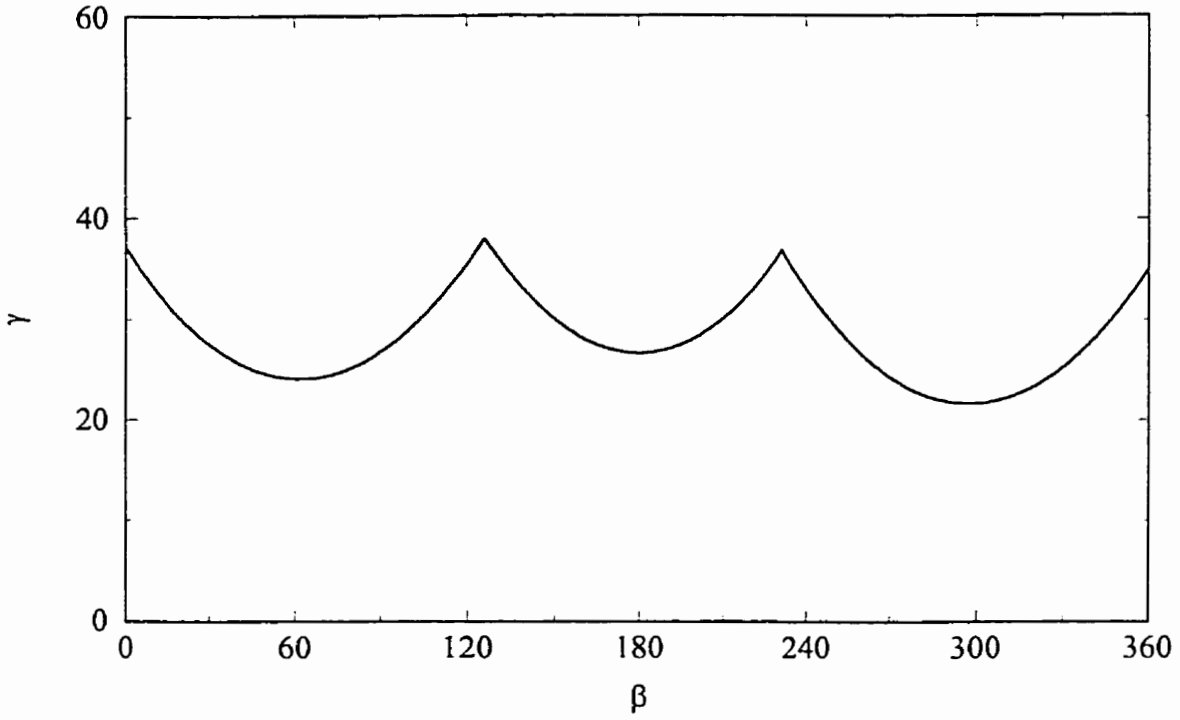

Figure 7.7 The uniqueness domain for the AUSPEX probe, with the red sensor placed in the u-v plane (β=0). Probe characteristics as in Table 7.3

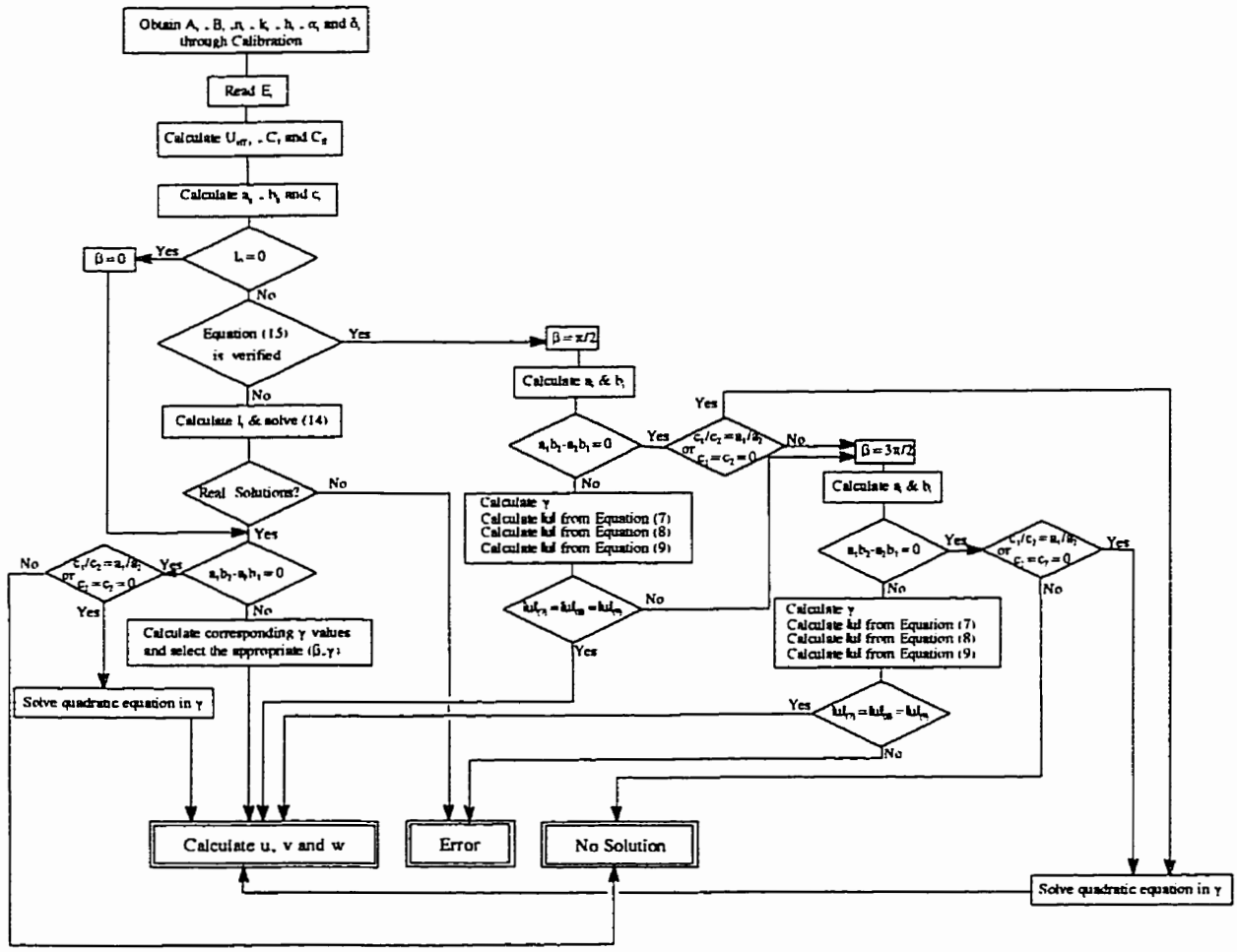

Figure 7.8 Flow chart corresponding to the solution algorithm for the three sensor probe.

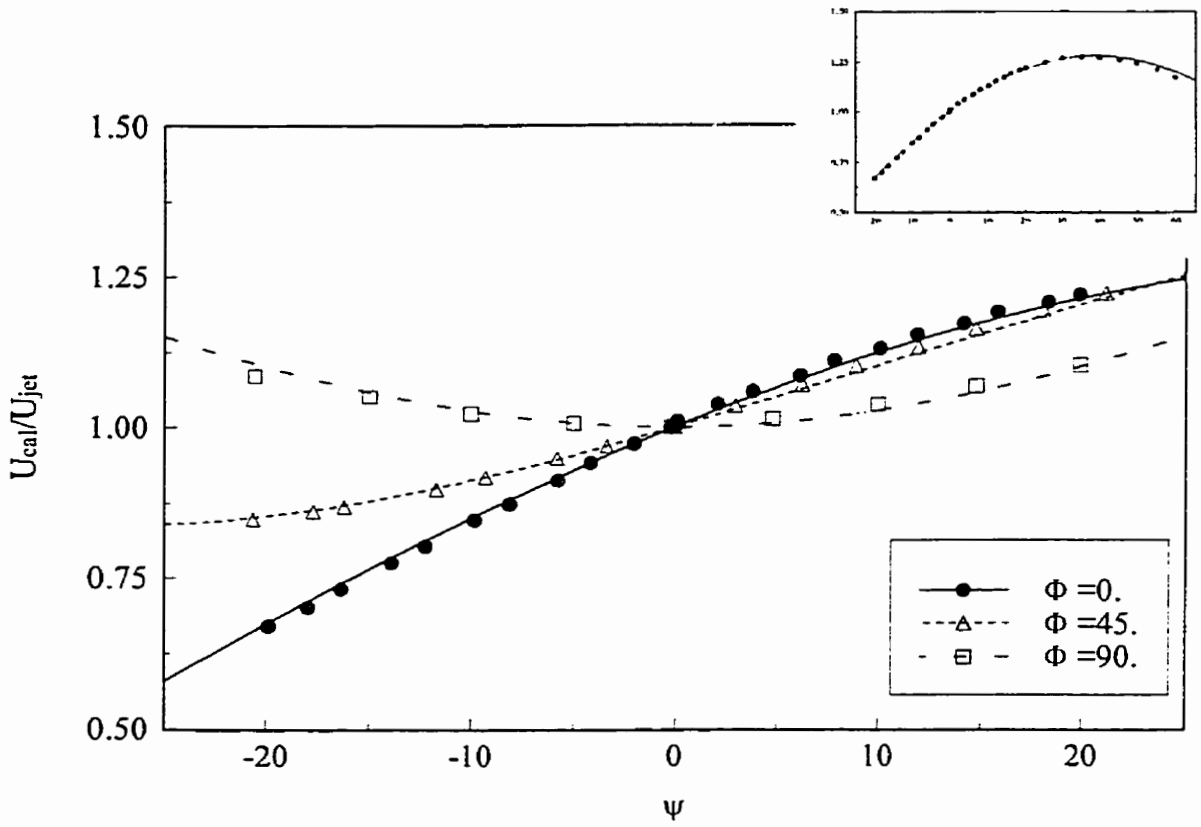

Figure 7.9 The dependence of the response of the blue sensor to yaw and pitch. Measured data points (symbols) and fitted model (lines).

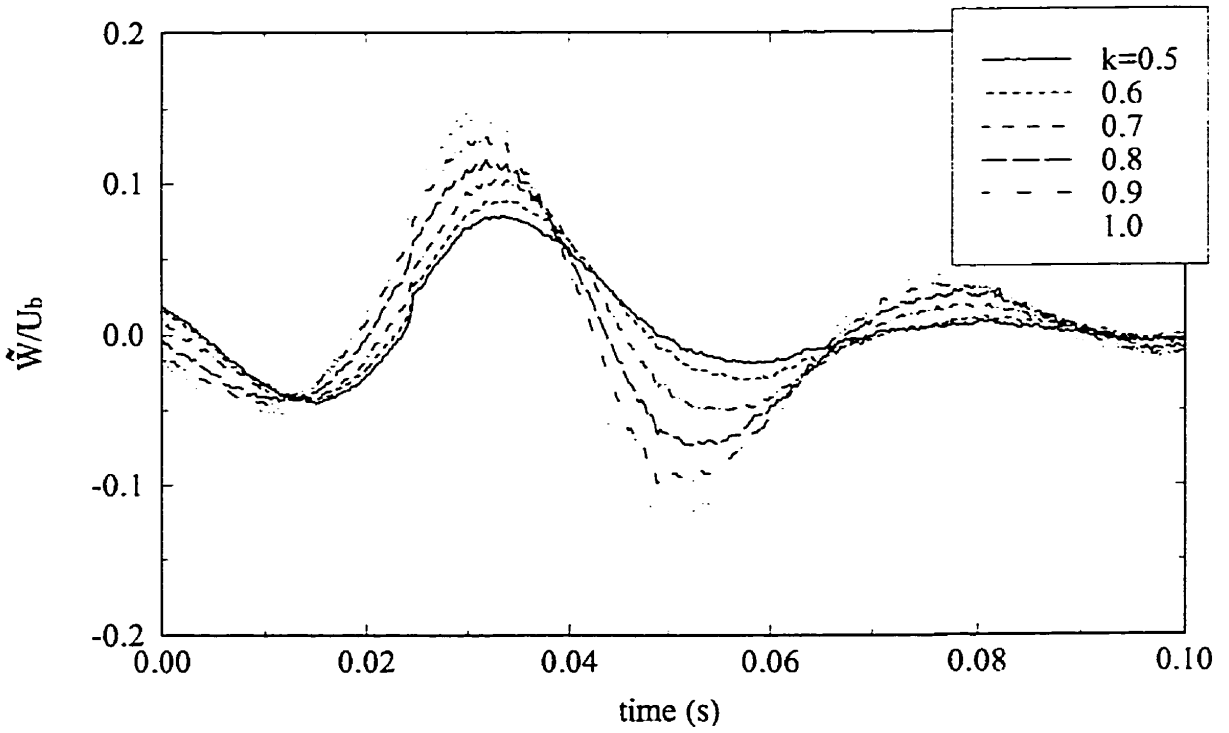

Figure 7.10 Coherent spanwise velocity component obtained, for different threshold values, k, by ensemble averaging the VITA educed signals.

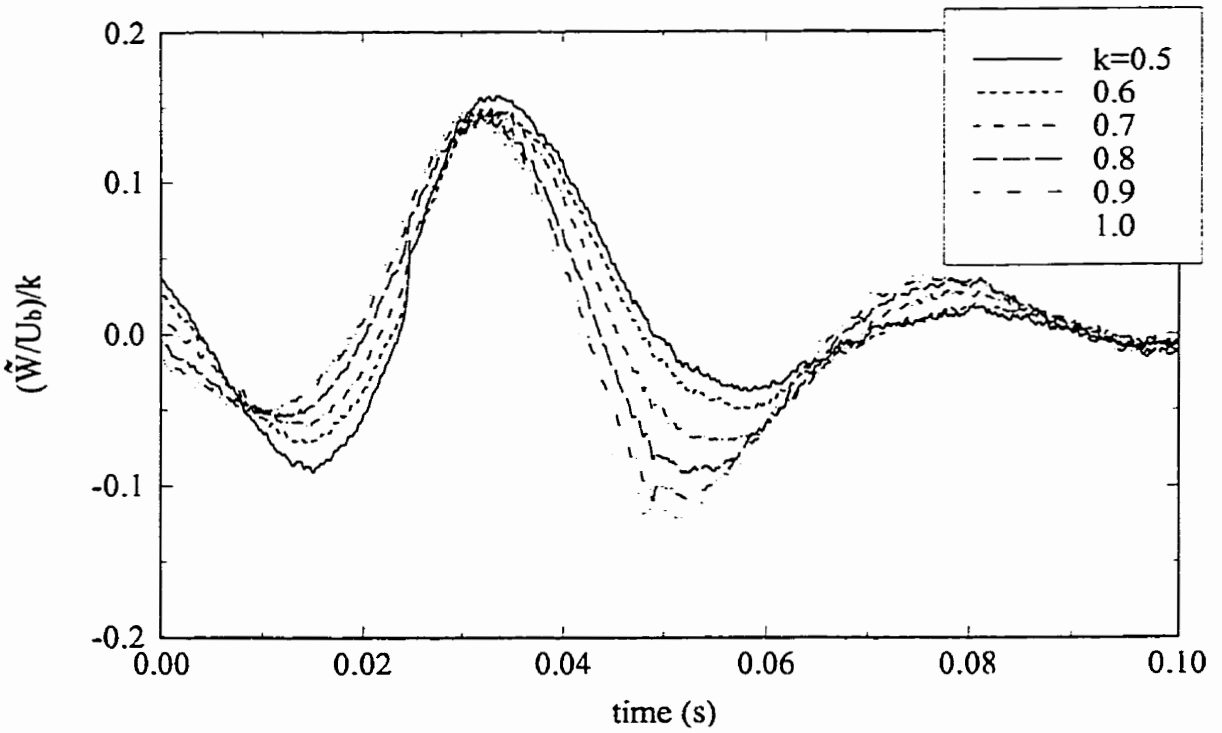

Figure 7.11 Coherent spanwise velocity component normalized by their respective VITA threshold value, k.

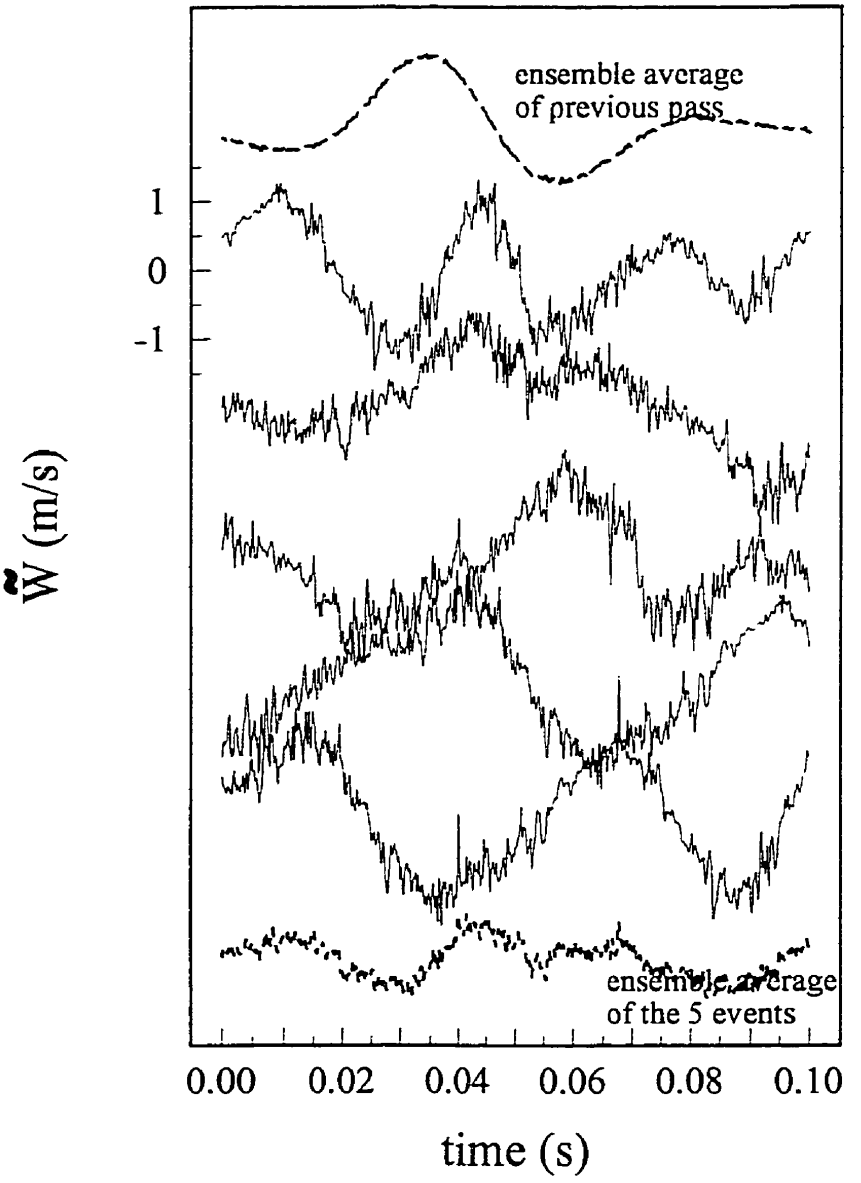

Figure 7.12 A sample of VITA educed signals corresponding to the coherent spanwise velocity component, and their ensemble average.

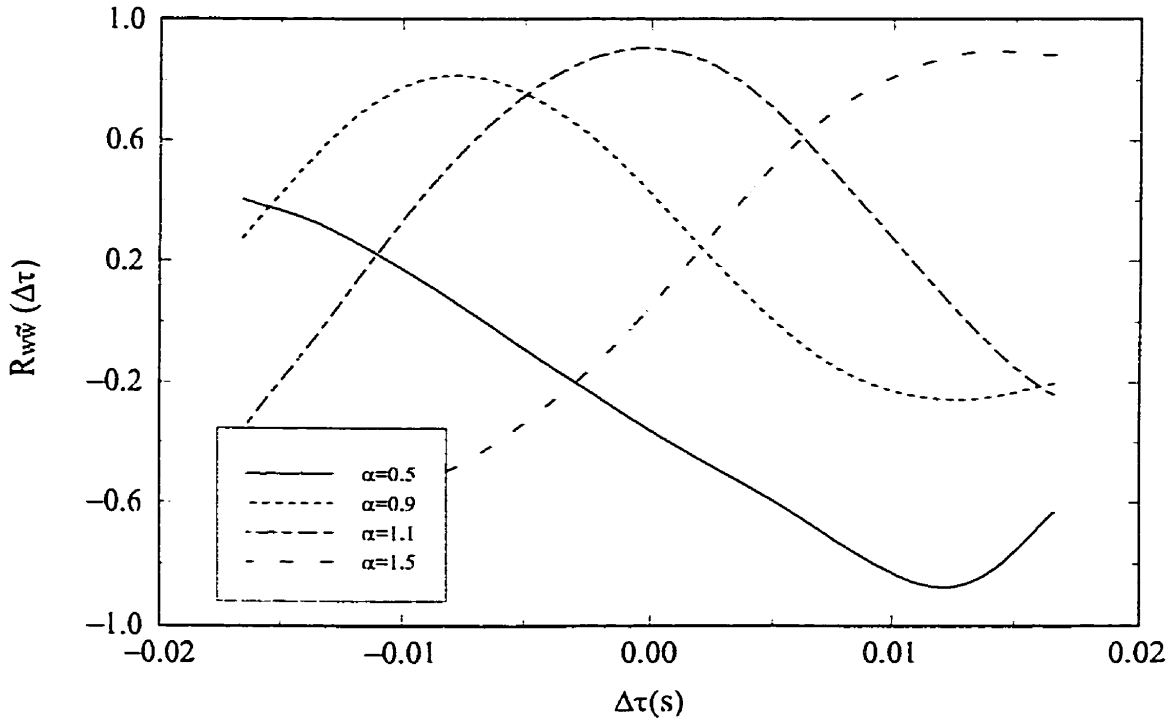

Figure 7.13 Typical correlation functions of an educed signal with the previous pass ensemble average, for various contraction/expansion factors α (the educed signal used here is the middle signal of Figure 7.12).

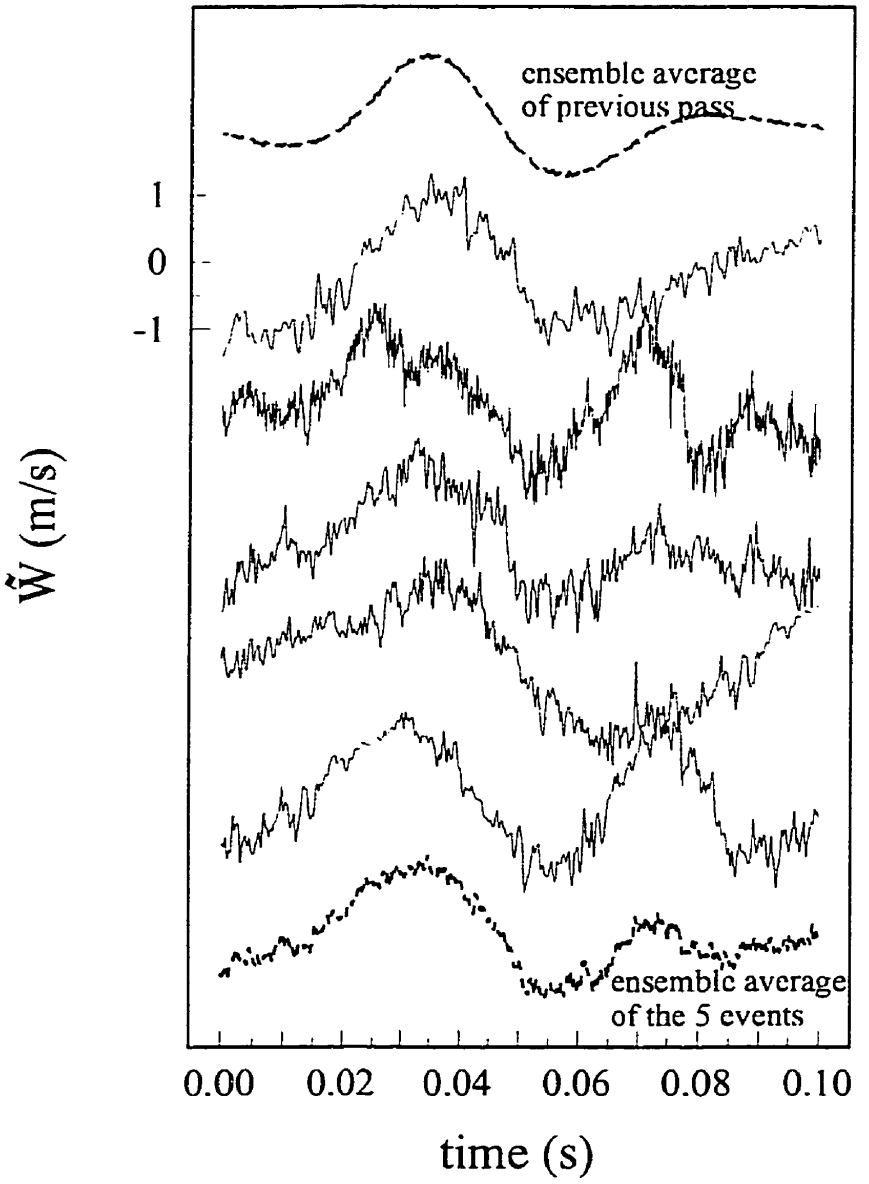

Figure 7.14 The VITA educed signals of Figure 7.12 after contraction/expansion and alignment (to match the previous pass ensemble average) and their ensemble average.

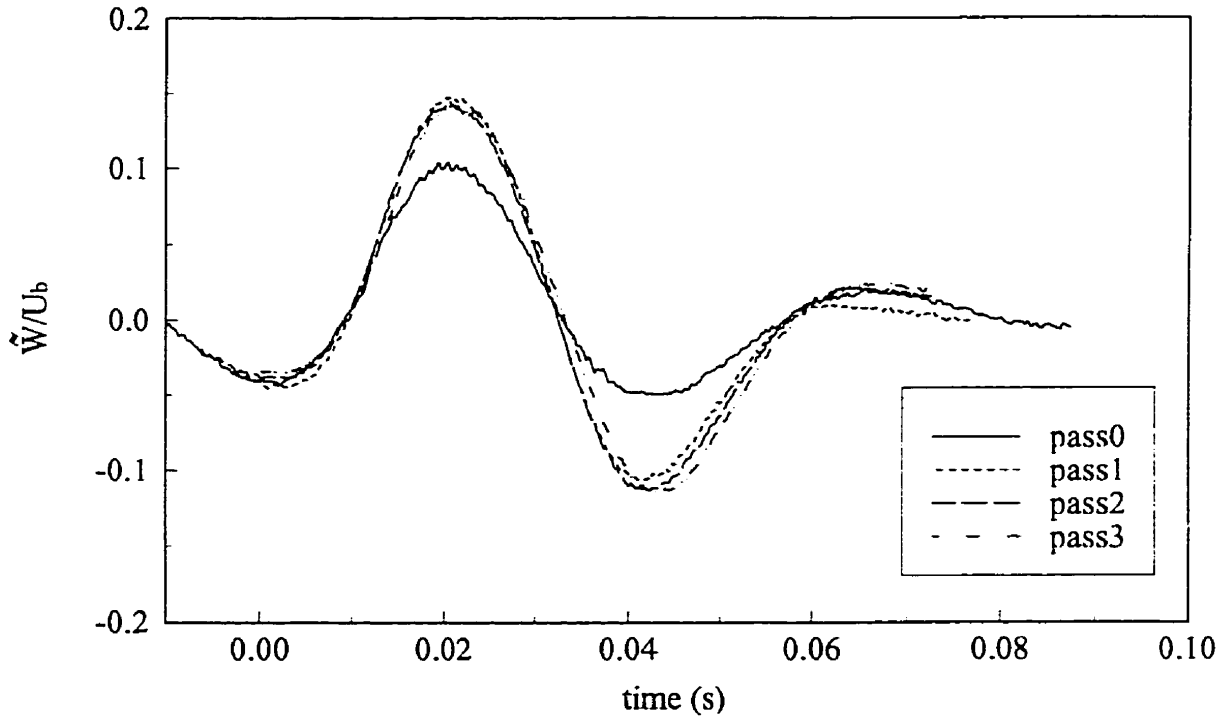

Figure 7.15 Coherent transverse velocity component obtained by VITA (pass 0) and the enhanced VITA after 1, 2 and 3 iterations (passes 1 to 3), for a threshold k=0.7.

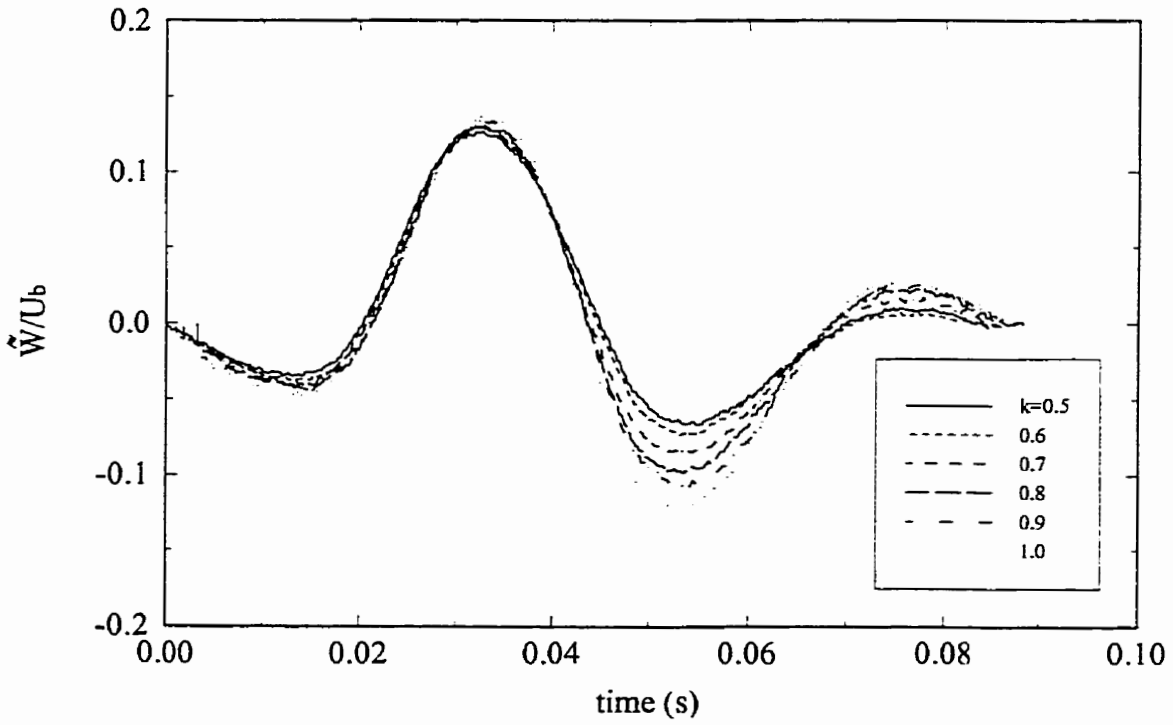

Figure 7.16 Coherent spanwise velocity component obtained, for different threshold values, k, by the enhanced VITA technique.

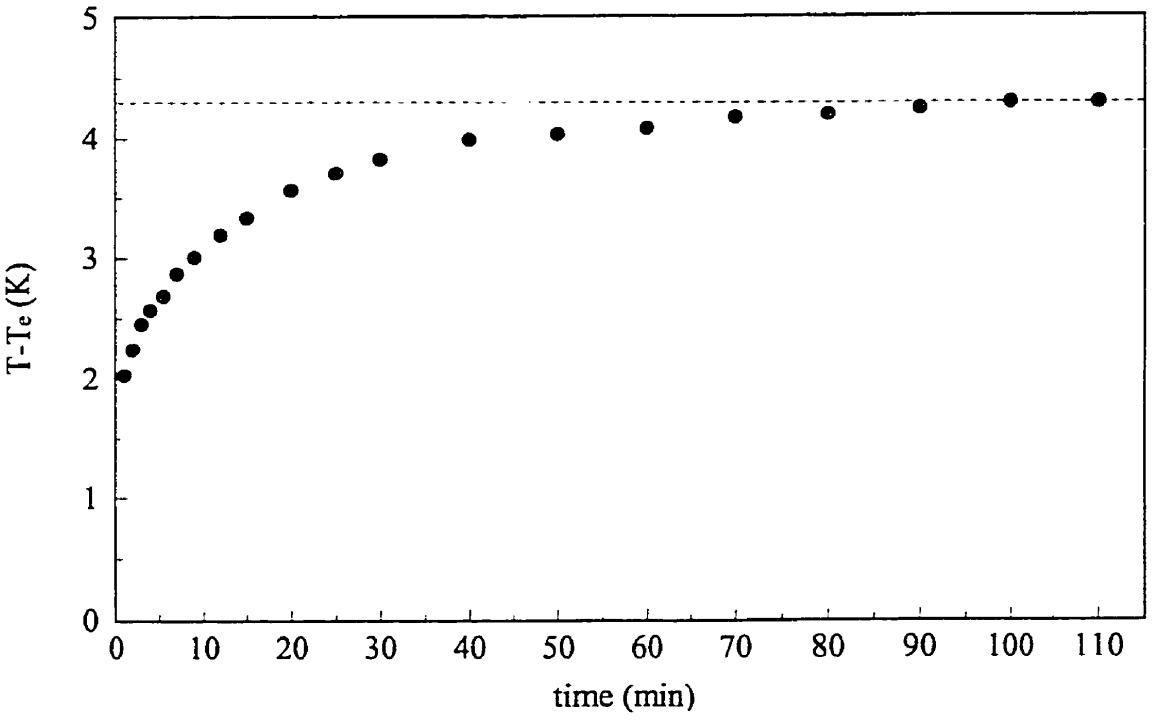

Figure 8.1 Flow temperature as a function of fan operating time.

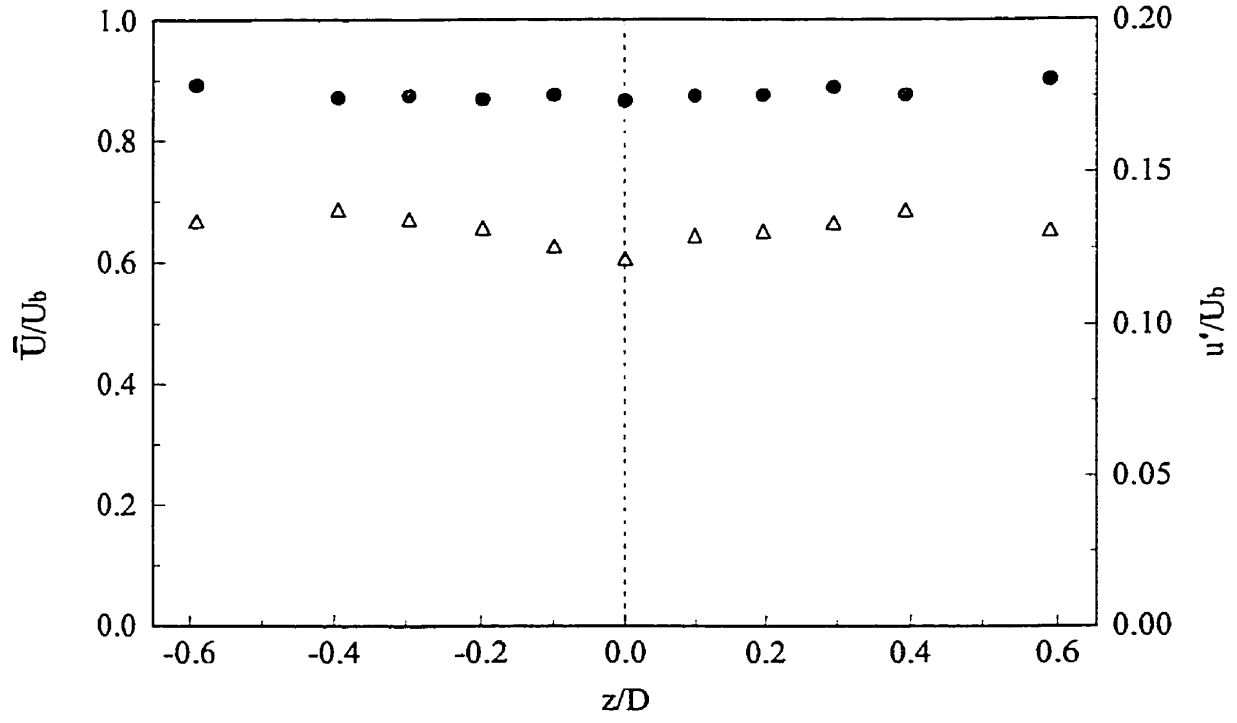

Figure 8.2 Spanwise profiles of the axial mean velocity, ●, and the axial rms velocity fluctuation, △, at *y/D=0.0625. W/D=1.125.*

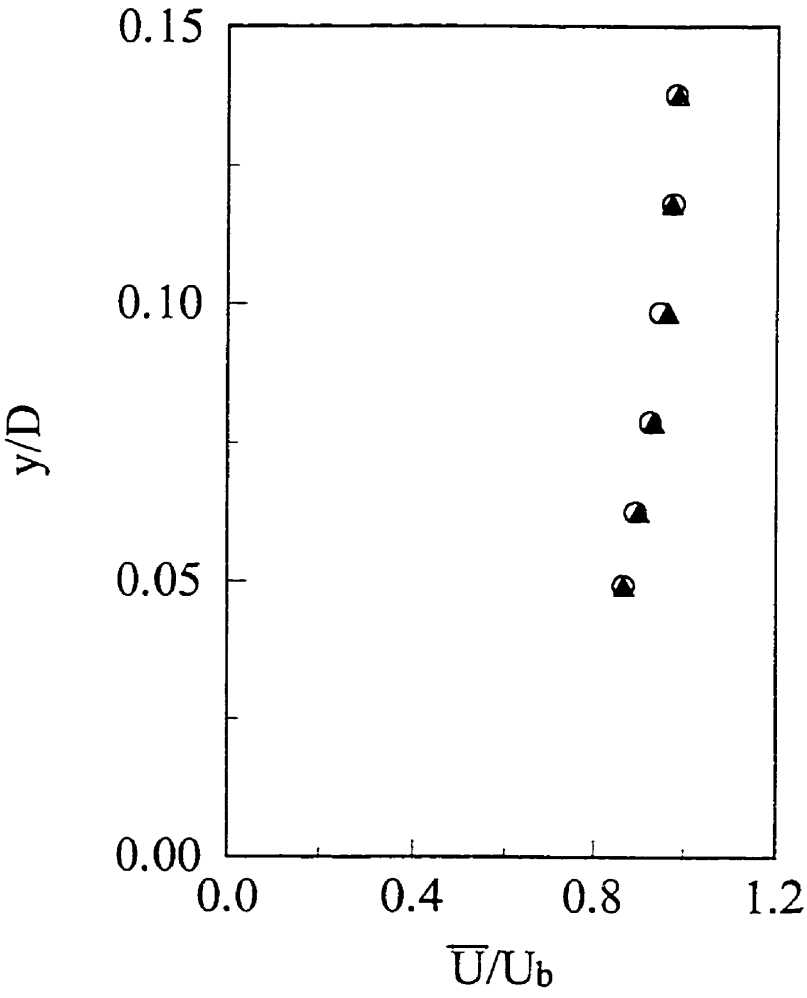

Figure 8.3 Axial velocity profile normal to the channel base for *z/D=0.59* (▲) and *z/D=-0.59* (○) for *W/D=1.125*.

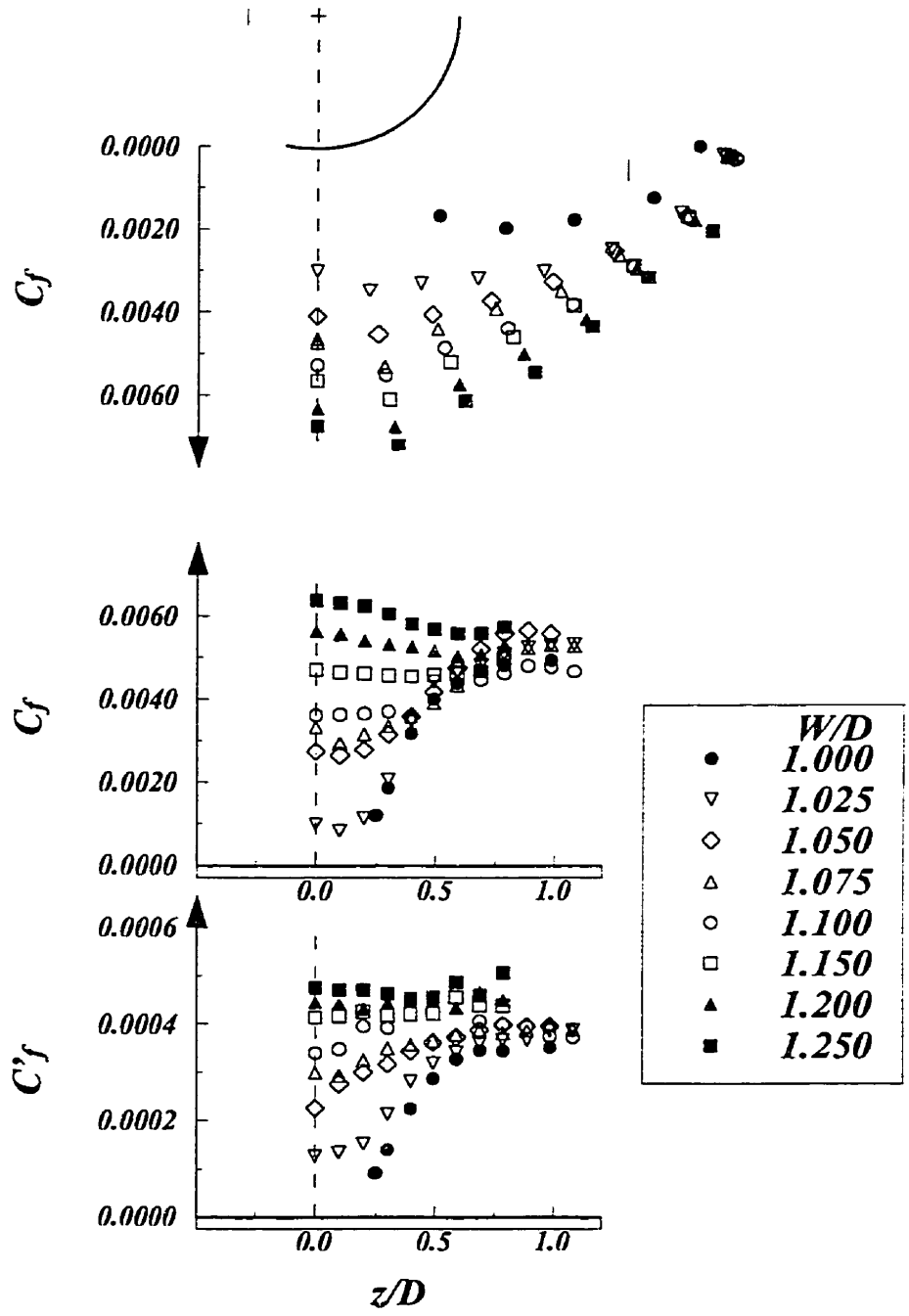

Figure 8.4 Mean wall shear stress around the rod (top; polar coordinates) and along the bottom wall (middle) of the channel; rms wall shear stress along the bottom wall (bottom) of the channel.

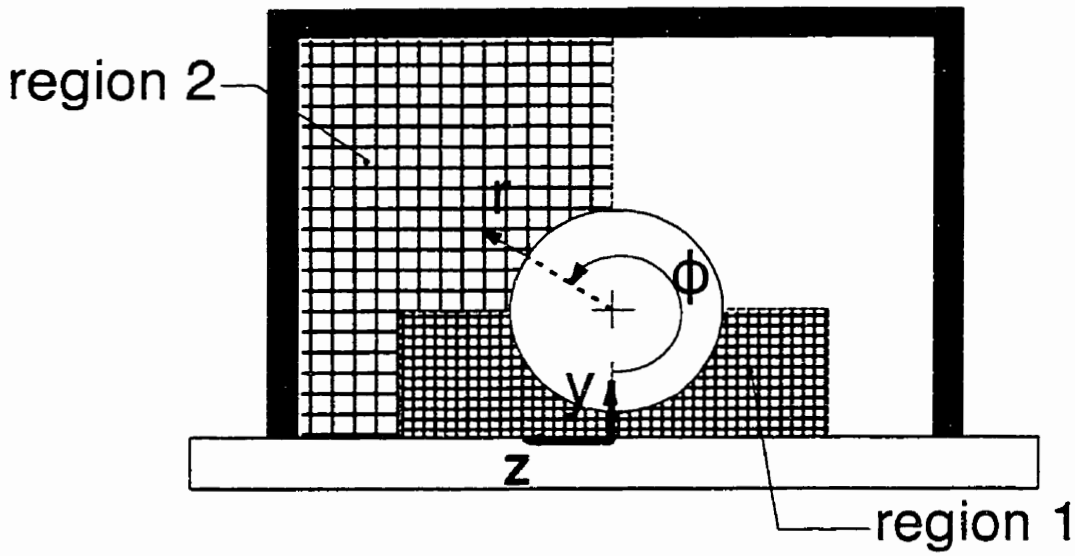

Figure 8.5 Coordinate systems and grid (5×5 mm in region 1 and 10×10 mm in region 2) for the three-sensor probe measurements.

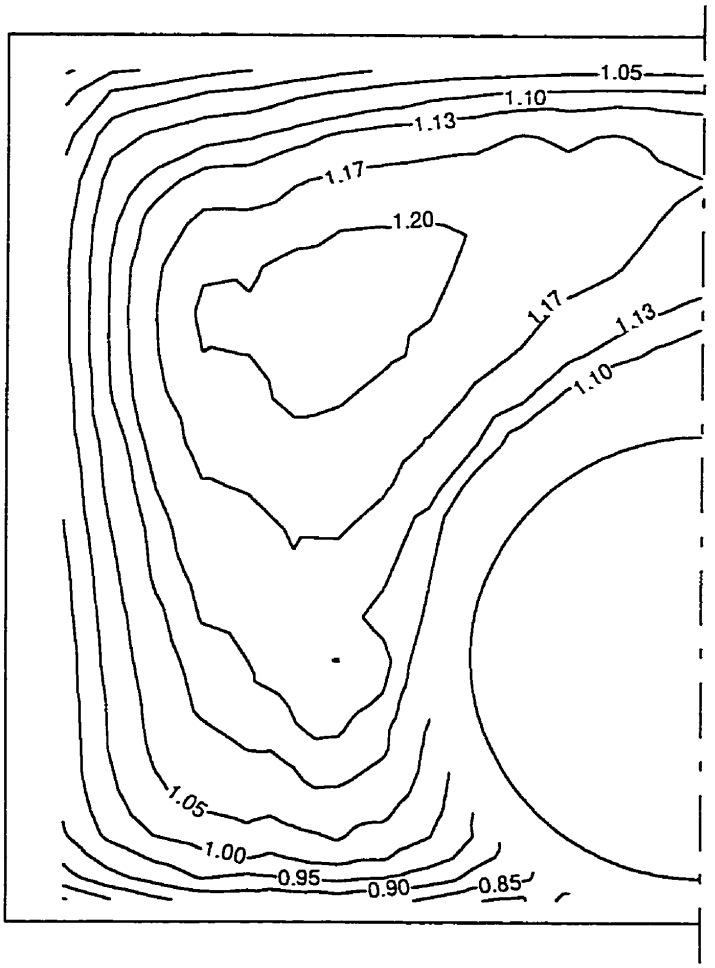

Figure 8.6 Isotachs (contours of constant $\bar{U}/U_b$) for W/D=1.100.

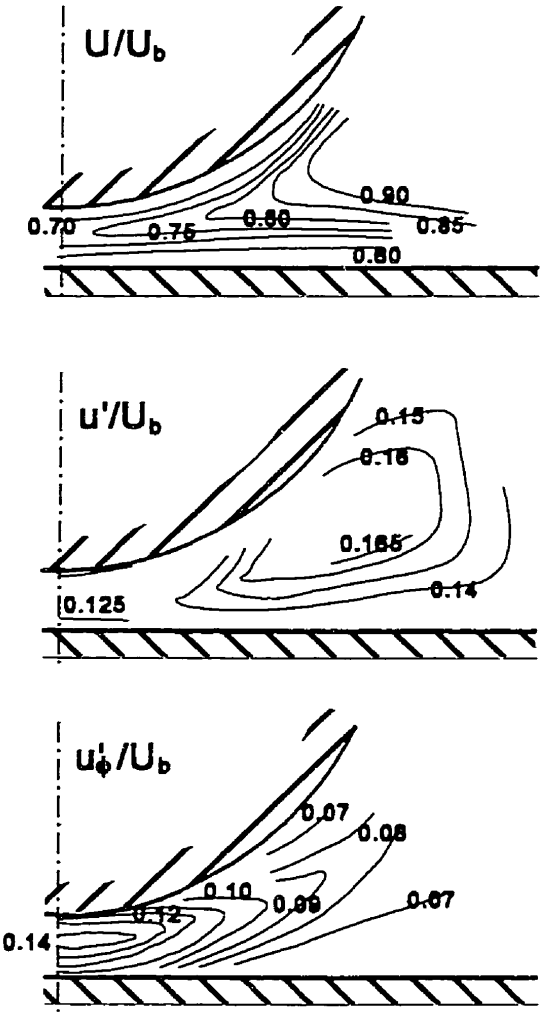

Figure 8.7 Isotachs (contours of constant $\bar{U}/U_b$) and contours of constant axial and azimuthal turbulent intensities (u'/U_b and u_ϕ'/U_b) in the rod-wall gap obtained by the cross-wire probe for W/D=1.100.

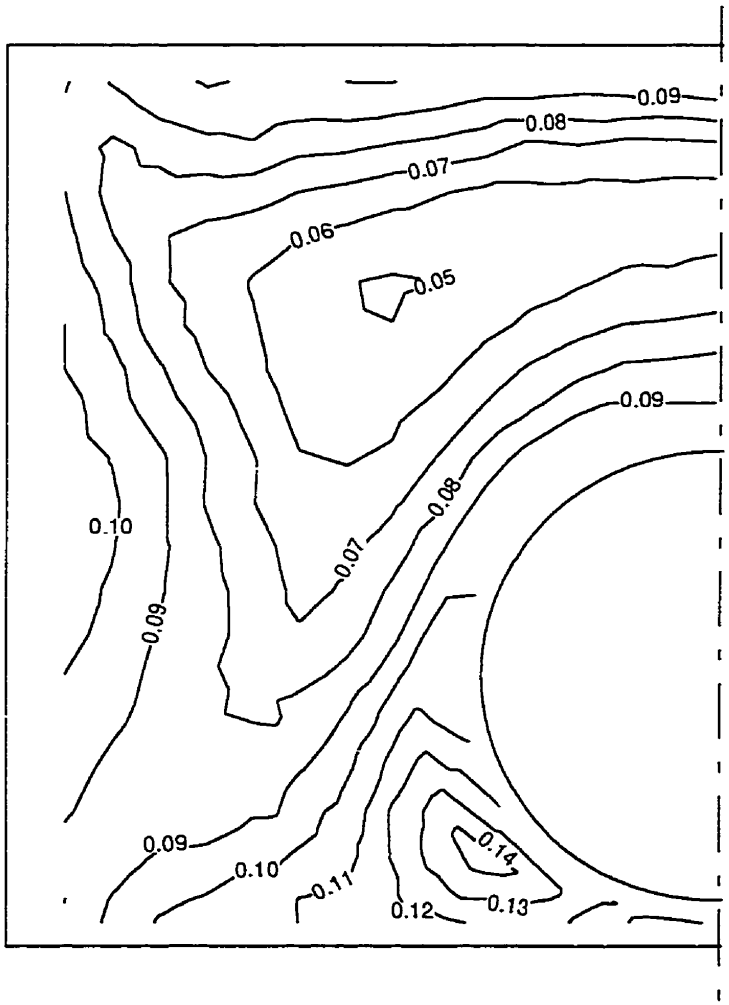

Figure 8.8 Contours of the rms axial turbulent velocity (u'/U_b) for W/D=1.100.

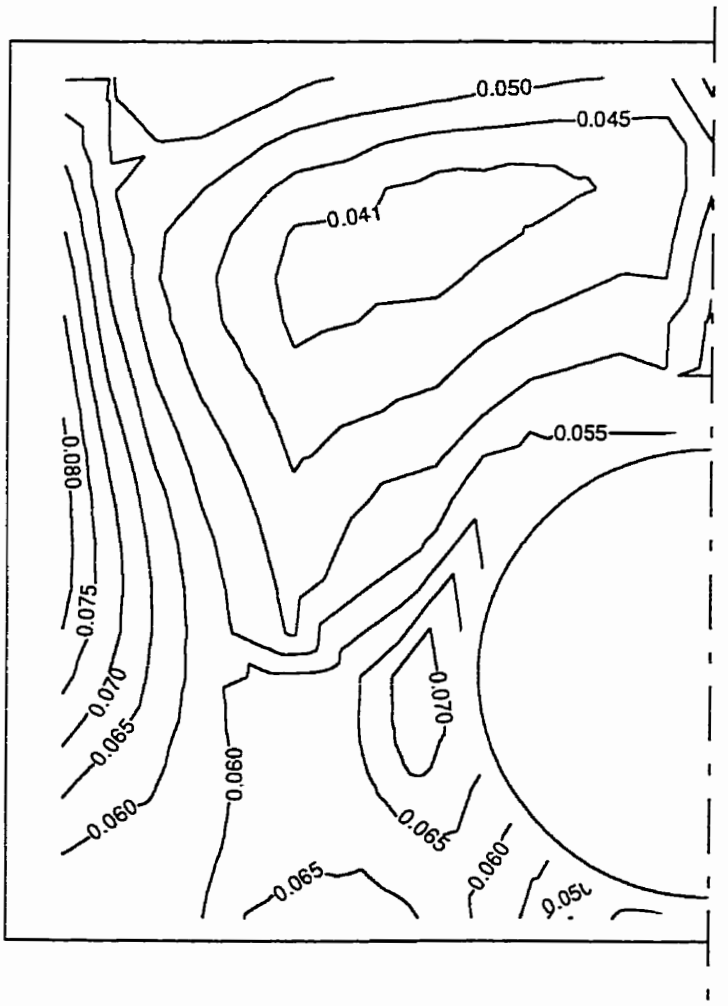

Figure 8.9 Contours of the rms transverse turbulent velocity (v'/U_b) for W/D=1.100.

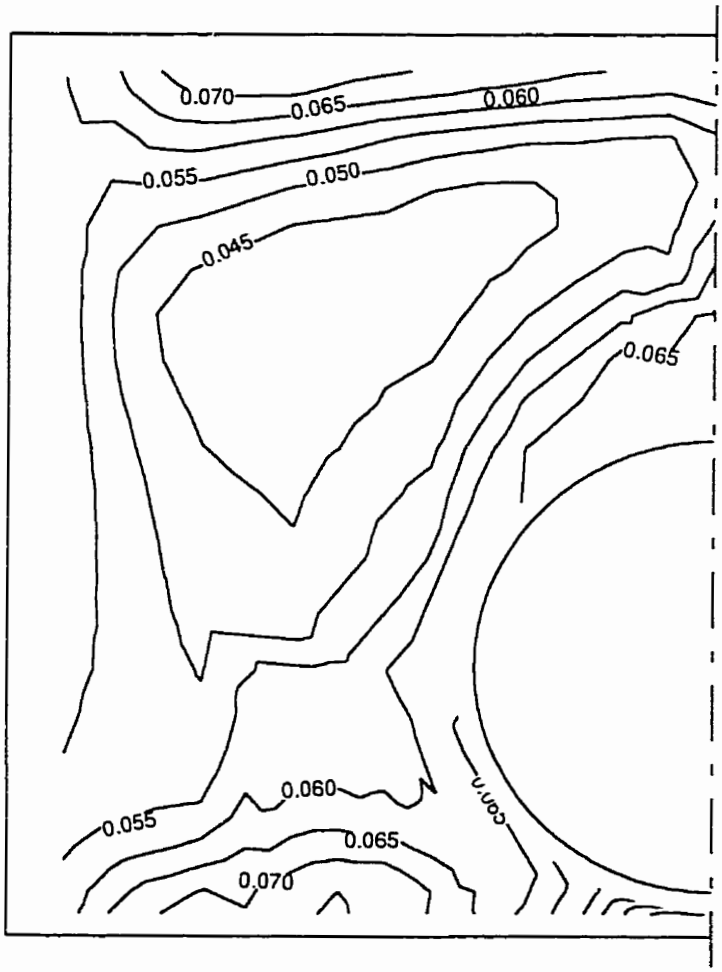

Figure 8.10 Contours of the rms spanwise turbulent velocity (w'/U_b) for W/D=1.100.

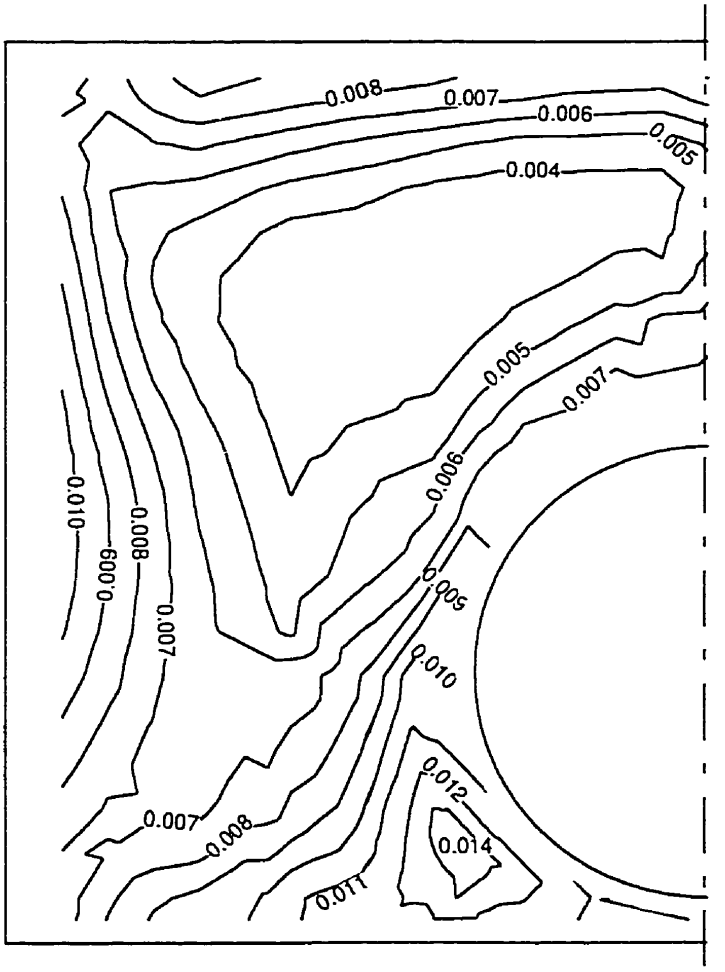

Figure 8.11 Contours of constant turbulent kinetic energy (k/U_b^2) for W/D=1.100.

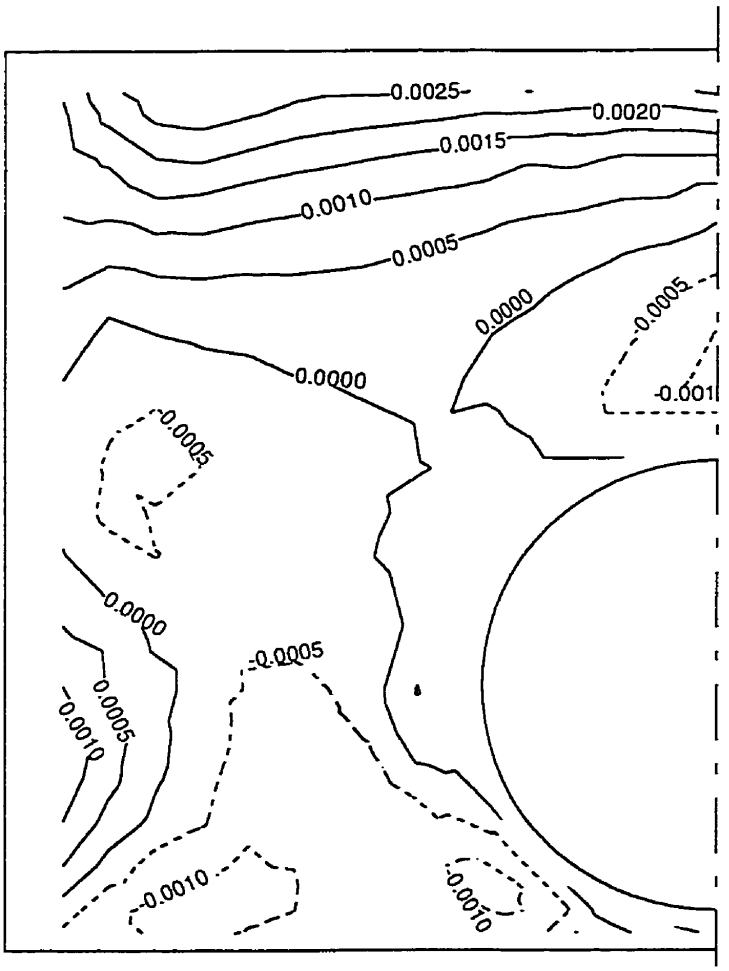

Figure 8.12 Contours of constant turbulent shear stress, $\overline{uv}/U_b^2$, for W/D=1.100.

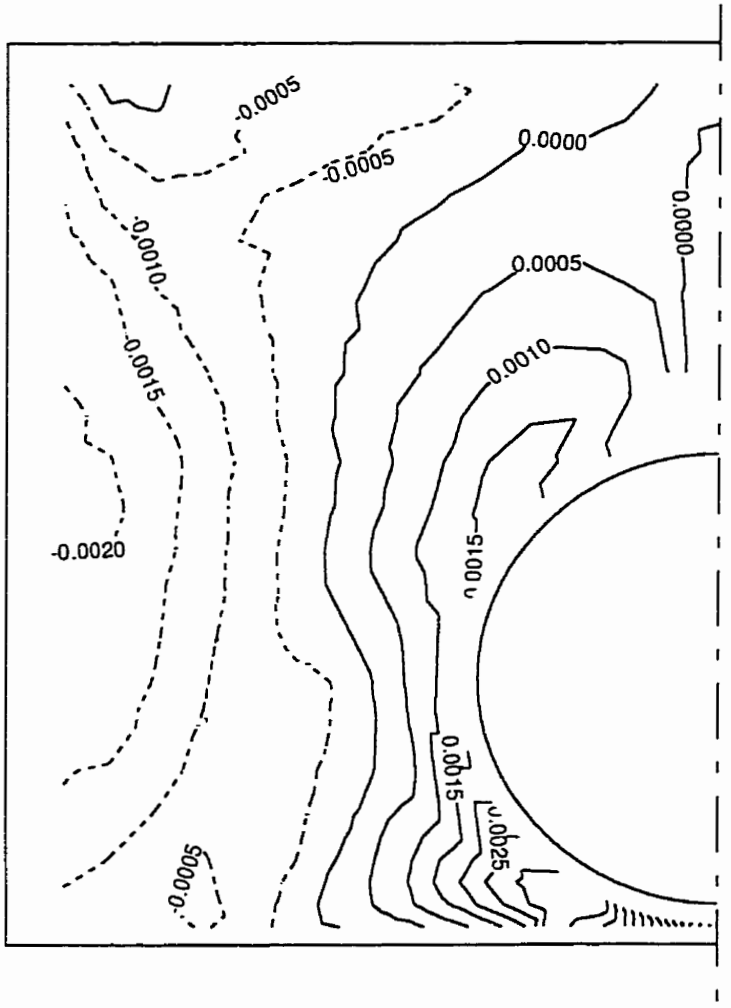

Figure 8.13 Contours of constant turbulent shear stress, $\overline{uw}/U_b^2$, for W/D=1.100.

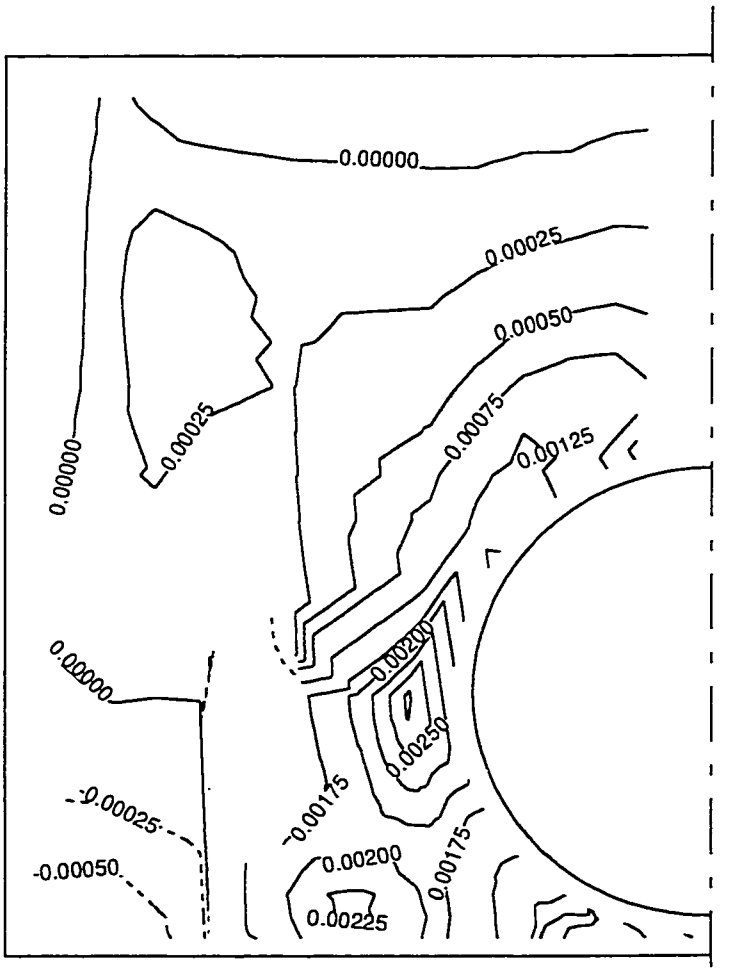

Figure 8.14 Contours of constant turbulent shear stress, $\overline{vw}/U_b^2$, for W/D=1.100.

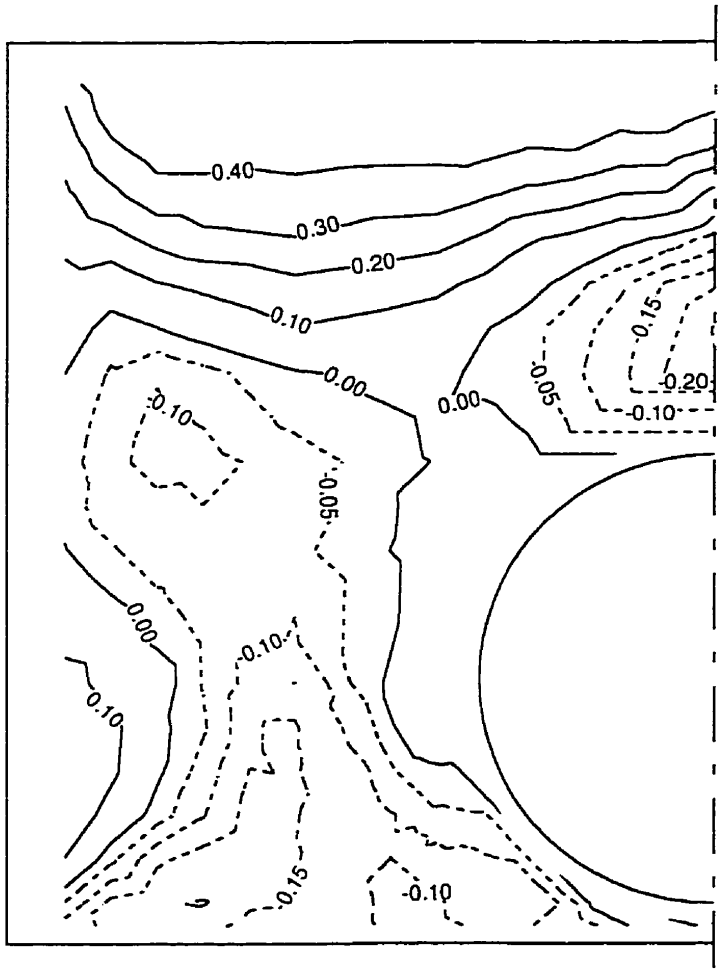

Figure 8.15 Contours of constant shear stress correlation coefficient $\overline{uv}/u'v'$, for W/D=1.100.

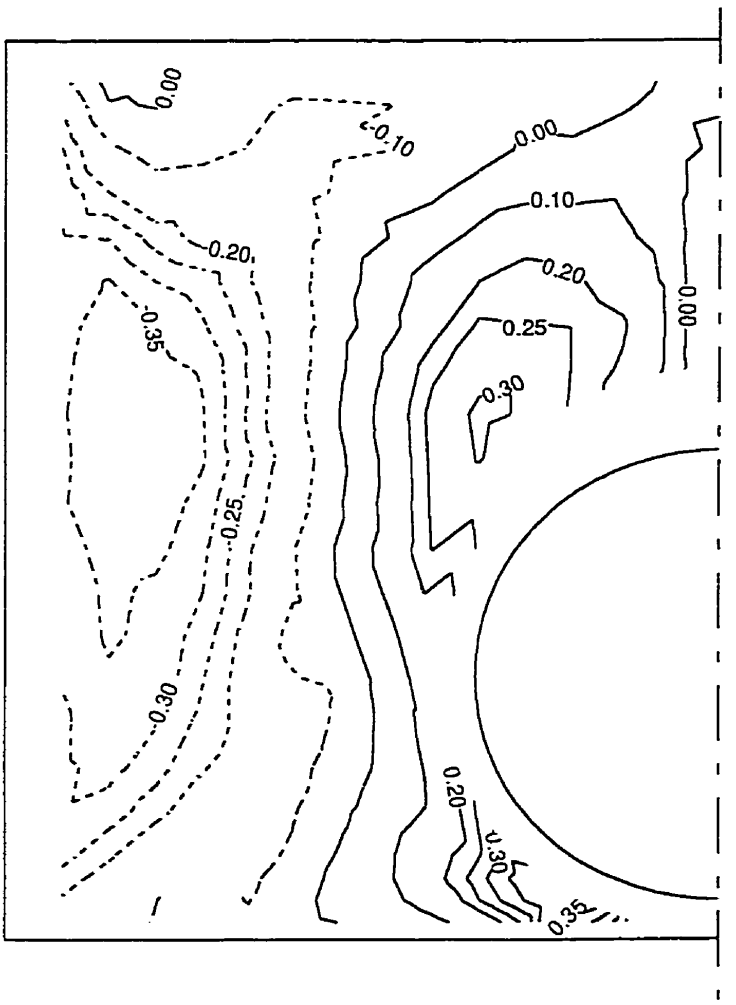

Figure 8.16 Contours of constant shear stress correlation coefficient, $\overline{uw}/u'w'$, for W/D=1.100.

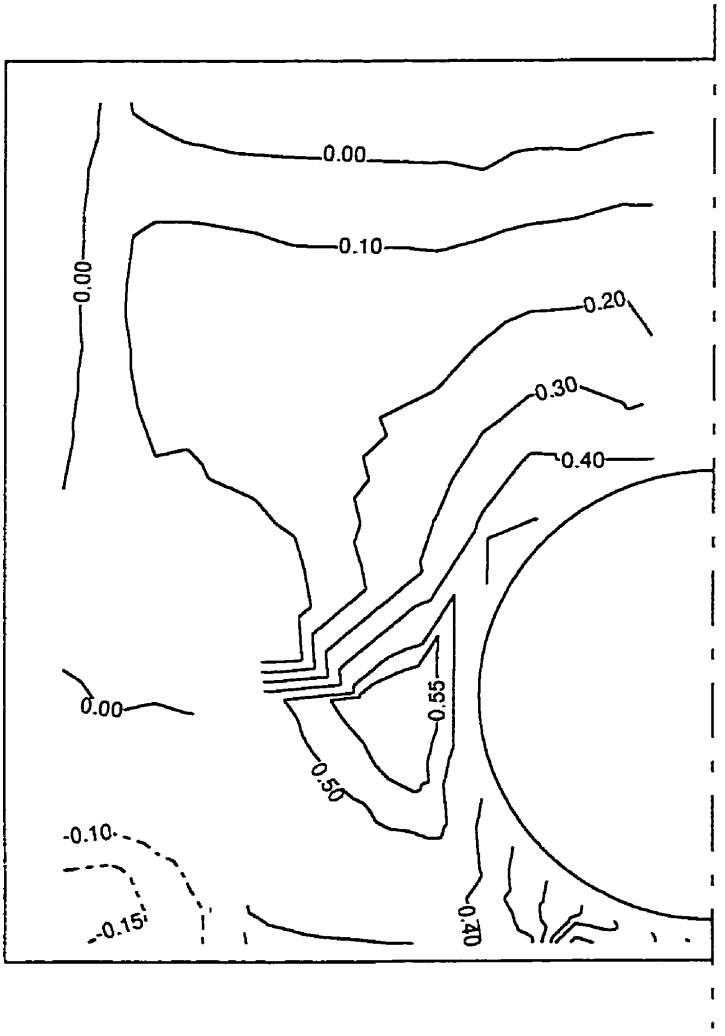

Figure 8.17 Contours of constant shear stress correlation coefficient, $\overline{vw}/v'w'$, for W/D=1.100.

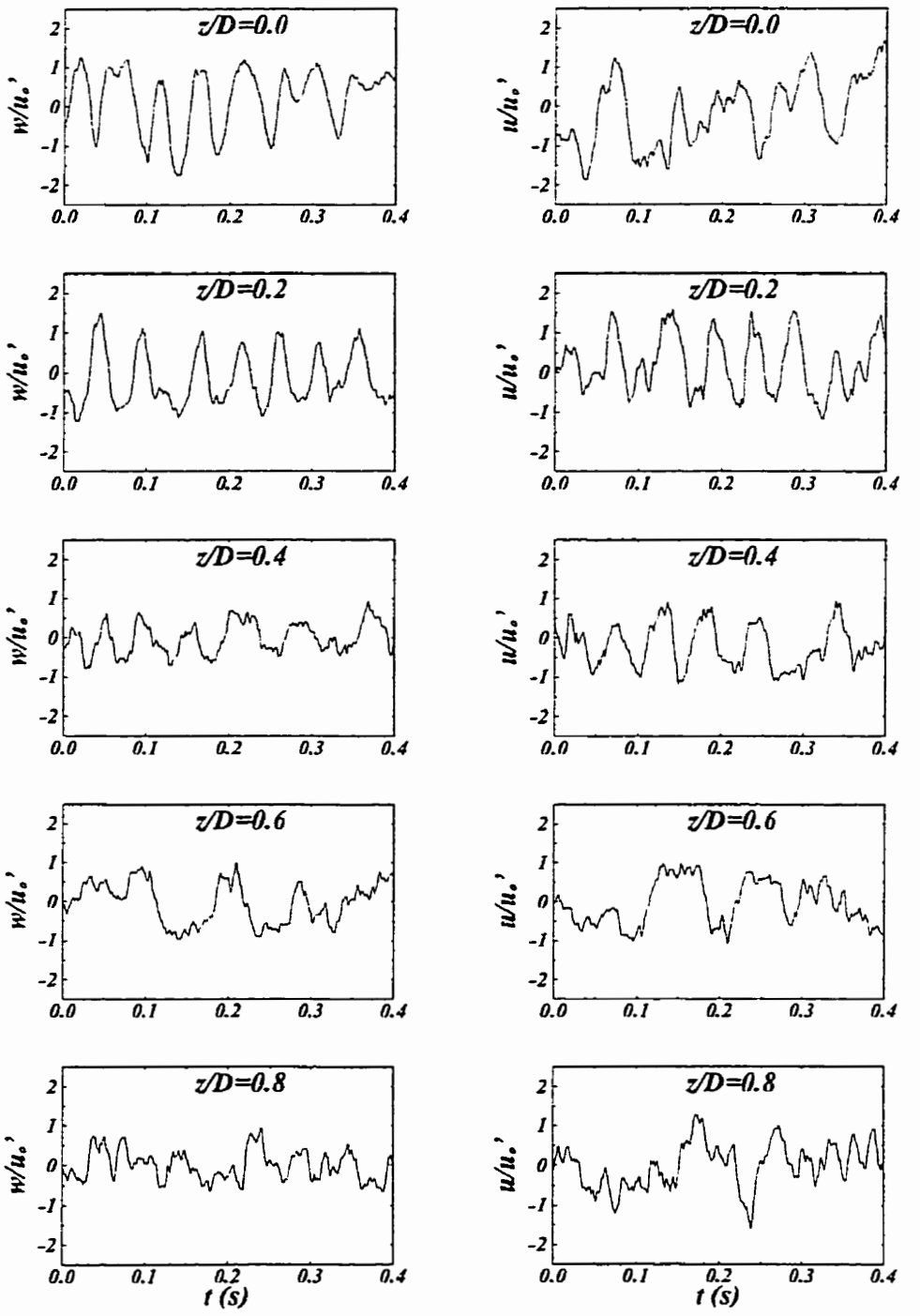

Figure 8.18 Spanwise and streamwise velocity traces at several transverse positions, normalized by the rms streamwise velocity, u_0', at z/D=0.0 (W/D=1.100 and y/D=0.050).

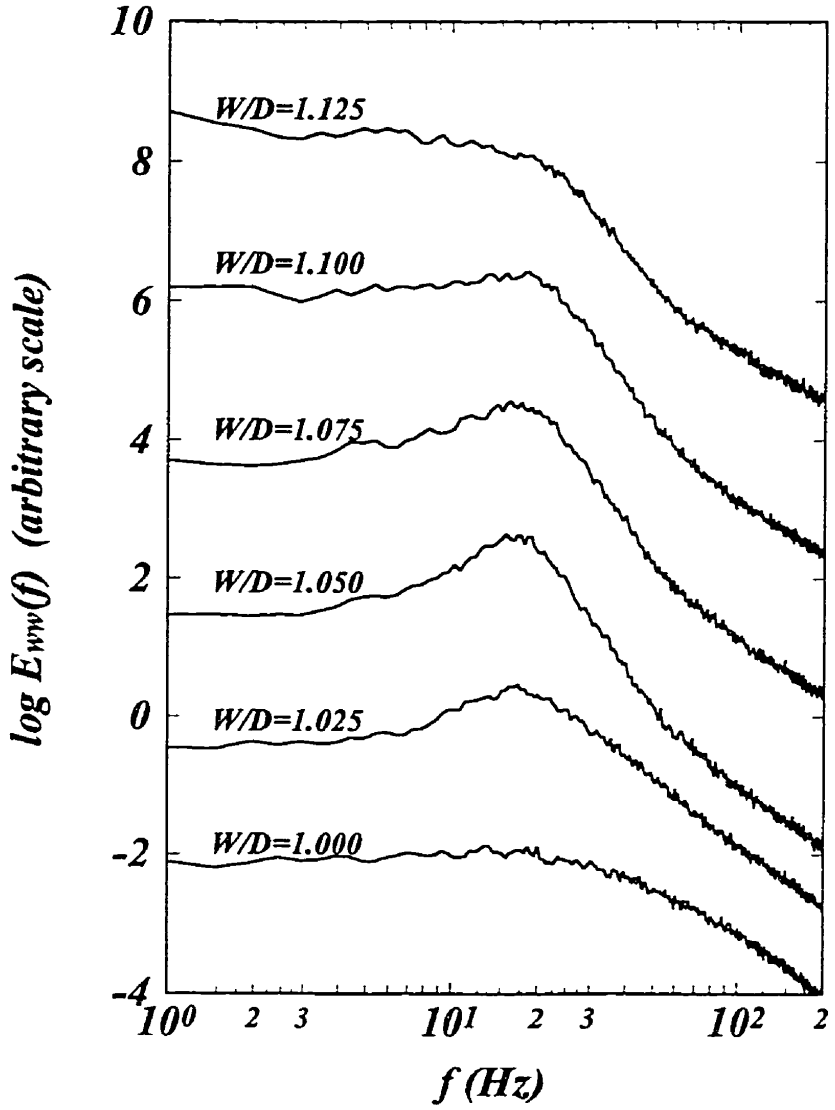

Figure 8.19 Power spectra of the spanwise velocity component at the center of the gap, except for the cases with W/D=1.000 and 1.025, for which z/D=0.25 (arbitrary scale; different spectra have been staggered by two decades).

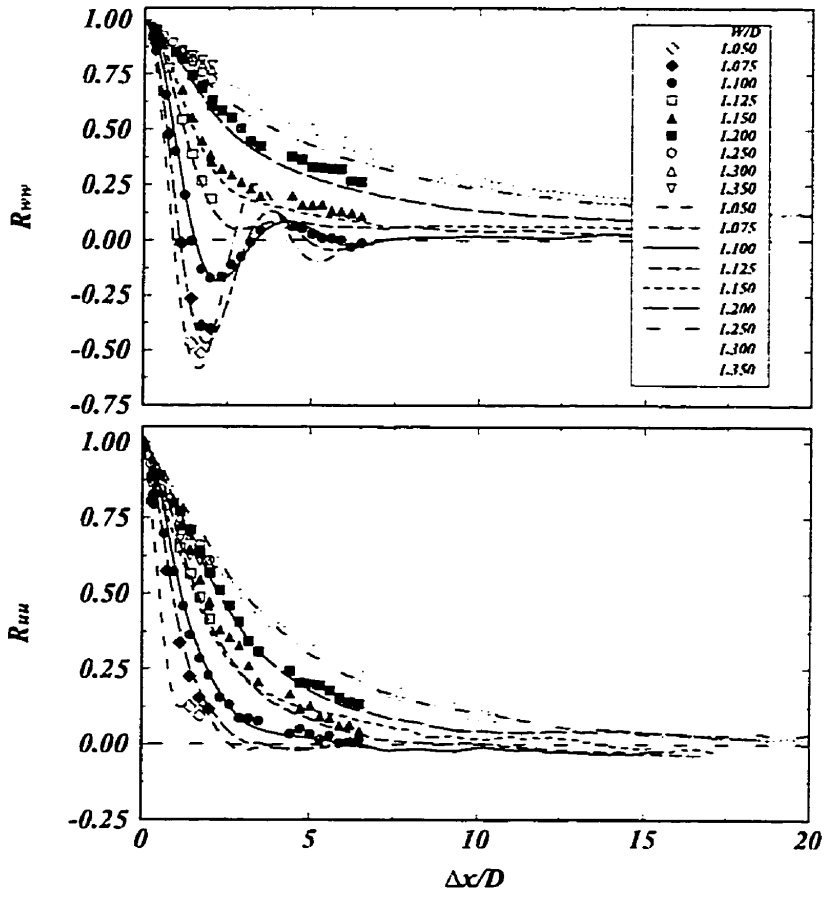

Figure 8.20 Two-point velocity correlations measured for several gap widths with the two probes aligned on the symmetry plane of the test section. Symbols represent actual measurements, while lines are estimates from corresponding single-point time correlations.

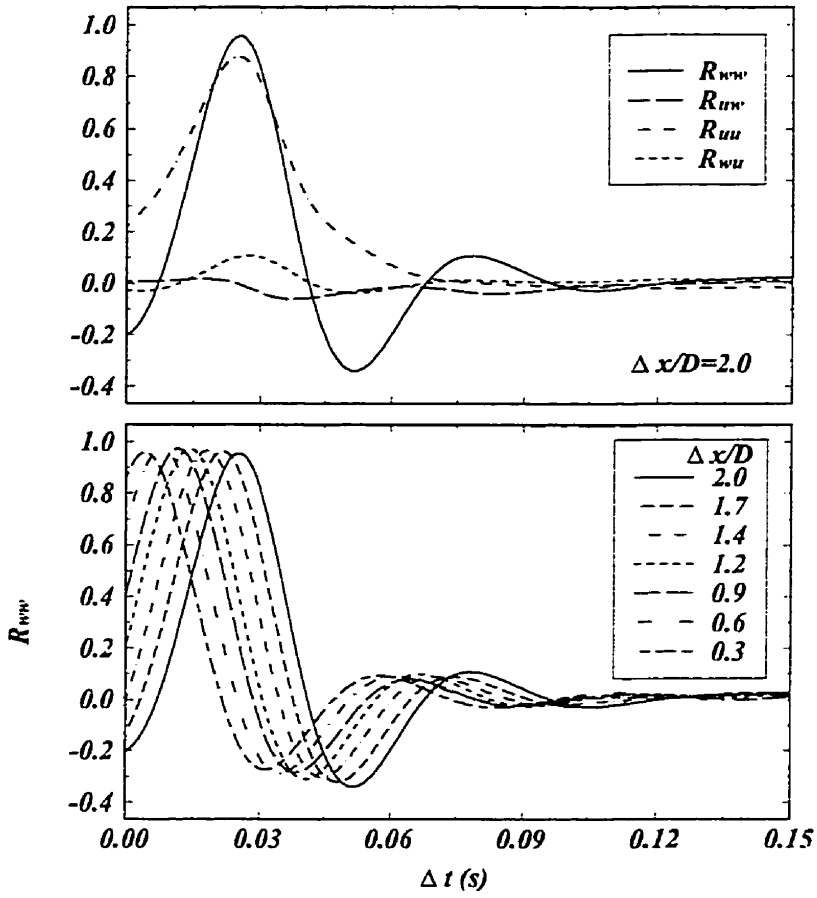

Figure 8.21 Space-time correlations with both probes located on the centreplane (W/D=1.100).

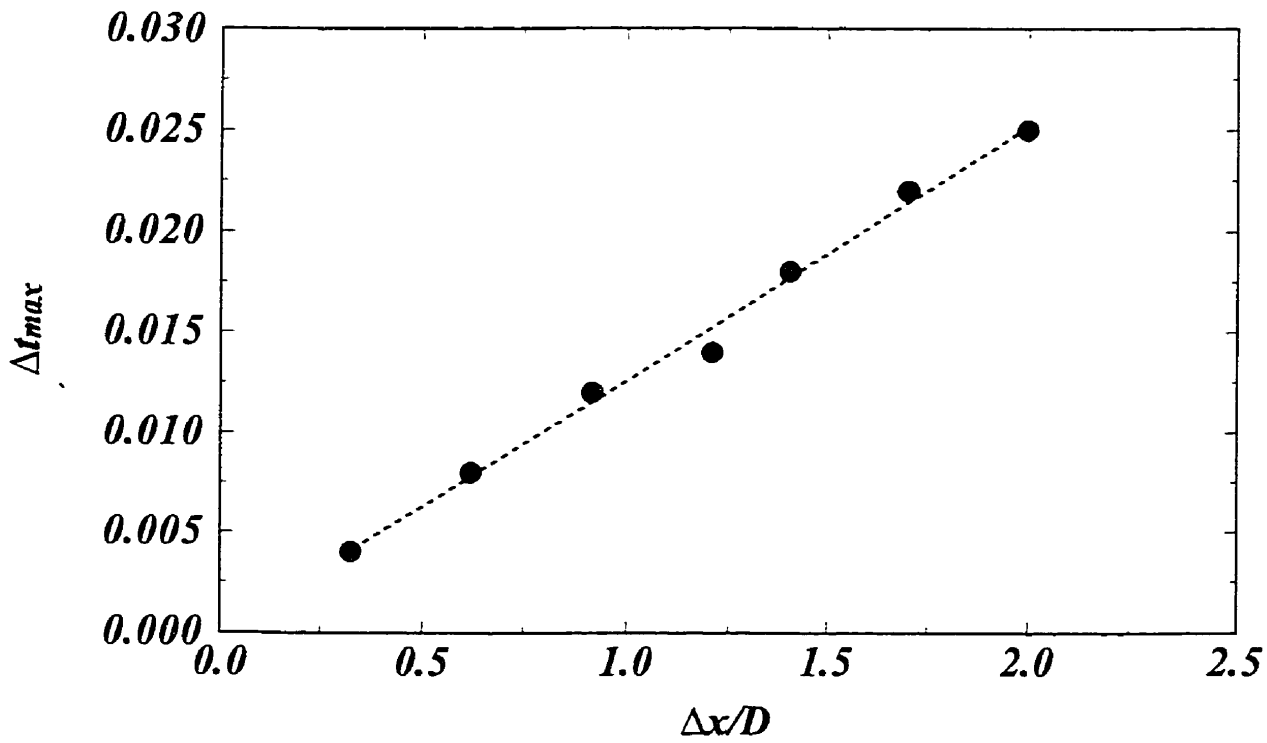

Figure 8.22 Time delay corresponding to the maximum correlation, R_{www}, as a function of streamwise probe separation (W/D=1.100).

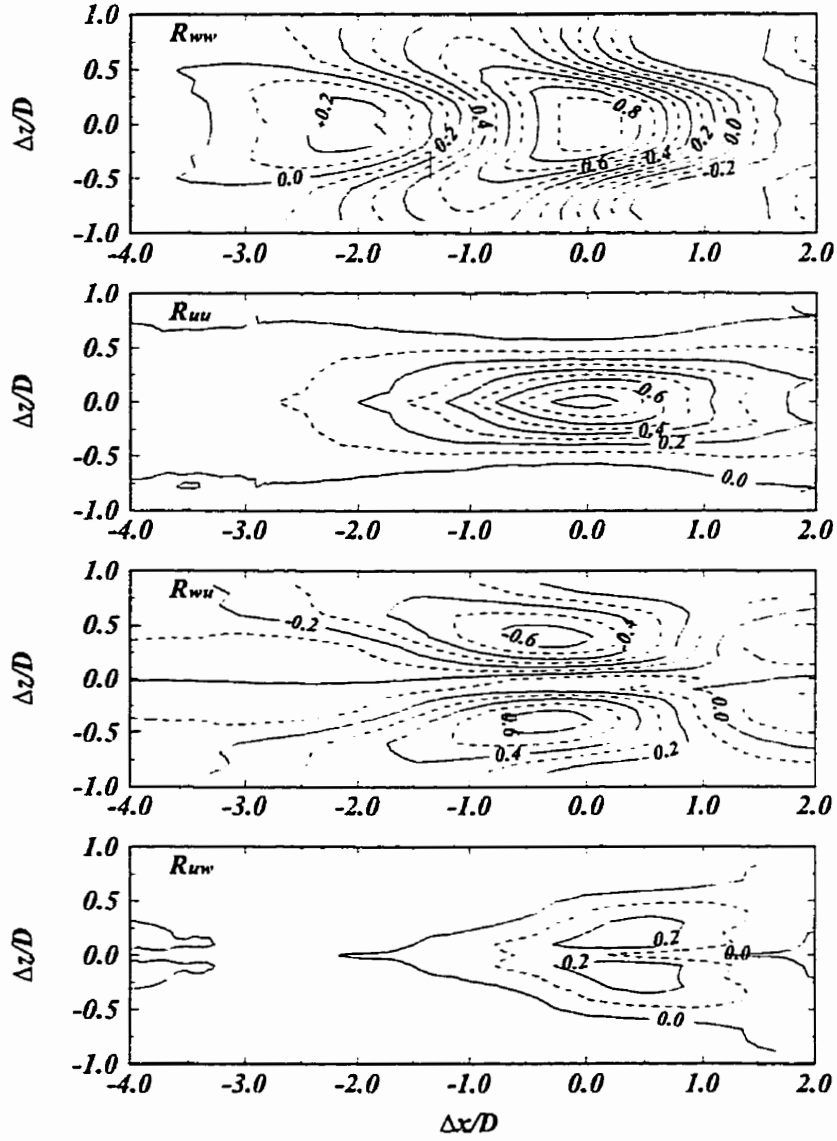

Figure 8.23 Iso-correlation contours for W/D=1.100.

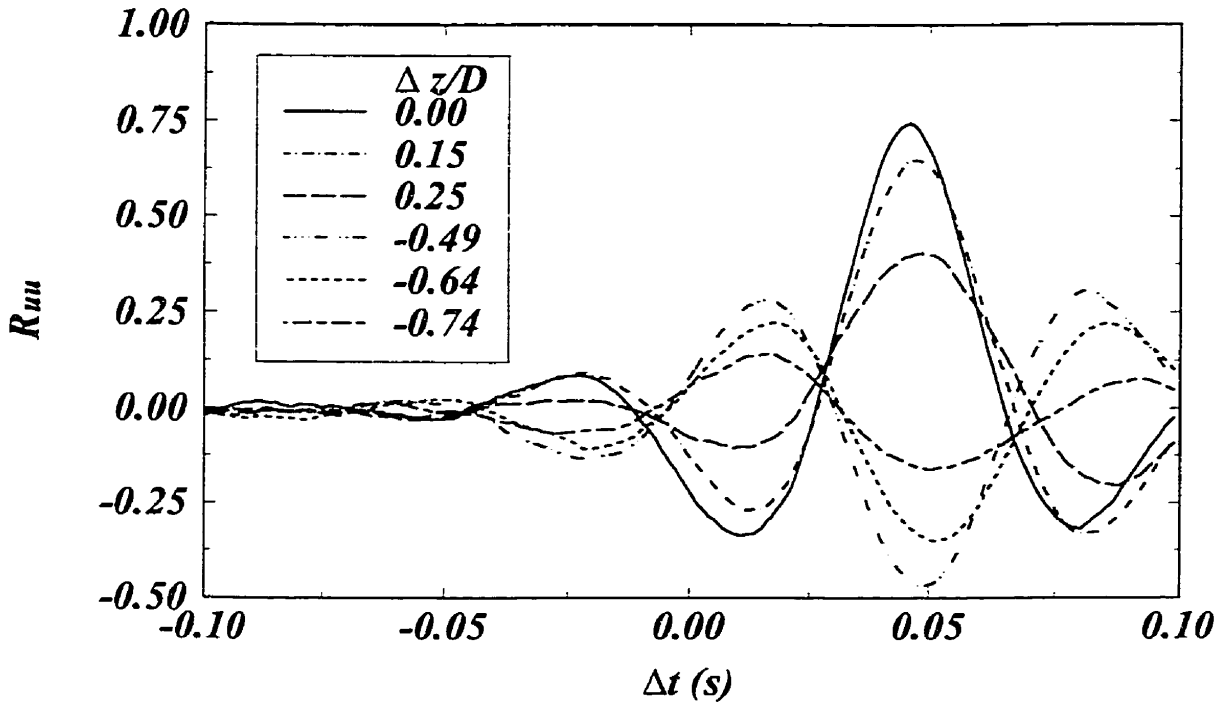

Figure 8.24 Space-time correlations R_{uu} (z/D=0.25; $\Delta x/D$=2.0; W/D=1.025).

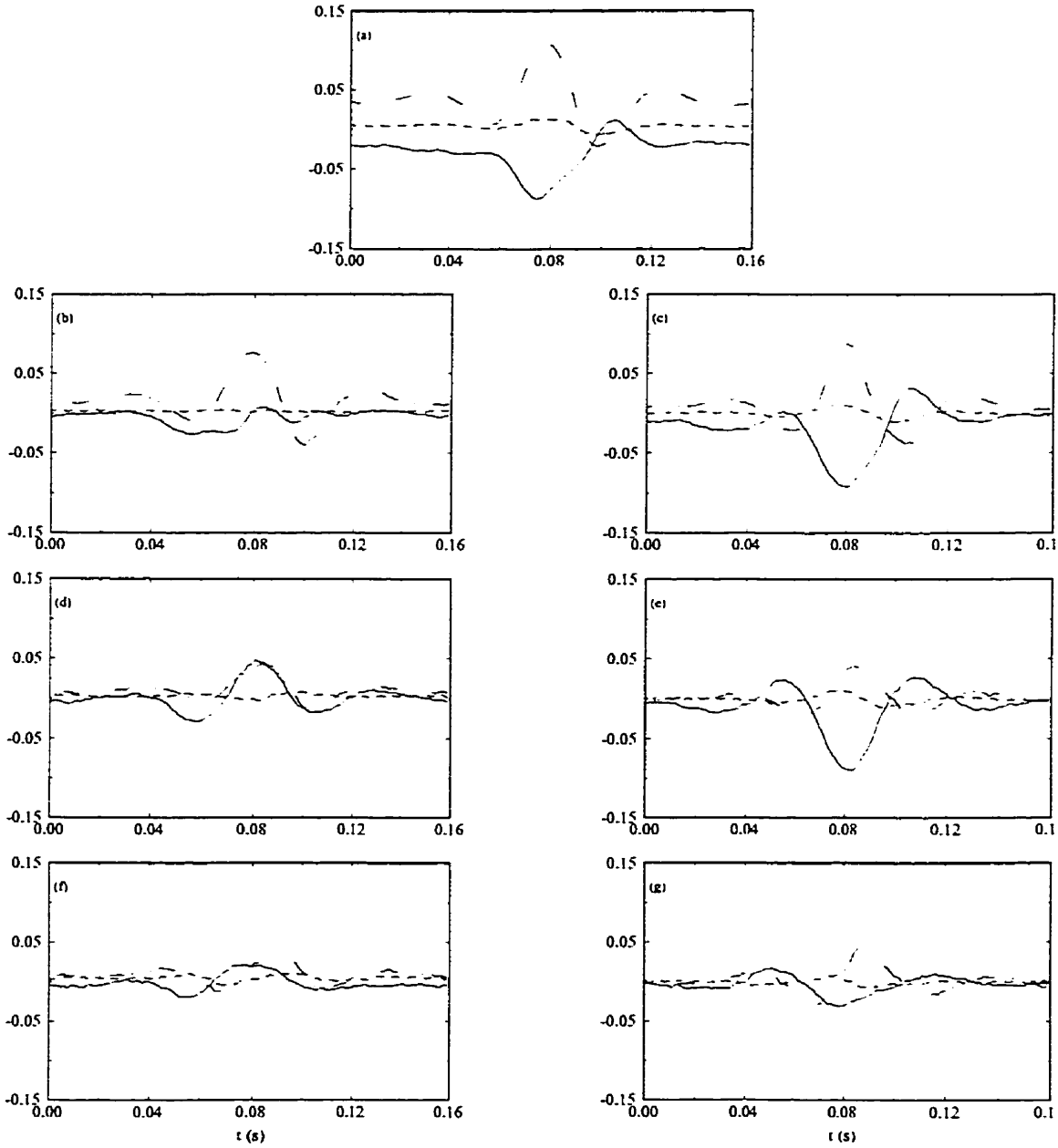

Figure 8.25 Examples of educed coherent velocities $\tilde{U}/U_b$ (———), $\tilde{V}/U_b$ (----) and $\tilde{W}/U_b$ (·····) at (a) y/D=0.050 and z/D=0.000,(b) y/D=0.050 and z/D=-0.200,(c) y/D=0.050 and z/D=0.200,(d) y/D=0.050 and z/D=-0.400,(e) y/D=0.050 and z/D=0.400,(f) y/D=0.050 and z/D=-0.600,(g) y/D=0.050 and z/D=0.600.

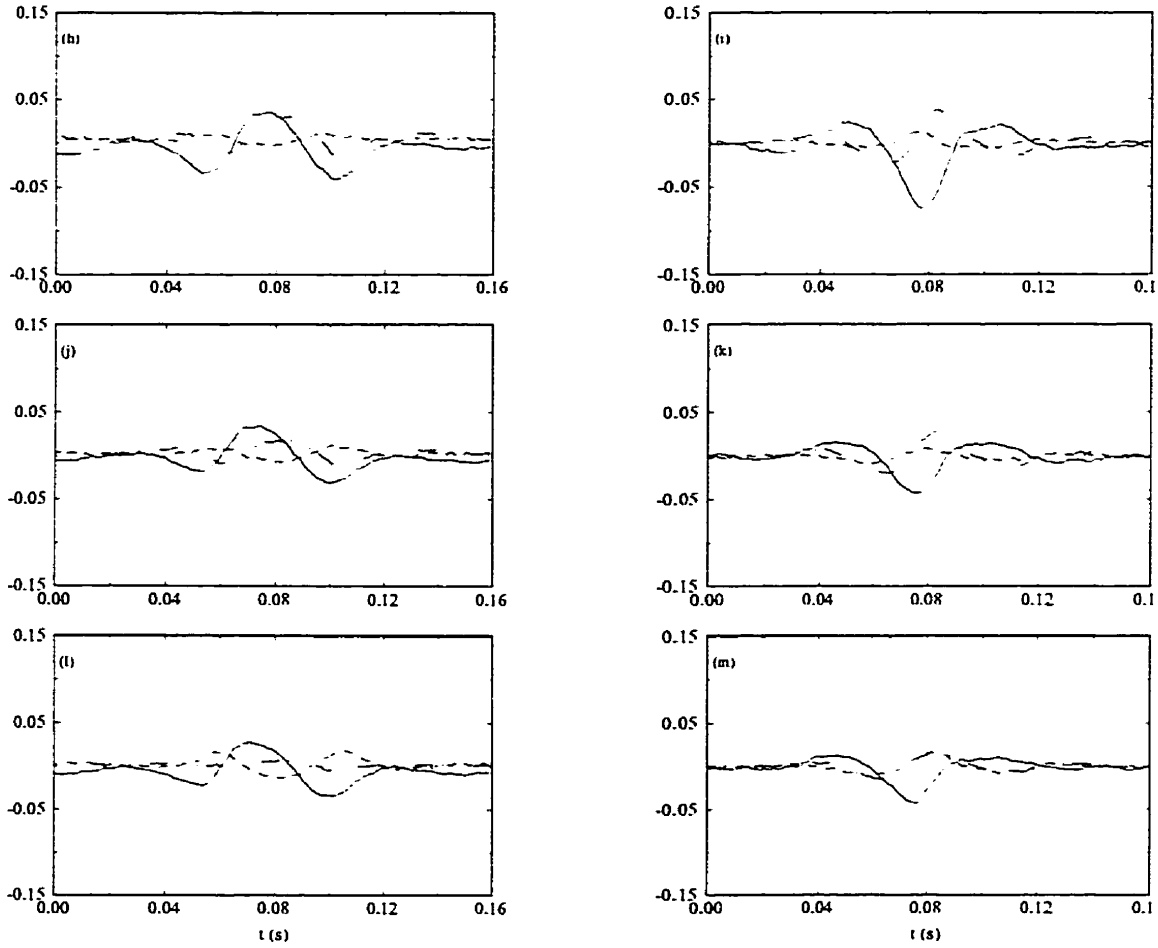

Figure 8.25 (continued): (h) y/D=0.100, z/D=-0.600, (i) y/D=0.100, z/D=0.600, (j) y/D=0.200 and z/D=-0.700,(k) y/D=0.200 and z/D=0.700, (l) y/D=0.300 and z/D=-0.700 and (m) y/D=0.300 and z/D=0.700

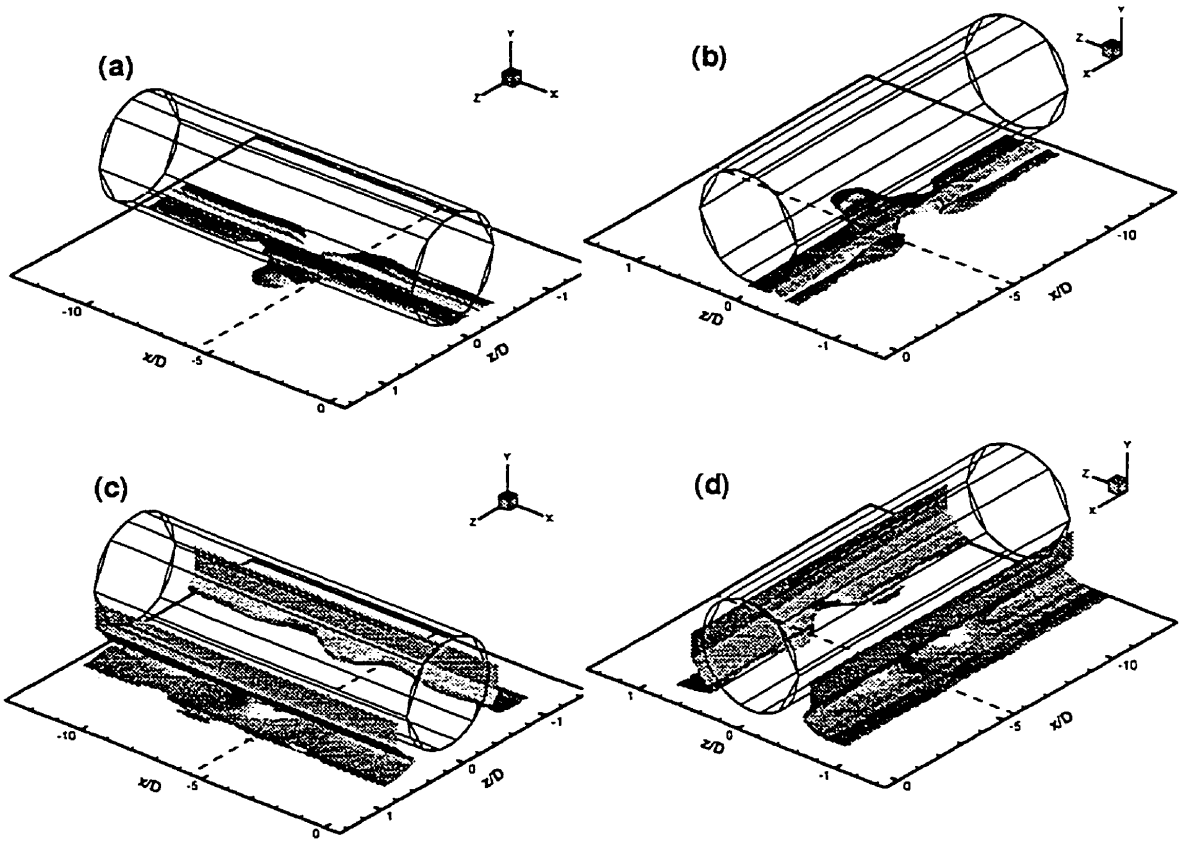

Figure 8.26 Iso-surfaces of $(\langle U \rangle - U_c)/U_b$ for W/D=1.100; (a) and (b) -0.050, and (c) and (d) +0.100 (the dashed lines represent the detection location).

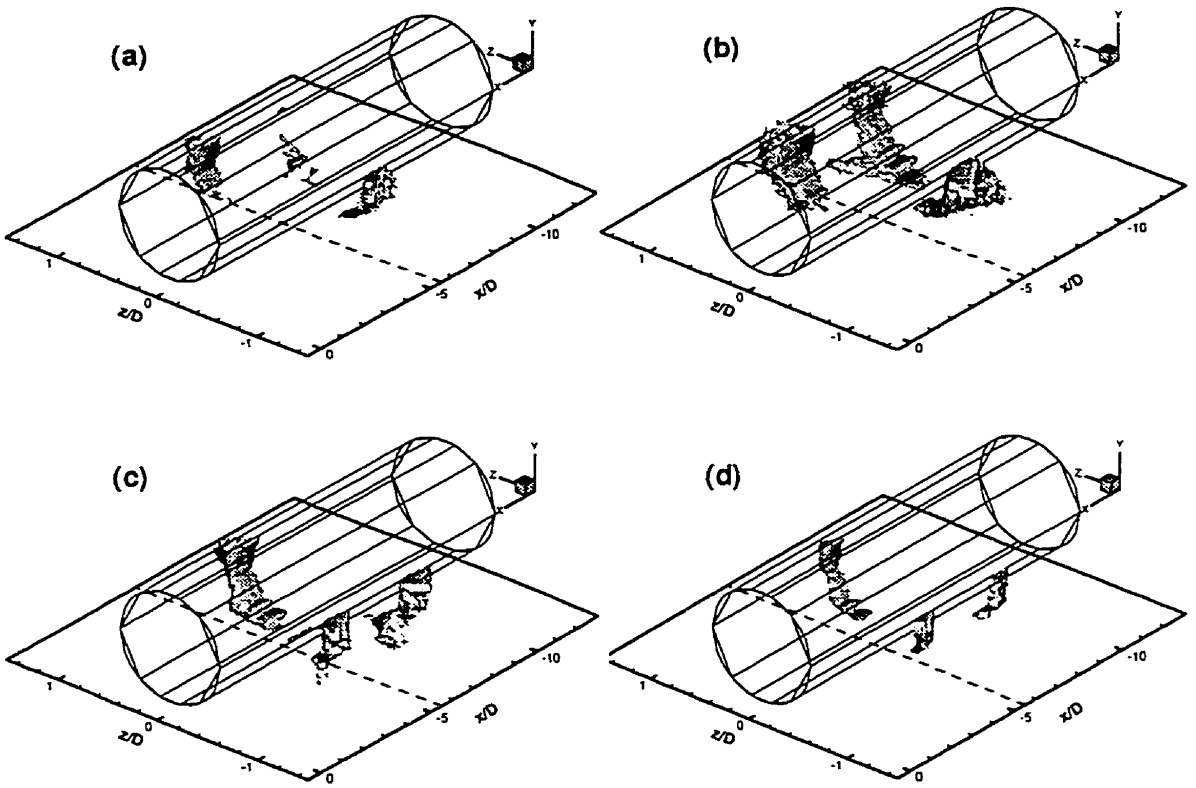

Figure 8.27 Iso-surfaces of $\langle V \rangle / U_b$ for W/D=1.100; (a) -0.010, (b) -0.005, (c) +0.010 and (d) +0.015 (the dashed lines represent the detection location).

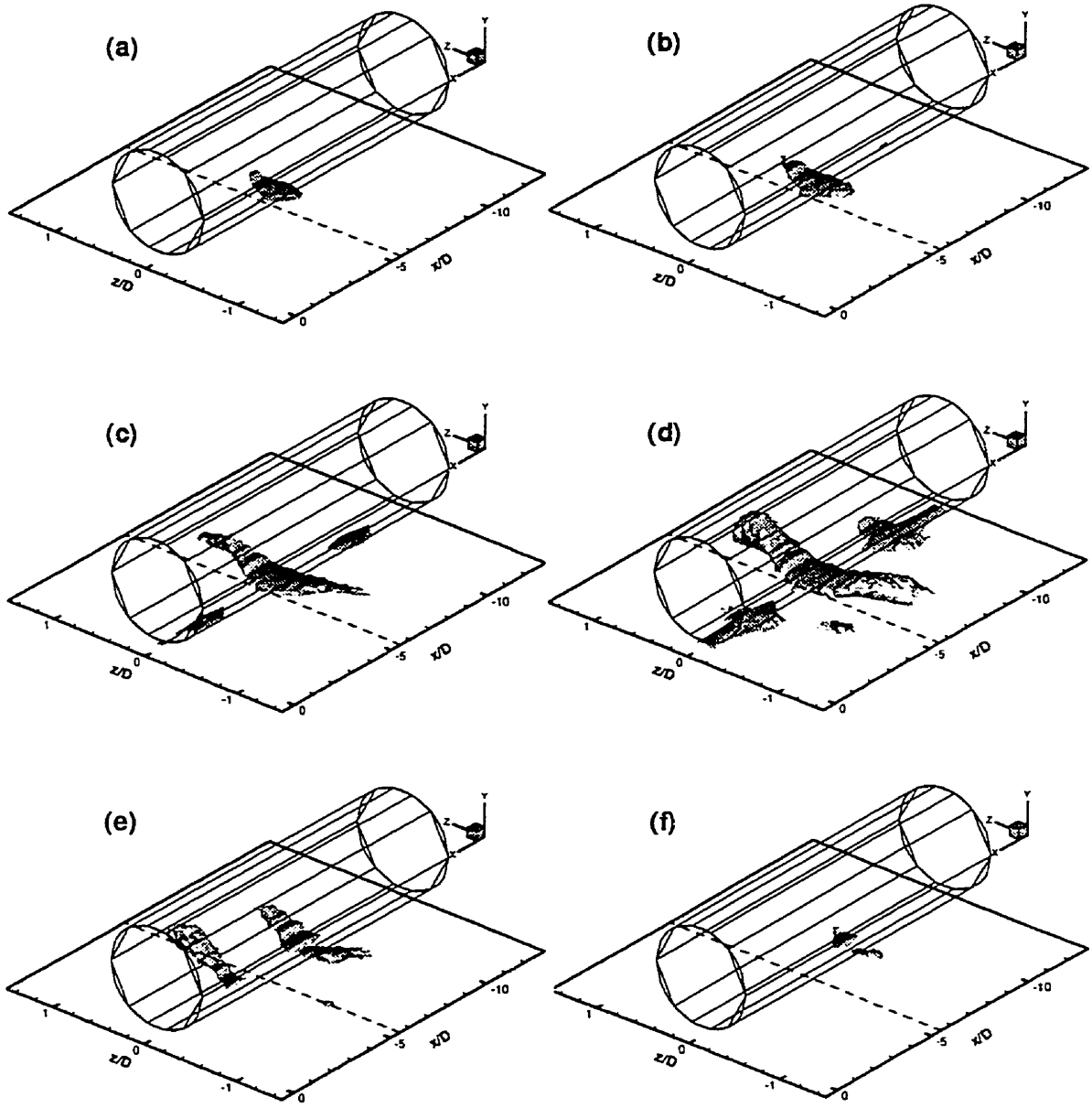

Figure 8.28 Iso-surfaces of $\langle W \rangle / U_b$ for W/D=1.100; (a) +0.065, (b) +0.050, (c) +0.035, (d) +0.015, (e) -0.015, and (f) -0.035 (the dashed lines represent the detection location).

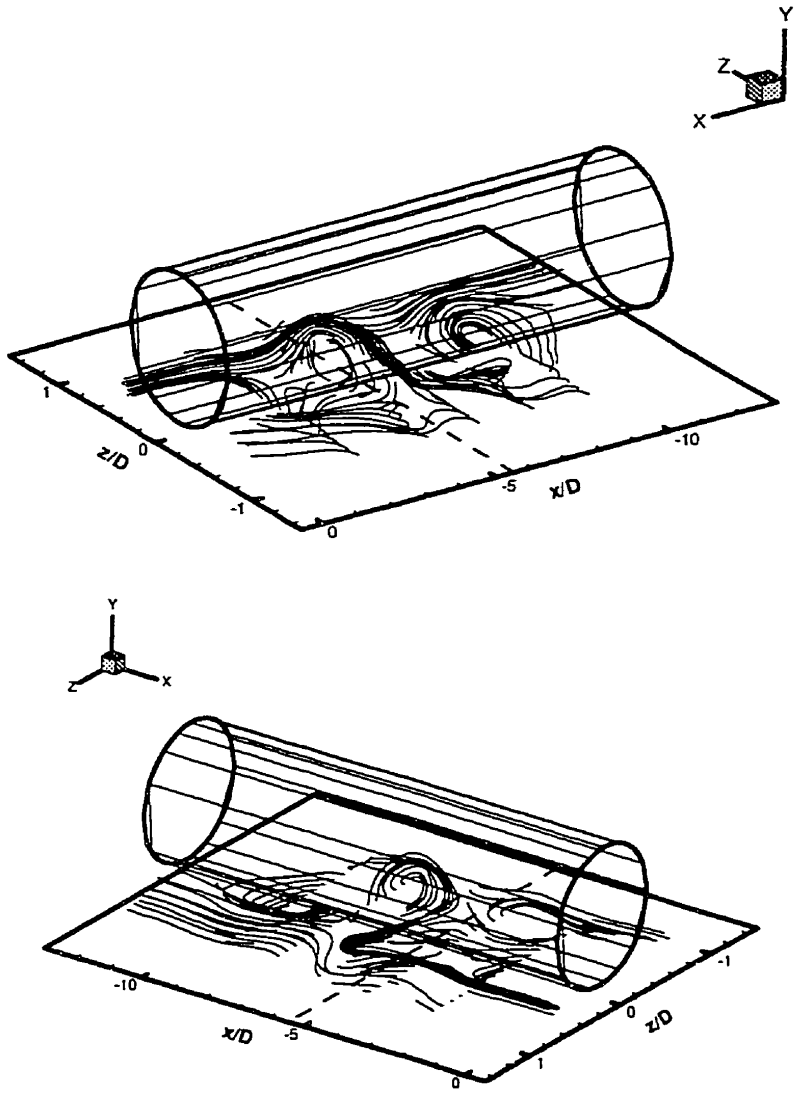

Figure 8.29 Software generated pathlines, based on the measured coherent velocity field for *W/D*=1.100, as seen by an observer travelling with the convective speed of the structures (the dashed lines represent the detection location).

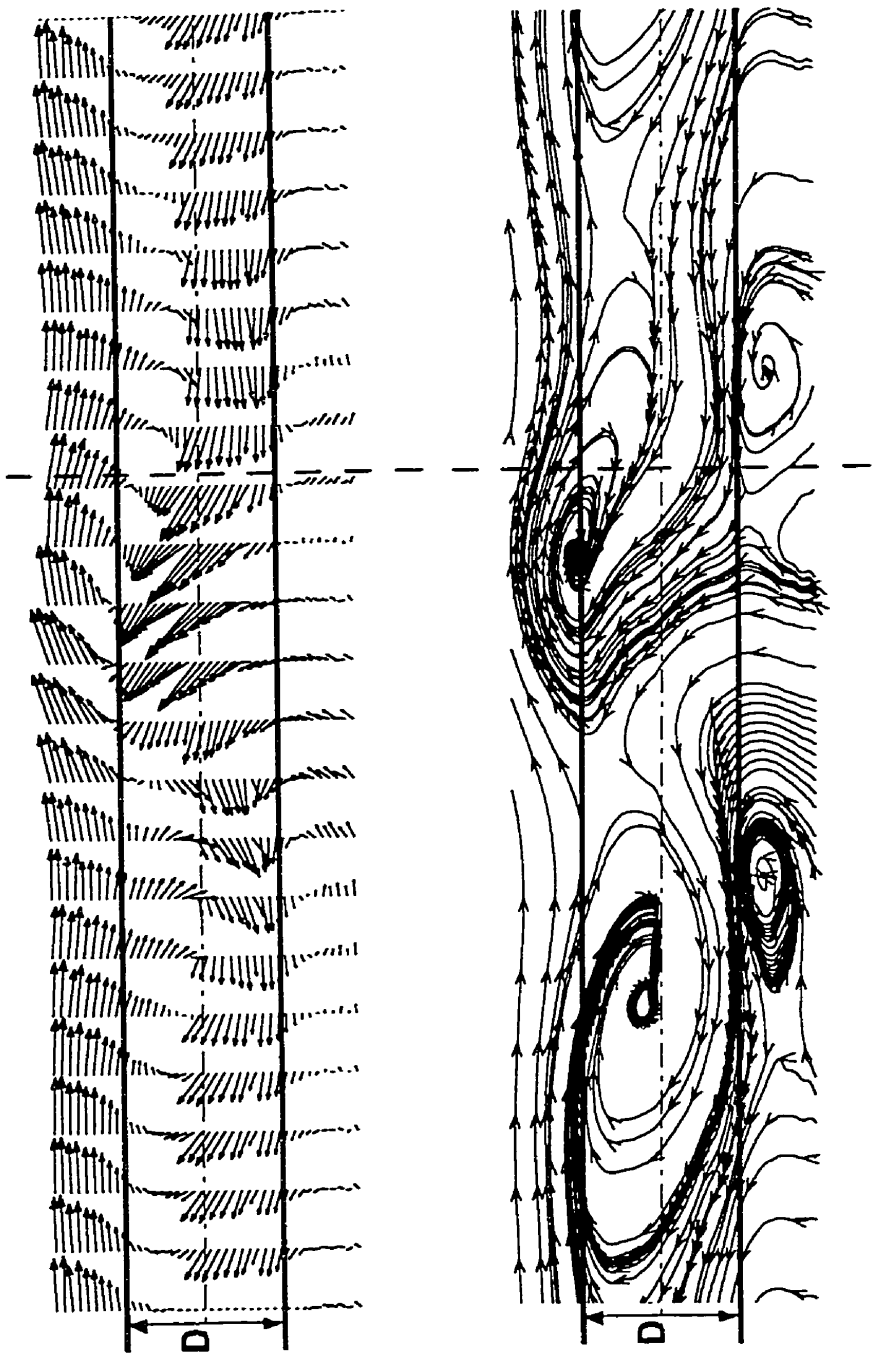

Figure 8.30 A cross section, at y equal to half the gap width, of the measured coherent velocity field of Figure 8.29, shown in a vector plot and visualized by software generated pathlines (W/D=1.100).

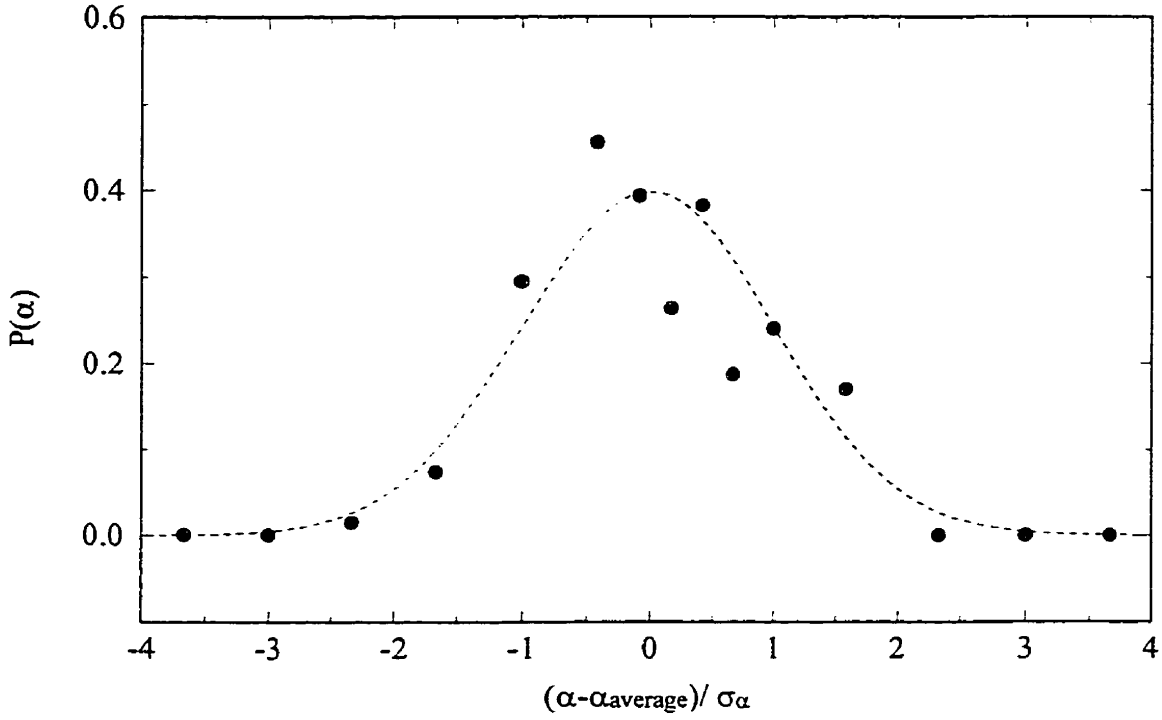

Figure 8.31 Probability density function (Pdf) of the expansion/contraction factor α (σ_α = 0.284 $\alpha_{average}$).

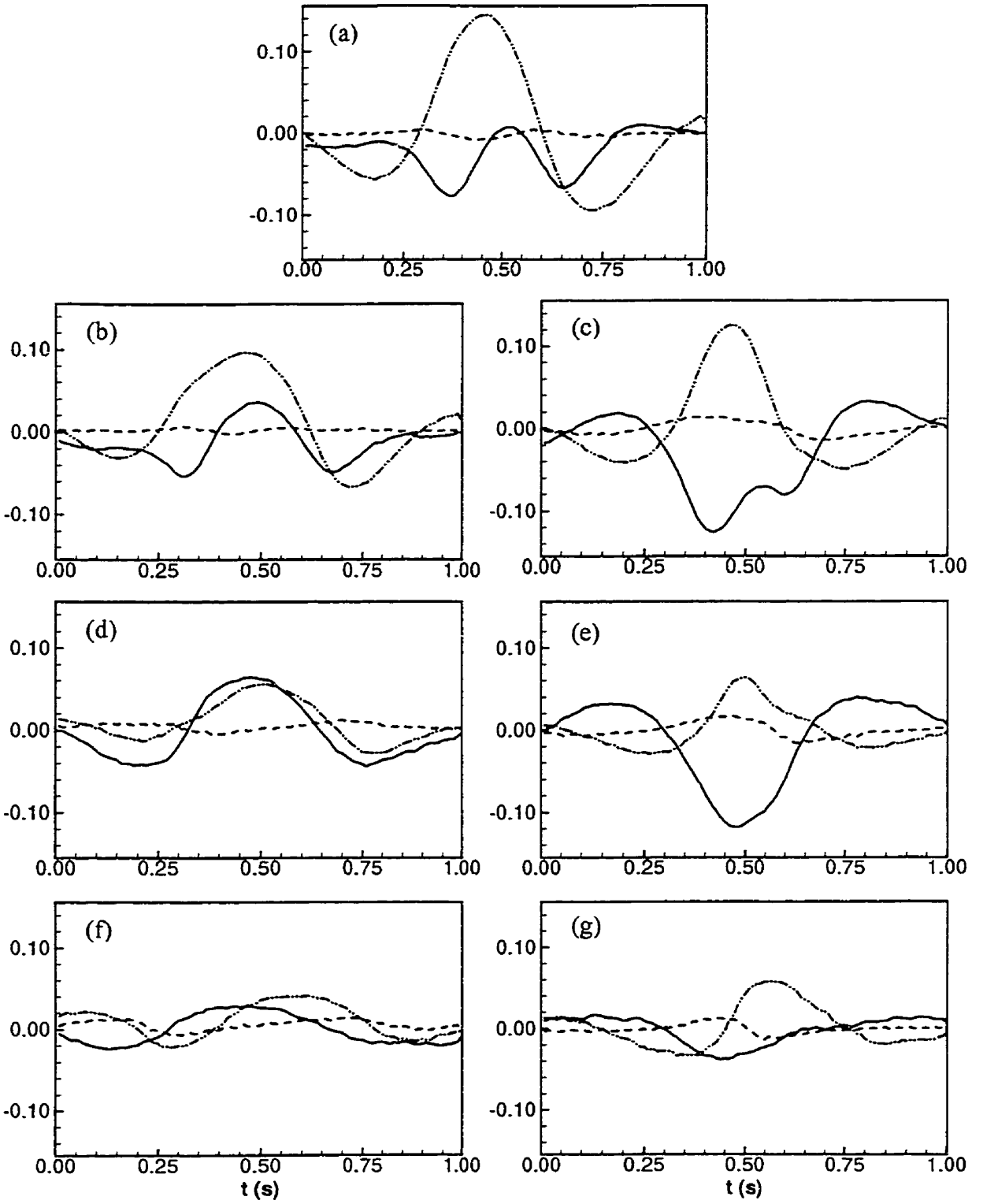

Figure 8.32 Examples of coherent velocities, educed by the enhanced VITA technique, $\tilde{U}/U_b$ (———), $\tilde{V}/U_b$ (----) and $\tilde{W}/U_b$ (·····) at (a) y/D=0.050 and z/D=0.000,(b) y/D=0.050 and z/D=-0.200,(c) y/D=0.050 and z/D=0.200,(d) y/D=0.050 and z/D=-0.400,(e) y/D=0.050 and z/D=0.400,(f) y/D=0.050 and z/D=-0.600,(g) y/D=0.050 and z/D=0.600.

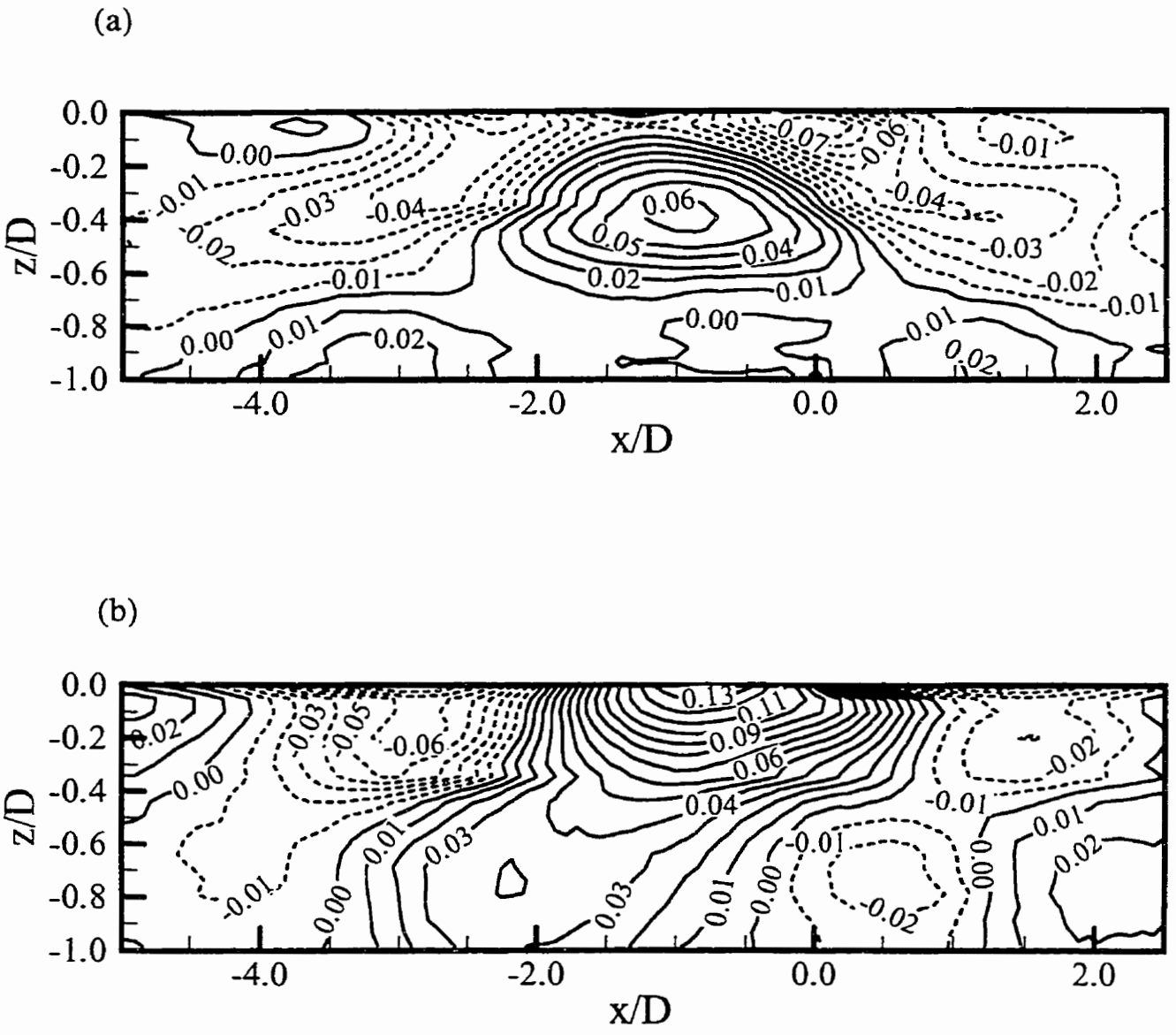

Figure 8.33 Contours of (a) the streamwise, $\tilde{U}$, and (b) the spanwise, $\tilde{W}$, coherent velocities, normalized by the bulk velocity, U_b , in the plane at y equal to half the gap width (W/D =1.100). The detection location is at x/D= 0.

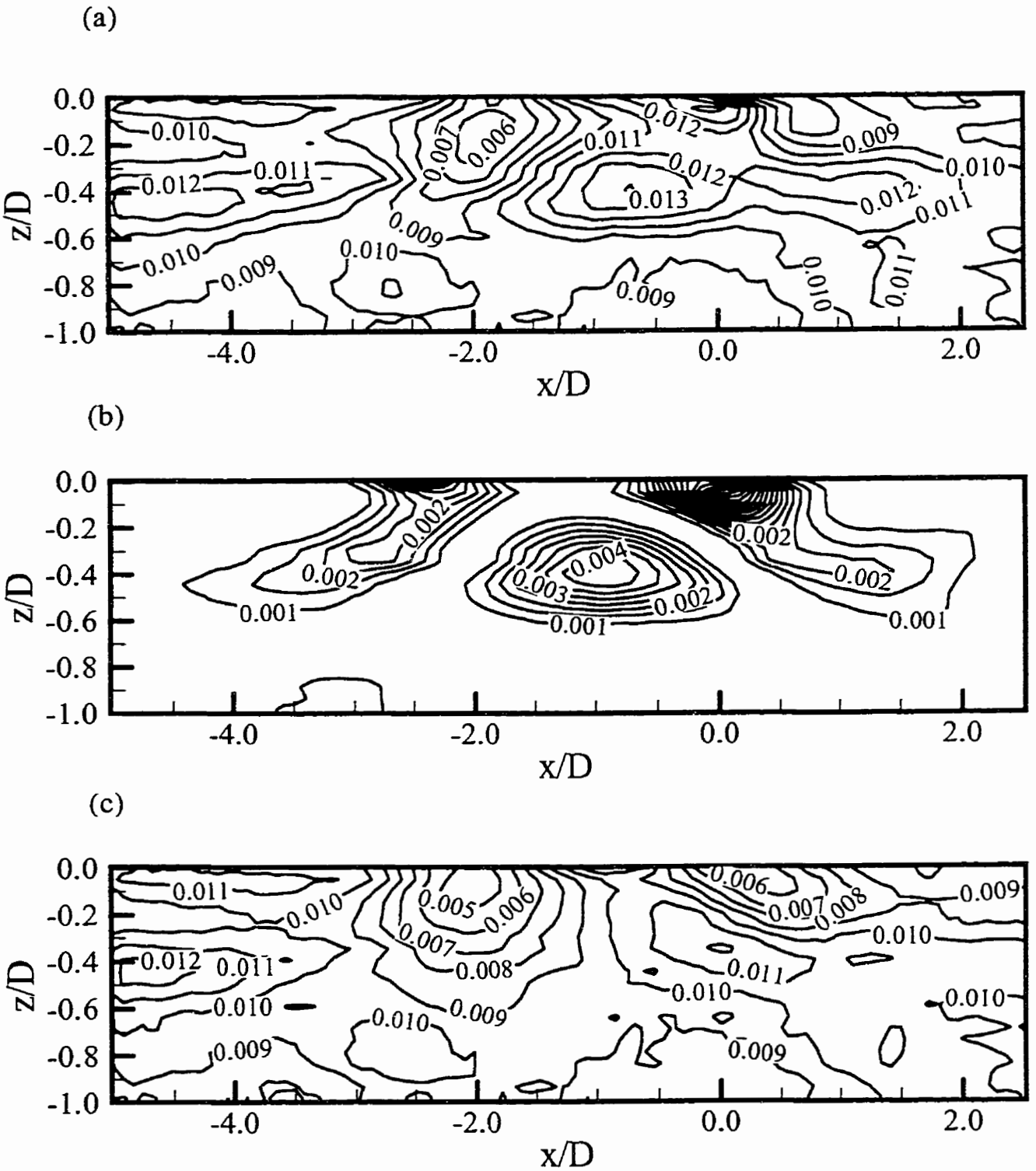

Figure 8.34 Contours of (a) $< (U-\bar{U})^2 > / U_b^2$, (b) $\tilde{U}^2 / U_b^2$, and (c) $< u_r^2 > / U_b^2$ in the plane at y equal to half the gap width (W/D =1.100). The detection location is at x/D= 0.

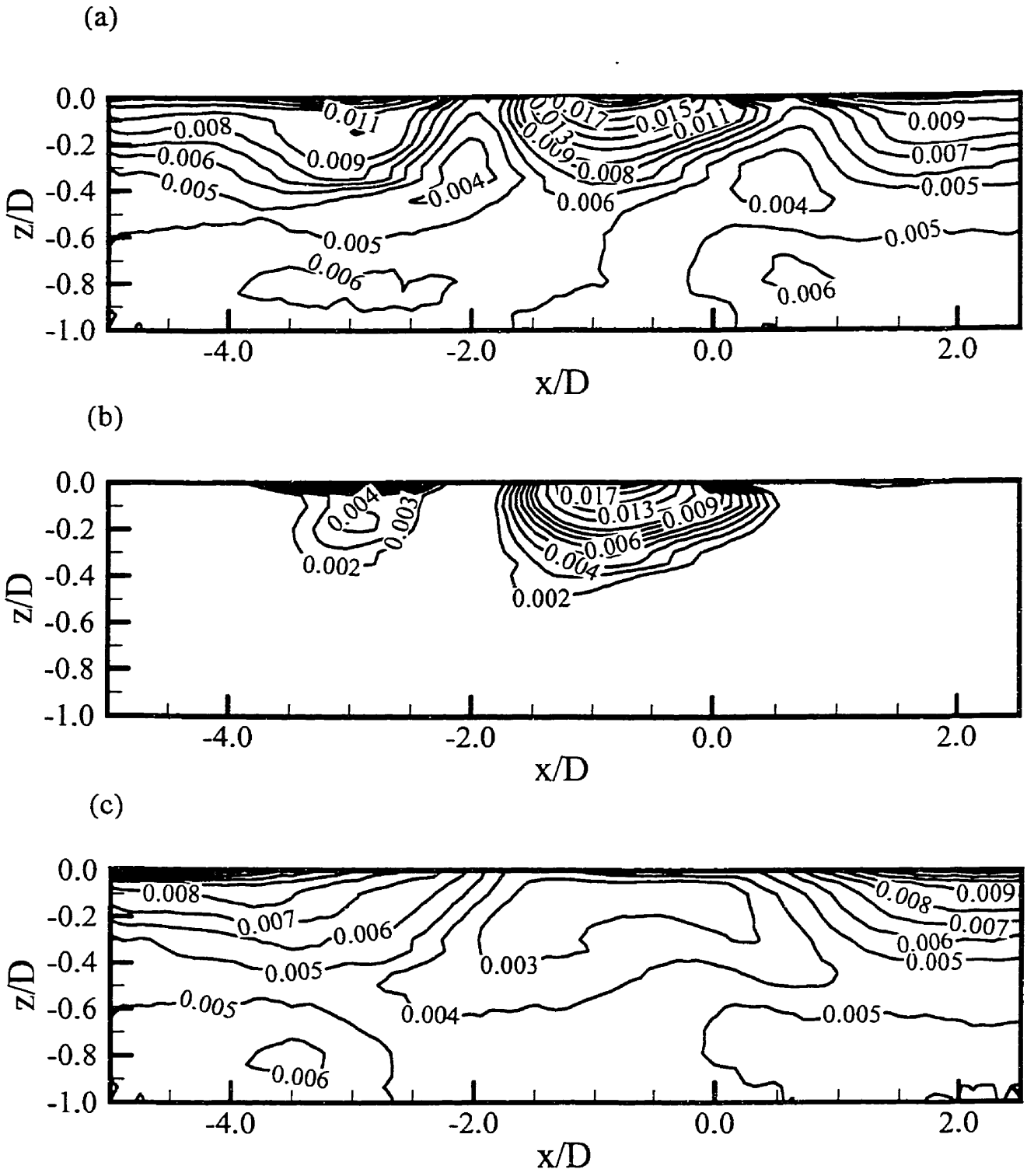

Figure 8.35 Contours of (a) $\langle(W-\overline{W})^2\rangle/U_b^2$, (b) $\tilde{W}^2/U_b^2$, and (c) $\langle w_r^2\rangle/U_b^2$ in the plane at y equal to half the gap width (W/D =1.100). The detection location is at x/D= 0.

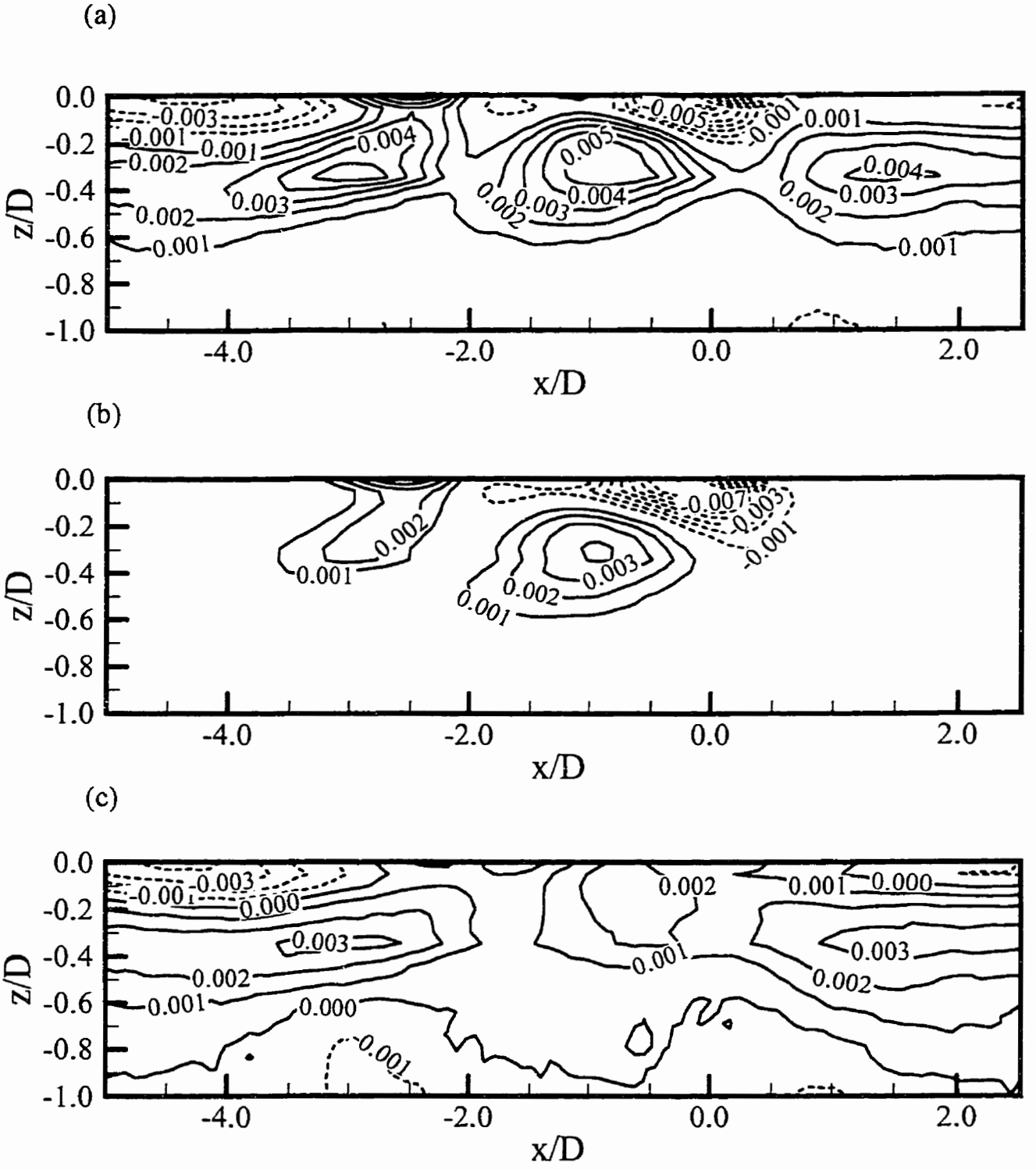

Figure 8.36 Contours of (a) $\langle (U-\overline{U})(W-\overline{W})\rangle / U_b^2$, (b) $\tilde{U}\tilde{W}/U_b^2$, and (c) $\langle u_r w_r \rangle / U_b^2$ in the plane at y equal to half the gap width (W/D =1.100). The detection location is at x/D= 0.

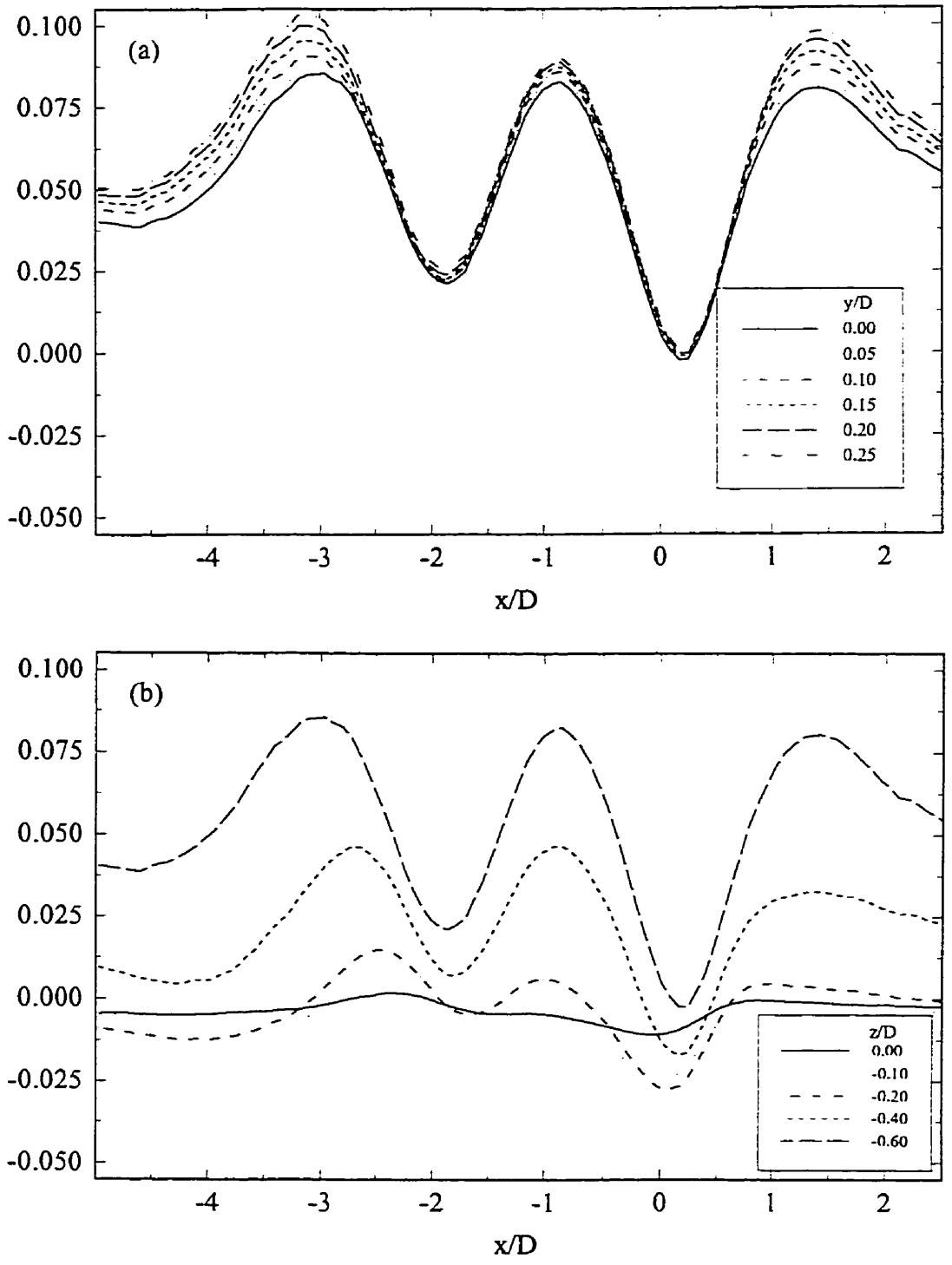

Figure 8.37 Samples of streamwise profiles of $<(U-\overline{U})(W-\overline{W})>/U_b^2$ at (a) $z/D = 0.60$ and (b) $y/D = 0.05$ (W/D =1.100).

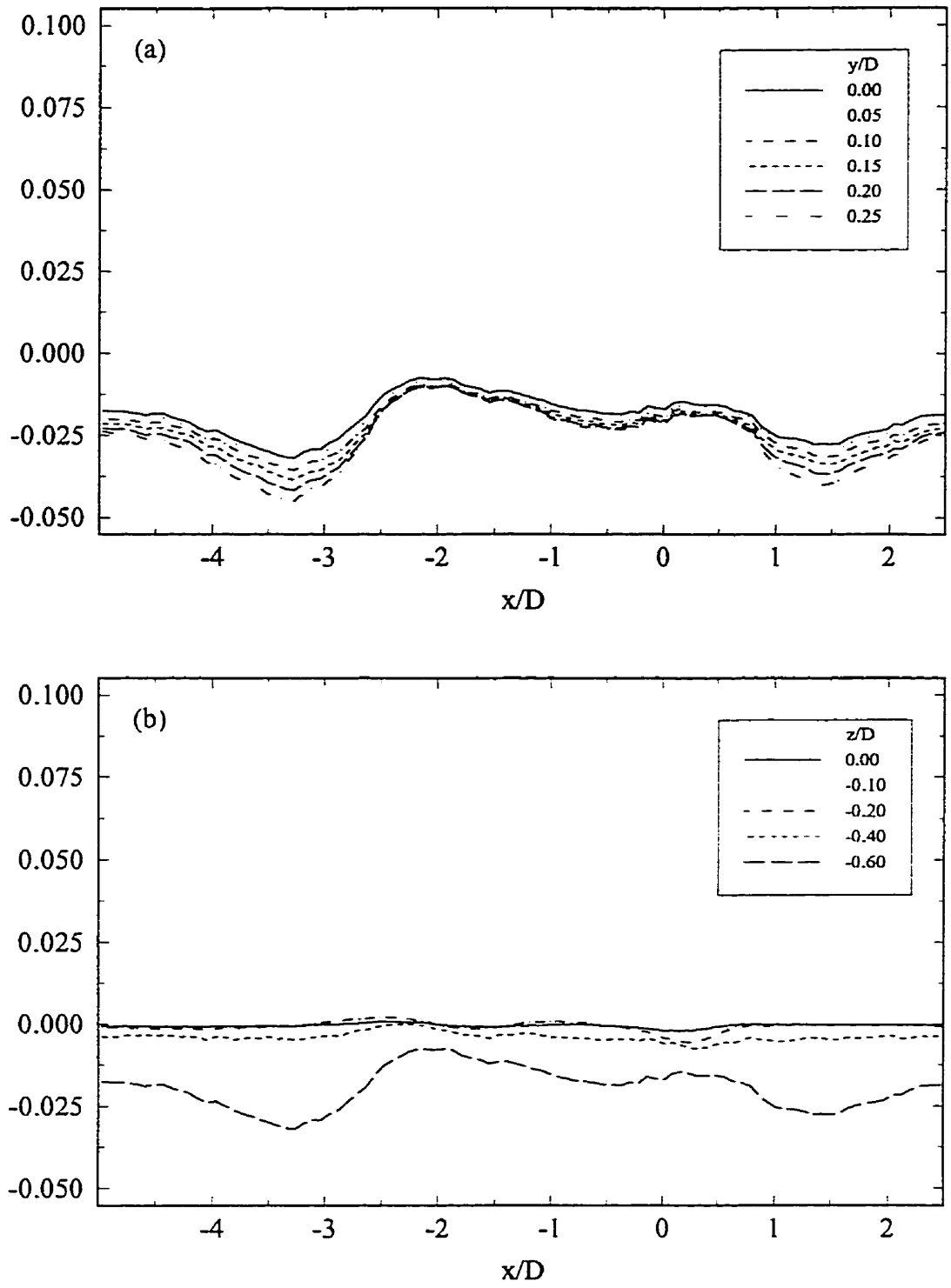

Figure 8.38 Samples of streamwise profiles of $<(U-\overline{U})(V-\overline{V})>/U_b^2$ at (a) $z/D = 0.60$ and (b) $y/D = 0.05$ ($W/D = 1.100$).

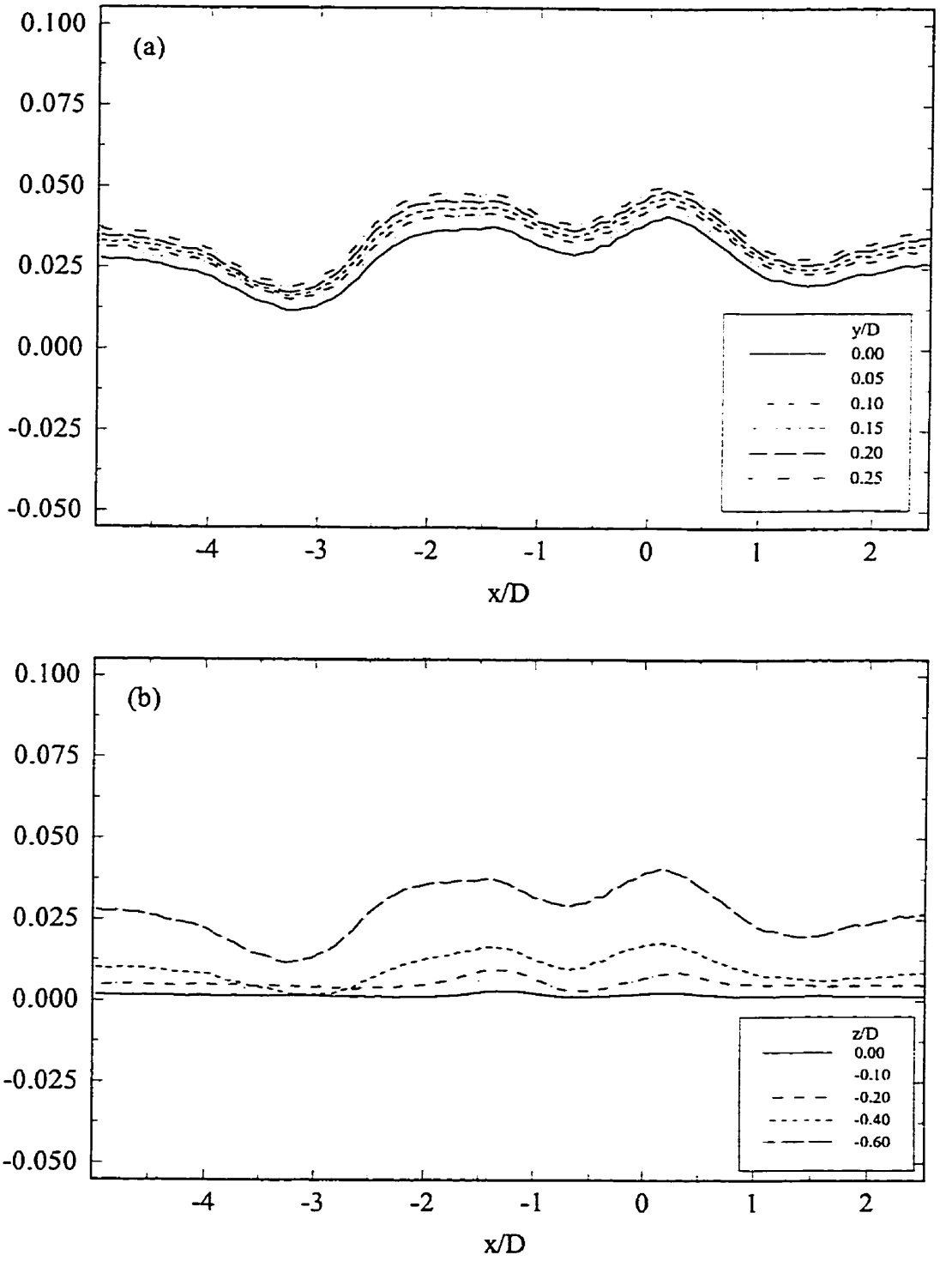

Figure 8.39 Samples of streamwise profiles of $\langle (V-\overline{V})(W-\overline{W})\rangle / U_b^2$ at $z/D = 0.60$ and (b) $y/D = 0.05$ ($W/D = 1.100$).

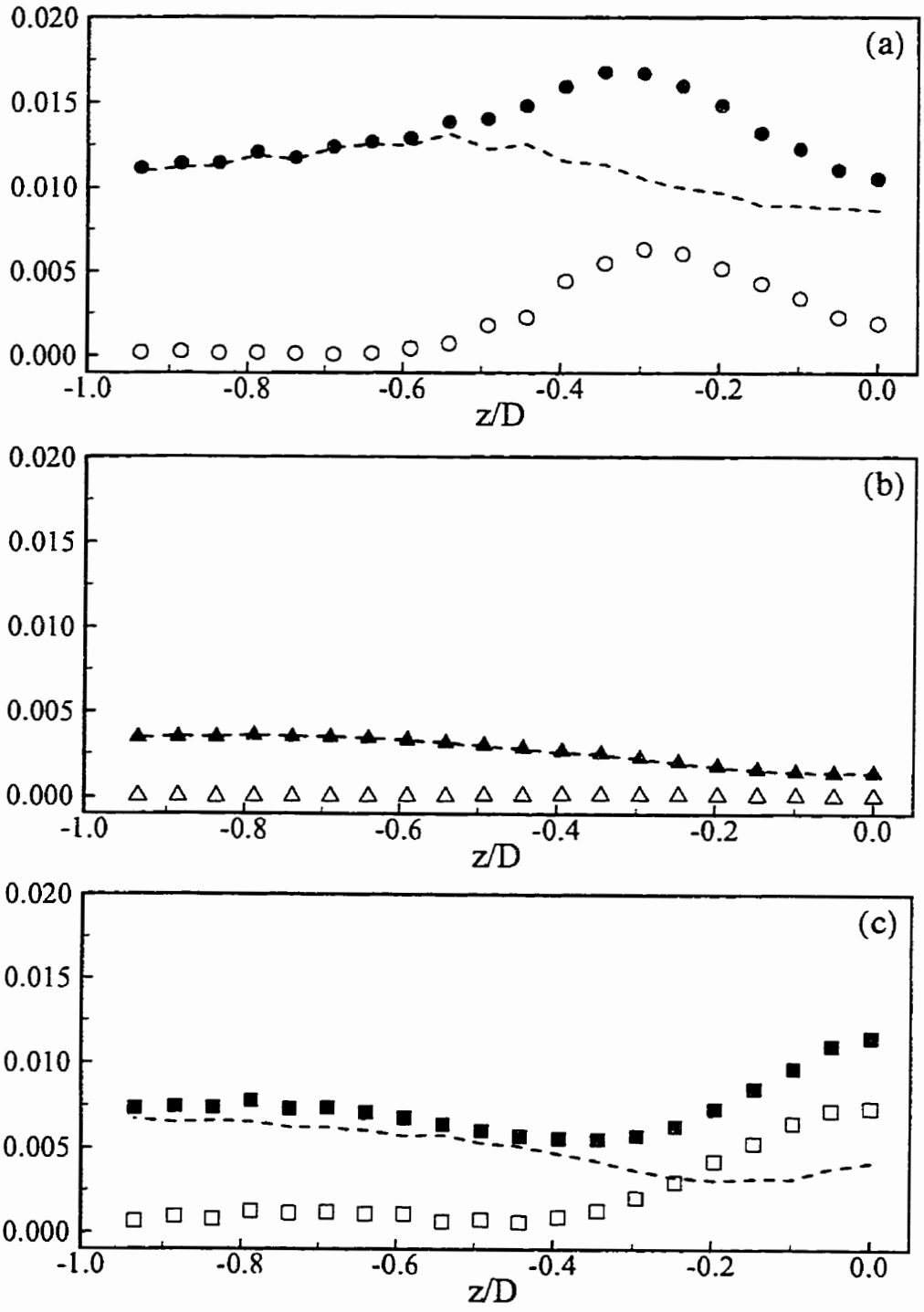

Figure 8.40 Spanwise profiles of (a) $\overline{\tilde{U}^2}/U_b^2$ (○), $\overline{u^2}/U_b^2$ (●), and $\overline{u_r^2}/U_b^2$ (----) ;
(b) $\overline{\tilde{V}^2}/U_b^2$ (△), $\overline{v^2}/U_b^2$ (▲), and $\overline{v_r^2}/U_b^2$ (----) ; and
(c) $\overline{\tilde{W}^2}/U_b^2$ (■), $\overline{w^2}/U_b^2$ (□), and $\overline{w_r^2}/U_b^2$ (----) for $y/D = 0.050$ and W/D=1.100.

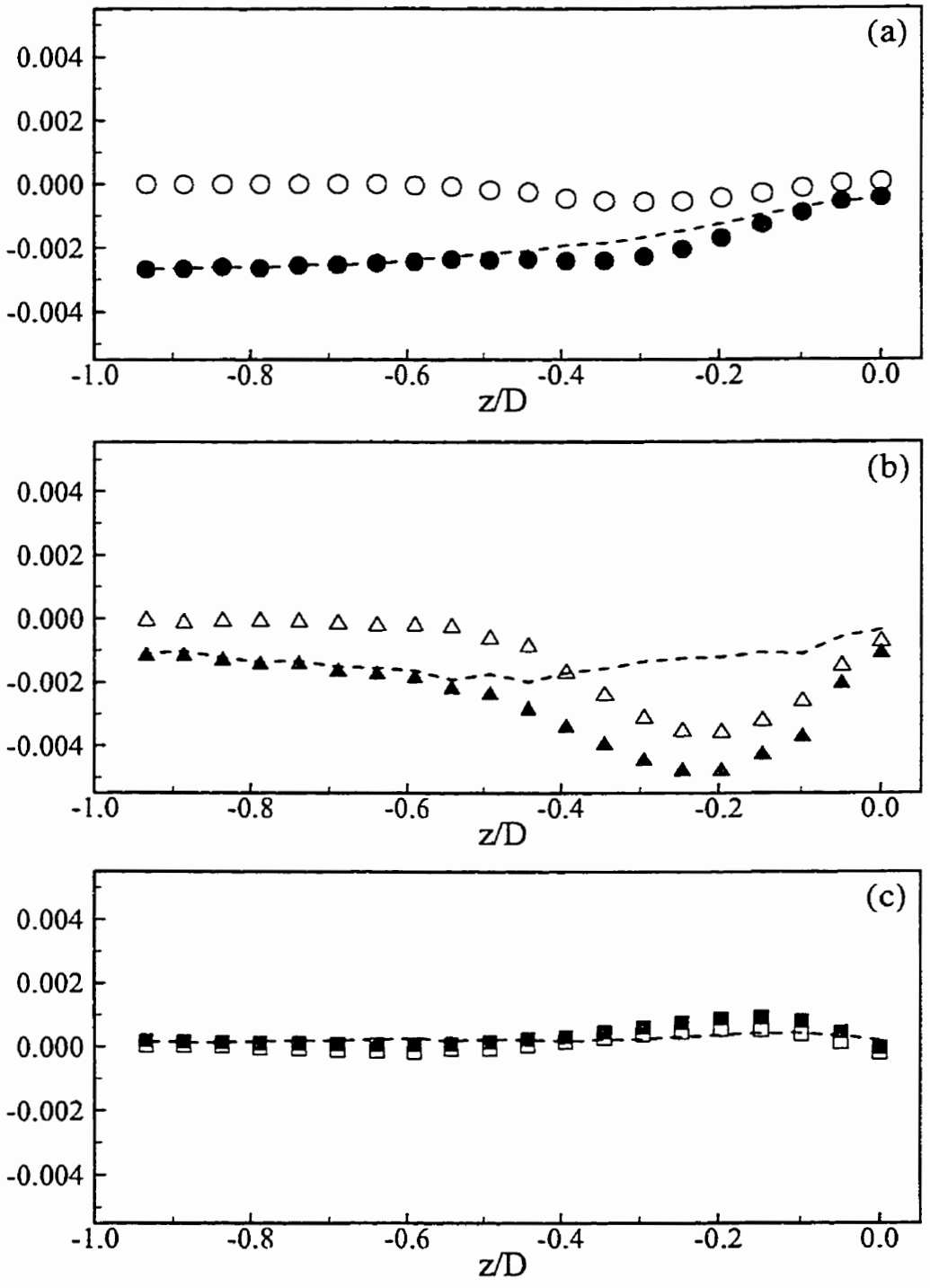

Figure 8.41 Spanwise profiles of (a) $\overline{\tilde{U}\tilde{V}}/U_b^2$ (○), $\overline{uv}/U_b^2$ (●), and $\overline{u_r v_r}/U_b^2$ (----) ; (b) $\overline{\tilde{U}\tilde{W}}/U_b^2$ (△), $\overline{uw}/U_b^2$ (▲), and $\overline{u_r w_r}/U_b^2$ (----) ; and (c) $\overline{\tilde{V}\tilde{W}}/U_b^2$ (■), $\overline{vw}/U_b^2$ (□), and $\overline{v_r w_r}/U_b^2$ (----) for $y/D = 0.050$ and W/D=1.100.

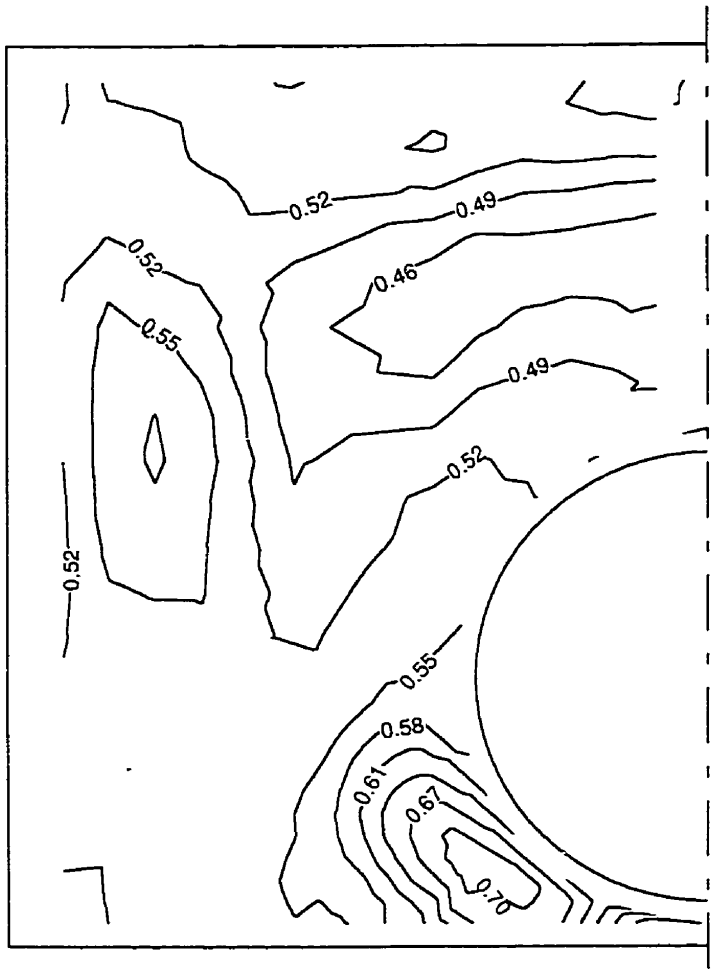

Figure 9.1 Contours of constant $\overline{u^2}/2k$ for W/D=1.100.

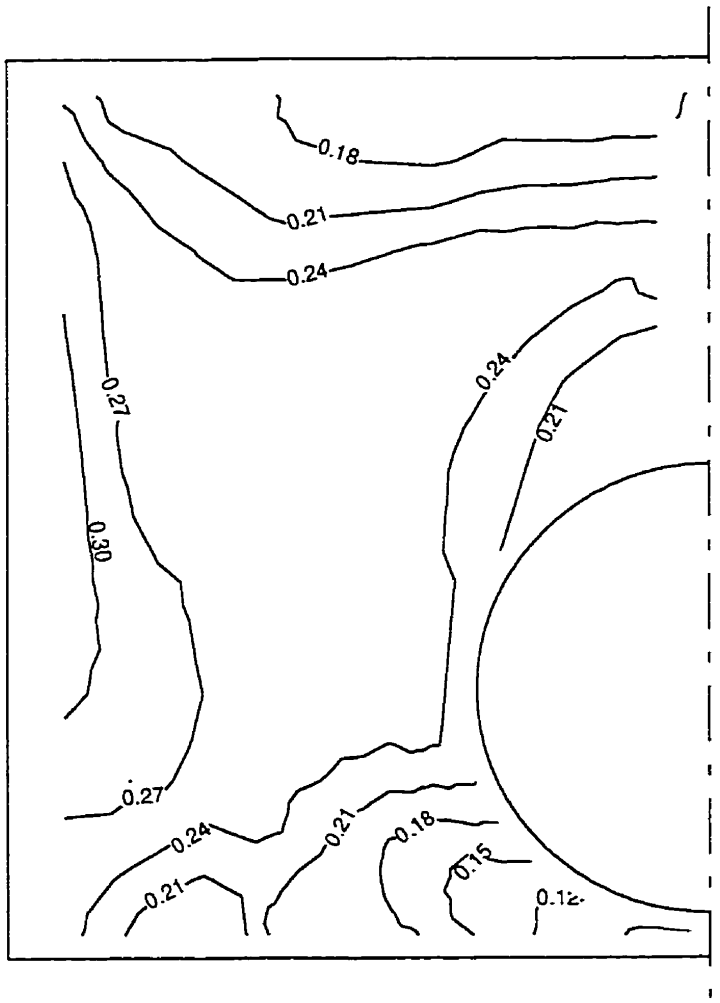

Figure 9.2 Contours of constant $\overline{v^2}/2k$ for W/D=1.100.

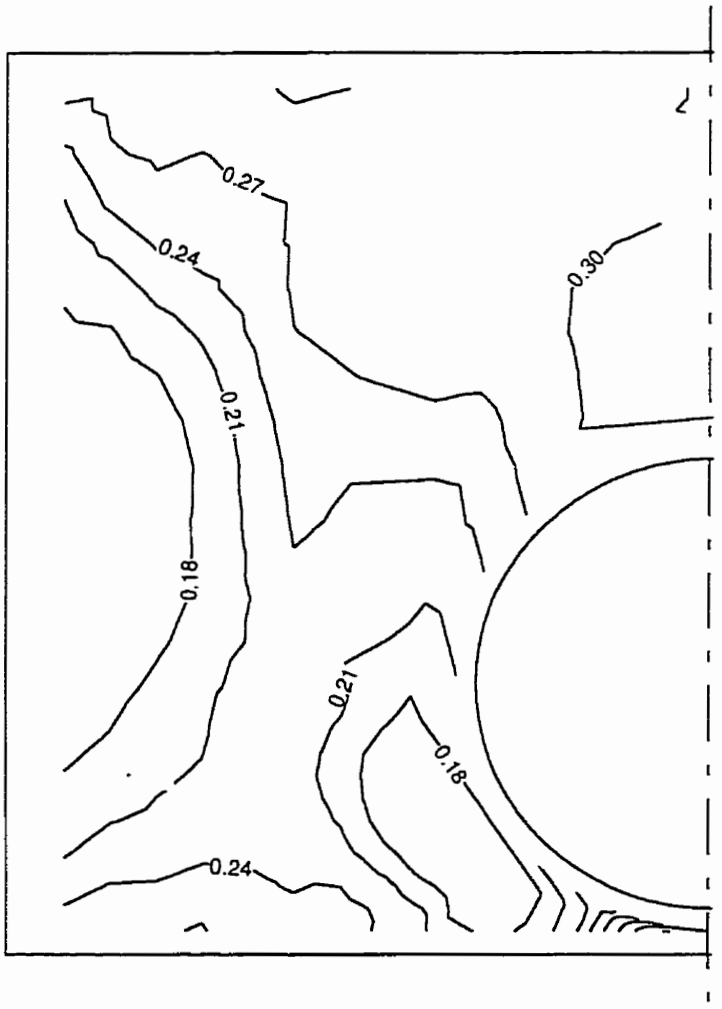

Figure 9.3 Contours of constant $\overline{w^2}/2k$ for W/D=1.100.

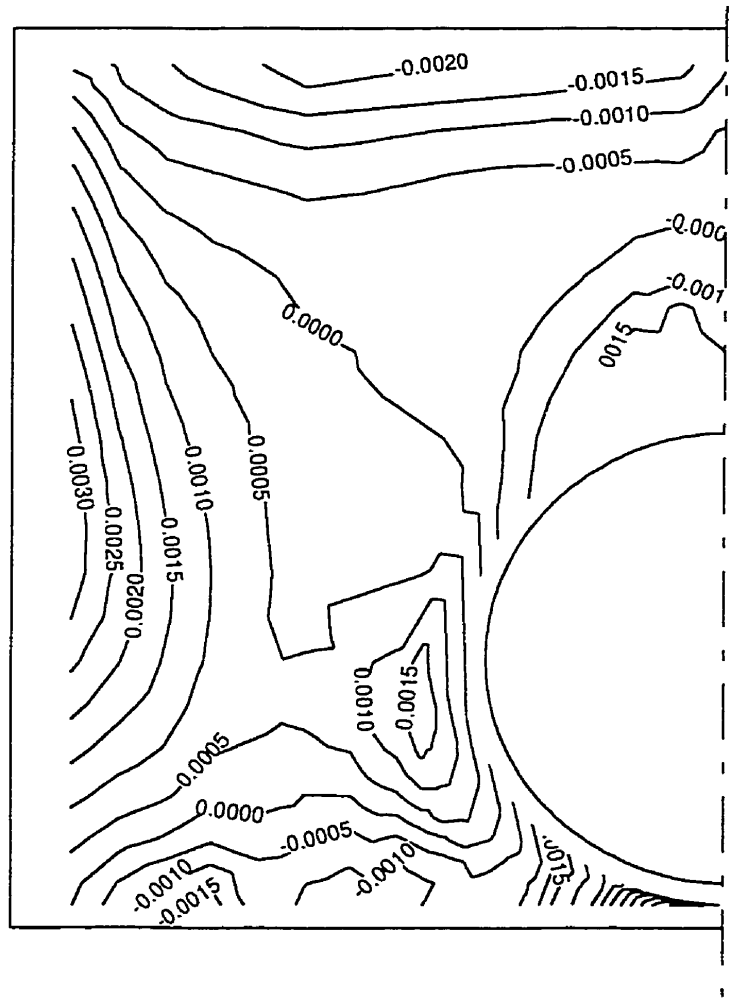

Figure 9.4 Contours of constant $\left(\overline{v^2}-\overline{w^2}\right)/U_b^2$ for W/D=1.100.

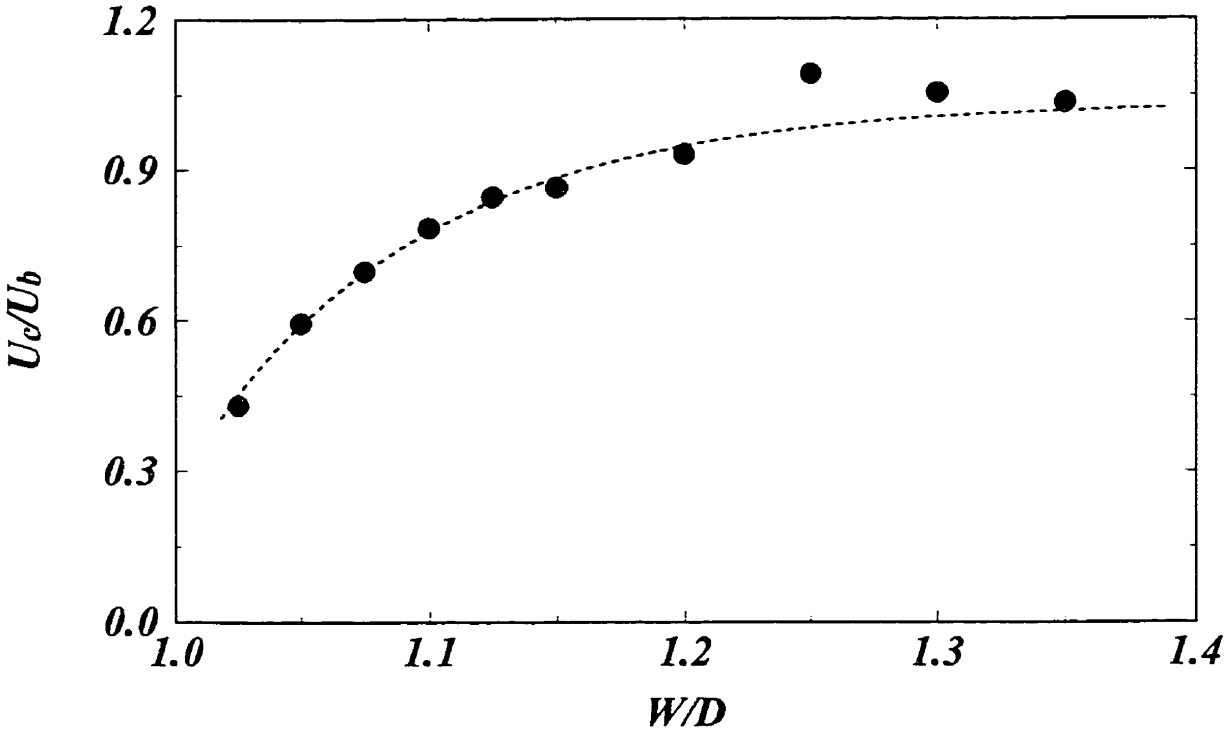

Figure 9.5 Average convective speed of the structures as a function of the wall subchannel width (the dashed line is the fitted relation of Equation(3) in chapter 9) .

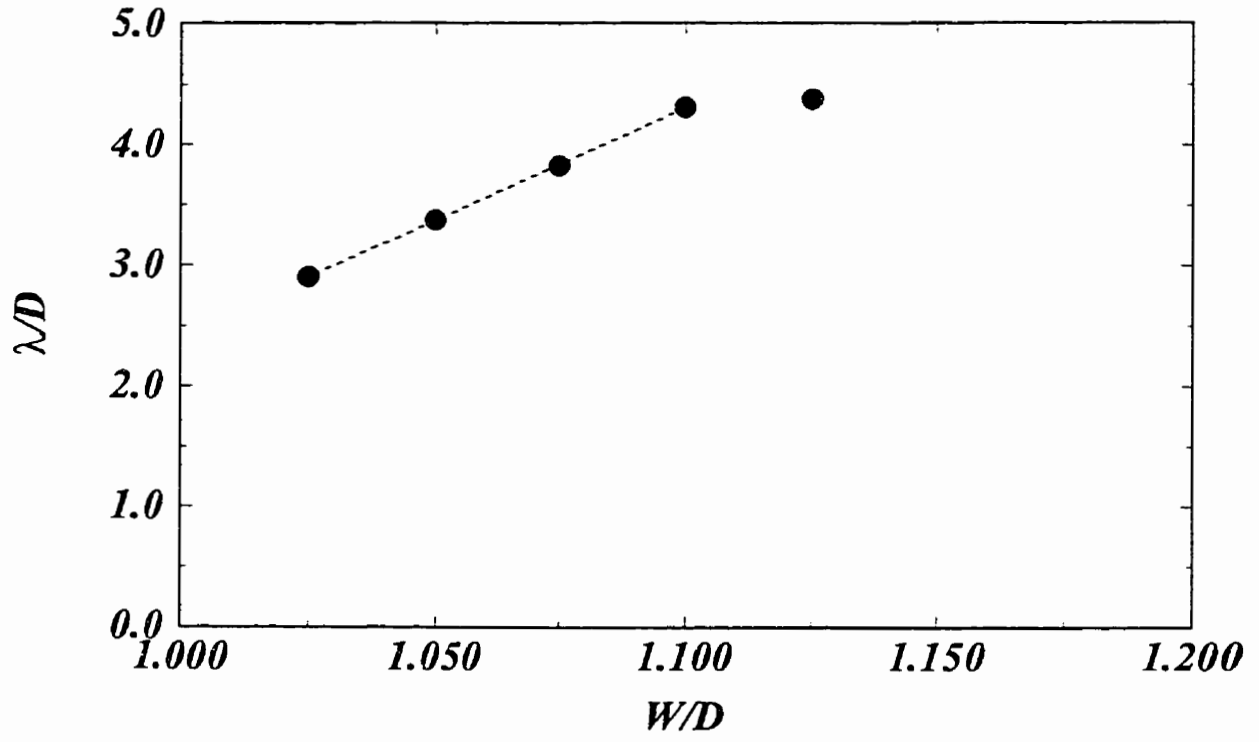

Figure 9.6 Average streamwise spacing of the structures as a function of the wall subchannel width (the dashed line is the fitted relation of Equation(5) in chapter 9) .

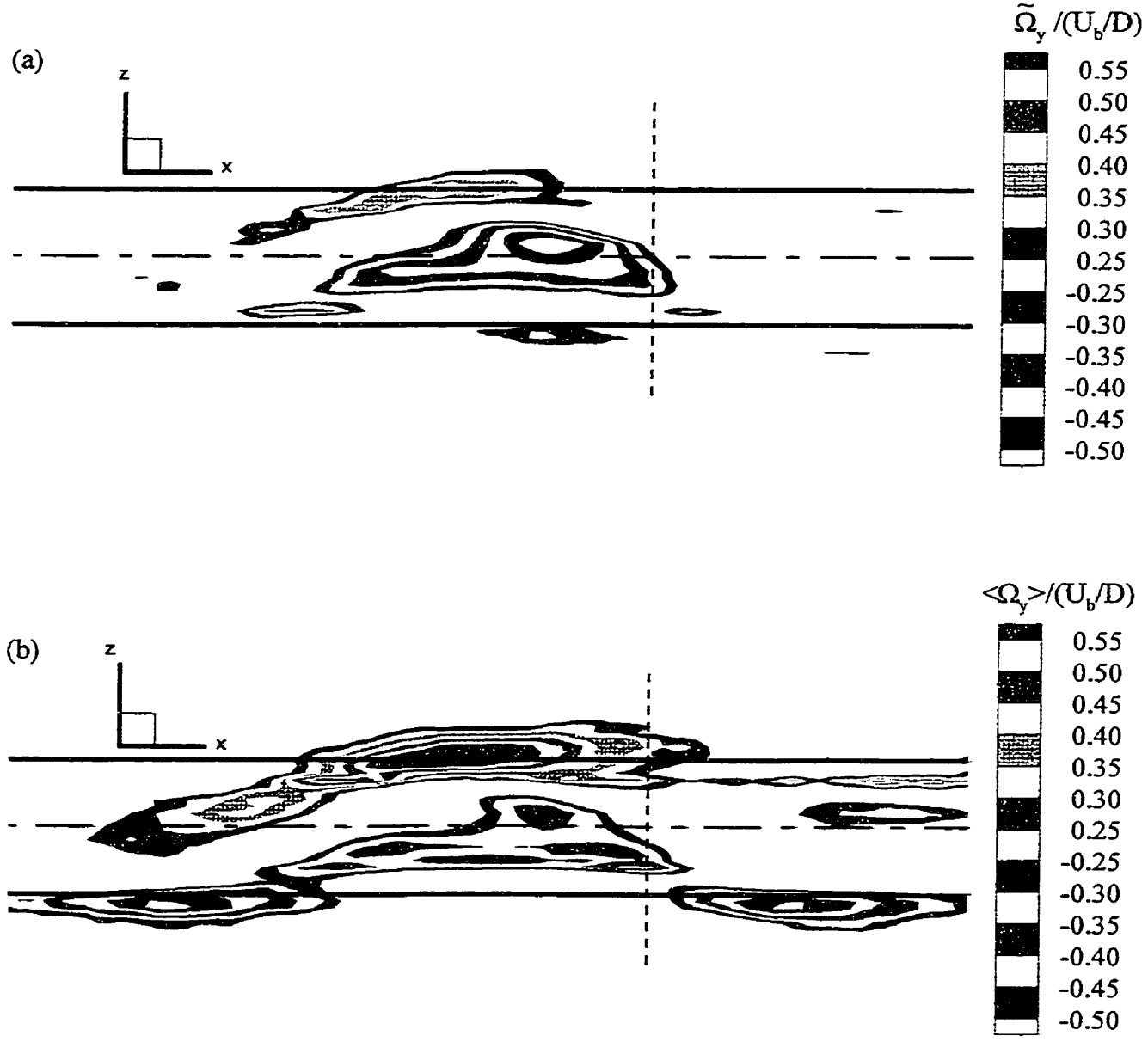

Figure 9.7 Contours of the coherent transverse vorticity according to (a) the triple decomposition and (b) the double decomposition. Cross-section at a height equal to half the gap width for W/D=1.100 (the dashed lines represent the detection location).

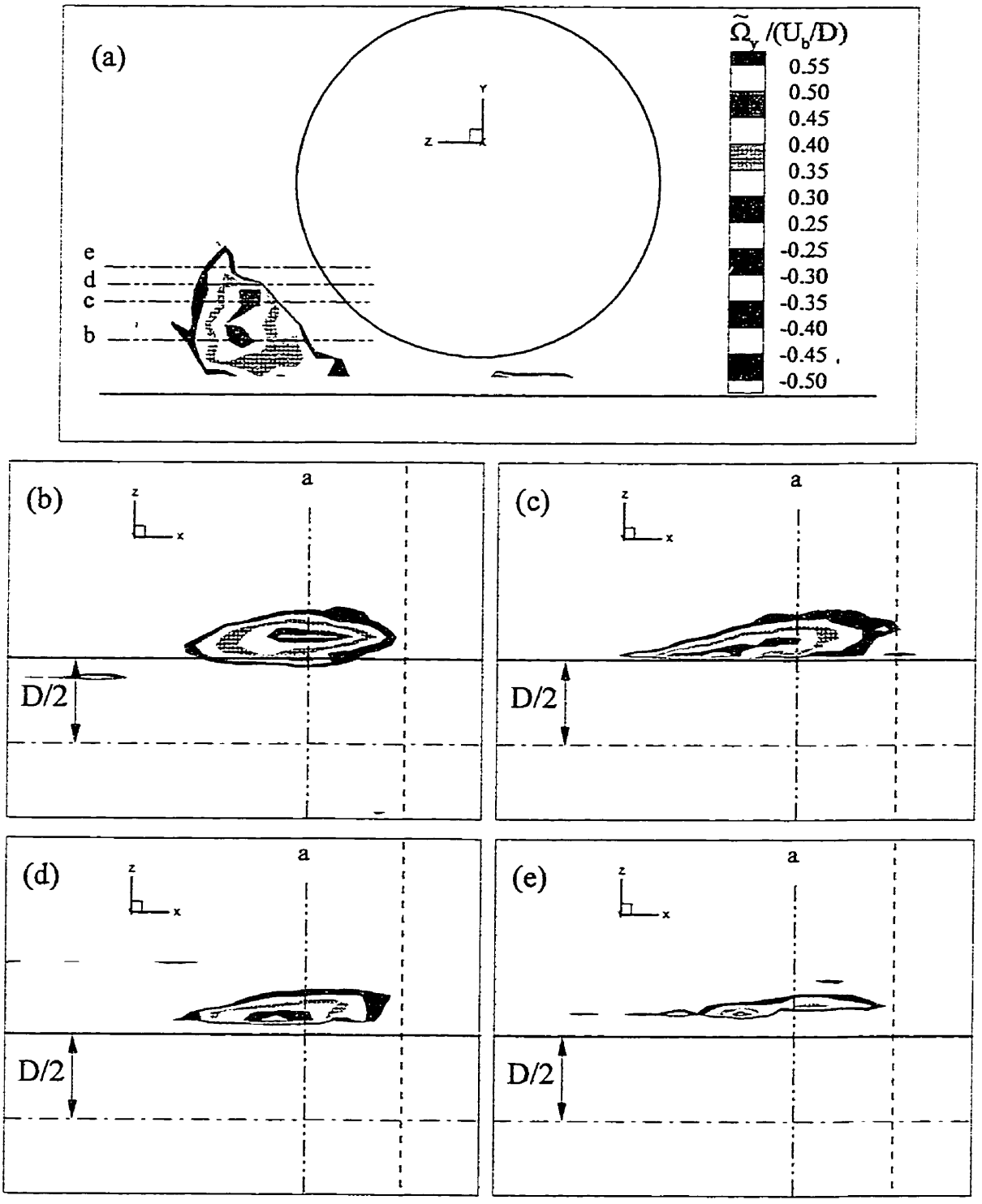

Figure 9.8 Contoursof the coherent transverse vorticity according to the triple decomposition. Spanwise and transverse cross-sections (the dashed lines represent the detection location).

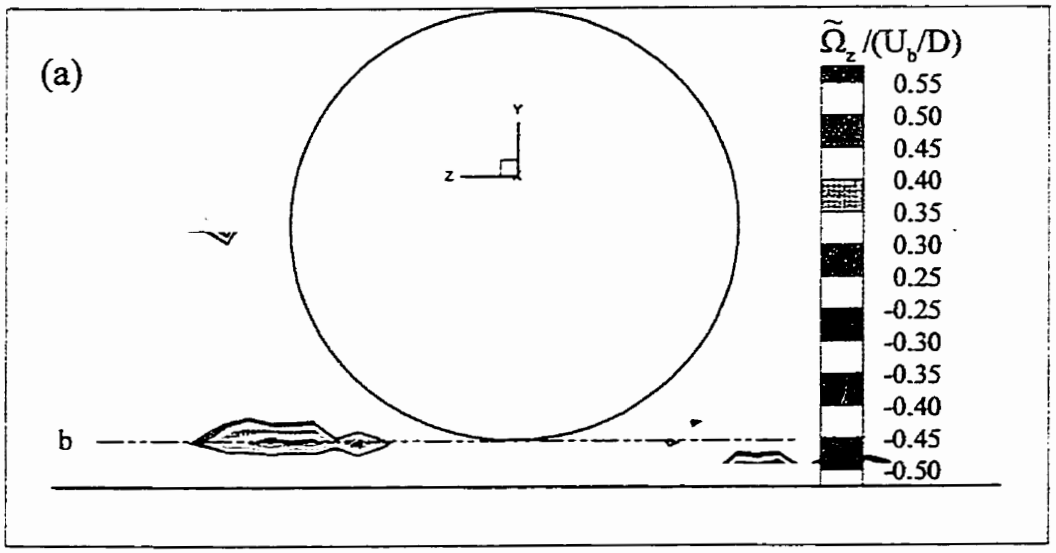

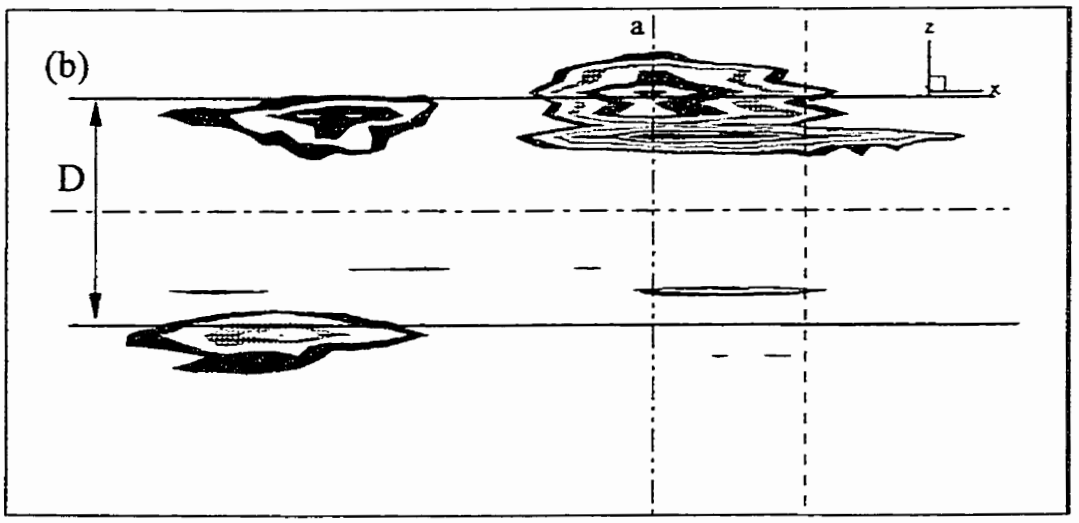

Figure 9.9 Contours of the coherent spanwise vorticity according to the triple decomposition. Spanwise and transverse cross-sections (the dashed lines represent the detection location).

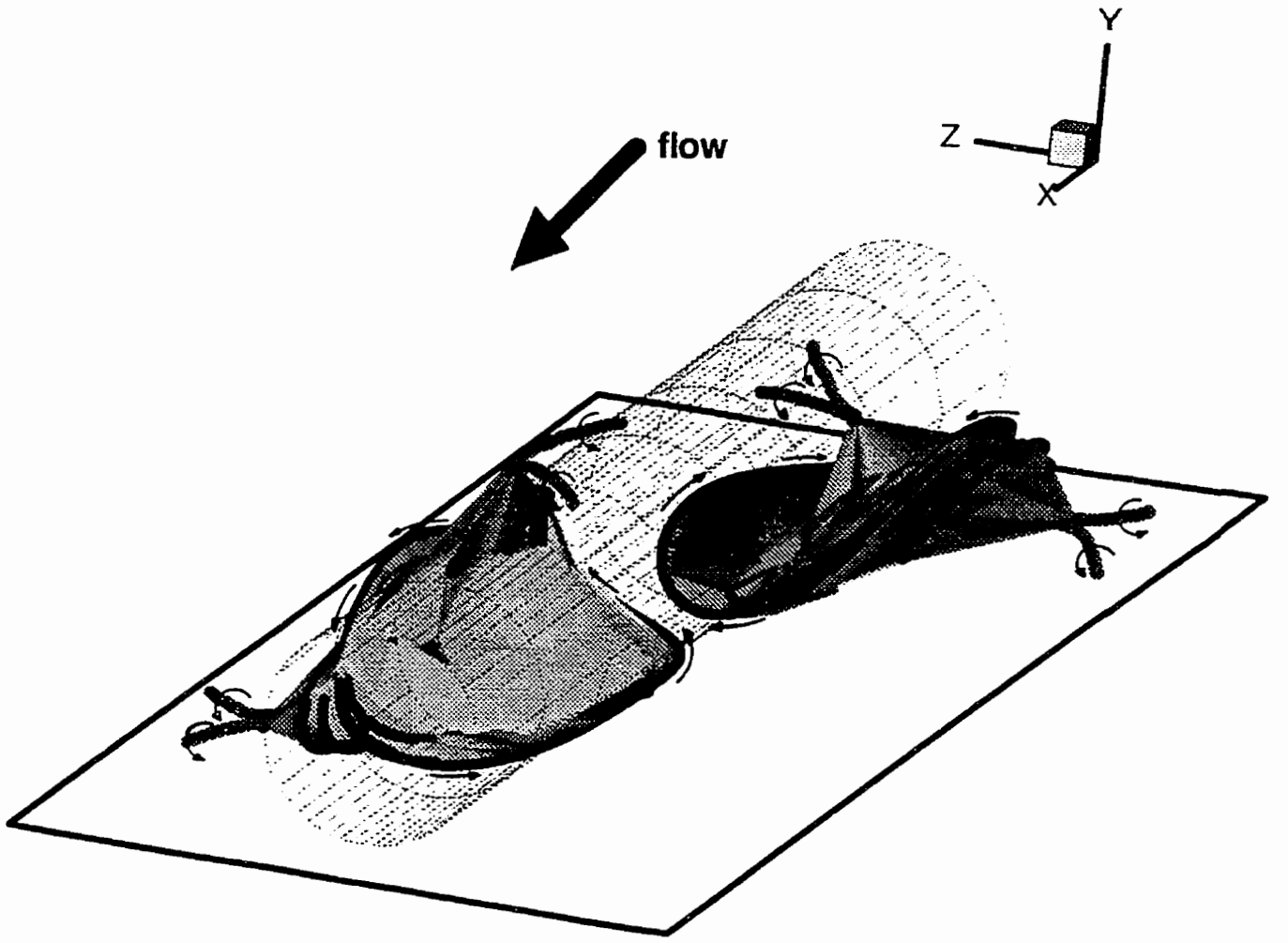

Figure 9.10 Sketch of a physical model of the coherent structures that form in the gap region.

Appendix

Sequence of Video Frames of Smoke-Visualization of Coherent Structures

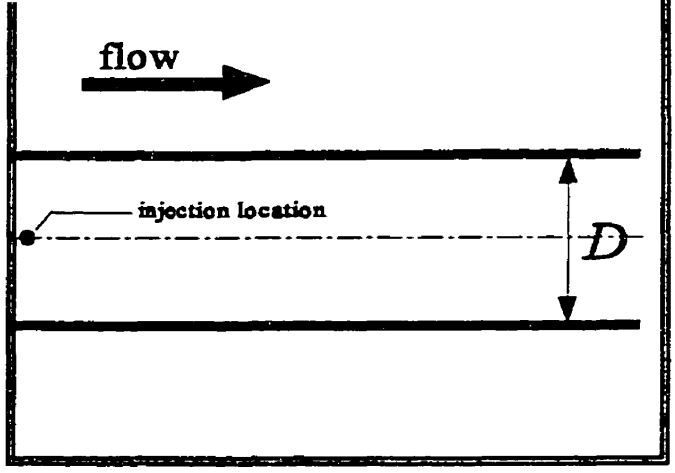

Information Pertinent to the Presented Sequence of Video Frames

- The frames correspond to a bottom view of the test-section.
- The flow is from left to right.
- Smoke was isokinetically injected in the centre of the gap.
- The rod is shown in the figure above with the same scale and at the same location as in the video frames.
- The presented frames are separated by a time lapse equal to 4 s.
- The Reynolds number, based on the bulk velocity and the hydraulic diameter of the entire channel, was Re_h = 16,000.
- The gap width was such that W/D=1.050.

Instruction for use

To view an animated sequence of flow visualization frames, hold the corresponding 13 pages together from the top right corner, bend at a 45° angle and release the pages one by one at a steady rate.

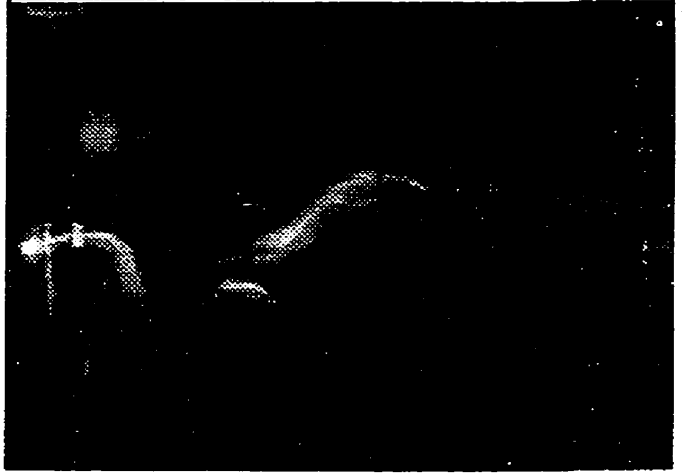

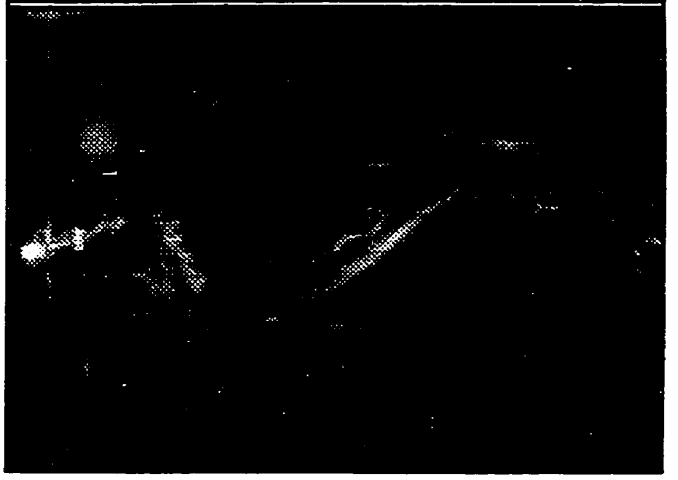

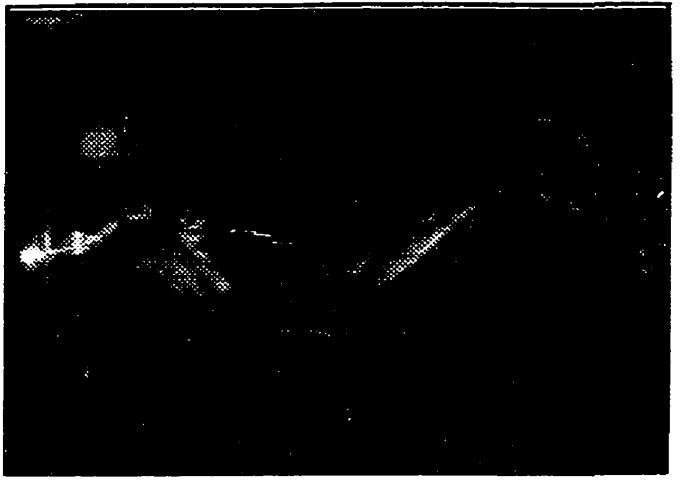

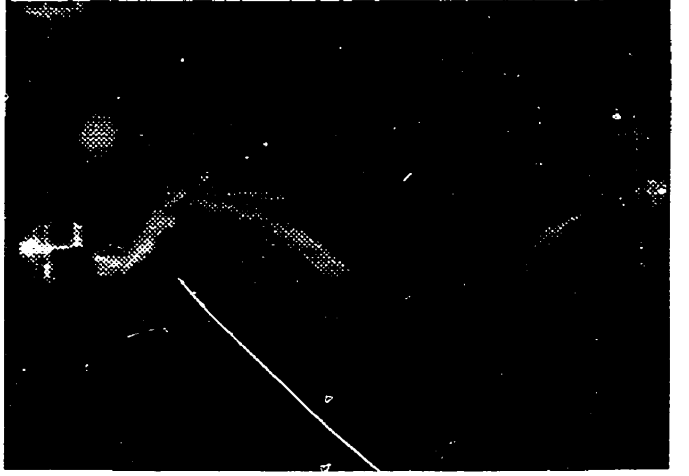

IMAGE EVALUATION
TEST TARGET (QA-3)

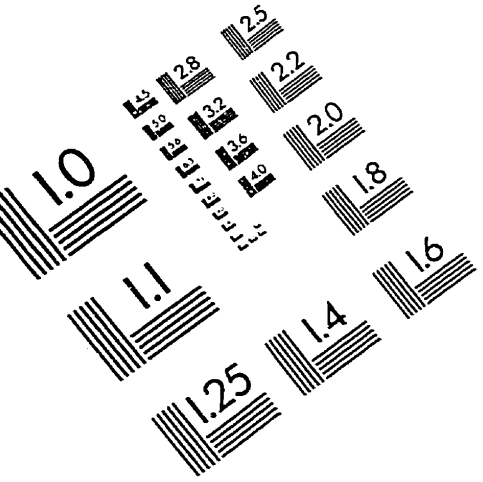

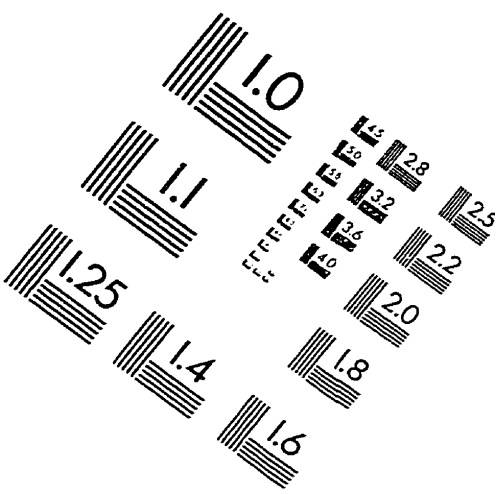

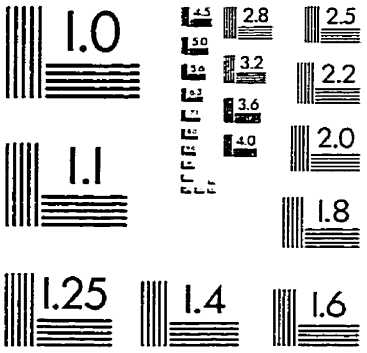

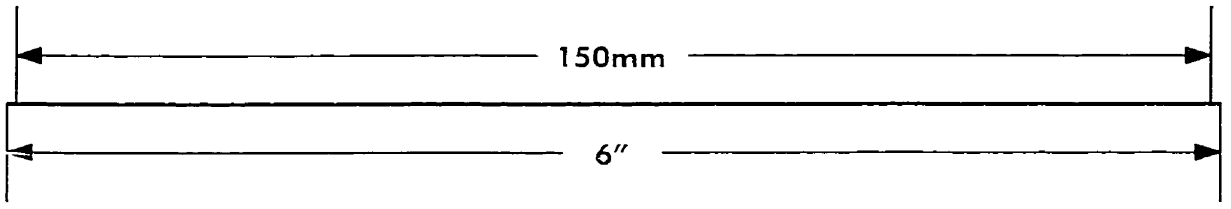

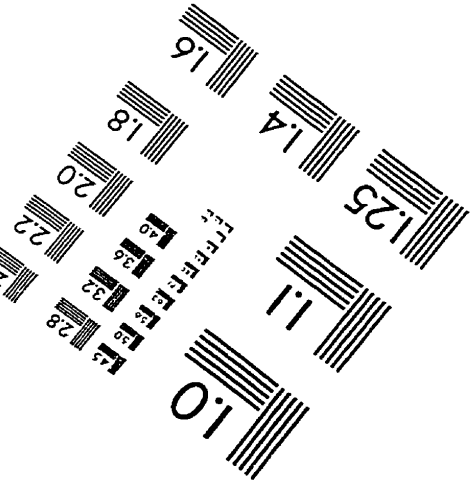

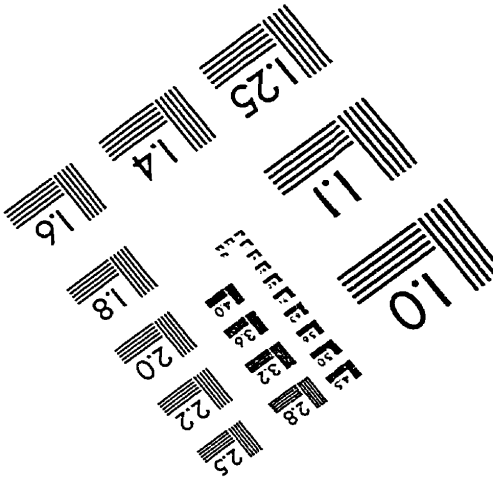

APPLIED IMAGE, Inc
1653 East Main Street
Rochester, NY 14609 USA
Phone: 716/482-0300
Fax: 716/288-5989